X-ray spectral and timing properties of the High Mass X-ray Binaries GX 304-1 and Vela X-1

Dissertation

der Mathematisch-Naturwissenschaftlichen Fakultät
der Eberhard Karls Universität Tübingen
zur Erlangung des Grades eines
Doktors der Naturwissenschaften
(Dr. rer. nat.)

vorgelegt von
Christian Malacaria
aus Catanzaro, Italy

Tübingen

2016

Tag der mündlichen Qualifikation: 29.9.2016

Dekan:	Prof. Wolfgang Rosenstiel
1. Berichterstatter:	Prof. Dr. Andrea Santangelo
2. Berichterstatter:	Prof. Dr. Kazuo Makishima

Every man and every woman is a star

Liber AL vel Legis

Abstract

Accreting X-ray pulsars are binary systems hosting a rotating, highly magnetized neutron star, and an optical companion star whose expelled plasma is accreted onto the compact object, a process that eventually leads to pulsed X-ray emission. Discovered more than forty years ago, substantial progress has been reached in the comprehension of these objects, in terms of both their individual binary components and of the X-ray emission properties. However, further efforts (both observational and theoretical) are needed to constrain the many unsolved aspects. Among the key open issues there are the details of the emission mechanism, the geometry and the radiation beaming pattern of the accretion structure, as well as the influence of the optical companion on the observed X-ray properties.

This thesis is focused on the spectroscopical and timing analysis of two accreting X-ray pulsars: the Be/X-ray Binary GX 304-1, and the wind-fed binary Vela X-1. *INTEGRAL* data ($5-100\,\mathrm{keV}$) have been used for the analysis of GX 304-1, which was observed during a bright outburst in 2012. *MAXI* data ($2-20\,\mathrm{keV}$), on the other hand, provide continuous observations of Vela X-1 since 2009 and therefore offer a valuable opportunity for studying its orbital variability.

The *INTEGRAL* analysis of GX 304-1 allowed to characterize the spectral and timing behaviour of the source as a function of the luminosity. A timing solution valid throughout the outburst has been found, which allowed to construct pulse profiles at different luminosities and for different energy bands. The pulse profiles appear strongly luminosity-dependent, thus suggesting a change of the radiation beam pattern with luminosity. Pulse profiles also appear strongly energy-dependent, possibly due to a geometrical effect arising from the rotation of the neutron star or to a distorted magnetic dipole field. Also, contrary to other accreting pulsars, GX 304-1 pulse profiles show only a small pulsed fraction that does not correlate with energy nor luminosity. The pulse period has negative derivative during the accretion phase, implying a spin up episode, and likely indicating the presence of an accretion disk. The pulse-phase averaged spectroscopy confirms the correlation between the cyclotron line energy and the luminosity, with a more precise detector photon energy calibration, and therefore a better estimation of the neutron star magnetic field and of its critical luminosity. The spectral photon index and folding energy have been found to be negatively correlated with luminosity (as expected for a Comptonization spectrum), thus suggesting that Compton cooling becomes more efficient at higher luminosities. The timing solution has also been used to identify pulse-phases of the rotating neutron star, which allowed to perform pulse-phase resolved spectroscopy. Pulse-phase resolved spectra of individual *INTEGRAL* observations show a variation of the cyclotron line energy up to $\sim 16\%$ with pulse phase. Furthermore, pulse-phase resolved spectra of stacked observations have been analyzed, again favoring a small variation of the cyclotron line energy with pulse phase. These results can be interpreted in terms of a geometrical configuration such that the observer is exploring only a small part of the radiation beam pattern emerging from the accretion structure, thus causing the spectral parameters to result mostly insensitive to the pulsar rotation, a scenario that is also supported by the observed small pulsed fraction.

Concerning Vela X-1, spectral analysis on the sub-orbital timescale has been performed, to explore the light curve features and the effects of large scale (i.e. of the order of the optical companion size) structures that are known to affect the binary system. Such studies are important to constrain the stellar wind properties and to study the mechanisms behind the high X-ray variability typical of such sources. First, a sample of double-peaked orbital light curves has been extracted from the entire population of orbital profiles. The double-peaked sample shows a dip around the inferior conjunction that is difficult to explain invoking absorption by neutral matter alone. Instead, Thomson scattering from an extended and ionized accretion wake is shown to be a possible reason for the observed dip. Orbital-phase resolved spectra show that a phenomenological cutoff power-law model, commonly used in literature for accreting pulsars, leads to orbital variation of the photon index, thus it is likely inadequate to describe the Vela X-1 spectral properties. The addition of a partial covering component to model certain orbital phase-bins spectra avoids the photon index modulation and offers a physical interpretation: a highly structured ambient wind that affects only a part of the original X-ray emission, leaving the other part unaffected. The partial covering component is usually attributed to the clumpy nature of the stellar wind, but the observed orbital modulation of such a component does not favor this interpretation. The necessity of such a component in Vela X-1 seems to be more likely due to either a wobbling, or to an intrinsically structured accretion wake. Due to the ability of the neutron star traveling in the ambient wind to develop density inhomogeneities (i.e. the structured accretion wake), the compact object itself can be considered responsible for the formation of clumps which are then accreted, thus feeding the observed high X-ray variability typical of this system.

ZUSAMMENFASSUNG

Akkretierende Röntgenpulsare sind Doppelsternsysteme bestehend aus einem rotierenden Neutronenstern mit starkem Magnetfeld sowie einem optischen Begleiter, dessen ausgestoßenes Plasma auf das kompakte Objekt akkretiert wird - ein Prozess, bei dem es zur Emission gepulster Röntgenstrahlung kommt. Seit der Entdeckung derartiger Systeme vor über 40 Jahren wurden substantielle Fortschritte beim Verständnis der beiden stellaren Partner und der Mechanismen der Röntgenemission erzielt. Dennoch sind sowohl in der Beobachtung wie auch in der theoretischen Beschreibung weitere Anstrengungen notwendig, um zahlreiche bislang unverstandene Aspekte erklären zu können. Diese offenen Fragen betreffen etwa Details der Emissionsprozesse, die Geometrie des Akkretionsflusses und die Abstrahlcharakteristik sowie den Einfluss des optischen Begleiters auf die beobachtete Röntgenstrahlung.

Diese Arbeit umfasst spektroskopische und zeitliche Analysen zweier akkretierender Röntgenpulsare: Das Be-Röntgenbinärsystem GX 304-1 und das durch Windakkretion charakterisierte Binärsystem Vela X-1. Für die Analyse von GX 304-1 wurden *INTEGRAL*-Daten im Bereich $5-100$ keV verwendet, die während einem hellen Ausbruch im Jahr 2012 aufgenommen wurden. Das japanische *MAXI*-Teleskop liefert seit 2009 durchgehend Beobachtungsdaten ($2-20$ keV) von Vela X-1 und bietet damit eine wertvolle Möglichkeit zur Untersuchung der Variabilität entlang des Orbits.

Die Analyse der *INTEGRAL*-Daten von GX 304-1 erlaubt eine Charakterisierung des spektralen und zeitlichen Verhaltens der Quelle als Funktion der Leuchtkraft. Es wurde eine während der Ausbrüche gültige Lösung für die zeitliche Struktur gefunden, die es erlaubt, Pulsprofile bei verschiedenen Leuchtkräften und für verschiedene Energiebänder zu konstruieren. Die Pulsprofile zeigen eine starke Abhängigkeit von der Leuchtkraft und der Energie und legen damit Veränderungen der Abstrahlcharakteristik mit der Leuchtkraft nahe sowie unterschiedliche Erzeugungsorte der weichen und harten Röntgenstrahlung. Weiterhin zeigen die GX 304-1-Pulsprofile, anders als bei anderen akkretierenden Binärsystemen, nur einen kleinen Anteil gepulster Strahlung, der nicht mit der Energie oder der Leuchtkraft korreliert ist. Die Ableitung der Pulsperiode ist während der Akkretionsphase negativ, was eine Episode der Rotationszunahme impliziert und damit auf das Vorhandensein einer Akkretionsscheibe schließen lässt. über die Pulsphasen gemittelte Spektren, bei deren Aufnahme eine präzisere Kalibrierung der Photonenergie verwendet worden war, bestätigen die Korrelation zwischen der Energie der Zyklotronlinie und der Leuchtkraft und erlauben dadurch eine genauere Abschätzung des Magnetfeldes des Neutronensterns und seiner kritischen Leuchtkraft. Die spektralen Parameter Photonenindex und die *Folding*-Energie sind mit der Leuchtkraft negativ korreliert, wie es für ein comptonisiertes Spektrum erwartet werden würde. Dies suggeriert, dass die Compton-Kühlung bei höherer Leuchtkraft effizienter abläuft. Die Lichtkuve wurde weiterhin benutzt um die Pulsphasen des rotierenden Neutronensterns zu identifizieren und damit Spektroskopie der einzelnen Pulsphasen zu ermöglichen. Die nach Pulsphasen aufgelöste Spektren einzelner *INTEGRAL*-Beobachtungen zeigten eine Veränderung der Energie der Zyklotronlinie um bis zu $\sim 16\%$ mit der Pulsphase. Des Weiteren wurden die Spektren mehrerer Beobachtungen während der einzelnen Ausbruchsphasen aufsummiert analysiert, woraus sich ebenfalls eine entsprechende Variation der Energie der Zyklotronlinie über die Pulsphasen ergab. Diese Ergebnisse können durch eine geometrische Konfiguration erklärt werden, bei der der Beobachter nur einen kleinen Ausschnitt des Strahlungskegels untersuchen kann und somit die beobachteten spektralen Eigenschaften

überwiegend unabhängig von der Rotation des Pulsars sind. Dieses Szenario wird auch durch den nur geringen gepulsten Strahlungsanteil in den Beobachtungen gestützt.

Für Vela X-1 wurde eine spektrale Analyse auf Zeitskalen innerhalb eines Orbits durchgeführt, um die Eigenschaften der Lichtkurve und die Effekte ausgedehnter Strukturen von der Größenordnung des optischen Begleiters, die bekanntermaßen das Binärsystem beeinflussen, zu untersuchen. Solche Studien sind wichtig, um die Eigenschaften des Sternwindes einzugrenzen und um die Mechanismen zu erforschen, die zur typischerweise hohen Variabilität solcher Systeme führen. Zunächst wurde eine Auswahl von Lichtkurven, die eine Doppelpeakstruktur im Maximum aufweisen, aus den vorliegenden Daten extrahiert. Diese Kurven zeigen einen Einbruch im Bereich der unteren Konjunktion, der kaum mit Absorption durch ausschließlich neutrale Materie zu erklären ist. Stattdessen konnte gezeigt werden, dass Thomson-Streuung in einer ausgedehnten ionisierten Akkretionsschleppe die Ursache für den beobachteten Einbruch sein könnte. Nach orbitalen Phasen aufgelöste Spektren zeigten, dass ein phänomenologisch begründetes gebrochenes Potenzgesetz, wie es in der Literatur für akkretierende Pulsare häufig angewendet wird, zu einer Variabilität des Photonenindexes über den Orbit führt und damit höchstwahrscheinlich die spektralen Eigenschaften von Vela X-1 unzutreffend beschreibt. Die Hinzufügung einer teilweise verdeckenden Komponente bei der Modellierung der Spektren einzelner orbitaler Phasen vermeidet hingegen eine Modulation des Photonenindex und liefert eine physikalische Erklärung: Ein in hohem Maße strukturierter Wind umgibt das System und beeinflusst einen Teil der ursprünglichen Röntgenemission, während der andere Teil unverändert bleibt. Die teilweise verdeckende Komponente wird üblicherweise der hochgradig inhomogenen Natur des Sternenwindes zugeschrieben, aber die beobachtete Modulation über den Orbit widerspricht dieser Interpretation. Dieses Verhalten in Vela X-1 scheint viel eher durch ein Taumeln oder eine intrinsische Struktur im Akkretionsfluss hervorgerufen zu werden. Wenn der sich bewegende Neutronenstern Inhomogenitäten in der Dichte des umgebenden Windes hervorruft - wie etwa die beschriebene Struktur -, so können diese wiederum für die Bildung von Materieklumpen verantwortlich sein, die im weiteren Verlauf akkretiert werden und damit die beobachtete und für solche Systeme typische Variabilität hervorrufen.

Contents

Abstract **i**

Zusammenfassung **iii**

1 Introduction **1**
1.1 A brief review of the X-ray astronomy 1
1.2 Thesis outline 3

2 Stellar evolution and the origin of compact objects **5**
2.1 Final stages of stars 5
2.2 Neutron stars as astronomical objects 8
2.3 Using Neutron Stars as fundamental physics laboratories 10

3 Accreting X-ray Pulsars **13**
3.1 X-ray binaries 13
3.2 Accretion power 14
3.2.1 The Eddington luminosity 15
3.3 Mass transfer 15
3.3.1 Mass transfer mechanisms in X-ray binaries 17
3.4 Accretion onto highly magnetized Neutron Stars 24
3.4.1 Accretion geometry 24
3.4.2 Accretion onto polar caps 26
3.4.3 X-ray pulse profiles 27
3.5 X-ray spectra 29
3.5.1 Cyclotron lines 30

4 X-ray Observatories **35**
4.1 The INTEGRAL telescope 35
4.1.1 The payload 35
4.1.2 Dithering Strategy 44
4.2 The MAXI monitor 45
4.2.1 GSC camera design 46
4.2.2 GSC detector units 47

5 *INTEGRAL* observations of GX 304-1 **51**
5.1 History 51
5.1.1 A more recent context 51
5.2 Motivation 53
5.3 *INTEGRAL* observations of the outburst 54
5.3.1 The outburst event and the *INTEGRAL* coverage 54
5.3.2 Available data 56
5.4 Timing analysis 57
5.4.1 Timing solution using phase-connection 57
5.5 Spectral analysis 61
5.5.1 Phase-averaged spectroscopy 61

5.5.2 Phase-resolved spectral analysis 67
5.6 Summary 76

6 *MAXI* observations of Vela X-1 **77**
6.1 Introduction 77
6.2 Motivation 80
6.3 MAXI/GSC archival data 81
6.4 Analysis of the orbital profiles 81
6.4.1 Statistical and physical significance of the double-peaked sample . . . 84
6.5 Orbital-phase averaged spectral analysis 92
6.6 Phase-resolved spectral analysis 93
6.6.1 Orbital phase-resolved spectroscopy of the double-peaked sample . . . 93
6.6.2 Orbital phase-resolved spectroscopy of the standard sample 98
6.7 Summary 101

7 Discussion **103**
7.1 GX 304-1 103
7.1.1 A timing solution for the entire outburst 103
7.1.2 Phase-averaged spectral results 106
7.1.3 Phase-resolved spectral analysis 111
7.2 Vela X-1 115
7.2.1 Double-peaked orbital light curve 115
7.2.2 Spectral results 118

8 Summary and conclusions **123**
8.1 *INTEGRAL* observations of GX 304-1 123
8.2 *MAXI* analysis of Vela X-1 124
8.3 Future prospects 125
8.3.1 Optical observations of GX 304-1 125
8.3.2 Flux-resolved analysis of Vela X-1 129

Bibliography **131**

A Appendix A **145**

List of Figures **155**

1

INTRODUCTION

1.1 A brief review of the X-ray astronomy

Earth's atmosphere is opaque to most of electromagnetic wavelengths, and X-rays are one of those energy bands whose passage through it is impossible. For this reason, X-ray astronomy is a relatively modern field compared to, e.g., optical or radio-astronomy.

The first extraterrestrial X-ray signal has been recorded in 1946 by a photon counter onboard a V2 rocket. The V2 rose to 150 km height and pointed to the Sun, to observe its X-ray emission (Tousey, Watanabe, and Purcell, 1951; Friedman, Lichtman, and Byram, 1951). Due to the weakness of the observed signal, astronomers considered fundamentally impossible to detect sources other than the Sun. Therefore, it took more than 10 years to achieve an extrasolar X-ray detection, and to open a new era of astronomy. The first X-ray Galactic source was serendipitously detected using an Aerobee rocket, originally designed to observe the Moon X-ray emission (Giacconi et al., 1962). The source, located in the Scorpius constellation, was named *Sco X-1*. Its X-ray emission (see Fig. 1.1) has been recorded using Geiger counters. In the following years, several balloon experiments were carried out, leading to the discovery of many Galactic and extragalactic X-ray sources and to the growing interest of the scientific community in the X-ray astrophysics.

However, a process capable of producing intense X-ray emission reimaned unknown for quite some time after the discovery of Sco X-1. First suggestions have been proposed by Morton (1964), who suggested a *neutron star* as a potential source for Sco X-1 X-ray emission, while Salpeter (1964) suggested how accretion of matter onto massive (not necessarily compact) objects can be an important astrophysical process for producing X-rays. At that time, neutron stars had not yet been observed, and their theory was not consolidated. Their existence emerged only after a long effort that went through theoretical investigations and related speculations (a recent review on the history of neutron stars can be found in Yakovlev et al. 2013). First, Chandrasekhar theoretically showed white dwarfs as unstable beyond a certain mass limit (Chandrasekhar, 1931). On the other hand, Landau (1932) predicted the existence of dense stars that resemble giant atomic nuclei. Such exotic objects were named "neutron stars" by Baade and Zwicky (1934), who also suggested that they originate from supernova explosions. However, their experimental evidence came only 35 years after. In 1967 the first radio pulsar (PSR1919+21) was discovered by J. Bell, a student of A. Hewish (Hewish et al., 1968). Thanks to this discover, Hewish obtained the Nobel prize for physics in 1974. The discovery of Sco X-1 came a few years later and triggered an incredible boost for the space-based exploration of the X-ray Universe (see Santangelo and Madonia 2014 for a recent review of the history of X-ray astronomy). In 1970, the first X-ray satellite was launched by NASA. It was named *Uhuru* (meaning *freedom* in Swahili language). Its principal investigator

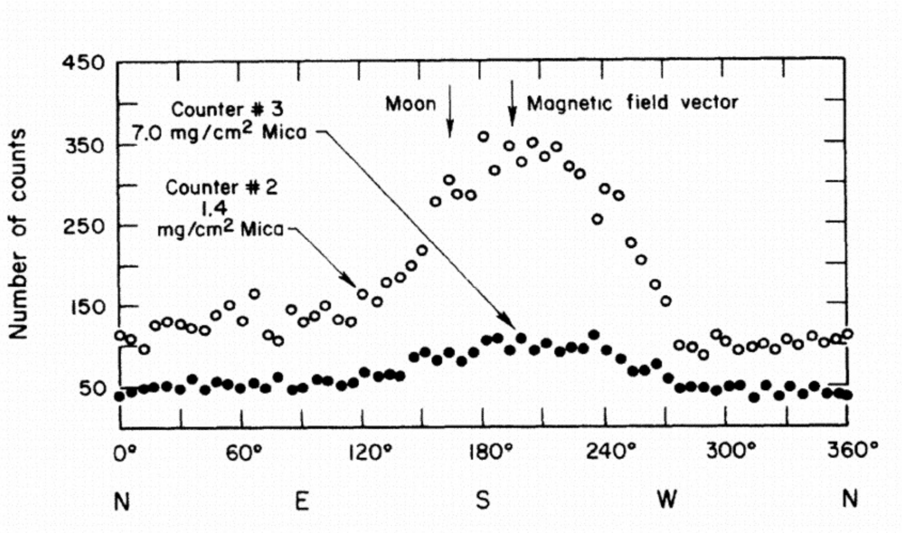

Figure 1.1: First measured signal from an extra-solar X-ray source: Sco X-1. The y-axis shows the number of X-ray detected counts, while the x-axis shows the azimuthal angle. Figure from Giacconi et al. (1962).

was Riccardo Giacconi (Giacconi et al., 1971). The observatory had two proportional counters sensitive in the range $2-20\,\mathrm{keV}$, down to a limiting sensitivity of $1.5 \times 10^{-11}\,\mathrm{erg/cm^2/s}$, and operated over two years. During its mission, *Uhuru* achieved outstanding scientific advances, and the discovery of many accretion-powered binary systems, the most famous being Cen X-3, Vela X-1, and Her X-1 (Forman et al., 1978). It also discovered Cygnus X-1, the first black hole candidate.

Thenceforth, many other X-ray missions have been launched: *Ariel V* (Smith and Courtier, 1976), *SAS-3* (Mayer, 1975) and *HEAO-1* (Peterson, 1975). However, a major improvement comes only in 1978, with the launch of the *HEAO-2* (named *Einstein* after launch) observatory, which hosted the first fully imaging X-ray telescope put into space (Giacconi et al., 1979). It allowed to study and to image extended sources with an angular resolution of a few arcseconds. *Einstein*'s results completely changed the view of the X-ray sky. Many other observatories followed (e.g., in chronological order of launch, *EXOSAT*, *Ginga*, *ROSAT*), improving the angular resolution, the field of view, the spectral resolution, and extending the energy band coverage.

In the mid 1990s, the Rossi X-ray Timing Explorer (*RXTE*) and *BeppoSAX* (Boella et al., 1997) were launched. Both satellites provided unprecedented spectral coverage of $1-100\,\mathrm{keV}$. They had excellent timing capabilities and good spectral resolution. Starting from the end of 1990s, a series of outstanding observatories were launched and are still in orbit and actively operating at the time of writing. The first two are the NASA's Advanced X-ray Astrophysics Facility, (AXAF, Canizares 1990; Weisskopf et al. 2000), better known as *Chandra*, and the ESA's X-ray Multi-Mirror Mission (*XMM-Newton*, Mason et al. 1995). *Chandra* is the observatory with the best spatial resolution in X-rays as yet, while XMM-Newton's advantage is its larger effective area. The subsequent mission is the ESA's INTErnation Gamma-Ray Astrophysics Laboratory, or *INTEGRAL*. Launched in 2002, *INTEGRAL* is equipped with coded-mask telescopes and detectors operating in the Gamma-ray, X-ray and optical bands. After *INTEGRAL* two other observatories were launched: *Swift* (Gehrels et al., 2004), in

2004, optimized to quickly locate X-ray bursts up to 150 keV and to relay their position to other observatories on the ground; and *ASTRO-E2*, (or *Suzaku*, Mitsuda et al., 2004), in 2005, characterized by a broad-band (0.4 – 600 keV) high-resolution spectral coverage.

In the last years, two gamma-ray observatories were launched: first *AGILE* (Astro–Rivelatore Gamma a Immagini Leggero, Tavani et al. 2008), in 2007, an Italian mission with a very light payload and a relatively cheap budget, designed to scan the universe in the Gamma-ray and X-ray bands; second the Gamma-ray Large Area Space Telescope (GLAST, renamed *Fermi* after launch, Ritz et al. 2007), in 2008, a NASA mission with contribution from Europe and Japan, sensitive up to 300 GeV and a moderate spatial resolution. Afterwards, the Monitor of All-sky X-ray Image (*MAXI*, Matsuoka et al., 2009) was launched in 2009. *MAXI* is a JAXA mission aboard the International Space Station, sensitive in the range 0.5 – 20 keV, capable to conduct a full sky survey every 96 minutes. In 2012, NASA launched the Nuclear Spectroscopic Telescope Array (*NuSTAR*, Harrison et al. 2013), the first telescope able to focus X-ray images in the 3 – 79 keV enegy band. Finally, *ASTROSAT* (Agrawal, 2006), launched in 2015, is a multi-wavelength mission hosting 4 X-ray instruments (plus an UV telescope) that allow a collective spectral coverage in the 0.3 – 150 keV energy band.

On 17 February 2016 *Astro-H* was launched, a Japanese mission with participation from NASA, Netherlands, and Canada, which was designed to provide spectral resolution of 7 eV in the 0.3 – 10 keV energy band. Unfortunately, contacts with the spacecraft were lost on 26 March 2016, due to multiple incidents with the attitude control system leading to an uncontrolled spin rate and breakup of structurally weak elements . Also, many other X-ray facilities are currently proposed to fly in the next future: The Neutron star Interior Composition Explorer *NICER* (NASA 2017, Gendreau, Arzoumanian, and Okajima 2012), the X-ray Imaging Polarimetry Explorer *XIPE* (ESA 2017, Soffitta et al. 2013), The Extended Roentgen Survey with an Imaging Telescope Array *eROSITA* on board the Spektrum-Roentgen-Gamma (SRG) Russian Satellite (MPE 2017, Merloni et al. 2012), the Wide-Field MAXI *WiFi-MAXI* (JAXA 2010s, Arimoto et al. 2015), and the Advanced Telescope for High-ENergy Astrophysics *ATHENA+* (ESA 2020s, Nandra et al. 2013).

1.2 Thesis outline

This thesis focuses on X-ray timing and spectral studies of two X-ray binary accreting pulsars: GX 304-1 and Vela X-1. The insights gained by studing this type of astrophysical objects is crucial to understand the physics of accretion, the X-ray emission mechanisms and properties, as well as the properties of neutron stars and their optical companion along with the binary environment.

This thesis is organized as it follows. Chapter 2 gives an overview on the evolution from Main Sequence stars to final compact products. Chapter 3 introduces the X-ray binary systems, with special mention to accreting magnetized neutron stars. Chapter 4 presents the X-ray facilities whose observations have been studied in this work. Chapters 5 and 6 describe the sources and the analysis presented in this thesis. The results are discussed in Chapter 8. A summary of this work is given in Chapter 9, with mention to future planned works.

2

STELLAR EVOLUTION AND THE ORIGIN OF COMPACT OBJECTS

2.1 Final stages of stars

Depending on the initial mass, the final stage of a star's evolution can be very different. Every star starts its life on the Main Sequence (MS) in the Hertzsprung-Russell diagram (Rosenberg, 1910; Hertzsprung, 1911; Russell, 1914). During its life on the MS, the star's evolution is due to the evolving interplay between gravitational and thermal (radiation plus gas) pressure forces, realizing a condition of hydrostatic equilibrium:

$$\frac{dP}{dr} = -\frac{GM(r)}{r^2}\rho(r) \tag{2.1}$$

For a time period of the order of the nuclear timescale, the star stays on the MS burning hydrogen in the core, and converting gravitational energy into thermal energy by nuclear fusion. For a Sun-like star, the dominant nuclear fusion process is the "proton-proton chain reaction" (*p-p chain*, see Wolschin 2003 for a review), in which protons are fused, step-by-step, into different products, with a final production of helium, high-energy photons, and neutrinos (see Fig. 2.1).

An estimate of the nuclear timescale can be obtained by comparing the total amount of nuclear energy available and the rate of energy loss (i.e. the luminosity). The total nuclear energy is proportional to the mass of hydrogen available for nuclear fusion in the core of the star. It is tipically $f \sim 10\%$ of the total mass. The proportionality factor is defined by the *efficiency* of the process, that is the capability of the nuclear fusion to convert mass into radiation via nuclear fusion: for hydrogen burning the efficiency ϵ is $\sim 0.007c^2$. Thus, the nuclear time scale (i.e. the MS lifetime) can be written as:

$$\tau_n = f\epsilon\frac{Mc^2}{L} \simeq 10^{10}\frac{M}{M_\odot}\frac{L_\odot}{L}[yr] \tag{2.2}$$

After the hydrogen-burning phase, the fate of the star depends on its mass. The mass ranges that determine the star evolution are known only approximately due to considerable uncertainty in our knowledge of the evolution of massive stars. However, in general, the larger is the initial mass of the star, the more compact will be the final product. More specifically, if the progenitor star is not very massive ($0.8\,M_\odot \lesssim M \lesssim 11\,M_\odot$), after the hydrogen runned out, its core will contract to guarantee another equilibrium phase. At this stage, the internal temperature rises up, and the star starts to burn helium into carbon and oxygen in the

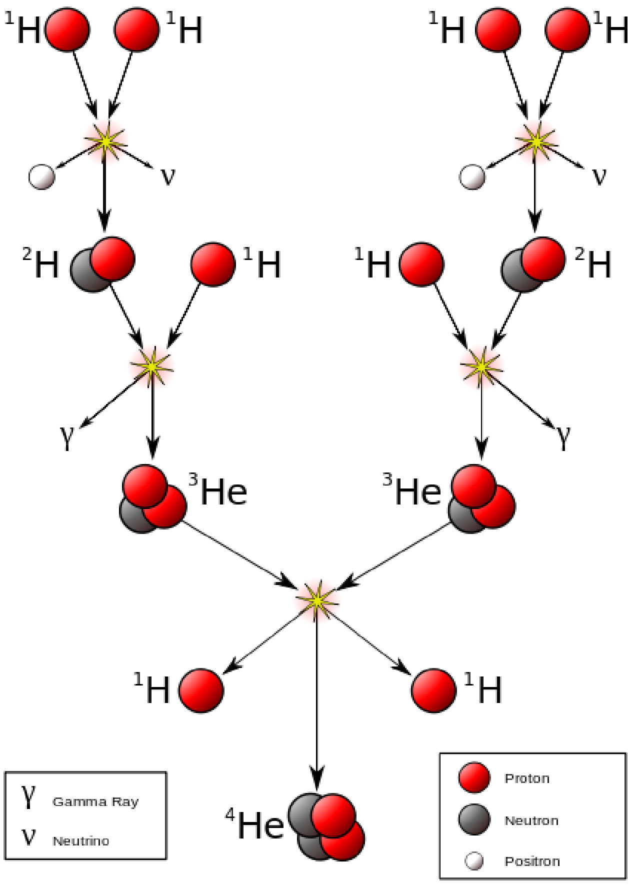

Figure 2.1: A proton-proton chain reaction shown as it should occur in Sun-like stars. (Credit: `https://upload.wikimedia.org/wikipedia/commons/7/78/FusionintheSun.svg`)

core. At the same time, the heating triggers the fusion of hydrogen into helium in a shell surrounding the core. Shell nuclear fusion brings more energy (heat and radiation) to the outer layers, and the star expands its envelope, turning into a *red giant*. However, when the helium fuel in the core is also used up, stars with a mass $\lesssim 0.5\,M_\odot$ (Iben, 1991) have not enough gravitational potential to rise the temperature in the core up to the ignition of the next fusion. Therefore, those stars have no more balancing force against gravity, and will collapse. The only force that can stop the collapse is the degenerate pressure of electrons:

$$P_{deg} = \frac{15m}{\hbar^2\pi^3}\left(\frac{3N}{\pi V}\right)^{5/3} \tag{2.3}$$

with m being the mass of the particle producing the degeneracy pressure (electrons in this case), N is the number of particles, and V is the volume they occupy. This will leave an Earth-sized inactive core with a density of $\rho \sim 10^{15}\,\mathrm{kg\,m^{-3}}$ that gradually cools down: such an object is a *white dwarf* (WD), and its maximum mass is $M \sim 1.4\,M_\odot$, that is the Chandrasekhar limit beyond which no stable white dwarf can exist (Chandrasekhar, 1931).

For those stars whose initial mass is $0.8\,M_\odot \lesssim M \lesssim 9\,M_\odot$ (Van Horn, 2015), the core will become sufficiently hot to fuse helium into carbon (C) and oxygen (O). The remnant object is therefore a WD composed of C and O, and such is the destiny of our star, the Sun.

When the initial star mass is about $9\,M_\odot \lesssim M \lesssim 11\,M_\odot$ (Roger, Pérez-Fournon, and Sanchez, 1999), the core density is such that after the helium-burning phase, it contracts even more until it reaches temperatures which allow to burn carbon into neon (Ne). Therefore, more massive (and rarer) stars can produce an oxygen-neon-magnesium (O-Ne-Mg) white dwarf.

However, the above-mentioned mass limits are not firnly established yet (see, for example, Prada Moroni and Straniero 2009 and references therein). The exact values of stars' initial masses for a given evolutionary path can be constrained only when more complex scenarios are taken into account (e.g. magnetic fields, mass loss through stellar winds, theory of stellar nuclear fusion ignition, etc.). Furthermore, in the last decade the super-Chandrasekhar WDs hypothesis (e.g. the existence of WDs with $M_{WD} > M_{Ch} \approx 1.44 M_\odot$) is collecting evidences on both observational and theoretical grounds (see Das and Mukhopadhyay 2014 and references therein).

If the progenitor star is even more massive ($11\,M_\odot \lesssim M \lesssim 20\,M_\odot$), the nuclear fusion goes on until iron (the last element obtainable by endothermic reactions) is produced in the core. Different lighter elements are produced in the external core layers (a simple onion-like model is shown in Fig. 2.2). When the whole core is converted into iron, no further fusion can take place in it, and the collapse is unavoidable: the degeneracy pressure of electrons is not enough to stop the collapse of such a massive star, and the core collapses further. The temperature increases up to $5 \times 10^9\,\mathrm{K}$, where electrons are captured by nuclear protons through *electron capture*:

$$e^- + p^+ \to n + \nu_e \tag{2.4}$$

and neutrons are formed, leading to a degenerate neutron gas. Due to their larger mass, neutrons are packed more densely than electrons ($\rho_n = 10^{24}\,\mathrm{kg\,m^{-3}} = 10^9 \times \rho_e$, where ρ_n and ρ_e are the neutron and electron densities, respectively), and the resulting degenerate pressure is 10^{10} times higher than that of white dwarfs. This is able to halt the collapse of such massive stars and create a stable compact object: the core of the star is thus transformed into a *neutron star* (NS). At the same time, the external layers bounce over the compact core causing the implosion to rebound outwards: an expanding shock wave is formed which has enough energy to accelerate the external material up to the escape velocity (close to the speed of light), thus creating a Type-II (core-collapse) Supernovae. For a detailed discussion of the physics of supernova explosions, see Woosley, Heger, and Weaver (2002), while an X-ray perspective of Supernovae (focused on the Supernovae remnants) is given by Vink (2012). Although the basic mechanisms that drive the formation of NSs are generally assessed, the theory behind their formation and evolution is much more complex and not yet fully understood (see, e.g., Lattimer and Prakash 2004 for a review, and Sect. 2.3).

Finally, the most extreme cases are obtained when the mass of the progenitor star is $M \gtrsim 20\,M_\odot$, corresponding to a core mass of $M \gtrsim 3\,M_\odot$, that is the so-called Tolman-Oppenheimer-Volkoff (TOV) limit for NSs (Oppenheimer and Volkoff, 1939). In such cases not even the neutron degeneracy pressure can avoid further collapse. Before the catastrophic event, the external layers will bounce over the compact iron core, thus forming a Supernovae also in this case. However, the compact core can not arrest its contraction and is therefore destined to collapse into a singularity, i.e. to become a *black hole* (BH). Once again, the mass limit and actual process of BHs formation is a complicated matter, and needs more observations and studies to constrain the real scenario. A review of BHs and NSs formation

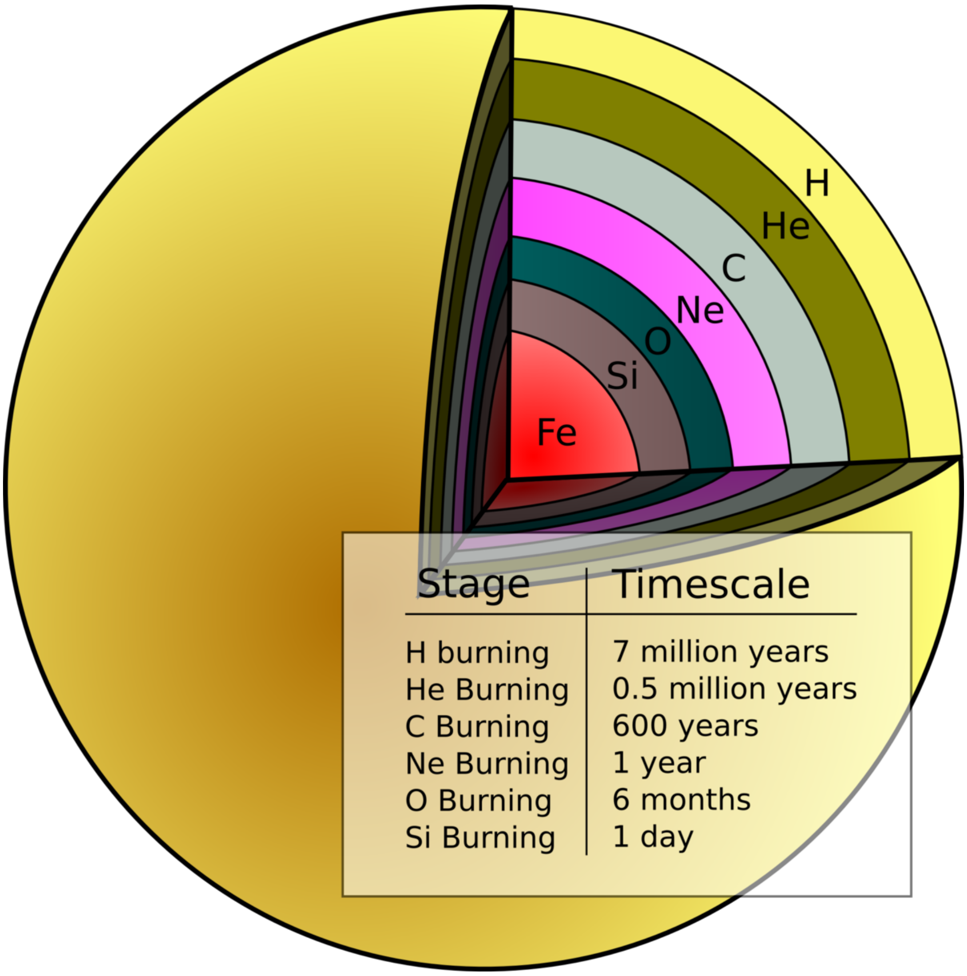

Stage	Timescale
H burning	7 million years
He Burning	0.5 million years
C Burning	600 years
Ne Burning	1 year
O Burning	6 months
Si Burning	1 day

Figure 2.2: Artistic impression of the interior of a massive star before it explodes as a supernova. The whole star can reach the size of the Mars' orbit, but the nuclear furnace is not much bigger than the Earth and comprises a set of nested shells each burning a different nuclear fuel, from ligher elements on the outside to heavier elements towards the center. The innermost region is a ball of highly compressed inert iron which ultimately collapses to trigger the explosion. Also indicated are the timescales for each element fusion process. Figure from Phillips (1999).

as a function of their mass and metallicity is given by Heger et al. (2003).

2.2 Neutron stars as astronomical objects

Even before the experimental discovery of the neutron (Chadwick, 1932), Landau anticipated the basic idea of a giant nucleus star (Yakovlev et al., 2013), while Subrahmanyan Chandrasekhar formalized the final stage of a degenerate-core star (Chandrasekhar, 1931). In his seminal paper, Chandrasekhar calculated the maximum mass of a stable white dwarf star, refined in later works as $\sim 1.4\,M_\odot$ (i.e., the Chandrasekhar limit). Beyond this limit, the

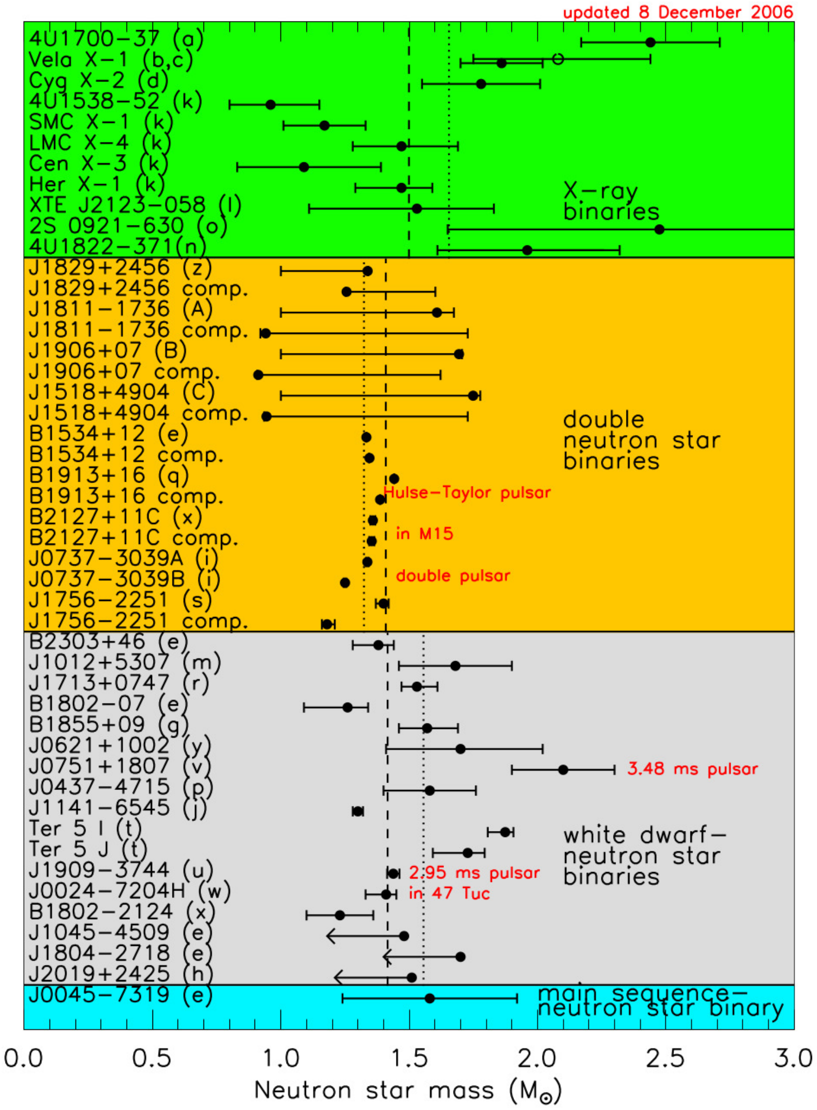

Figure 2.3: Measured and estimated masses of Neutron Stars for different classes of binary systems. Figure from Lattimer and Prakash (2007).

electron degenerated gas pressure is not sufficient to halt the collapse of the core. Therefore, the object contracts itself to even denser states, until it reaches a density such that the core can only be supported by neutron degeneracy pressure. The first suggestion about *how* such a degenerate object may form, was initially advanced by Walter Baade and Fritz Zwicky, who had the idea that neutron stars can result after the supernova explosions (Baade and Zwicky, 1934).

However, it was not clear what kind of observational signature one should expect from NSs until 1967, when Pacini (1967) pointed out that radio emission could be powered by a rotating magnetized neutron star. The same year, the first ever discovered X-ray extrasolar source, Scorpion X-1 (Sco X-1), was interpreted as a neutron star accreting matter from a companion (Shklovsky, 1967). Soon later, independently, the first radio pulsar (PSR 1919+21) was serendipitously discovered by Jocelyn Bell, a Ph.D. student of Antony Hewish (Hewish et al., 1968). Due to their radio emission characterization, these objects were named *pulsars*, i.e.,

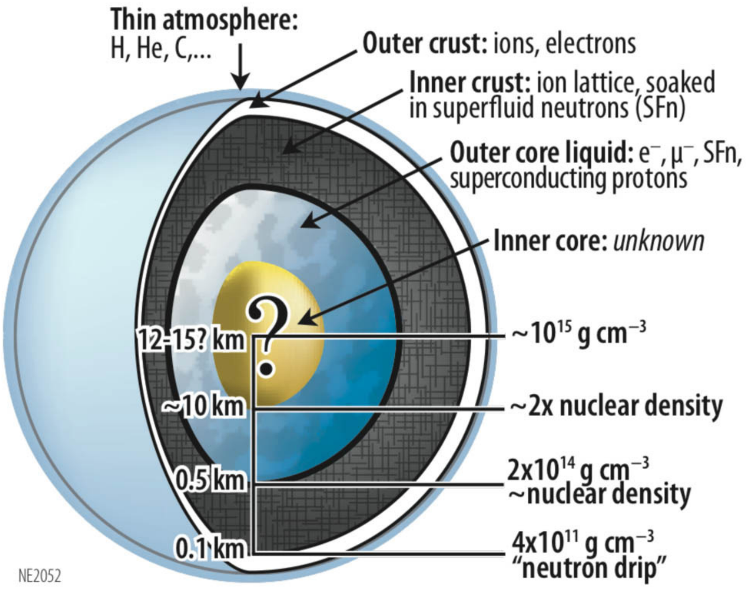
Thin atmosphere: H, He, C,...
Outer crust: ions, electrons
Inner crust: ion lattice, soaked in superfluid neutrons (SFn)
Outer core liquid: e⁻, μ⁻, SFn, superconducting protons
Inner core: *unknown*
~10¹⁵ g cm⁻³
~2x nuclear density
2x10¹⁴ g cm⁻³ ~nuclear density
4x10¹¹ g cm⁻³ "neutron drip"
12-15? km
~10 km
0.5 km
0.1 km
?
NE2052

Figure 2.4: An interior model of a neutron star. Different layers are composed of matter at different states. Figure from Gendreau, Arzoumanian, and Okajima (2012).

pulsating radio stars. In the meanwhile, others two of the most famous pulsars were also observed: the Crab pulsar, in the Crab Nebula (Staelin and Reifenstein, 1968), and the Vela pulsar, in the Vela nebula (Large, Vaughan, and Mills, 1968). Both of them are located in the center of a wide supernova remnant, thus supporting the Zwicky & Baade hypothesis.

Shortly thereafter, pulsation in X-rays was observed by Uhuru for Centaurus X-3 (Giacconi et al., 1971), and Hercules X-1 (Tananbaum et al., 1972). However, Her X-1 and Cen X-3 show pulsation periods that are noticeably longer than the rotation-powered radio pulsars, and are part of binary systems, thus pointing to a possibly different emission mechanism. Following Pringle and Rees (1972), Davidson and Ostriker (1973) propose the accretion as a mechanism to power this new class of objects. Indeed, such high X-ray luminosites can be explained by a model where the matter is accreted from the donor star (a Main Sequence or a giant star) onto the NS.

However, it has been found that X-rays are also emitted by Isolated Neutron Stars (INSs). The X-ray emission observed from INSs can be powered by internal heat, rotational energy, accretion, or magnetic field decay. The dominant mechanism depends on the age and physical properties of the NS, even if all of them can also operate at the same time (see Mereghetti 2011 for a recent review).

2.3 Using Neutron Stars as fundamental physics laboratories

Neutron stars are very exotic objects. They are the most compact known objects with a surface and no event horizon, and therefore represent a unique opportunity to study matter's behaviour at extreme conditions. Since their discovery, NSs allowed to test a number of physical scenarios that are not reproducible on Earth: high magnetic fields, plasma conditions in accretion disks, Equation of State (EoS) of matter at densities beyond nuclear saturation, relativistic effects at very intense gravitational fields. Not all of these phenomena have been fully explored so far, although outstanding progress has been reached in the last years.

The basic properties of NSs have been tightly constrained by several studies, both theoretical and observational. The considered canonical values for mass M and radius R of NSs are obtained by theoretical arguments (Lorimer and Kramer, 2012) and are $M = 1.4\,M_{\odot}$ and $R = 10\,\mathrm{km}$. On the other hand, the observed masses values are shown in Fig. 2.3 for a number of NSs. They result well in agreement with the theoretical expectations.

Observational studies are routinely carried out to constrain other properties of NSs, such as the magnetic field strength and its geometrical configuration, the emission processes that take place within the accretion structures, and more. Studying the X-ray emission from NSs in binary systems may also allow to probe the wind properties of the companion star, thus constraining stellar wind models that are of crucial importance for the comprehension of stellar evolution of massive stars.

On the other hand, the EoS (i.e. the relation between pressure and density) and the composition at the core of NSs (see Figure 2.4), are still unknown, and need to be constrained by observational studies in the future.

3

ACCRETING X-RAY PULSARS

3.1 X-ray binaries

Roughly half of the stars in our Galaxy are part of binary systems. These systems are composed by two gravitationally bound stars orbiting around the common center of mass. The evolution of a star in a binary system can significantly differ from that of an isolated star with the same mass and chemical composition. This may be due to a number of effects that take place in the binary system, e.g. modification of gravitational and radiation field by the companion, the centrifugal effects due to the rotation of the stars around the common center of mass and, more importantly, the catastrophical effects that follow from the rapid evolution of the more massive star. As a consequence of the faster evolution of the more massive star, binary systems are often found composed by at least one degenerate star, a white dwarf, a neutron star, or a black hole. When this configuration is reached, the compact object (if close enough) can accrete mass from the companion (or *donor star*), a process that eventually leads to X-ray emission. Besides those systems whose compact object is a WD (e.g., Cataclismic Variables, or CVs), X-ray emitting binary systems are divided in two groups, according to the mass of the companion star (Lewin, van Paradijs, and van den Heuvel, 1997):

- High Mass X-ray Binaries (HMXBs): here, the donor star is a massive star (O or B spectral type), tipically with $M \geq 5\,M_\odot$. The system is generally younger, and the donor star can sustain the accretion onto the compact object by means of strong stellar winds or Roche-lobe overflow (see Sec. 3.3). When the compact object is a NS, its magnetic field is usually of the order of 10^{12} G. These objects are usually found on the Galactic plane, especially along the spiral arms.

- Low Mass X-ray Binaries (LMXBs): here, the donor star can be a spectral type A or later star, or a white dwarf, with a mass of $M \leq 1.2\,M_\odot$. These systems are generally older than HMXBs, and the companion is not able to sustain the accretion through stellar wind anymore, thus the main channel of matter transfer is via Roche-lobe overflow. The NS magnetic field has usually decayed down to 10^{7-8} G. LMXBs are concentrated towards the Galactic center, but some of them have been observed in globular clusters.

3.2 Accretion power

Accretion is the physical process responsible for the emission of X-rays from accreting X-ray pulsars. It consists fundamentally of the gravitational attraction of matter onto the NS surface, a process that ultimately leads to releasing the gravitational energy of the infalling matter.

Let us consider a particle of mass m infalling in the potential dwell created by a star with mass M (with $M \gg m$). The gravitational potential energy of the particle at a distance R is:

$$\Phi = -\frac{GMm}{R} \tag{3.1}$$

If the particle falls from the distance R_{in} to R, then the potential energy $\Delta\Phi = \Phi(R_{in}) - \Phi(R)$ is released. If the particle falls from the infinite ($R_{in} = \infty$), then

$$\Delta\Phi = \frac{GMm}{R} \tag{3.2}$$

The speed of arrival (the *free-falling speed*) v_{ff}, is given by:

$$\frac{1}{2}mv_{ff}^2 = \frac{GMm}{R} \tag{3.3}$$

When the gas is brought to rest at the surface of a star, the amount of energy ΔE dissipated is

$$\Delta E = \frac{1}{2}mv_{ff}^2 = \frac{GMm}{R} \tag{3.4}$$

If, instead, it goes into a circular Kepler orbit at distance r:

$$\Delta E = \frac{1}{2}\frac{GM\dot{m}}{r} \tag{3.5}$$

where $\dot{m} = dM/dt$ is called the *accretion rate*, and represents the rate by which the mass M of this object increases.

The dissipated energy may go into internal energy of the gas, and into radiation which escapes to infinity. The luminosity given by the accretion of a particle is given by:

$$L_{acc} \approx \frac{GM\dot{m}}{R} \tag{3.6}$$

The accretion luminosity can be also expressed as:

$$L_{acc} = \eta\dot{m}c^2 \tag{3.7}$$

where η is called the accretion *efficiency*. Equating the last two equations, we obtain:

$$\eta \propto \frac{M}{R} \tag{3.8}$$

where M/R is called *compactness*. For compact obejcts like NSs, the efficiency is of the order of $\eta \sim 0.1$ (Longair, 1981), which is about 20 times larger then the efficiency of nuclear burning. Therefore, accretion onto compact objects is the most efficient engine known so far in the Universe.

3.2.1 The Eddington luminosity

The luminosity emitted by a spherically symmetric source in a steady state is limited by the balance condition between the inward force of gravity and the outward radiation pressure. This limiting luminosity is called the *Eddington luminosity*, and can be calculated as follows. The inward gravitational force generated by a mass M upon an electron-proton pair at a distance r from its center is:

$$F_g = \frac{GM(m_e + m_p)}{r^2} = \frac{GMm_p}{r^2} \tag{3.9}$$

where m_e and m_p are the mass of electron and proton, respectively, and where the m_e has been neglected on the right hand of the equation. Also, the radiation force induced by the photons onto the electrons through Thomson scattering is:

$$F_r = \frac{\sigma_T L}{4\pi r^2 c} \tag{3.10}$$

where $\sigma_T = 6.6 \times 10^{25}\,\mathrm{cm}^{-2}$ is the Thomson scattering cross-section. These two forces balance each other when the Eddington luminosity is reached:

$$L_{Edd} = \frac{4\pi GMm_p c}{\sigma_T} \approx 1.3 \times 10^{38} \frac{M}{M_\odot}\, erg\, s^{-1} \tag{3.11}$$

The Eddington luminosity can also be interpreted in terms of a mass accretion limit, in which case it results (for a typical NS mass and applying the Eq. 3.7):

$$\dot{M}_{Edd} = \frac{4\pi GMm_p}{\eta\sigma_T\, c} \approx 10^{-8}\, M_\odot\, yr^{-1} \tag{3.12}$$

Beyond this limit, and under the assumption of a steady and spherically symmetric accretion flow, the accretion rate can not grow further, since a higher accretion rate implies a luminosity radiation so strong that can blow the accreting material away. However, the Eddington luminosity differs according to the accretion geometry (Basko and Sunyaev, 1976). For objects accreting only on a fraction f of the spherical surface, the maximum luminosity is calculated as $f \times L_{Edd}$. On the contrary, for very small values of the fraction f, like in the accretion column case (see 3.4.2), the radiation can escape through the walls of the columns, leading to local *Super-Eddington luminosities*.

3.3 Mass transfer

In a binary system, the source of the accreted material is, of course, one of the two stars. However, the mass transfer modality in each binary system is ruled by the equipotential surfaces which, in turn, are determined by the gravitational force between the two stars and by the inertial forces in the rotating frame. In the Roche approximation, the gravitational

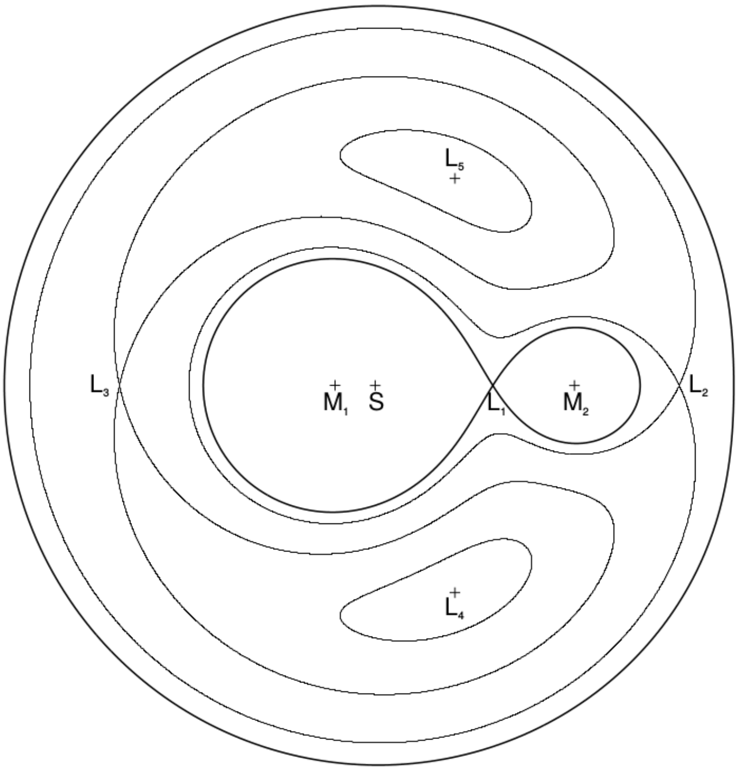

Figure 3.1: Section in the orbital plane of the Roche equipotential surfaces for a binary system with a mass ratio of $M_1/M_2 = 5$. Shown are also the centers of mass S, and the *Lagrangian points* $L_1 - L_5$. Figure from Kretschmar (1996).

field is approximated by two point masses, M_1 and M_2, corresponding to the masses of the two stars. Thus, in a frame co-rotating with the binary system, the full (gravitational + centrifugal) potential can be written as

$$\phi_R = -\frac{GM_1}{|\vec{r} - \vec{r}_1|} - \frac{GM_2}{|\vec{r} - \vec{r}_2|} - \frac{(\omega \times \vec{r})^2}{2} \tag{3.13}$$

where ϕ_R is the *Roche* potential, ω is the orbital angular velocity, while $\vec{r}_1$ and $\vec{r}_2$ are the position vectors of the centers of the two stars, and $\vec{r}$ is the position vector of the test particle, whose coordinate system is centered at the baricenter of the binary. An example of equipotential surfaces in the case of a mass ratio of $M_1/M_2 = 5$ is shown in Fig. 3.1. Here, it is worth to note the innermost equipotential surfaces (one for each star), and five points of equilibrium, called the *Lagrangian points* $L_1 - L_5$.

The regions surrounding each star and defined by the equipotential surfaces closing at the *inner* Lagrangian point, L_1, are known as the *Roche lobes*. Within its own Roche lobe, the material is gravitationally bound to that star. Therefore, the Roche lobe defines the maximum size of a star. Due to the complicate form of the Roche potential in case of real systems, the sizes of the Roche lobes can be only found either by numerical solutions or through some approximations. According to Eggleton (1983), a good approximation for the Roche lobe size is

$$\frac{R_1}{a} = -\frac{0.49q^{2/3}}{0.6q^{2/3} + ln(1 + q^{1/3})} \tag{3.14}$$

where R_1 is the Roche lobe of the star with mass M_1, a is the separation between the two stars, and $q = M_1/M_2$ is the mass ratio.

In a binary system, the two Roche lobes intersect through the Lagrangian point L_1. If either of the two stars exceeds its Roche lobe, then the exceeding material is no more gravitationally bound to that star and can either flow away or be captured by the gravitational influence of the other star. Therefore, it is interesting within the context of this work, to understand how a star can fill and exceed its Roche lobe.

In the context of this thesis, the most important scenario to consider is the filling of a Roche lobe due to stellar evolution. Since more massive stars evolve faster, it is useful to consider a binary system in which $M_1 \gg M_2$, such as the one approximated in Fig. 3.1. In this scenario, the star with M_1 will soon leave the Main Sequence, starting to expand. As it expands, its radius will exceed the Roche lobe, letting the exceeding material to be transferred to the lower mass companion. At this point, the fate of the massive star is dictated by the evolutionary stage in which it exceeds the Roche lobe, but in general it looses much of its material, ending up as a white dwarf of various compositions according to different initial masses and evolutionary stages. Now the system is composed of a white dwarf and a main sequence star whose initial mass has been increased trough mass transfer. Also, the mass transfer leads to orbital shrinkage, so that the binary gets closer. Thus, the main sequence star also will evolve rapidly, and will quickly exceed its Roche lobe. A common-envelope binary system forms and, eventually, the second white dwarf will be born. The binary system ends therefore as a binary white dwarf. About 90% of binary systems end as a binary white dwarf (Iben and Tutukov, 1984).

If the initial masses of the stars are large, the system undergoes a more disruptive event. The more massive star will, as in the previous case, evolve faster, until it looses about 50% of its mass through mass transfer onto the companion. At this point, if the star is massive enough, the object explodes as a Supernova, forming a neutron star. The explosion event is critical for the binary system: it can either change the binary orbit to a high-eccentricity orbit, or it can disrupt the binary system, leaving behind two unbound stars (Lewin, van Paradijs, and van den Heuvel, 1997). The difference between these two cases depends, as already mentioned, on the initial masses, and also on the ability of the massive star to transfer and loose part of its initial mass.

Finally, if the initial mass of one star is extremely high ($M \geq 20\,M_\odot$), the Supernova event will leave a Black Hole. In the end, this system will evolve in a BH/BH, a BH/NS, or a BH/WD binary, depending on the mass of the other star.

3.3.1 Mass transfer mechanisms in X-ray binaries

Depending on the binary system properties, three different ways of mass transfer can take place in X-ray Binaries: Roche lobe overflow (RLO), wind accretion and accretion in Be/X-ray Binary systems. These mechanisms will be separately discussed below.

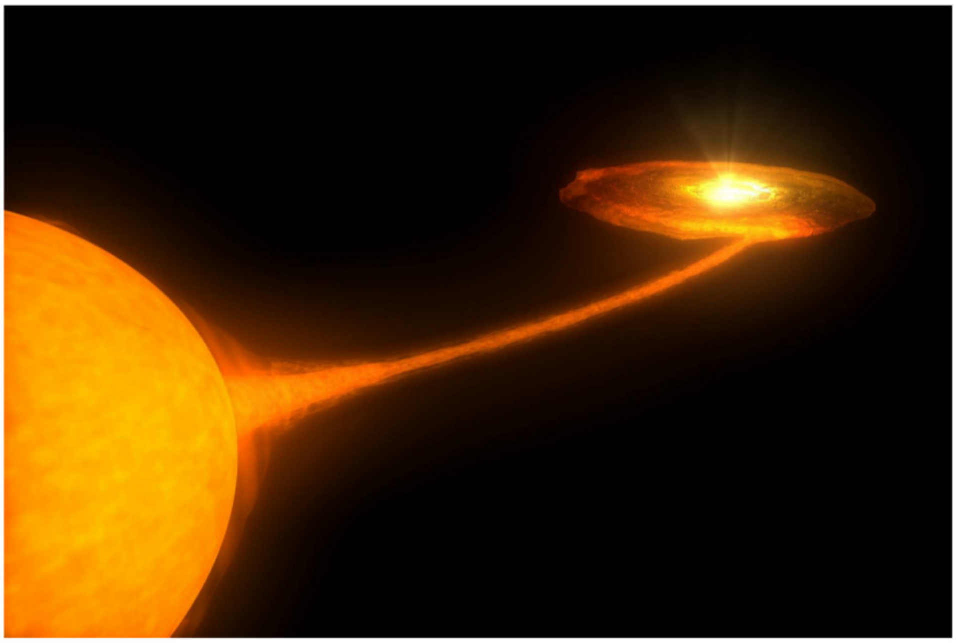

Figure 3.2: Illustration of mass transfer mechanism in a LMXB. The evolved low mass optical companion has filled its Roche lobe and is loosing material through Roche-lobe overflow. The overflowing material is transferred from the star to the accretion disk around the compact object. Figure from Kreykenbohm (2004).

3.3.1.1 Roche lobe overflow

As already discussed to some extent in the previous section, at certain evolutionary stages of the binary system, a star can loose a substantial part of its mass when it expands beyond its Roche lobe. A similar result is obtained if the binary orbit shrinks. Part of this material can then flow to the secondary through the inner Lagrangian point L_1. This process is called *Roche lobe overflow* (RLO). When RLO takes place, the mass flow does not directly impact the secondary star, due to the intrinsic orbital angular momentum J of the transferred material. Instead, the gas will initially orbit the accretor, forming an *accretion disk* (see Fig. 3.2), supposed that the *circularization radius* (Lewin, van Paradijs, and van den Heuvel, 1997):

$$R_{circ} = \frac{J^2}{GM_x} \tag{3.15}$$

is larger than the size of the accretor (of mass M_x). This is always the case for X-ray binaries where the accretor is a compact object and the mass transfer occurs via RLO (while, when the accretion occurs via stellar wind, J is generally much lower). Within the accretion disk, the material can loose angular momentum through friction forces between adjacent layers, moving inwards and eventually being accreted by the compact object. The mechanism through which the gas looses its angular momentum has been generally referred to as *viscosity.* The viscosity has been modelled in the seminal paper of Shakura and Sunyaev (1973) according to the famous *α-prescription*:

$$\nu = \alpha c_s H \tag{3.16}$$

where ν is the viscosity coefficient, H is the disk vertial extent, and $\alpha \leq 1$.

The structure and physics of such accretion disks is quite complex. However, there are some useful approximations which are commonly used to treat the problem in a simpler way. Indeed, in many cases the disk flow is confined almost entirely to the orbital plane, and it can therefore be regarded as a two-dimentional gas flow. In this case, the *thin disk approximation* (Shakura and Sunyaev, 1973) has proved to be very successful. Within the thin disk approximation, the local Keplerian velocity of a disk element, $v_k = \sqrt{GM/R}$, is assumed higly supersonic, while H, is negligible:

$$H = \frac{c_s}{v_k} R \ll R \tag{3.17}$$

with c_s local sound speed, and R the distance to the accretor. This also is a condition on the cooling mechanism of the disk, which needs to be efficient in order that the matter can not have dynamically significant pressure, so that the gas orbit is actually Keplerian.

The radial temperature distribution $T(R)$ within the disk is given by:

$$T(R) = \left[\frac{3GM\dot{M}}{8\pi\sigma R^3}\left(1 - \sqrt{\frac{R_{in}}{R}}\right)\right]^{1/4} = 1.3 \times 10^7 \dot{M}_{17}^{1/4} M_1^{1/4} R_6^{-3/4}\, K \tag{3.18}$$

(where $R_{\rm in}$ is the inner radius of the disk, $\dot{M}_{17} = \dot{M}/10^{17}\,\mathrm{g\,s^{-1}}$, $M_1 = M/M_\odot$, $R_6 = R_{NS}/10^6\,\mathrm{cm}$), which yields the proportionality $T \propto R^{-3/4}$. Thus, larger central objects have cooler disks, and emit at lower energy bands. Under the thin disk approximation, the disk is assumed to be optically thick. Therefore, each annulus can be considered as a blackbody emitter with the local temperature $T(R)$. This results in an overall power-law spectral shape, whose flux follows the so-called *multicolor blackbody* emission:

$$F_\nu \propto \nu^{1/3} \tag{3.19}$$

Accretion disks around NSs are thus expected to peak their emission in the UV energy band. In these cases, if the binary companion is an O or B giant or supergiant star, it completely swamps any disk contribution. To observe disk emission from accreting objects, it is better to turn to LMXBs and CVs, where the disk accretion luminosity of the inner disk dominates the soft X-rays, the hot corona (if present) emission dominates the hard X-ray band, while the emission from the outer part of the disk dominates in the UV/blue wavelengths (Hynes, 2010).

3.3.1.2 Wind accretion

Accretion from stellar wind is particularly relevant when the donor star is a MS or supergiant O/B star. Indeed, the stellar wind from these stars are dense, with mass loss rates of $\dot{M}_w \approx 10^{-6} - 10^{-7}\,M_\odot\,\mathrm{yr^{-1}}$, and highly supersonic, with terminal velocities of $v_\infty = 1000 - 2000\,\mathrm{km\,s^{-1}}$. In general, only a small fraction of the stellar wind is accreted onto the compact object, in contrast to the RLO case, where almost all the mass lost by the companion is captured by the accreting component. Thus, accretion from the stellar wind is an inheritently

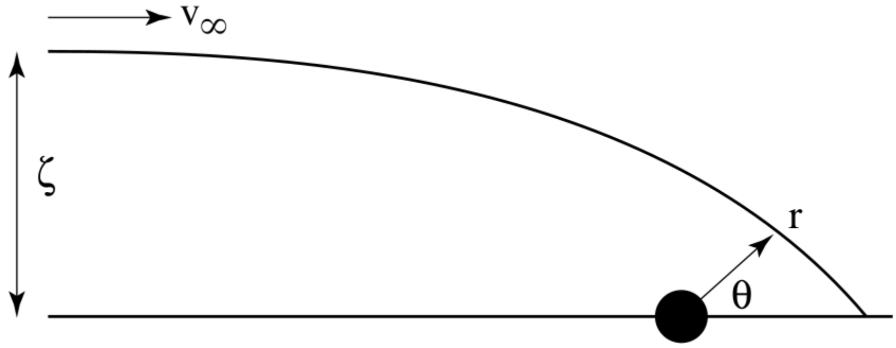

Figure 3.3: Sketch of the Bondi–Hoyle–Lyttleton accretion geometry. Figure from Edgar (2004).

less efficient accretion process (although the accretion rate in wind accreting and RLO systems is generally the same).

Tipically, in such systems the compact object orbits the companion at a close distance, roughly half of the companion star radius, thus deeply embedded in the stellar wind. This is counterposed to HMXBs with large eccentricities and long orbital periods. The reason for such orbital difference with respect to other HMXBs is generally attributed to the different mass-loss efficiency. Those systems which loose a large amount of mass and angular momentum during their evolution, will also pass through a stage where the companion expands and a common envelope forms, which is eventually lost, carrying away the angular momentum responsible for the spiral-in mechanism (Paczynski, 1976).

The accretion process in these X-ray binary systems has been initially formalized by Bondi, Hoyle, and Lyttleton (Hoyle and Lyttleton, 1939; Bondi and Hoyle, 1944), and recently reviewed by Edgar (2004). In the framework of the Bondi-Hoyle-Lyttleton wind accretion model, the gravity of the compact object focuses the flow into a wake which is then accreted (see Fig. 3.3 and Fig. 3.4). Assuming that material will be accreted if it is bound to the star, the following relation holds

$$\frac{1}{2}v_{\infty}^{2} - \frac{GM_{NS}}{r} < 0 \tag{3.20}$$

which defines the critical impact parameter, known as the Hoyle–Lyttleton radius, as

$$\psi < \psi_{HL} = \frac{2GM_{NS}}{v_{\infty}^{2}} \tag{3.21}$$

When the relative velocity of the neutron star with respect to the wind, v_{rel}, is taken into account, the Hoyle-Lyttleton radius is called *accretion radius* (see Fig. 3.4):

$$R_{acc} \cong \frac{2GM_{NS}}{v_{rel}^{2}} \tag{3.22}$$

where $v_{rel} \cong \sqrt{v_{wind}^{2} + v_{NS}^{2}}$, with v_{NS} and v_{wind} being the orbital velocity of the neutron star and the wind velocity at the NS orbit, respectively. A common expression for the the velocity law of the wind is known as the "β-velocity law" (Castor, Abbott, and Klein, 1975):

$$v_{wind}(r) = v_{\infty}\left(1 - \frac{R_{\star}}{r}\right)^{\beta} \tag{3.23}$$

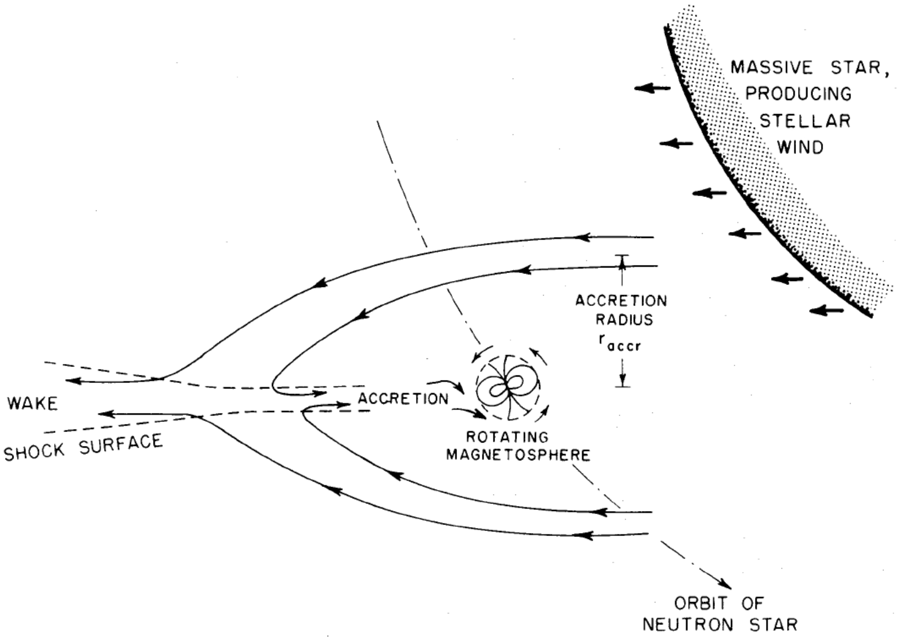

Figure 3.4: Streamlines of stellar wind accretion onto a neutron star (not to scale). Figure from Davidson and Ostriker (1973).

where $\beta = 0.5 - 1.5$ determines how steeply the velocity reaches the terminal velocity (although a general approximation of the wind velocity is given by the escape velocity of the stellar wind with respect to the donor star, $v_{wind}(r) \sim v_{esc} = \sqrt{GM_\star/R_\star}$ – see Frank, King, and Raine (1992) and Owocki (1994)). Passing within the accretion radius, the stellar wind is accreted onto the neutron star, powering the X-ray emission with luminosity:

$$L_X = \frac{(GM_{NS})^2}{R_{NS}} \frac{\dot{M}_w}{v_{rel}^4 D^2} \tag{3.24}$$

where D is the distance of the compact object from the center of the companion. For typical NS parameters, this becomes:

$$L_X \sim 10^{37} \left(\frac{\dot{M}}{10^{-4} \dot{M}_w} \right) \left(\frac{\dot{M}_w}{10^{-5}\, M_\odot\, yr^{-1}} \right) erg\, s^{-1} \tag{3.25}$$

The interaction of the neutron star with the ambient wind leads to both gravitational and radiative effects, which are important to consider due to their modification of the observed X-ray spectra from the compact source. These effects can be summarized as follows:

- An *accretion wake*, which is due to the gravitational focusing of a significant fraction of the stellar wind by the neutron star;
- A *photoionization wake*, which results from the X-ray photoionization of the stellar wind by the X-ray emission of the compact source. The radiatively-driven stellar wind is ionized when it enters the so-called "Strömgren sphere"[1], and leads to the formation of dense sheets of gas trailing the neutron star (Fransson and Fabian, 1980).

---

[1] A Strömgren sphere is defined as the region of ionized hydrogen (H II) surrounding a hot young star which is the source of the ionizing radiation (Strömgren, 1939).

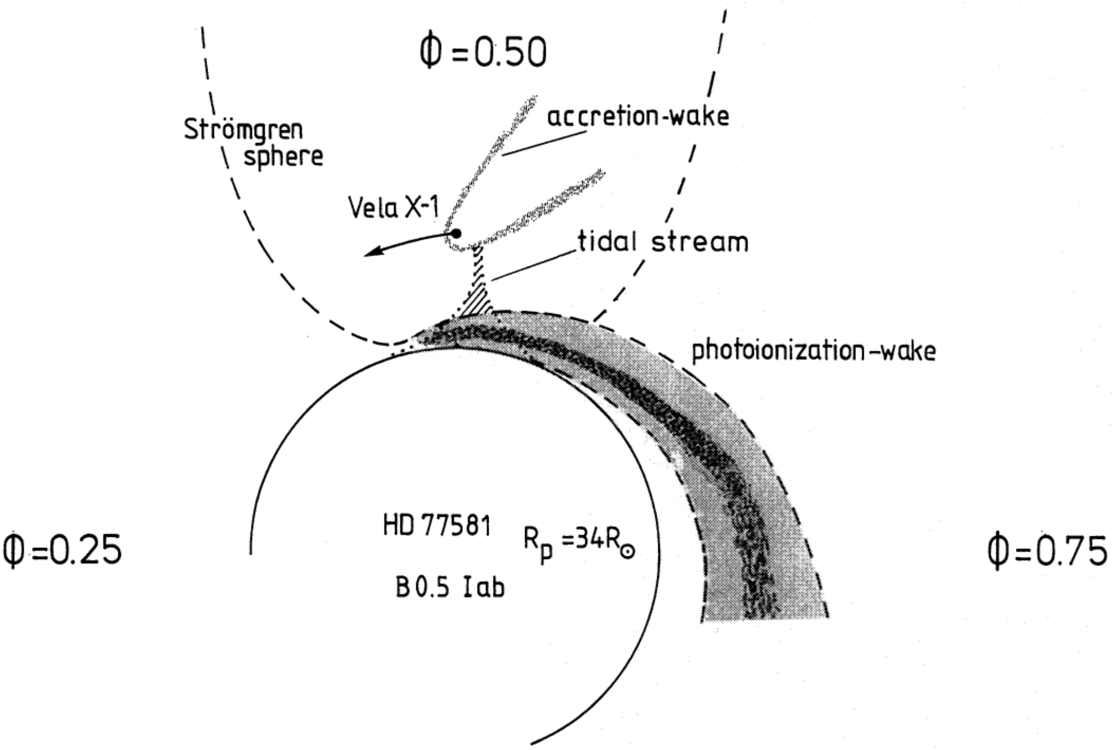

Figure 3.5: A sketch of the different structures due to both gravitational (the accretion wake and the tidal stream) and radiative effects (the photoionization wake with more - black - and less - gray - dense sheets of ionized wind), present in the Vela X-1 binary system. Figure from Kaper, Hammerschlag-Hensberge, and Zuiderwijk (1994).

- A *tidal stream*, due to the almost filled Roche lobe of the companion, which departs from the L_1 point and follows the orbiting star along the binary orbit.

A sketch of the binary system where all these structures are illustrated is shown in Fig. 3.5.

3.3.1.3 Be/X-ray binaries

Be/X-Ray Binary systems (BeXRBs) are a class of objects (first introduced by Maraschi, Treves, and van den Heuvel 1976), in which the donor star is of a B spectral type showing emission lines (from which the additional lower case e in the spectral type comes). BeXRBs are the most numerous class of HMXBs. Be stars have masses, in the range of $5 - 20\,\mathrm{M}_\odot$, and are tipically rapid (not critically) rotators, which is clearly a necessary (although not sufficient) ingredient to realize the expulsion of stellar material on the equatorial plane of the star, forming a decretion disk. The decretion disk is composed of ionized gas, thus producing emission lines. Of the almost 90 BeXRBs known, most host a NS as a compact object. MWC 656 (or AGL J2241+4454) was recently discovered to be the first Be star orbited by a black hole (Casares et al., 2014). Later on, pointed XMM observations detected a faint X-ray flux coming from this source (Munar-Adrover et al., 2014). Currently no Be/WD binaries have been observed in the Galaxy, while three of such systems have been proposed in the Small and Large Magellanic Clouds (Kahabka et al., 2006; Sturm et al., 2012; Li et al., 2012).

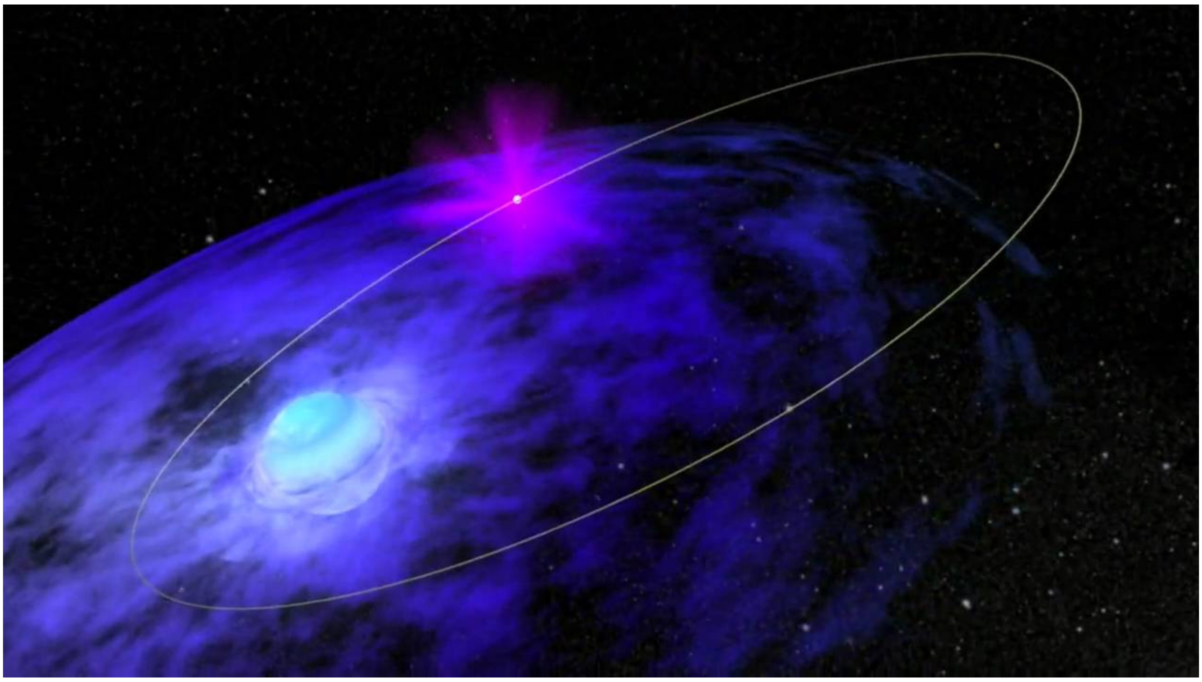

Figure 3.6: Schematic model (not in scale) of a Be-star X-ray binary system. The Neutron Star moves in an eccentric orbit around the Be-star, which is surrounded by a decretion disk. Near the periastron passage the Neutron Star is allowed to accrete from that disk, powering an X-ray outburst lasting several days. (Credit: NASA/Goddard Space Flight Center)

When the compact object in such is systems is a neutron star, it usually orbits around the Be star in an eccentric orbit $e \sim 0.3 - 0.5$ with moderate orbital periods $P_{orb} \sim 30 - 100\,\mathrm{d}$ (Bildsten et al., 1997). This is interpreted as due to the kick velocity imparted to the newly born neutron star from the (possibly asymmetric) Supernovae episode (Verbunt and van den Heuvel, 1995).

The mechanism by which the NS accretes material from the donor star, is connected to the decretion disk around the Be star. It is generally accepted that, during the periastron passage, the neutron star passes close to that disk, sometimes may even go through it causing major disruption. A large flow of matter is then accreted onto the compact object, giving rise to an X-ray outburst ($L_X \sim 10^{37}\,\mathrm{erg\,s^{-1}}$). Due to its large angular momentum, the gas will form an accretion disk around the neutron star before to be accreted onto the compact object, leading to spin-up episodes.

After the periastron passage, there is a rapid decrease of the available gas fueling the accretion. The X-ray activity persists until the accretion disk is depleted, after which the X-ray source will become fainter down to the quiescence level, until the next periastron passage. Therefore, such systems are periodic sources of X-ray outbursts, and are defined *transients*, although persistent sources also exist.

However, the scheme that has just been summarized, is very simplistic. In fact, depending on the geometry of the orbit, the activity of the Be star, or the characteristics of the decretion disk, outburst properties can substantially differ from a periodic transient source behavior. For example, there are systems in which no X-ray activity is seen despite the periastron passage of the neutron star.

On the other hand, BeXRBs also show outbursts that are not periodic and not correlated with the periastron passage. These outbursts are more rare, and generally more luminous ($L_X \sim 10^{38}\,\mathrm{erg\,s^{-1}}$), and are therefore called *giant outbursts*. They are also generally longer than the periodic outbursts, lasting for a large fraction of an orbital period or even for several orbital periods. Giant outbursts are likely related to a precessing warped disk (Okazaki, Hayasaki, and Moritani, 2013; Moritani et al., 2013; Nakajima et al., 2014). Such a distorted disk influences the accretion modalities in different ways. It can either be inclined in a way that the accretion from the NS is favored, or it can grow in size (due to inefficient tidal truncation) thus crossing the NS orbit. In both cases, the compact object can accrete more efficiently and at different orbital phases than the periastron.

Recently, a new subclass of HMXBs with long orbital periods ($P_{orb} \geq 30\,\mathrm{d}$) and low eccentricities ($e \leq 0.2$) has been suggested by Pfahl et al. (2002).

3.4 Accretion onto highly magnetized Neutron Stars

Neutron stars are known for being the most magnetized objects in the Universe. Their strong magnetic field was inferred by simple arguments already by Woltjer (1964), assuming magnetic flux conservation during the collapse of the progenitor star, leading to:

$$B \propto R^{-2} \tag{3.26}$$

Therefore, the magnetic field of NSs would increase by a factor of 10^{10}, with respect to that of the progenitor star, whose magnetic field is typically of the order of $0.1 - 10\,\mathrm{kG}$ (Walder, Folini, and Meynet, 2012), thus leading to a final magnetic field for the compact object of $10^{12} - 10^{14}\,\mathrm{G}$.

3.4.1 Accretion geometry

Accretion of matter onto a neutron star with a strong magnetic field occurs in a highly anisotropic configuration. In the simplest approximation, a dipole geometry may be considered for the magnetic field, and its strength B, at a given distance r from the center of the neutron star and outside the star, is given by

$$B \sim \frac{\mu}{r^3} \tag{3.27}$$

with μ being the magnetic moment of the NS. Therefore, the magnetic pressure at a given distance is

$$P_{mag} \simeq \frac{\mu^2}{8\pi r^6} \tag{3.28}$$

and P_{mag} quickly increases toward the NS surface. At a certain distance, the magnetic pressure will exceed the ram pressure of the infalling gas, which has a weak dependence on the radius

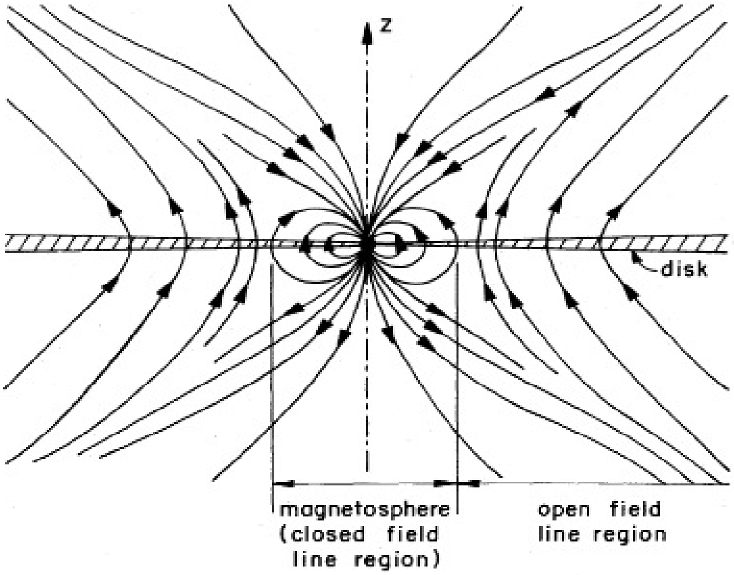

Figure 3.7: Sketch of a strongly magnetized NS accreting from a disk. At the transition layer the magnetic field disrupts the disk and the material follows the magnetic field lines onto the neutron star. In the region where the magnetic field lines become open, the matter can leave through those lines, carring angular momentum away. Figure from Lovelace, Romanova, and Bisnovatyi-Kogan (1995).

$$\frac{\mu^2}{8\pi r^6} = \frac{(2GM)^{1/2}\dot{M}}{4\pi r_A^{5/2}} \tag{3.29}$$

This will happen at the so-called *Alfvén radius* (Frank, King, and Raine, 1992):

$$r_A = 2.9 \times 10^8 M_1^{1/7} R_6^{-2/7} L_{37}^{-2/7} \mu_{30}^{4/7}\, cm \tag{3.30}$$

(also called, the *magnetospheric radius* r_M). Therefore, within the Alfvén radius, the magnetic field pressure is strong enough to control the incoming gas flow, disrupting the transient accretion disk or channeling the spherical infall, and forcing the gas to follow the magnetic field lines.

Another characteristic radius in the accretion configuration of NSs, is the *co-rotation radius*:

$$r_c = \frac{GM_{NS}}{\omega^2} \approx 2.8 \times 10^8 P^{2/3} M_{NS}^{1/3}\, cm \tag{3.31}$$

where P is the NS spin period in seconds. The co-rotation radius is the radius at which the linear velocity of the magnetosphere ωr and the Keplerian velocity of the disk $\sqrt{GM_{NS}/r}$ are equal. When the Alfven radius exceeds the co-rotation radius, the accretion is inhibited by the centrifugal forces, and the material if blown away. This is referred to as the *propeller effect* (Illarionov and Sunyaev, 1975).

Although the basic picture of the magnetosphere-disk interaction is well known, the real scenario is much more complicated. Several models have been developed to describe

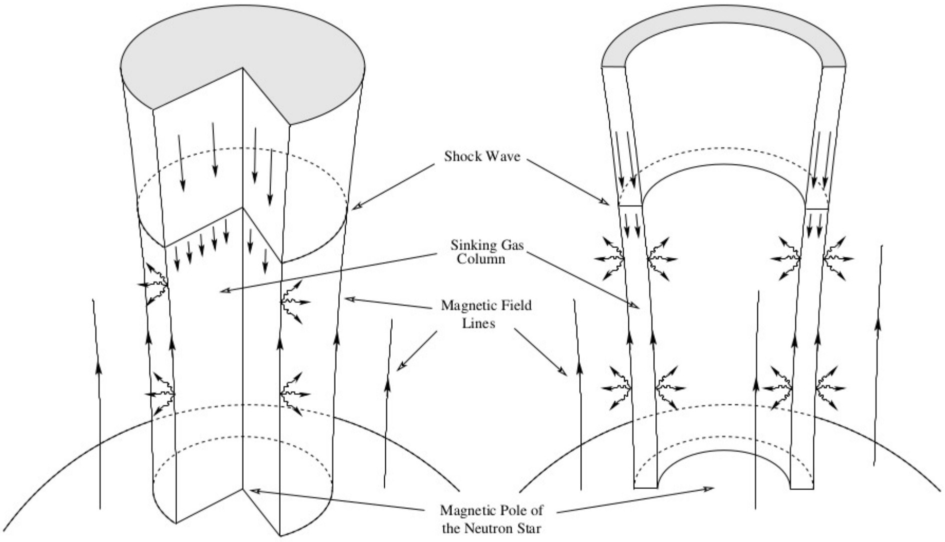

Figure 3.8: Column-like accretion structures above the polar caps of Neutron Stars. *Left:* Solid accretion column configuration. *Right:* Hollow accretion column configuration. Figure from Kuster (2003).

the interaction between the magnetized central objects and their accretion disks (see, e.g., Ghosh and Lamb 1979; Lovelace, Romanova, and Bisnovatyi-Kogan 1995). A key difference between those models, is the behaviour of the magnetic field lines under the influence of the accreting matter (an example is shown in Fig. 3.7). The main physical processes of the magnetosphere-disk interaction have been recently reviewed by Lai (2014).

3.4.2 Accretion onto polar caps

When the accretion is taking place onto a magnetized neutron star, matter is channeled onto the magnetic poles by the magnetic field lines creating funnels and forming, in the dipole approximation, two *polar caps*. The infalling plasma is moving at supersonic speed of roughly $0.6\,c$. Above the polar caps, a column-shaped structure is formed, also named *accretion column*. Theoretical models of the accretion structure have been proposed already by Basko and Sunyaev (1976), where different configurations (i.e. solid and hollow accretion columns) are considered (see Fig. 3.8). In their seminal work, the flow of matter is governed by different hydrodynamical effects at different accretion rates. As a consequence, depending on the mass accretion rate (thus on the luminosity), the *emission diagram* of the accretion column (also called, the *beaming pattern*) also switches from a pencil-beam to a fan-beam dominated pattern (with some ibrid pattern configurations in between). At higher accretion rates, a radiation dominated shock forms, which decelerates the plasma to subsonic speed, which in turn gets very hot and subsequently sinks down to the NS surface, cooling through the emission of X-rays. In this case, an accretion column raises, whose walls have an extended surface that also emits X-rays, thus resulting in a *fan beam* pattern (see Fig. 3.9). On the other hand, at lower accretion rates the radiative shock is not formed, and the plasma is stopped by Coulomb interactions and collective plasma oscillations (Nelson, Salpeter, and

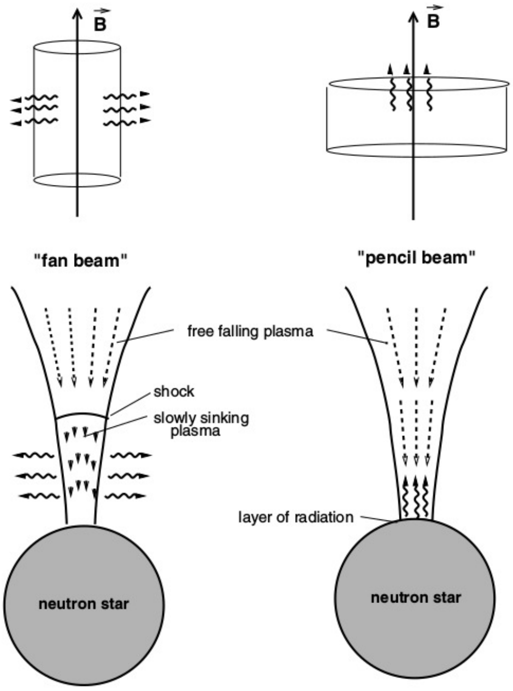

Figure 3.9: Accretion geometries and radiation patterns of accreting columns onto a mangetized neutron star. *Left:* at high accretion rates a radiation shock front forms, and the sinking plasma emits X-rays through the wall of the columns in a *fan beam* geometry. *Right:* at lower accretion rates no shock forms and the plasma falss directly onto the neutron star surface, forming an accretion mound and emitting in a *pencil beam* geometry. Figure from Schönherr et al. (2007).

Wasserman, 1993; Staubert et al., 2007). In this case, the radiation mostly escapes along the column axis, thus producing a *pencil beam* pattern.

Recently, Becker et al. (2012) calculated the critical luminosity at which the radiative shock becomes effective, as (for typical neutron star parameters):

$$L_{crit} = 1.5 \times 10^{37} \, B_{12}^{16/15} \, erg \, s^{-1} \tag{3.32}$$

(where B_{12} is the surface magnetic field strength in units of 10^{12} G). More recently, a different calculation of the critical luminosity has been obtained by Mushtukov et al. (2015b). These authors take into account the exact effective cross-section for Compton scattering in a strong magnetic field including the resonances, altogether with the polarization composition, the geometry of the accretion flow and the temperature of the accreting gas. As a consequence, the critical luminosity results in a non monotonic function of the magnetic field strength.

3.4.3 X-ray pulse profiles

Due to the high magnetic field of the NS that channels the accreted matter, both the accretion geometry and the emitted radiation are strongly anisotropic. As a consequence,

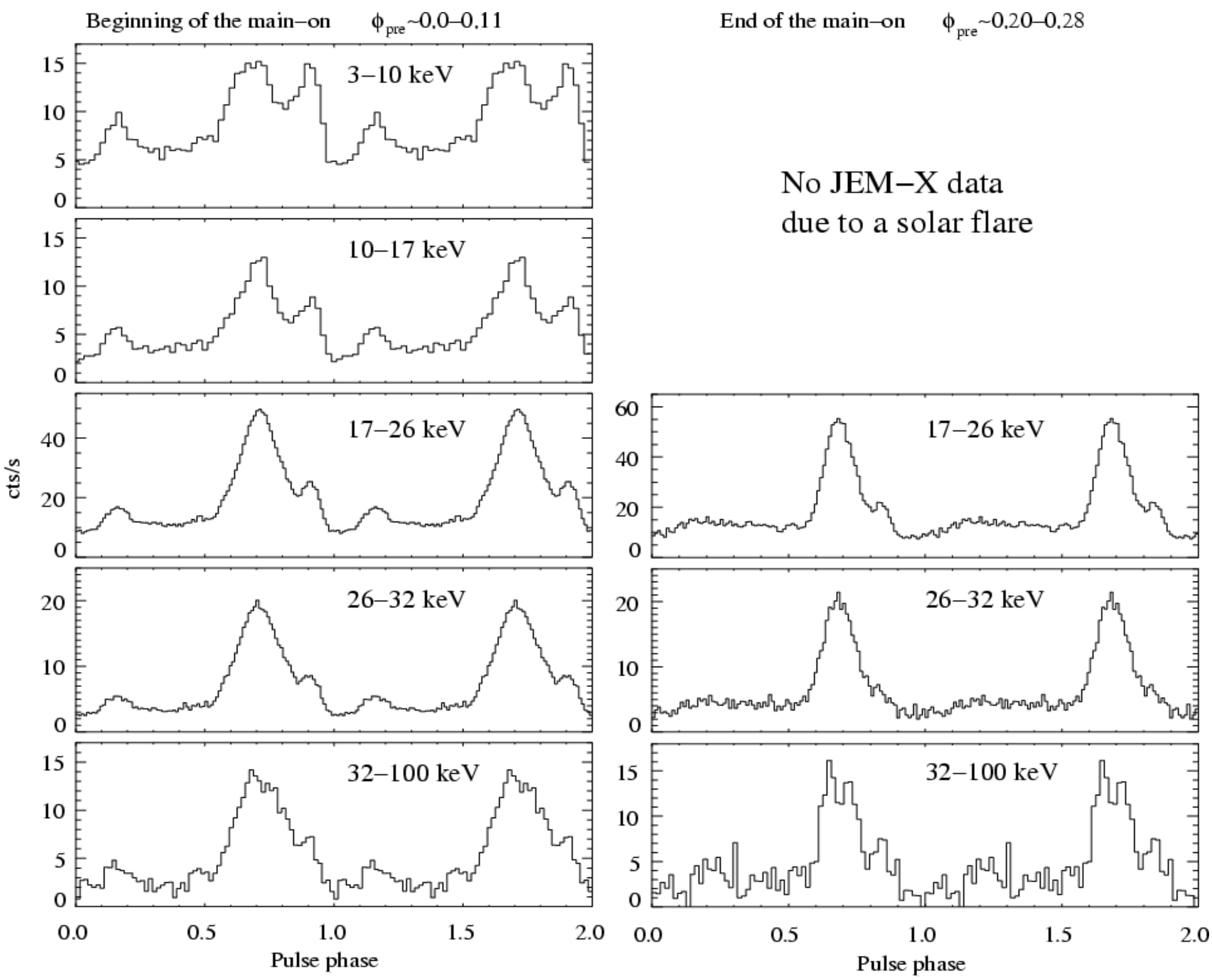

Figure 3.10: Energy-resolved X-ray pulse profiles of Her X-1. *Left:* pulse profiles at the start of the main-on cycle. *Right:* pulse profiles at the end of the main-on cycle. Figure from Klochkov et al. (2008).

if the magnetic field dipole is misaligned with the rotation axis, the observer will detect a modulated flux from the spinning source (the so-called *lighthouse effect*). The observed modulated intensity as a function of the NS rotational phase (often folded over several rotational periods in order to increase the statistics), is referred to as *pulse profile.*

Pulse profiles are very important diagnostic features of accreting NSs. However, their modelling is very complex and still far from giving a quantitative description of the accretion processes. Indeed, the morphology of pulse profiles is a result of many effects, some of which we do not yet fully understand. Different sources exhibit very different pulse profile shapes, which makes the modelling even more complex.

In general, accreting pulsars show pulse profiles with a more complex shape at lower energies, while a simpler profile appears at higher energies (see Fig 3.10 for an example of Her X-1 pulse profile variability on energy). Besides the energy dependence, pulse profiles also show clear dependence on luminosity, and are therefore hard to describe under a common scenario.

Nonetheless, it is possible to divide the factors shaping the pulse profiles into four major categories:

- Geometrical configuration: it is defined by the angle between the spin and the dipole axes (referred to as the *obliquity* angle), and by the angle between the observer's line of sight and the spin axis (referred to as the *observer* angle) (Harding and Muslimov, 1998).
- Beaming pattern of the emitted radiation, i.e., the observed flux from one emission region as a function of the direction to the observer: this needs detailed models of the accretion processes in the vicinity of the NS surface (see Section 3.4.2).
- Relativistic light deflection: the high gravitational field of the NS must be taken into account, to properly determine the amount of emitted light which is deflected and therefore visible from a given observer as the star rotates (Riffert and Meszaros, 1988; Kraus, 2001).
- Magnetic configurations: different magnetic configurations than a simple symmetric dipole (e.g., asymmetric dipole or multipole magnetic field) have been shown to affect the resultant pulse profile (Kraus et al., 1995; Kraus et al., 1996).

Another important quantity used to characterize pulsations is the *pulsed fraction*, defined as:

$$P_f = \frac{I_{max} - I_{min}}{I_{max} + I_{min}} \tag{3.33}$$

where I_{max} and I_{min} are the maximum and minimum intensity, respectively, observed in the pulse profile. The pulsed fraction of accreting X-ray pulsars is tipically large ($\geq 50\%$) and usually increases with photon energy (Bildsten et al., 1997). The observed pulsed fraction can be used to constrain the orientation and geometry of the neutron star (Sturner and Dermer, 1996).

3.5 X-ray spectra

First attempts to model the X-ray spectra of accreting pulsars have been carried out by Zel'dovich and Shakura (1969), under the assumption of spherical accretion. Their scenario describes a flow of accreted plasma decelerated in the neutron star atmosphere by Coulomb collisions with electrons. This process deposits most of the energy in the atmosphere, which is successively released as thermal radiation. The resulting spectrum is dominated by a blackbody component, which is the result of bremsstrahlung emission by the hot electrons ($T_{BB} \sim 10^7$ K), and a hard tail resulting from inverse Compton by hot electrons off soft photons.

Later models considered more complicated and realistic scenarios: a radiation-dominated shock by which the infalling gas is decelerated (Davidson, 1973) forming a thermal accretion mound that is the source of a blackbody spectrum; the accretion geometry for both solid and hollow accretion columns and the possibility for super-Eddington luminosities (Basko and Sunyaev, 1976).

More detailed calculations of the spectrum emerging from a pulsar accretion column have been carried out recently by Becker and Wolff (2005), Becker and Wolff (2007), and Postnov et al. (2015). These authors took into account various effects, such as the contribution of both bulk and thermal Comptonization. Comptonization processes are of key importance to reproduce the power-law shape of the spectrum observed in X-ray pulsars as well as the high-energy cutoff (see below).

Accreting X-ray pulsars exhibit luminosities ranging from $10^{32} - 10^{33}\,\mathrm{erg\,s^{-1}}$ during the quiescent state, to $10^{36} - 10^{38}\,\mathrm{erg\,s^{-1}}$ during the peak of the outbursts. Although the mass accretion in these systems is a very complex physical process, broad band X-ray spectra of X-ray pulsars can be successfully described by relatively simple phenomenological models: by a power-law model, a broken power-law model or a power-law with a high-energy cutoff.

Many HMXBs display in their X-ray spectra iron emission between 6.4 and 6.9 keV. The 6.4 keV line is likely due to the fluorescence of cold and dense material close to the NS, while the other lines are produced in a region that is far from the neutron star, probably in the highly photo-ionized wind of the companion star (whose typical metallicity allows it to be source of such lines), or in the magnetosphere/accretion disk corona of the NS (Naik and Paul, 2012).

3.5.1 Cyclotron lines

Many NSs in X-ray binaries are known to have very strong surface magnetic field of the order of $\sim 10^{12}$ G. The surface magnetic field for these objects can be determined by using Cyclotron Resonance Scattering Features (CRSFs), appearing as absorption lines in their X-ray spectrum. These features are the result of the strong magnetic field that quantizes the energy levels of the electrons in the "Landau levels", as described in the following.

Considering an electron that follows a magnetic field line, subject to the Lorentz force, its trajectory will be helicoidal with a gyration (or Larmor) frequency equal to:

$$\omega_L = \frac{v_\perp}{r} = \frac{eB}{m_e} \tag{3.34}$$

where $v_\perp$ and r are the normal velocity and the radius of the helicoidal orbit covered by the electron, respectively, and e, B and m_e are the electron charge, the magnetic field strenght and the electron mass, respectively. Then, the gyration (or Larmor) radius can be written as:

$$r_L = \frac{m_e v_\perp}{eB} \tag{3.35}$$

that is inversely proportional to the magnetic field strenght. Quantum effects become important when the Larmor radius becomes comparable to the characteristic de Broglie wavelength of the electron (Araya and Harding, 1996):

$$\lambda_{deBroglie} = \frac{\hbar}{mv} \tag{3.36}$$

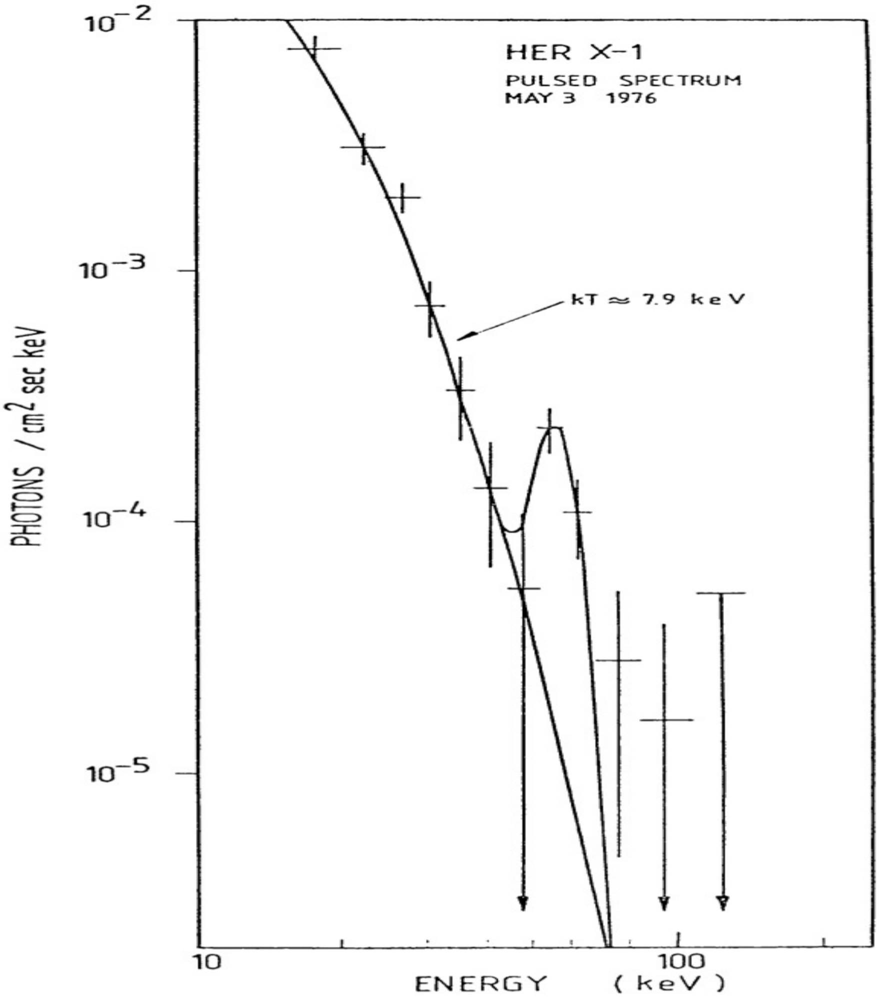

Figure 3.11: X-ray spectrum of Her X-1 where a cyclotron line is observed for the first time. The line in this spectrum has been initially wrongly associated with an emission line. Figure from Trümper et al. (1977).

(where $\hbar = \frac{h}{2\pi}$ is the reduced Planck's constant, and m and v are the electron mass and the velocity, respectively). If this is the case, the kinetic energy of the electron perpendicular to the magnetic field becomes quantized, and the allowed kinetic energy values are called Landau levels (as Landau was the first to formalize this problem), given by:

$$E_n = m_e c^2 \sqrt{1 + \left(\frac{p_\parallel}{m_e c}\right)^2 + 2n\frac{B}{B_c}} \tag{3.37}$$

Here n is the level number, $p_\parallel = m_e v_\parallel$ is the momentum of the electron parallel to the magnetic field, and $B_c \sim 4.4 \times 10^{13}$ G is the critical value of the magnetic field at which the kinetic energy E_n of the electron becomes comparable to its rest mass. In the non-relativistic approximation the levels are equidistant (Lipunov, 1987), the first energy level being equal to:

$$E_{n_1} = \hbar\omega = \frac{\hbar e B}{m_e} \sim 11.6 \frac{B}{10^{12}\,G} \tag{3.38}$$

When the kinetic energy of electron becomes quantized, it can change only in a discrete way.

This means that the Compton scattering cross-section process is enhanced for photons whose energy is equal to the first Landau energy level, or its mutiples, $E_\gamma = nE_{n_1}$. However, after the excitation, the electron decays in the lower energy level with a very high probability, expressed by the following decaying rate (Latal, 1986):

$$\nu_r = \left(\frac{\alpha m_e c^2}{\hbar}\right)\left(\frac{B}{B_c}\right)^{1/2} \sim 10^{15}\frac{B}{10^{12}\,G}s^{-1} \tag{3.39}$$

(where α is the fine structure constant). This allows the electron to be in the excited state only for a very short time. As a consequence, a photon is almost immediatly re-emitted, with an energy corresponding to the discrete energy level $E_\gamma = nE_{n_1}$. The energy of the photon is unchanged, but its direction changes, so the process is called "resonant scattering", because the scattering can occur only for energies that are close to the Landau levels. This process results in a series of line-like absorption features in the emerging X-ray spectrum, because the probability to leave the environment is strongly suppressed for photons with resonant energies, due to shortening of their mean free path. The line correspondent to $n = 1$ is called the “fundamental” cyclotron line, while those at $n \geq 2$ are called harmonic lines. As the energy of the cyclotron lines depend on the magnetic field strenght, the observed spectrum with such an energy resolution to allow the estimation of the lines centroid energy, also allows to estimate the magnetic field of the NS.

Actually, the discussion on the nature of the cyclotron feature was quite debated after its discovery. It was first discovered in Hercules X-1 (Trümper et al., 1977) in a balloon experiment carried on in 1976, and was initially interpreted as an emission feature at ~ 58 keV (see Fig. 3.11). In the following years, theoretical considerations on the Thomson optical thickness of the radiating plasma and on the temperature distribution (Voges et al., 1982), altogether with much greater spectral energy resolution data (Mihara et al., 1990), led to the general agreement that the observed feature was not an emission line at ~ 58 keV, but rather an absorbtion line at ~ 42 keV. Modern instruments with even better energy resolution clearly show that the line is in absorption.

Several other spectra were obtained from other discovered X-ray pulsars, and also they were characterized with similar features. In some cases, also higher harmonics than the fundamental were detected, strongly supporting the resonant scattering argument. The record holder among cyclotron line sources is 4U 0115 + 63, which shows up to four harmonics (Santangelo et al., 1999).

In the last decade, the continuos monitoring of Her X-1, where a prominent cyclotron line is observable even with shorter observations than in other X-ray binary pulsars at a similar flux level, has shown a secular variation of the cyclotron line energy for this source. This variation is characterized by an initial value of ~ 35 keV, and an abrupt jump up to ~ 44 keV between 1990 and 1994, followed by an appeerent secular decay (Staubert et al., 2007). Since the observed timescale for the decrease of the line energy (a few decades) is too short for a decay of the global magnetic field, the physical reason for such a secular trend could be connected to a geometric displacement of the cyclotron resonant scattering region in the polar field or to a true physical change in the magnetic field configuration at the polar cap by the continued accretion (Staubert et al., 2014). Up to know, Her X-1 is the only known source exhibiting such a secular variation of the cyclotron line energy.

The cyclotron line energy of many accreting pulsars has been found correlated with the observed luminosity (Klochkov et al. 2011, and references therein). A positive correlation has been observed in Her X-1 (Staubert et al., 2007), GX 304-1 (Klochkov et al., 2012; Malacaria et al., 2015), Vela X-1 (Fürst et al., 2014), and recently for A 0535+26 (Sartore, Jourdain, and Roques, 2015). The opposite dependence, a negative correlation between the cyclotron line energy and the luminosity, has been confirmed for only one source, V $0332+63$ (Tsygankov et al., 2006a). A negative correlation in 4U $0115+63$ is still under debate (Nakajima et al., 2006; Müller et al., 2013; Iyer et al., 2015). Such a luminosity-dependent behavior of the cyclotron line energy is not fully understood yet. Among different competing models, its origin is attributed to a variation in the condition of the accretion structure (Becker et al., 2012), to the Doppler effect in the accretion channel (Mushtukov et al., 2015a), or to a variable reflection contribution from the NS surface (Poutanen et al., 2013).

4

X-RAY OBSERVATORIES

In this chapter, the observatories whose data have been used in the present work will be discussed: *INTEGRAL* and *MAXI*. Despite they both observe in the X-ray band (even with overlapping ranges), they host very different instruments and serve different purposes. In this work *INTEGRAL* data have been used for the analysis of GX 304-1, while data from *MAXI* have been used for the analysis of Vela X-1. In the following, the two missions will be described separately.

4.1 The INTEGRAL telescope

The INTErnational Gamma Ray Astrophyisics Laboratory (INTEGRAL, Winkler et al. 2003, Goldwurm et al. 2003) is an ESA mission with contributions from 16 European countries plus the participation of Russia, which provided the Proton launcher, and NASA, with the Deep Space Network ground stations. The satellite was launched on October 17th, 2002 from Baikonur in Kazakstan and placed in a highly eccentric orbit, with an inclination of 51.6° at launch, so allowing long uninterrupted observations with an almost constant background. The revolution period of the orbit is $\sim$ 3 sideral days (slightly less than 72 hours). Its strongest points are fine spectroscopy (2.5 keV FWHM @ 1 MeV) and relatively fine imaging (angular resolution $\sim 12'$ FWHM) of celestial sources in the gamma-ray band. Furthermore, INTEGRAL can observe the sky in various concurrent bands, allowing a coverage from 3 keV to 10 MeV, and symultaneous source monitoring in the optical band (V band, 550 nm).

4.1.1 The payload

The INTEGRAL payload consists of 4 main instruments, two of them (IBIS and SPI) specifically designed for the gamma-ray analysis, and the other two designed to furnish multiwavelength observations. For an overview of the spacecraft and its properties, see Figure 4.1 and Table 4.1. All the instruments are coaligned. The 4 instruments which form the INTEGRAL payload are the following:

- the Imager on Board INTEGRAL Satellite, or IBIS = ISGRI + PICsIT (Ubertini et al., 2003)
- the Joint European Monitors for X-rays, or JEM-X1 and JEM-X2 (Lund et al., 2003)

Parameter	SPI	IBIS
Energy range	18 keV–8 MeV	15 keV–10 MeV
Detector	19 Ge detectors, each (6×7) cm cooled @ 85 K	16384 CdTe dets, each $(4 \times 4 \times 2)$ mm 4096 CsI dets, each $(8.4 \times 8.4 \times 30)$ mm
Detector area (cm^2)	500	2600 (CdTe), 2890 (CsI)
Spectral resolution (FWHM)	3 keV @ 1.7 MeV	8 keV @ 100 keV
Continuum sensitivity (photons cm^{-2} s^{-1} keV^{-1}) ($\Delta E = E/2$, 3σ, 10^6 s)	5.5×10^{-6} @ 100 keV 1.2×10^{-6} @ 1 MeV	6×10^{-7} @ 100 keV 5×10^{-7} @ 1 MeV
Line sensitivity (photons cm^{-2} s^{-1}) (3σ, 10^6 s)	3.3×10^{-5} @ 100 keV 2.4×10^{-5} @ 1 MeV	1.9×10^{-5} @ 100 keV 3.8×10^{-4} @ 1 MeV
Field of view (fully coded)	16° (corner to corner)	9° × 9°
Angular resolution (FWHM)	2.5° (point source)	$12'$
Source location (radius)	≤1.3° (depending on source strength)	$\leq 1'$ (for 10σ source)
Absolute timing accuracy (3σ)	≤200 μs	≤200 μs
Mass (kg)	1309	746
Power [max/average] (W)	385/110	240/208
Parameter	JEM−X	OMC
Energy range	4 keV–35 keV	500 nm–600 nm
Detector	Microstrip Xe/CH$_4$−gas detector (1.5 bar)	CCD + V-filter
Detector area (cm^2)	500 for each of the two JEM-X detectors[a]	CCD: (2061×1056) pixels Imaging area (1024×1024) pixels
Spectral resolution (FWHM)	2.0 keV @ 22 keV	–
Continuum sensitivity[b] (photons cm^{-2} s^{-1} keV^{-1}) (3σ, 10^6 s)	1.2×10^{-5} @ 6 keV 1.3×10^{-5} @ 30 keV	– –
Line sensitivity[b] (photons cm^{-2} s^{-1}) (3σ, 10^6 s)	1.9×10^{-5} @ 6 keV 8.5×10^{-5} @ 30 keV	– –
Limiting magnitude (mag) (3σ, 5000 s)	–	17.8
Field of view (fully coded)	4.8°	5° × 5°
Angular resolution (FWHM)	$3'$	$25''$
10σ source location (radius)	$\leq 30''$	$6''$
Absolute Timing accuracy (3σ)	≤200 μs	≥1 s
Mass (kg)	65	17
Power [max/average] (W)	50/37	20/17

Table 4.1: Key parameters for the INTEGRAL payload. Table from Winkler et al. (2003).

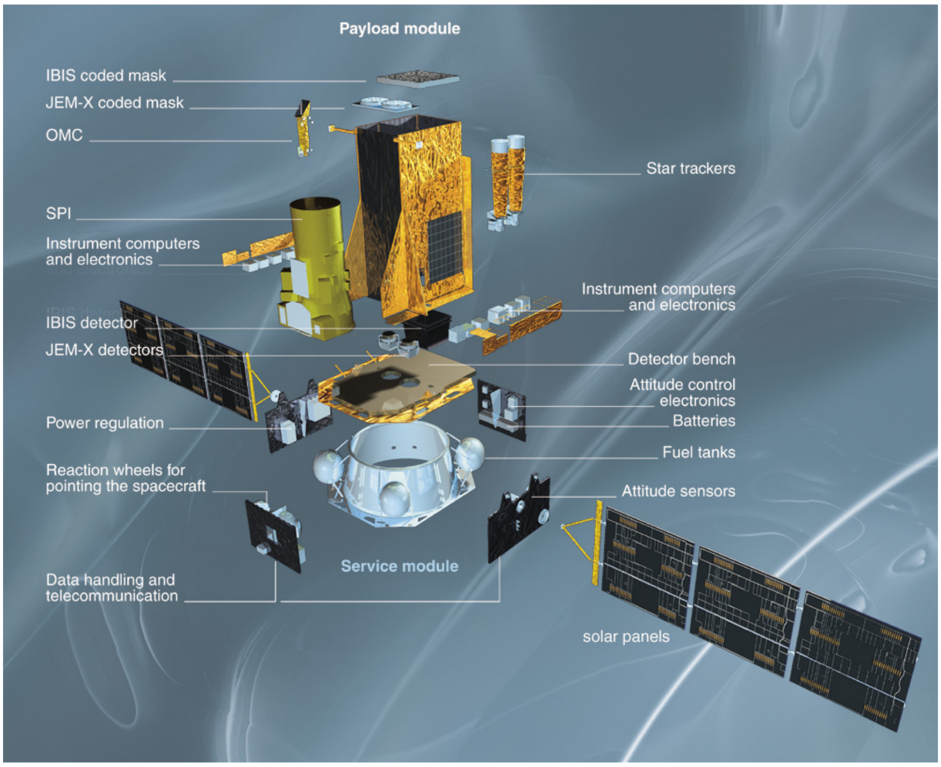
Payload module
IBIS coded mask
JEM-X coded mask
OMC
SPI
Instrument computers and electronics
IBIS detector
JEM-X detectors
Power regulation
Reaction wheels for pointing the spacecraft
Data handling and telecommunication
Service module
Star trackers
Instrument computers and electronics
Detector bench
Attitude control electronics
Batteries
Fuel tanks
Attitude sensors
solar panels

Figure 4.1: A scheme of INTEGRAL spacecraft with all instruments in detail (Credit: ESA).

- the Spectrometer on INTEGRAL, or SPI (Vedrenne et al., 2003)
- the Optical Monitoring Camera, or OMC (Lund et al., 2003)

In the present work, the PICsIT and OMC instruments have not been used, therefore they will not be discussed.

4.1.1.1 The coded masks on INTEGRAL

Before going into details of the instruments payload, it is worth to mention the common feature of the high-energy instruments onboard INTEGRAL: the coded mask. Since high-energy X-rays or gamma-rays can not be practically focused by using lenses or mirrors, another method is required in order to image the observed targets. The coded mask technique is a possible way for high energy imaging instruments, allowing to resolve sources (Caroli et al., 1987; Skinner and Ponman, 1994). Basically, the mask is a plate made of both opaque and transparent elements that are distributed in a pre-determinated pattern. The transparent elements form the so-called *aperture*. The instrument angular resolution $d\theta$ depends on the dimension C of the mask elements and on the distance H between the mask plane and the detector plane

$$d\theta = arctan\frac{C}{H} \tag{4.1}$$

However, the source location uncertainty can be strongly reduced depending on the source Signal-to-Noise Ratio (SNR), which in turn is proportional to the total open area of the aperture.

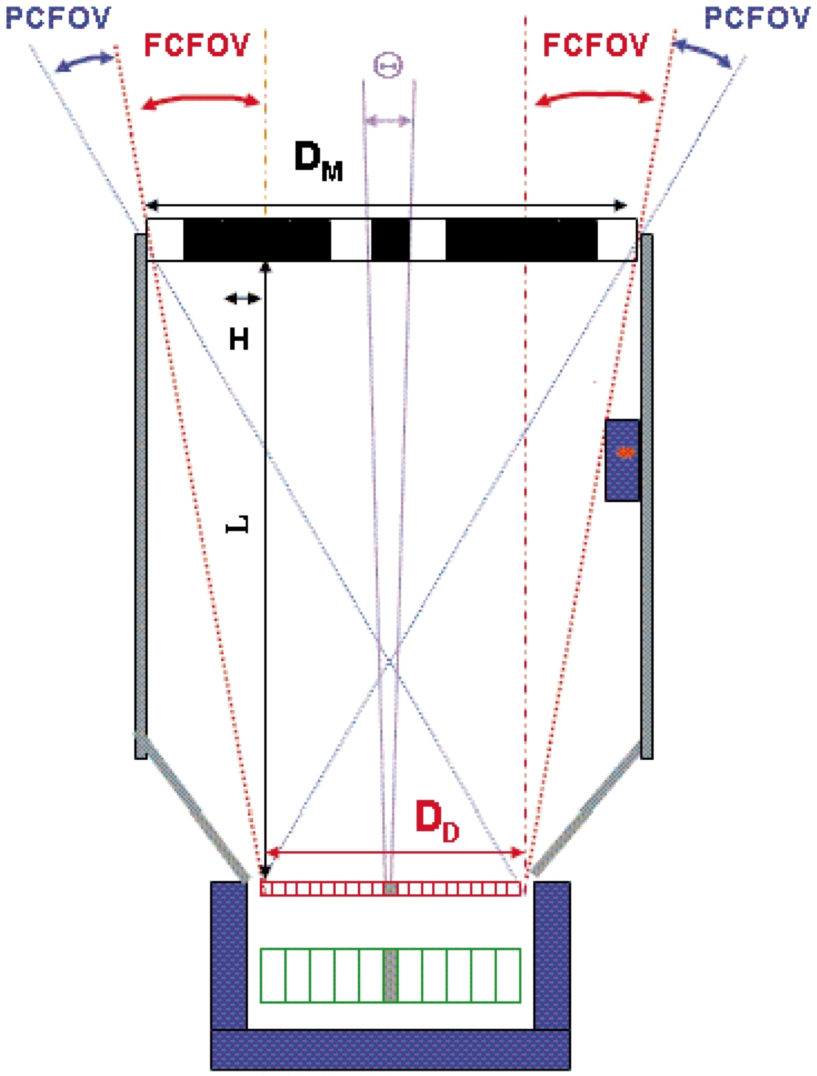

Figure 4.2: Sketch of the IBIS imaging system (figure from Goldwurm et al. 2003).

Another characteristics of coded mask instruments is their Field of View (FoV), that is the sky region seen by the detector where source radiation is modulated by the mask. This is determined by both the mask and the detector dimensions and their respective distance. To maximize the FoV, masks larger than the detector plane are usually employed. The FOV is thus divided in two parts: the fully coded (FC) FoV, for which all source radiation directed towards the detector plane is modulated by the mask, and the Partially Coded (PC) FOV, for which only a fraction of it is modulated by the mask. A sketch of the IBIS imaging system is whown in Fig. 4.2.

Photons coming from a certain direction in the sky project the mask pattern, called "shadowgram" (see Figure 4.3) onto a Position Sensitive Detector (PSD). For the FC FoV, the shadowgram reproduces the mask structure, but shifted depending on the direction of the incoming photons, while sources in the PC FoV, will project only part of the mask onto the detector, thus generating a background component. The complete FoV is therefore composed by the central FCFoV of constant sensitivity and optimum image properties surrounded by

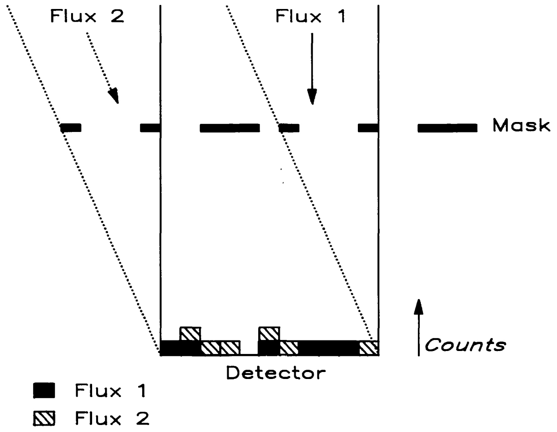

(a) Schematic diagram illustrating the working principle of a coded mask system. Each source contributes to the photon count rate on the detection plane, according to the modulation by the mask. In particular, two shadowgrams projected by two sources at infinite distance from the system are illustrated. Figure from Caroli et al. (1987).

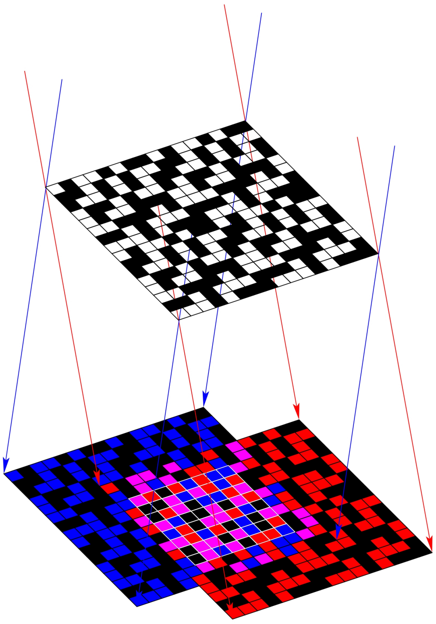

(b) Example of shadowgram projected by two sources, one red and one blue. The sky image is successively derived by decomposing methods (image credit: ISDC)

.

Figure 4.3: The working principle of a coded mask.

the PCFoV of decreasing sensitivity. Reconstruction of the sky image is generally based on a correlation procedure between the recorded image and a decoding array derived from the mask pattern. The IBIS/ISGRI mask is based on a cyclic replication of MURA (Modified Uniformly Redundant Array) of order 53, expanded to 95 pixels. Its decoding principle is explained as follows. Representing the mask with an array M of "1" (open elements) and "0" (opaque ones), the detector array D will be given by the convolution of the sky image S by M plus an unmodulated background array term B:

$$D = S \star M + B \tag{4.2}$$

MURA patterns have the remarkable property that their cyclic autocorrelation gives a delta function. If M has a *correlation inverse* decoding array, G, such that $G = 2M - 1$ (that is, $G = +1$ for $M = 1$ and $G = -1$ for $M = 0$) and $M \star G = \delta$, then the sky S' can be reconstructed as follows:

$$S' = D \star G = S + B \star G \tag{4.3}$$

where S' differs from S only by the $B \star G$ term. For a flat array B, the last term is a constant level that can be measured and removed.

4.1.1.2 IBIS

The Imager onboard the Integral satellite (IBIS) is an imager instrument which provides source identification and spectral sensitivity over a broad energy range, 20 keV – 10 MeV. The coded mask is made of tungsten, and located 3.2 m above the PSD, thus allowing a $d\theta \sim 12'$ (see Eq. (4.1.1.1)). However, the source location uncertainty depends on the source intensity, and is of the order of $\sim 1'$ for a $10\,\sigma$ source (Shen and Zhou, 2008). The coded pattern is a square array of dimension $\sim 1\,\mathrm{m}^2$, made up of 95×95 individual square tungsten cells of size 11.2×11.2 mm and with a height of 16 mm. As diffraction is negligible at gamma-ray wavelengths, the angular resolution obtainable with a coded mask telescope is limited by the spatial resolution of the detector array (see Fig. 4.2).

For an on-axis point source, the ISGRI point spread function presents a central peak (at the true position of the source in the image), plus 8 secondary, spurious peaks (ghosts) in well defined positions (determined by the size of the basic pattern). This also must be taken into account during the data analysis.

The IBIS detector is composed of two layers:

- Upper Detector Layer: *ISGRI*;
- Lower Detector Layer: *PICsIT* (which will not be discussed).

The ISGRI detector is sensitive in the $20 - 300$ keV energy band, and is made of semiconductor Cadmium-Telluride (CdTe) solid-state detectors, operating at ambient temperature. With their small area, the CdTe detectors are ideally suited to build up a pixellated imager with good spatial resolution. The detector area is $2600\,\mathrm{cm}^2$, with 128×128 pixels, each of $(4 \times 4 \times 2)$ mm (width×depth×height). The aperture is restricted by a lead shielding tube and shielded in all other directions by an active Bismuth Germanate (BGO) scintillator veto system. IBIS also includes a small on-board Calibration Unit (CU) that consists of a sodium (^{22}Na) and tungsten (W) radioactive sources, which produce fluorescence lines at 511 and 58.8297 keV, respectively.

More detailed properties of IBIS/ISGRI can be found in Goldwurm et al. (2003), Lebrun et al. (2003), and Ubertini et al. (2003).

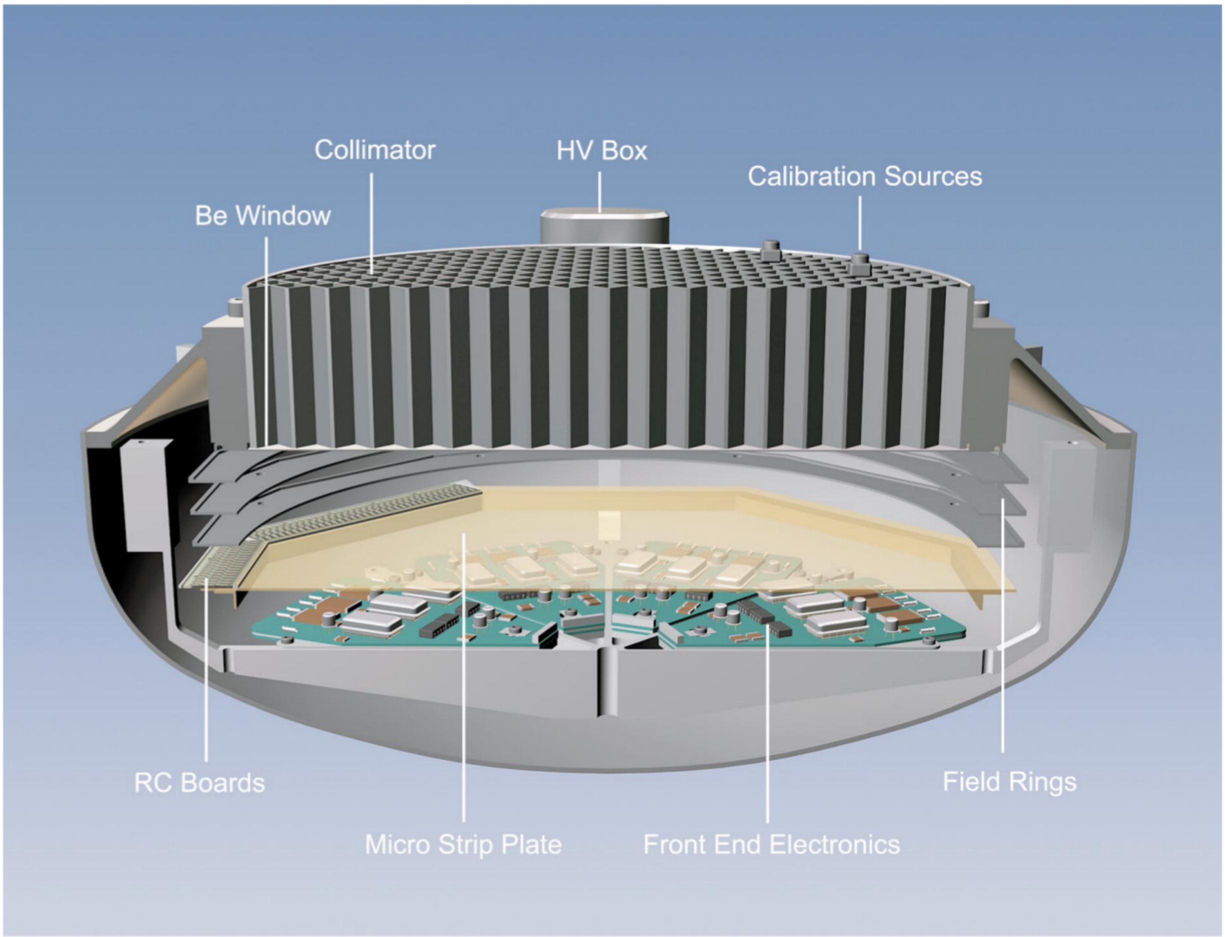

Figure 4.4: Section of the JEM-X detector. Figure from Lund et al. (2003).

4.1.1.3 JEM-X modules

JEM-X consists of two identical coded-aperture mask telescopes co-aligned with the other instruments on INTEGRAL. These modules are sensitive in the $3 - 35\,\mathrm{keV}$ energy range, providing images and spectra simultaneously with the main gamma-ray instruments.

The two masks are made of a 0.5 mm thick tungsten plate. The code patterns on the masks for the two units are identical but the masks are turned 180° with respect to each other to minimize common side lobes in the imaging process. Differently from the IBIS mask, only 25% of the JEM-X masks elements are open. This rather small value of open area enables to achieve better source separation in crowded fields (in’t Zand, Heise, and Jager, 1994) and also to reduce the background, as well as to save telemetry, which is limited on INTEGRAL. The angular resolution is about $3'$, but the source location uncertainty is $1'$ for a 5σ source. The FCFoV of each module is narrower than the other high energy instruments, i.e., about 4.8°.

The detector is a Micro strip Gas Chamber with a sensitive area of nominally $500\,\mathrm{cm}^2$. The gas inside the detector is a mixture of xenon (90%) and methane (10%) at 1.5 bar pressure. A section of the JEM-X detector is shown in Fig. 4.4. More detailed information about the JEM-X modules can be found in Lund et al. (2003).

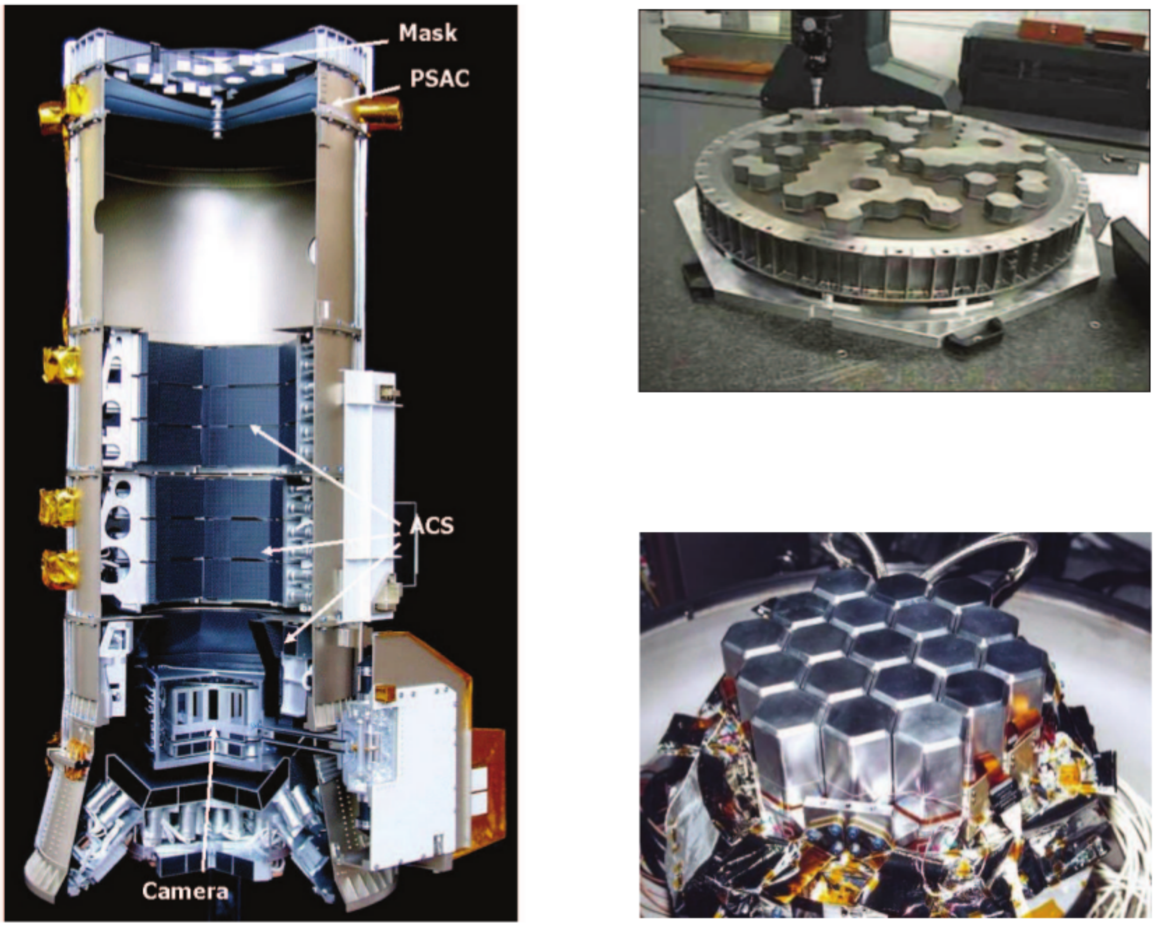

Figure 4.5: *Left:* A cut-away view of the SPI instrument. The mask, plastic scintillator, camera and ACS subsystems are highlighted. *Right:* view of the coded mask (top) and detector plane (bottom) (Credit to ISDC).

4.1.1.4 SPI

The SPectrometer on INTEGRAL (SPI), is a telescope designed to provide data in the 20 keV – 8 MeV range with excellent energy resolution (3 keV @ 1.7 MeV). The main component of SPI is the camera, which is made of a hexagonal array of 19 high-purity germanium detectors (GeD), with a total geometrical area for a flux parallel to the axis of the GeD array equal to 508 cm^2. The hexagonal shape was chosen to minimize the volume occupied by the GeD array and therefore the volume and the weight of the anticoincidence system which surrounds the camera. The size of each detector is 5.6 cm, flat-to-flat, with a height of 7 cm, and a distance between two adjacent detectors centers of 6 cm. These detectors are actively cooled, by a cryogenic system, down to $85 - 90$ K, as low temperatures are required for an optimum sensitivity and resolution, as well as to reduce the radiation damage. At the time of writing, 4 of the 19 detectors are died, resulting in an effective area which is about 85% of the original one. A hexagonal coded aperture mask with about 50% of open elements is located 1.7 m above the detection plane in order to image large regions of the sky (FC FoV of 16°). An

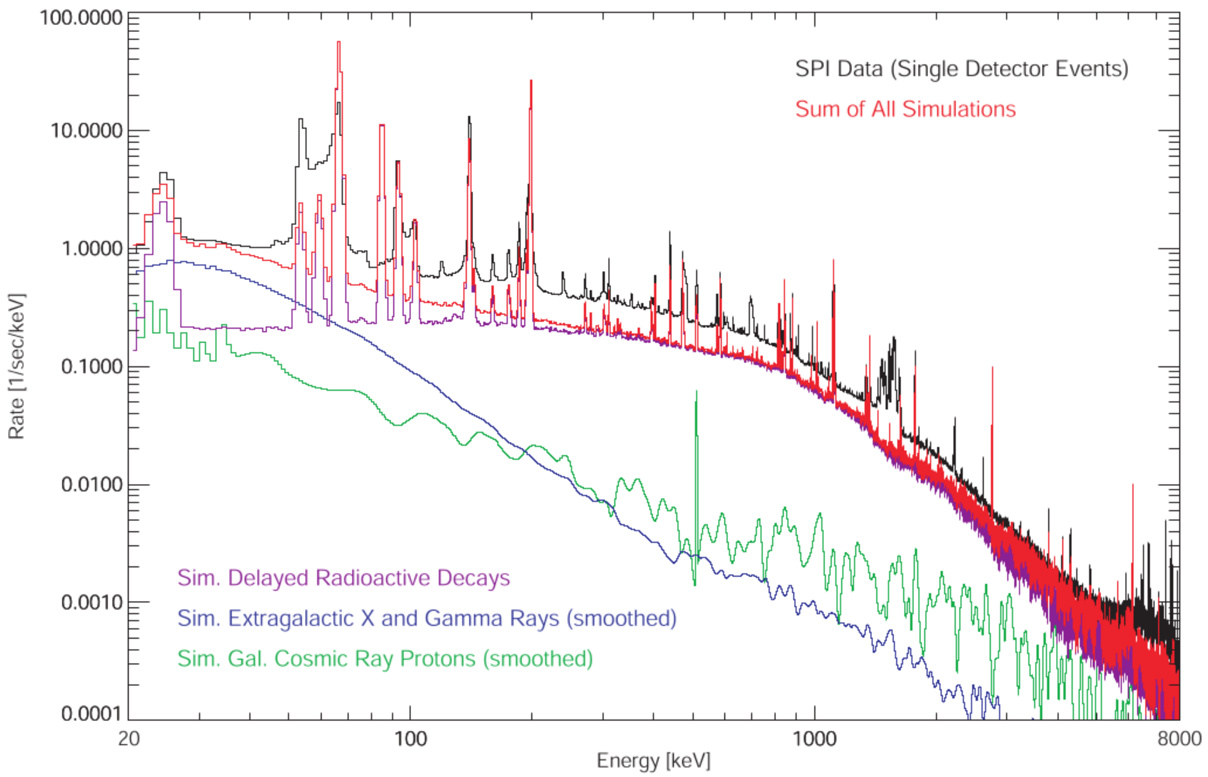

Figure 4.6: Comparison of SPI continuum background spectrum estimated by simulation before the launch of INTEGRAL with the measurements. Background components are shown separately. Figure from Weidenspointner et al. (2003).

overall view of the SPI components is shown in Fig. 4.5.

Due to the size of GeD, the angular resolution of SPI is only 2.5°, although the source location uncertainty is about 1° for a 10σ source. Complementary data from ISGRI can be used to localize the sources seen by SPI even more precisely ($\sim 1'$), if the source emits in the ISGRI energy range.

As it is generally the case for gamma-ray telescopes, SPI is a background-dominated instrument. This is due to the fact that the dimesions of the gamma-ray detector are comparable to the dimensions of the telescope itself. These instruments operate in an environment dominated by charged cosmic rays, which makes the background proportional to the detector area (see Weekes 2003 for an overview of gamma-ray astronomy and telescopes). Despite the background resulting from cosmic ray interactions with the telescope physical components is minimized through shielding (in order to increase the detector sensitivity), many other background components come into play. Thus, for a correct spectral analysis, a deep knowledge of the background components is necessary. A comprehensive background spectrum for SPI is shown in Fig. 4.6, and its major contributes are the following:

- the continuum background;
- the 511 keV emission line;
- the gamma-ray lines.

The continuum radiation: this is a continuum background component that originates from both radiation and particles. The particle contribution is mainly composed of cosmic-ray protons impinging on the detector, which trigger a cascade of reactions, whose end products deposit their energies within the dectetor and generate a continuum energy distribution in the event spectrum. On the other hand, the radiation component is mainly due to the cosmic γ-ray diffuse background.

The 511 *keV emission line:* the main source of this feature is the annihilation of positrons produced by β^+ decay induced by either unstable nuclei in the telescope material, or by high energy primary (e^-, p) and secondary $(\pi^0, \pi^\pm)$ cosmic rays.

The gamma-ray lines: these lines are emitted as a consequence of the interaction between the cosmic ray particles and the detector. The nuclei of the latter are excited by cosmic rays and de-excitation produces gamma-ray lines which are successively detected by the GeD.

To minimize the background components induced by cosmic radiation the detector needs to be shielded. This is achieved by using a veto system which is composed of an active anticoincidence system (ACS), and a thin plastic scintillator just below the tungsten mask, called the Plastic Scintillator Anticoincidence subassembly (PSAC). The ACS shields the GeD against background from sources outside the FoV. The PSAC reduces the 511 keV background due to particle emission by the coded-mask. These components are shown in Fig. 4.5. More detailed information about SPI can be found in Vedrenne et al. (2003).

4.1.2 Dithering Strategy

Since SPI observations are usually background dominated, a number of solutions need to be considered to reconstruct a meaningful sky image. Since the total FoV for SPI is $\sim (25°)^2$ and the instrumental angular resolution is $\sim 2°$, this yelds to about 156 "sky pixels" (that is $(\sim 25°/\sim 2°)^2$). These sky pixels are the number of unknowns to be solved in order to to reconstruct the image on the detectors from a single pointing (Bouchet et al., 2013). However, only a set of 19 equations (that is the number of GeD) is available to solve the system. This is impossible, thus a more complex strategy is needed. To make the system solvable, and thus solve the problem of background determination in the SPI detectors, a controlled and systematic spacecraft dithering maneuver is adopted. The imaging performance of SPI depends on the dithering pattern that is used. In general, the higher the number of pointings, the better the imaging. This maneuver consists of several off-pointings of the spacecraft pointing axis from the target in steps of 2 degrees. The integration time for each pointing on the raster is flexible in the range between 30 min up to 1 h. Two main, different pointing patterns are currently used (see Fig. 4.7):

(1) Hexagonal dither pattern: this consists of a hexagonal pattern around the nominal target location (1 source on-axis pointing, 6 off-source pointings, each 2 degrees apart);

(2) Rectangular, or 5 × 5, dither pattern: this consists of a square pattern around the nominal target location (1 source on-axis pointing, 24 off-source pointings, each 2 degrees apart).

The spacecraft continuously follows one dithering pattern throughout one observation; however, if scientific requirements exist to observe sources for long, uninterrupted periods of time using all 4 instruments then the dithering modes can be switched off, and the satellite

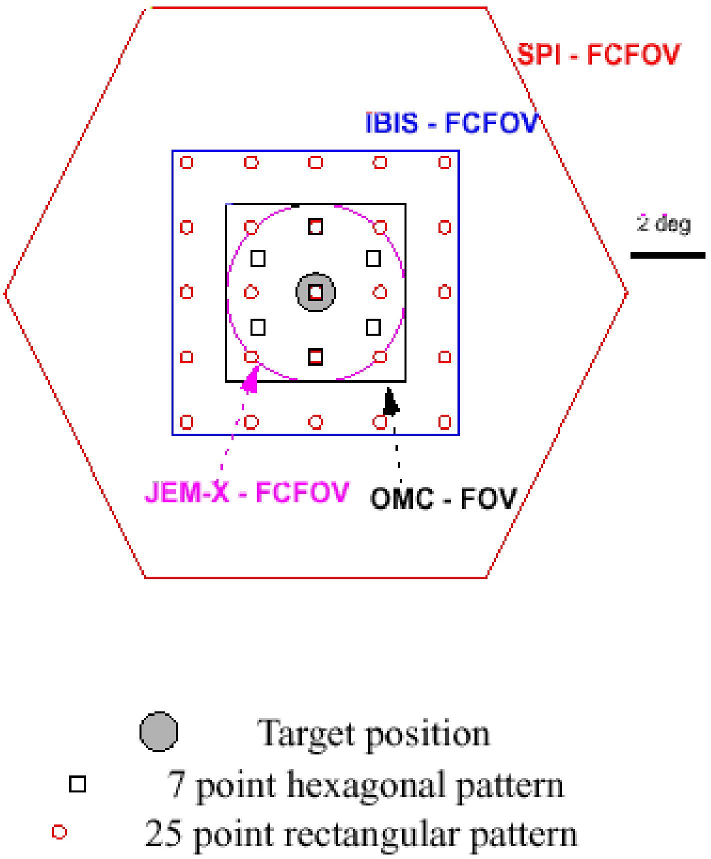

Figure 4.7: Schematic view of the dithering patterns and of the instrument FC FoV (Credit to ISDC).

will be set in "Staring Mode". During the Staring Mode, a mathematical determination of the background is impossible, and a model of the background distribution on the detector plane must be assumed. A common background model assumed in such cases is the "empty-field", composed of observations pointed to pieces of sky where no significant source is detected by SPI (within a moderate integration time). Dedicated observations with SPI are performed by the instrument team to provide updated empty-fields (see, e.g., Dubath et al. 2005).

4.2 The MAXI monitor

The Monitor of All-sky X-ray Image (MAXI, Matsuoka et al. 2009) is a Japanese observatory whose key science is to continuously monitor, through a systematic survey, X-ray sources as the International Space Station (ISS) orbits the Earth. MAXI is operating since August 2009, and is the first astronomical payload placed on the ISS, where it has been installed on the Japanese Experiment Module – Exposed Facility (JEM-EF or Kibo-EF). The mission was designed to achieve the best sensitivity and the highest energy resolution of all ASMs flown before MAXI.

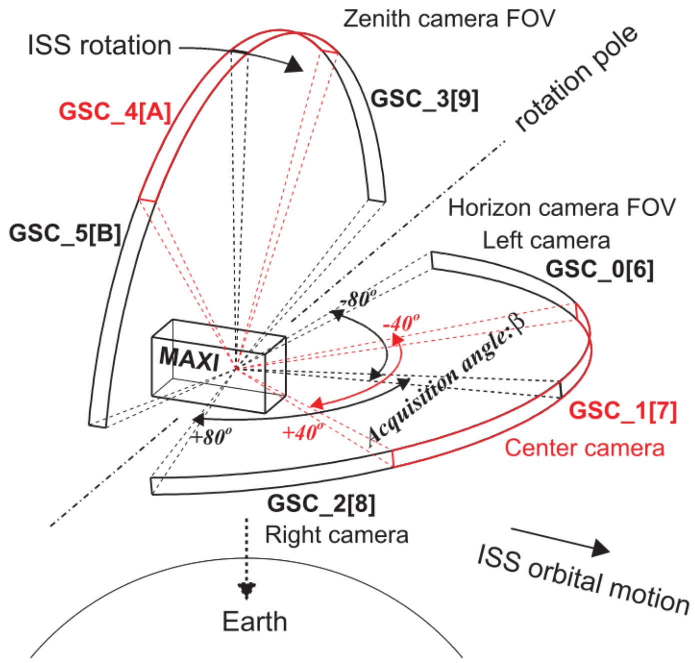
Zenith camera FOV
ISS rotation
GSC_4[A]
GSC_3[9]
rotation pole
GSC_5[B]
Horizon camera FOV
Left camera
GSC_0[6]
-80°
-40°
MAXI
Acquisition angle:β
GSC_1[7]
Center camera
+80°
+40°
GSC_2[8]
Right camera
Earth
ISS orbital motion

Figure 4.8: Schematic drawing of GSC cameras on MAXI. The 12 cameras are marked with an index between $0-9$ and A, B. Figure from Sugizaki et al. (2011).

MAXI consists of two slit cameras working in two complementary energy bands: the Solid-state Slit Camera (SSC, Tomida et al. 2011) in the $0.7-10\,\mathrm{keV}$, and the Gas Slit Camera (GSC, Mihara et al. 2011) in the $2-20\,\mathrm{keV}$ energy bands. In this work, SSC has not been used due to degradation of the energy resolution (Mihara et al., 2014), therefore it will not be discussed.

4.2.1 GSC camera design

The GSC module is composed of 12 proportional counters, each consisting of one-dimensional slit-slat collimator (that is, a slit in one axial direction with a set of evenly spaced slits perpendicular to the that slit direction) and a proportional counter filled with Xe gas. The advantage of the slit camera over the coded-aperture mask, is that it is free from source contamination, although it results in a limited aperture. The entire GSC system is composed of six identical units, arranged according to the scheme in Fig. 4.8.

Each unit consists of a slit and slat collimator and two proportional counters with one-dimensional position-sensitive X-ray detector. The six camera units are assembled into two groups, the horizon and zenith modules, whose FoVs are pointed toward the tangential direction of the ISS motion along the Earth horizon and the zenith direction, respectively (see Fig. 4.8).

Assembled, they allow to cover a FoV of $1.5 \times 160\,\mathrm{deg}^2$, observing about 75% of the whole sky at each ISS revolution ($\sim$92 min), and 95% per day. The GSC tipically scans a point source on the sky for $40-150\,\mathrm{s}$ during each ISS revolution (the actual time depends on the source incident angle for each GSC counter).

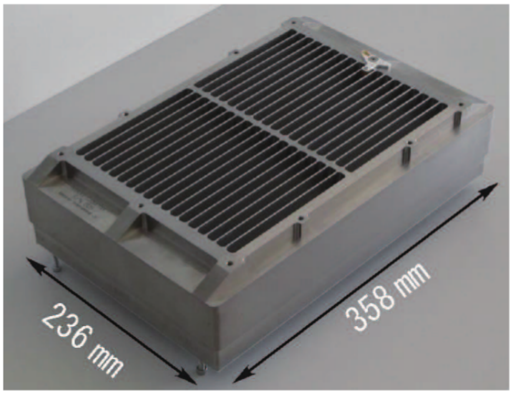

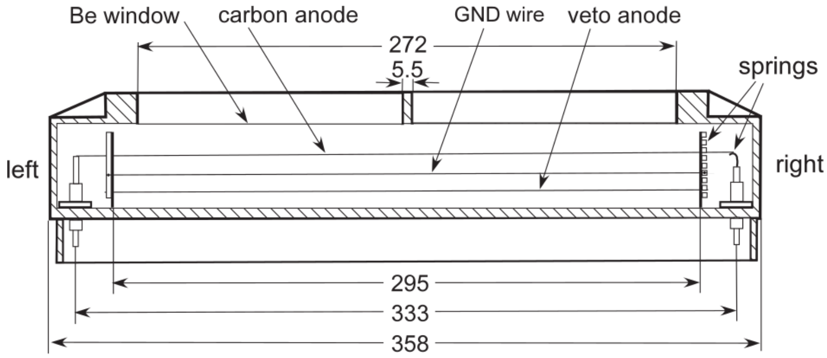

Figure 4.9: *Top*: GSC proportional counter with slat collimators. *Bottom*: Cross-section view of a GSC proportional counter along the wire direction. Numbers are in units of mm. Figures from Mihara et al. (2011).

4.2.2 GSC detector units

GSC is designed to optimize the position resolution of observed transients. The GSC proportional counters employ resistive carbon fibers with a diameter of 10 μm for anode wires. Carbon-wire anodes are used to acquire one-dimensional position sensitivity. Higher resistive anodes have been preferred for better position resolution, since the thermal noise on the readout signal is inversely proportional to the anode resistance. However, the carbon coated wires weak point, is that it is mechanically weak, thus easy to break by launch vibration.

The gas volume of each counter is separated into six carbon-anode cells for the main X-ray detectors and ten tungsten-anode cells for veto counters (see Fig. 4.9). The chosen gas mixture is a combination of Xe (99%) + CO_2 (1%) with a pressure of 1.4 atm at 0° C.

For MAXI, the higher gas gain (7000) and the operating high voltage (HV = 1650 V) have been chosen to achieve a sufficient position resolution and still keep an adequate energy resolution. The voltage is reduced to 0 V when the ISS passes through heavy particle background area, defined by an on-board Radiation-Zone (RZ) map and, in any case, to 1550 V if a counter suffers of any discharge event.

Each gas counter is equipped with a calibration source embodying the radioactive isotope

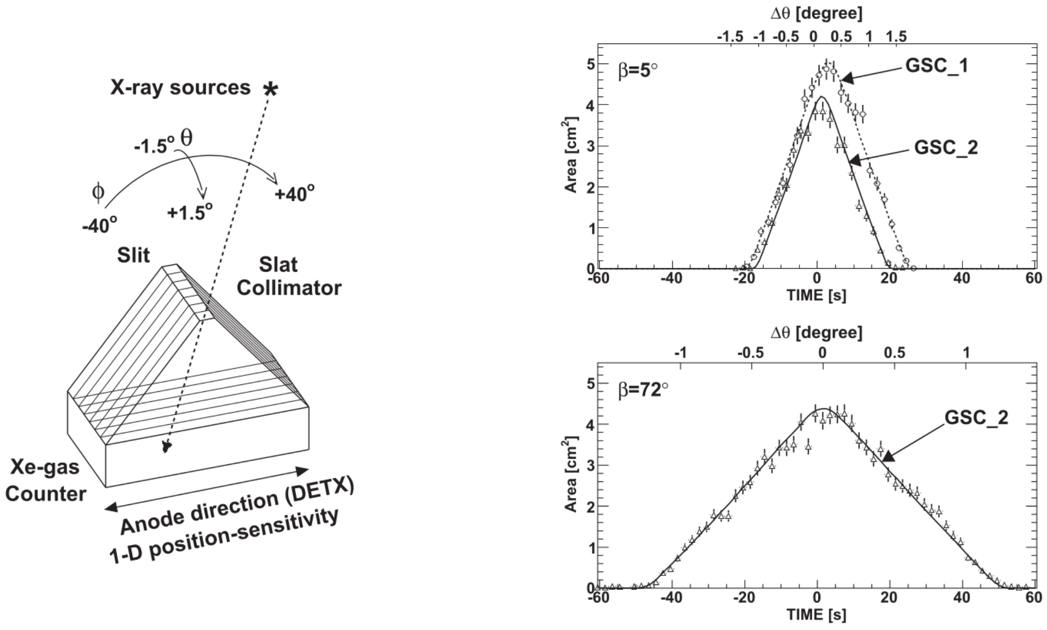

Figure 4.10: *Left*: Schematic view of a single GSC camera unit and its field of view of 1.5 × 80 degrees. *Right*: Time variable effective area during a scan transit targeted on Sco X-1. The source acquisition angle of 5° for GSC1 and GSC2 (top) and 72° for GSC2 (bottom) are shown in the respective panel. The angular scale of each transit is shown at the top of each panel. Error bars for raw event rates of Sco X-1 are shown at 1σ. Figures from Sugizaki et al. (2011).

^{55}Fe at the end of one of six carbon anodes, allowing a continuous monitoring of the counter gas gain and the energy resolution with the 5.9 keV reference emission line. The calibration line shows that, it is resolved with an energy resolution stable at a value of 18% (1σ c.l.).

The visibility and the area of each GSC unit for a given X-ray source on the sky are continuously changing. Thus, to derive the correct flux of each observed source, the time-dependent effective area for the target has to be known. Effective areas for each GSC unit are reconstructed by the light curve response builder, which takes into account source coordinates, ISS location, attitude, and the GSC unit area as a function of the source incident angle. Fig. 4.10 (right) shows time variations of the effective areas during scan transits at typical two source-acquisition angles.

Effective area reconstruction allows to calculate exposure maps of the sky for a given period of scan operation. An example of an actual exposure map is shown in Fig. 4.11, calculated since 2010 January 2nd, 00 : 00 (UT), for different time durations.

The effective exposure for an arbitrary direction on the sky is typically 4000 cm^2 s per day. This is about one third of the initial expectation because the HV operation at the high latitude above 40° was stopped, after the fracture of some counters between 2009 and 2010. Since then, the operation voltage was reduced to 1550 V if the counter had any discharge experience, which resulted in a reduction of the effective observation efficiency to about 40% of the nominal one which, in turn, results in a loss of sensitivity. The daily flux source sensitivity at 5σ c.l. in the full energy band is about 20 mCrab (Sugizaki et al., 2011).

At the moment of writing 4 GSC cameras are fractured and can not be recovered. For an overview of the spacecraft, see Table 4.2. More detailed information about MAXI/GSC can

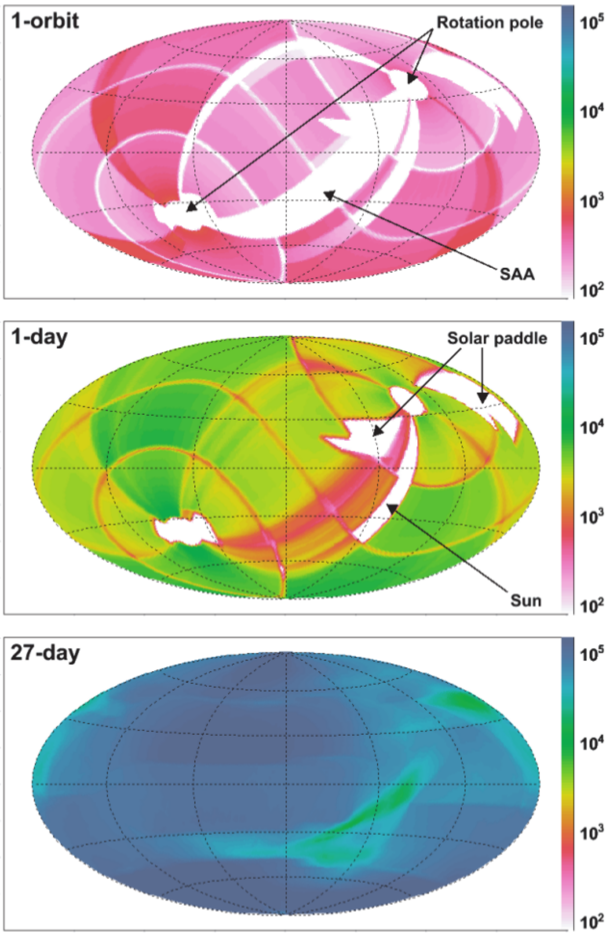

Figure 4.11: GSC exposure map obtained from observations integrated over 1 orbit (top), 1 day (middle), and 27 days (bottom). Color scale is the same in each of the three panels, and represent the effective exposure in units of [cm^2 s]. Uncovered areas are indicated by the arrows. Figure from Sugizaki et al. (2011).

Table 4.2: Summary of GSC in-orbit performance.

Spatial resolution	1.5 deg (FWHM)
Source localization accuracy	0.2 deg (90% containment radius)
All-sky coverage	75% per orbit (nominal 92 min), 95% per day
Exposure	4000 cm^2 s per day (typical)
Energy resolution	18% (1σ) @ 5.9 keV
Effective area accuracy	3% (1σ) @ $4-10$ keV
Sensitivity	15 mCrab per day in $2-30$ keV (typical)

be found in Mihara et al. (2011) and Sugizaki et al. (2011).

5

INTEGRAL OBSERVATIONS OF GX 304-1

5.1 History

GX 304-1 is a BeXRB system discovered as an X-ray source during a balloon observation in 1967 (Hewish et al., 1968; Lewin, Clark, and Smith, 1968). After the observation of X-ray pulsation with a period of $\sim 272\,\mathrm{s}$ (McClintock et al., 1977), the source was classified as an X-ray pulsar. A study of the recurrent outburst activity revealed a $\sim 132.5\,\mathrm{d}$ periodicity, that was attributed to the periodical passage of the NS at the periastron and thus identified with the orbital period (Priedhorsky and Terrell, 1983).

The optical counterpart of the binary is a B2 Vne star, V850 Cen, discovered using data from the Anglo-Australian Telescope (AAT) by Mason et al. (1978). The distance of the system has been estimated through spectroscopical analysis of the optical companion to be 2.4 ± 0.5 kpc (Parkes, Murdin, and Mason, 1980).

The history of GX 304-1 is studded with periods of quiescence and activity at different levels. The source was active since its discovery and until 1980. Afterward, it has entered an X-ray quiescence period (Pietsch et al., 1986), which lasted for 28 years, during which no detectable X-ray emission was registered. The quiescence was interrupted in June 2008, when *INTEGRAL* detected hard X-ray emission from the source (Manousakis et al., 2008). Since then, GX 304-1 resumed its periodical outburst activity, with the usual periodicity (i.e., $\sim$132.5 d). In 2013, the source entered a new quiescence period, although much shorter than the last one, i.e., for about 2 years. Finally, since December 2014, GX 304-1 started to show X-ray outbursts again, with the usual periodicity but with a much more moderate intensity. A plot of the entire light curve of GX 304-1 is shown in Fig. 5.1. Typical peak luminosities are $\lesssim 10^{37}$ erg/s in the $5 - 100\,\mathrm{keV}$ energy band, while the typical duration of an outburst is a few weeks.

5.1.1 A more recent context

In the last years, the source underwent two unusual episodes. The first one in mid 2010, when the source suddenly switched from a series of weak ($F_{15-50\,keV} \leq 150\,\mathrm{mCrab} \approx 1.992 \times 10^{-9}\,\mathrm{erg\,cm^{-2}\,s^{-1}}$) and periodic bursts, that were lasting since the reactivation in 2008, to an outburst with peak luminosity of the order of 10^{37} erg/s (in the $15 - 50\,\mathrm{keV}$ energy band). After that event, the outburst intensity resumed the typical level. The second episode is a more luminous (giant, Jenke et al. 2012) outburst towards the end of 2012 (see Fig. 5.3), during which the peak luminosity reached a level of $\sim 2 \times 10^{37}$ erg/s (in the $15 - 50\,\mathrm{keV}$ range).

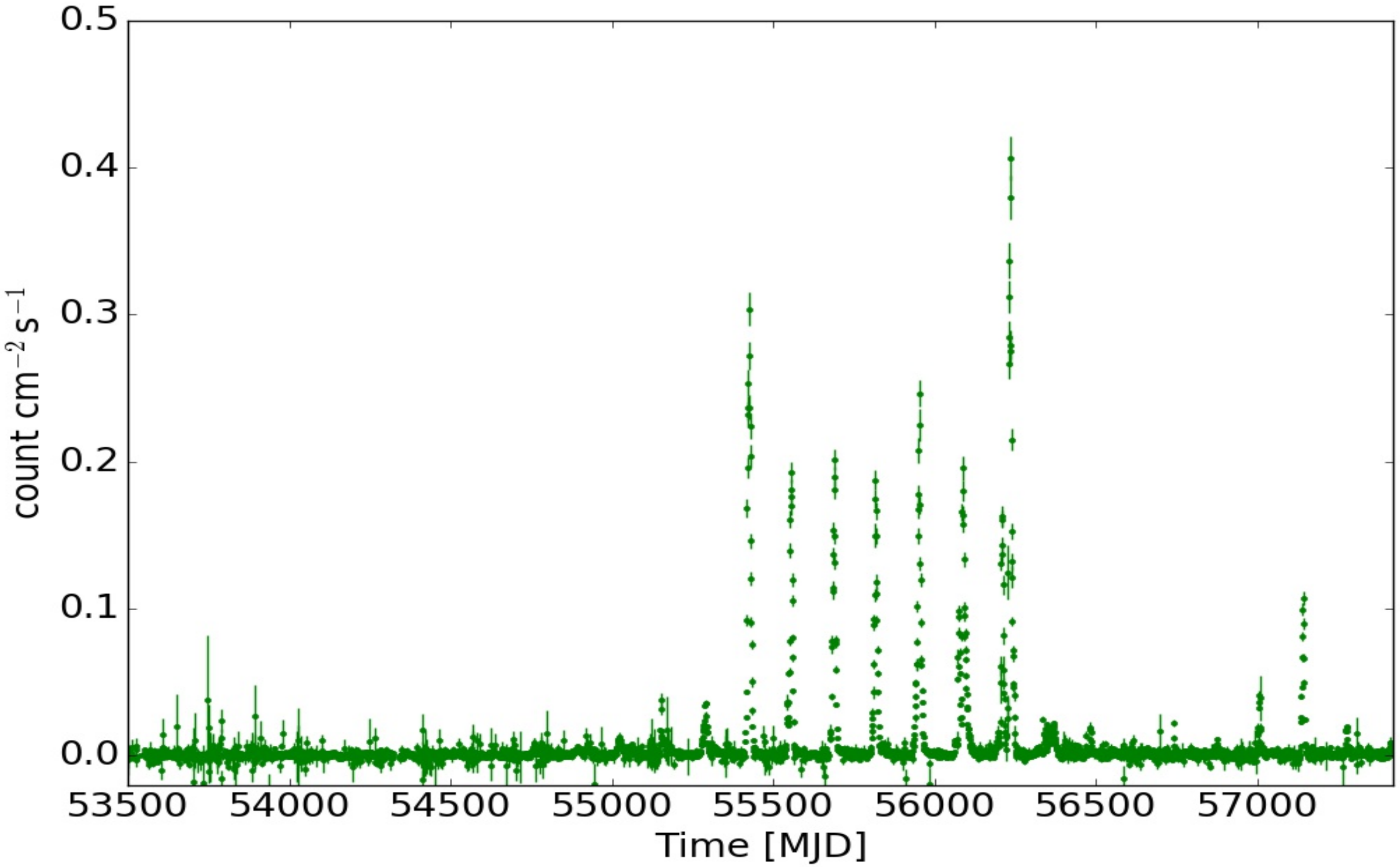

Figure 5.1: *Swift*/BAT light curve of GX 304-1 from MJD 53500 to 57423.

Beyond the higher luminosity level, this event was peculiar under many aspects. First, the outburst light curve shape was clearly double-peaked, with the dip roughly corresponding to the periastron passage. Second, the event lasted about 45 days, that is about twice the typical duration of GX 304-1 outbursts. Third, the outburst morphology had started to change already in the previous outburst(s). Finally, after this episode the source entered the quiescence period. All these unusual aspects represent a good opportunity to study the interaction between the NS and the Be disk, thus highlighting the necessity for further monitoring of GX 304-1. An optical monitoring program has indeed been carried out win order to study the evolution of the Be disk, but its results are beyond the purposes of this thesis (for more details, see Sec. 8.3).

In August 2010, GX 304-1 has been observed by *RXTE* and *Suzaku* (the latter triggered by the *MAXI* monitoring of the source, Mihara et al. 2010). The observations allowed to detect a cyclotron resonant scattering feature (CRSF), or *cyclotron line*, in its spectra, with a centroid energy of ~ 52 keV (Yamamoto et al., 2011). A timing analysis of *RXTE* observations of GX 304-1 during the outburst event has been performed by Devasia et al. (2011). These authors show that pulse profiles are energy and luminosity dependent, but do not perform any study of the cyclotron line. A spectral analysis of the same data from other authors is ongoing, and will be published soon (Rotschild et al., in prep.).

Taking advantage of an *INTEGRAL* pointed observation of the outburst occurred at the beginning of 2012, Klochkov et al. (2012) have shown that the cyclotron line energy in GX 304-1 is positively correlated with the observed luminosity. On the other hand, the active period between 2008 and 2013 allowed Sugizaki et al. (2015) to derive orbital elements for this binary system. Moreover, a *Suzaku* analysis of the outburst in August 2010 was performed by Jaisawal, Naik, and Epili (2016), who also confirm the strong energy dependence of pulse profiles and show that dips in the pulse profiles can be interpreted as due to increased absorption at the corresponding phases. These authors also found a significant variation of the spectral parameters with pulse phase.

5.2 Motivation

This chapter is focused on the spectral and timing analysis of the luminosity-dependent properties of GX 304-1 explored with *INTEGRAL* during an outburst event in January–February 2012. Particular effort has been put on the timing analysis, which allowed to produce pulse profiles at different luminosities and energy ranges, and to phase-connect the observations throughout the entire outburst thus obtaining a timing solution. This, in turn, allowed to perform pulse phase-resolved spectroscopy, with the goal of probing the spectral emission of the rotating NS at different viewing angles. Changes in the spectral parameters with pulse phase and luminosity are quite common among X-ray pulsars. Located relatively nearby and having a prominent cyclotron line feature, GX 304-1 is well suited for such studies.

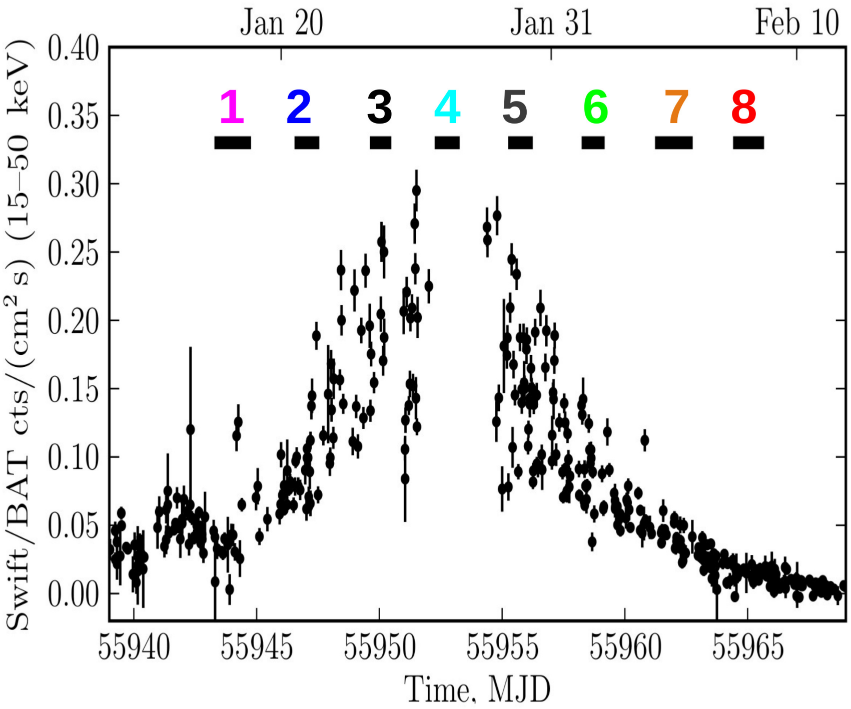

Figure 5.2: *Swift*/BAT light curve of GX 304-1 during the 2012 January - February outburst. The horizontal bars indicate the INTEGRAL observations. The numbers above the bars indicate the last digit "i" of the respective INTEGRAL Revolution number – 113i. Figure from Malacaria et al. (2015).

5.3 *INTEGRAL* observations of the outburst

5.3.1 The outburst event and the *INTEGRAL* coverage

INTEGRAL observed GX 304-1 with a pointed observation aimed at studying the outburst which took place during January–February 2012. Thanks to the dedicated time, the source was in the FoV of all *INTEGRAL* instruments, allowing a broad band energy coverage. Since JEM-X has a smaller FoV, the dedicated time guarantees the source to be Fully Coded by JEM-X too, thus collecting data in the softer energy band. Also, sources which are Fully Coded, suffer less background contaminations.

The outburst started on January 8th, 2012 (MJD ∼55934, Yamamoto et al. 2012), but the *INTEGRAL* observation started around MJD 55943.5, at the beginning of the rising edge of the outburst. At that time, the source flux in the $20-80$ keV energy band was already as high as ~ 250 mCrab. *INTEGRAL* performed a total of eight observations, one per each satellite orbit (i.e., one every ~ 3 d). The observation log is given in Table 5.1. The last observation was carried out at MJD ∼55965.5, at the very end of the decay tail, when the flux dropped down to ∼100 mCrab. The peak of the outburst was reached around MJD 55953, with a flux

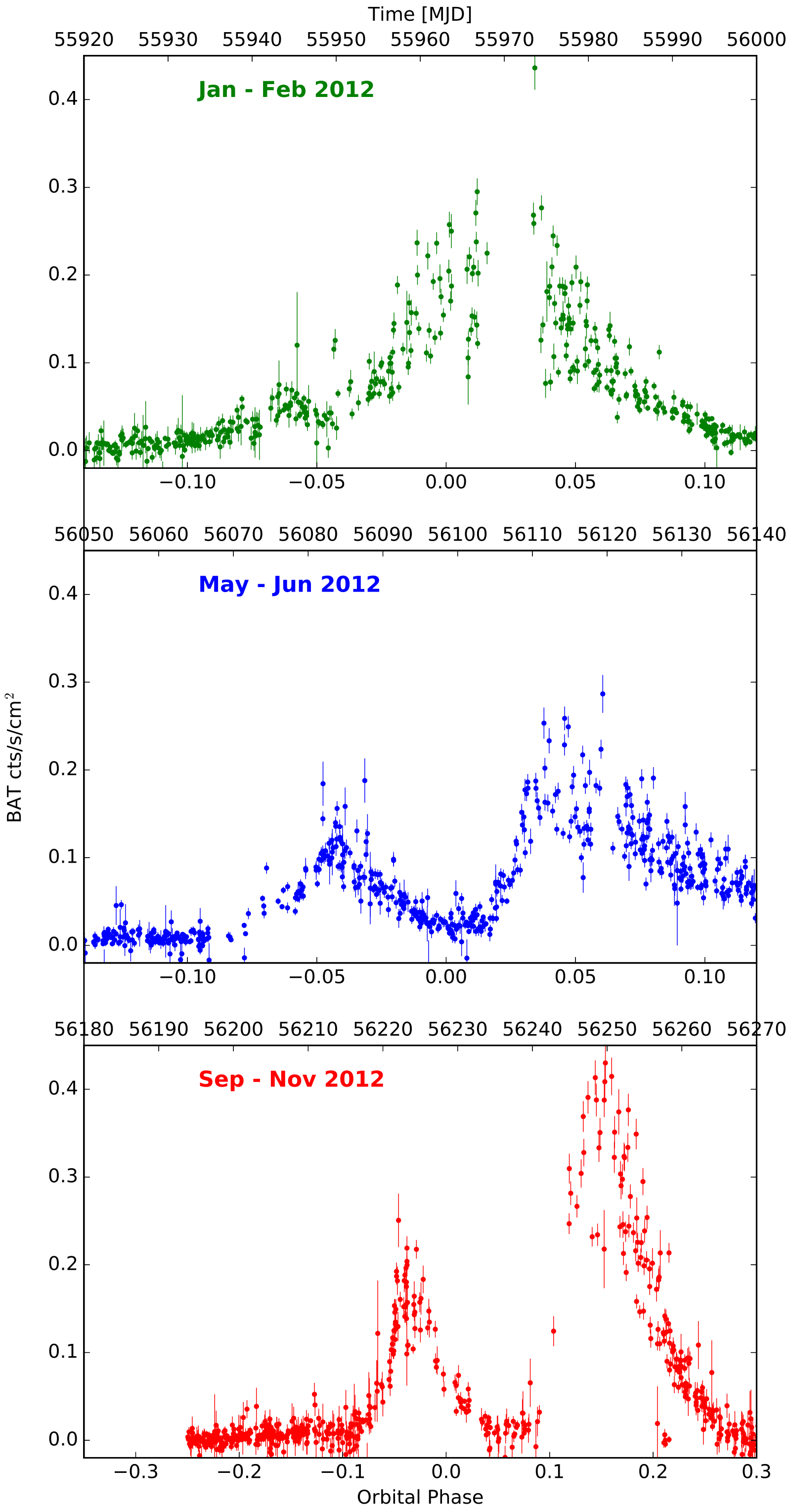

Figure 5.3: A comparison of GX 304-1 2012 outbursts. In each panel, the y-axis shows the *Swift*/BAT count rate, while the x-axis shows the orbital phase (bottom) and the MJD time (top). Ephemeris are taken from Sugizaki et al. (2015).

Table 5.1: INTEGRAL observations of the GX 304-1 outburst.

Rev#	Obs. ID	Mid. MJD	Exposure [ks]		
			JEM-X	ISGRI	SPI
1131	09400230006	55944.0	64.6	42.7	68.6
1132	09400230007	55947.0	42.4	31.9	36.6
1133	09400230008	55950.0	–	–	10.7
1134	09400230009	55952.8	7.3	25.4	37.8
1135	09400230010	55955.7	–	6.7	25.1
1136	09400230011	55958.7	36.9	28.1	32.9
1137	09400230012	55962.0	78.1	59.7	78.4
1138	09400230013	55965.0	60.7	45.2	52.3

exceeding one Crab. The typical nominal exposure of each observation is of a few tens of kiloseconds.

A light curve of the observed outburst is shown in Fig. 5.2. Here, the *Swift*/BAT light curve of the event is shown, which furnishes a more continuous coverage of the outburst[1] (except for the gap around the outburst peak). In the same figure, *INTEGRAL* observations are also indicated, identified by the revolution (Rev.) number. However, the actual exposures are shortened due to solar activity issues (solar flares), which forced the instruments teams to shut down the telescopes for a short period, thus leading to a reduction in the effective exposure times.

5.3.2 Available data

The same data set analyzed in this work was first analyzed and presented in Klochkov et al. (2012). The very first task of the present work was to reproduce the results from those authors and to compare them with the results obtained using a more recent energy calibration of the ISGRI detector (see Sec. 5.4.1). For this reason, it was essential that the same strategy as that from Klochkov et al. (2012) was applied to the present analysis. Following their approach, the data set was limited to those observations where all of the three high-energy instruments are available (see Table 5.1). This is to ensure a broad band coverage and a homogeneous analysis of the available data, especially to include JEM-X data in all observations. As a consequence, the revolutions 1133 and 1135 are not analyzed. This represents, however, a very minor loss, since those observations are strongly affected by solar flares and their exposure is severely reduced with respect to the requested one.

As already mentioned in Sect. 4.1, data from IBIS/PICsIT have not been used in this work; instead, only data from IBIS/ISGRI have been analysed. Furthermore, following the recommendation of the instrument team, we restricted the duty energy band of each instrument to a safer range that is believed to be free of strong systematics, and is therefore more reliable for spectral analysis. The used energy ranges are the following: $5-30$ keV for the two JEM-X modules, $22-100$ keV for ISGRI, and $25-100$ keV for SPI. The upper limit of 100 keV for ISGRI and SPI data is due to the reduced photon flux of GX 304-1 above this energy. Data reduction was performed with Version 10 of the Offline Science Analysis (OSA) software[2]. Following the OSA user manual, we added a systematic error to the final count rates at a level of 1% for ISGRI, 3% for JEM-X, and 0.5% for SPI.

---

[1] *Swift*/BAT quick-look data of GX 304-1 are publicly available through the website http://swift.gsfc.nasa.gov/results/transients/weak/GX304-1/

5.4 Timing analysis

An important step toward the analysis of GX 304-1 was to find a timing solution that is valid over the entire analyzed outburst. Such a timing solution can thus be applied to produce pulse profiles and to identify pulse phases, which eventually allows to perform pulse phase-resolved spectroscopy. To this aim, we extracted JEM-X1 and ISGRI light curves in the range $3-20$ keV and $18-80$ keV, respectively, for each of the analyzed *INTEGRAL* observations. The adopted time binning is 3 s (about 1/100 of the pulse period), which is permitted by the sufficient photon statistics and allows the characterization of various pulse profile features.

To correct the Doppler effect due to both Earth and satellite movements, all photon arrival times were translated to the solar system barycenter. At the time of preparation of this work, a correction for the orbital motion of the X-ray source in the binary was not possible, since the orbital parameters of the binary system were unknown. An orbital solution for GX 304-1 has been found only later by Sugizaki et al. (2015).

A pulse period for each observation was initially determined by appling the epoch-folding method (Leahy, 1987) to the extracted ISGRI light curves from individual observations. This method is based on the folding of data with a series of trial periods. The resulting pulse profiles are then tested (for the strength of the modulation) by means of the χ^2 statistic. The χ^2 tests the deviation from a uniform distribution (expected for a trial period far from the true one). The "best" period is assumed to be the one leading to the pulse profile with the maximum deviation from a flat distribution. The peak of the χ^2 distribution over trial periods is fitted with a Gaussian profile, whose centroid value is taken as the determined pulse period.

Using these preliminary pulse periods, ISGRI pulse profiles in the $18-80$ keV energy band have been generated, to provide templates for the next more accurate analysis.

5.4.1 Timing solution using phase-connection

To refine the obtained pulse periods, the phase-connection technique (Deeter, Boynton, and Pravdo, 1981) was applied to the $18-80$ keV ISGRI pulse profiles. For each INTEGRAL observations, the pulse profile constructed by means of the epoch-folding method was used to determine an absolute reference time (in MJD), also called the *arrival time*. Arrival times are

---

[2] http://www.isdc.unige.ch/integral/analysis

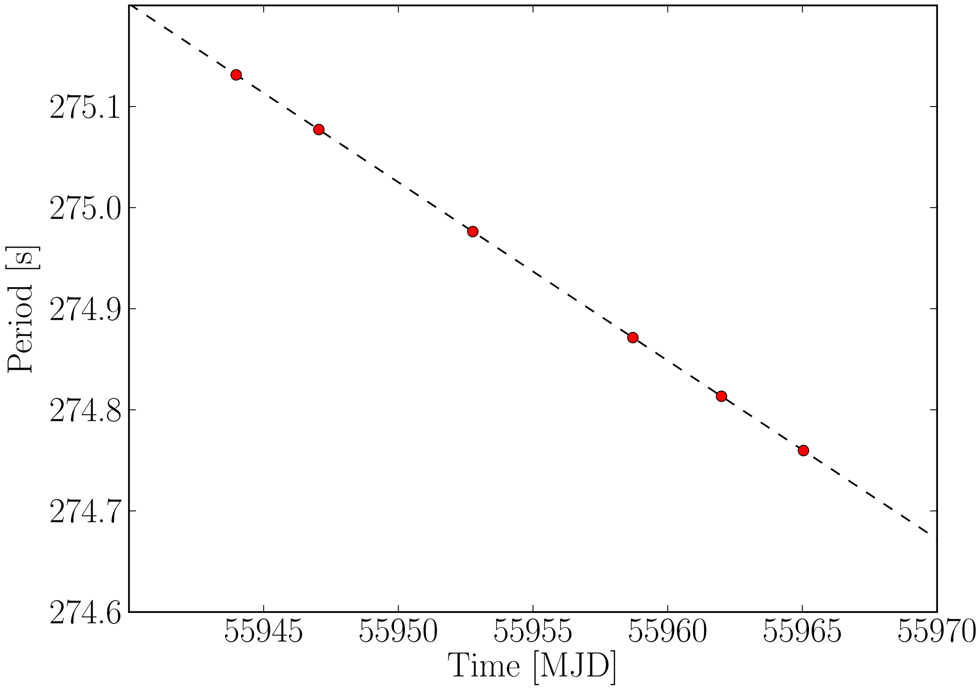

Figure 5.4: The pulse period of GX 304-1 as a function of time obtained by phase connection. The dashed line represents a linear fit to the data points, yielding a pulse period derivative of $\dot{P}$ = (-2.04 ± 0.01)×10^{-7}. The period error bars are smaller than the symbols. Figure from Malacaria et al. (2015).

identified through well defined sharp features in the template profiles. For ISGRI templates, there are three suitable features usable for this purpose, as illustrated in Fig. 5.5: (1) the peak near pulse phase zero, (2) the minimum around pulse phase 0.1, and (3) the time at the flux level centered at a point midway between the peak and the minimum.

If only the first derivative $\dot{P}$ of the pulse period P is taken into account, the expected arrival time t_n of the n-th pulse is

$$t_n = t_0 + nP_0 + \frac{1}{2}n^2 P\dot{P}. \tag{5.1}$$

Here, P_0 is the pulse period at the reference time t_0, n is the pulse sequence number, and $\dot{P}$ is the first period derivative. The pulse period at the time t can be determined as

$$P(t) = P_0 + (t - t_0)\dot{P} \tag{5.2}$$

A consistent determination of pulse arrival times is formally only possible if the pulse shape does not change with time. In our observations, however, the pulse shape varies substantially between the intervals, and yet the main features of the pulse profiles can be recognized clearly in all observations (with the exception of Rev. 1138).

Using the determined pulse arrival times, the phase connection between the observations can be achieved. A timing solution $(t_0, P_0, \dot{P})$ is derived by minimization of the difference between the observed arrival times and the expected arrival times predicted by the formula (5.1). This method allows to measure the pulse period evolution with substantially higher

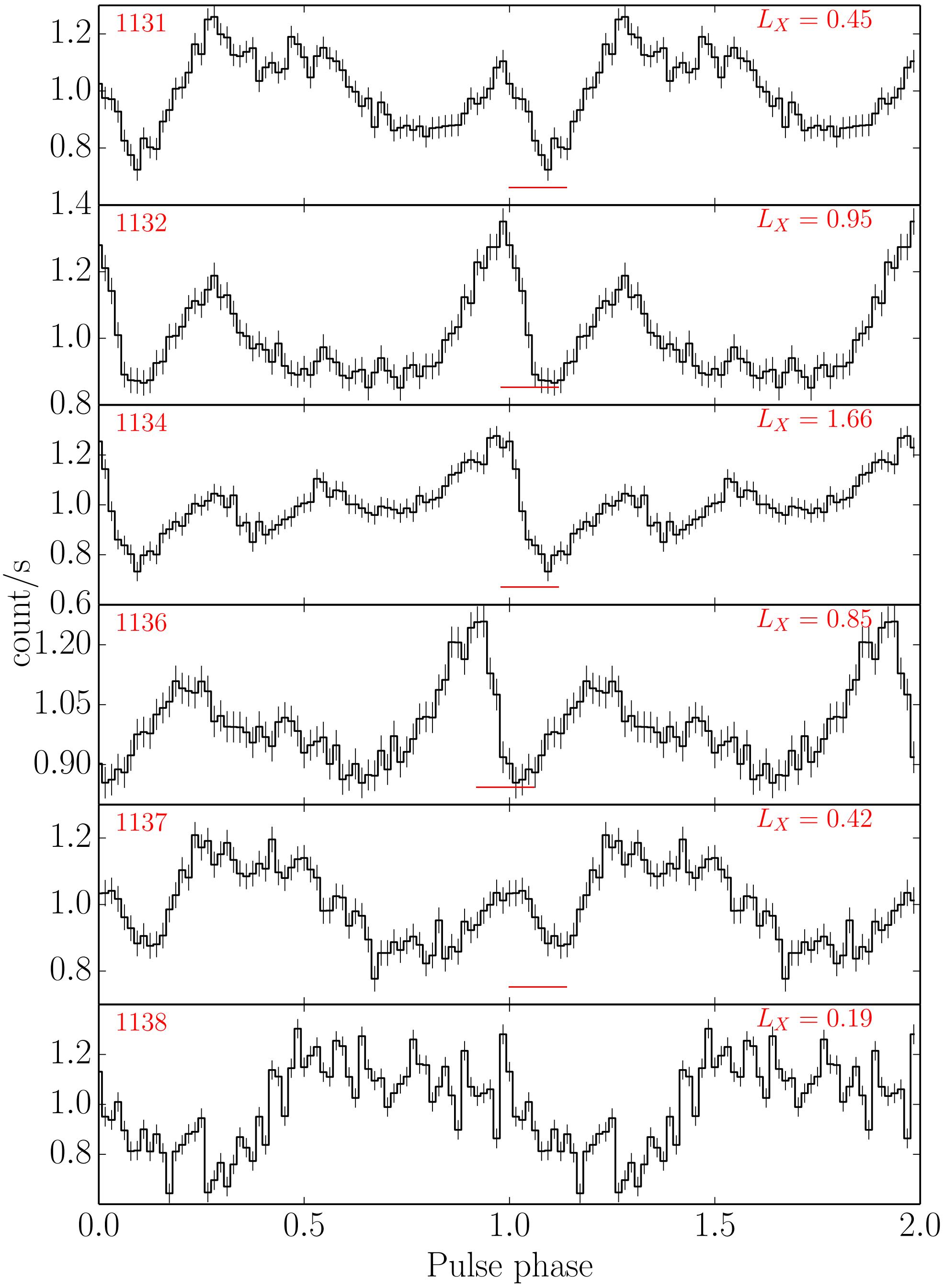

Figure 5.5: IBIS/ISGRI normalized pulse profiles in the $18 - 80\,\mathrm{keV}$ energy range. Each panel represents, from top to bottom, the successive INTEGRAL observations (from Rev. 1131 to 1138, shown in the top left corner). In the top right corner, the source luminosity (in the $3 - 80\,\mathrm{keV}$ range) is reported in units of $10^{37}\,\mathrm{erg/s}$. The thin horizontal line around phase 1.0 at the bottom of each panel (except Rev. 1138) approximately indicates the phase range where the sharp features used to phase-connect the observations are located (see text). Figure from Malacaria et al. (2015).

precision compared to epoch-folding. Uncertainties of pulse arrival times are determined by the quality of the profile and by sharpness of the considered feature. For istance, broadened

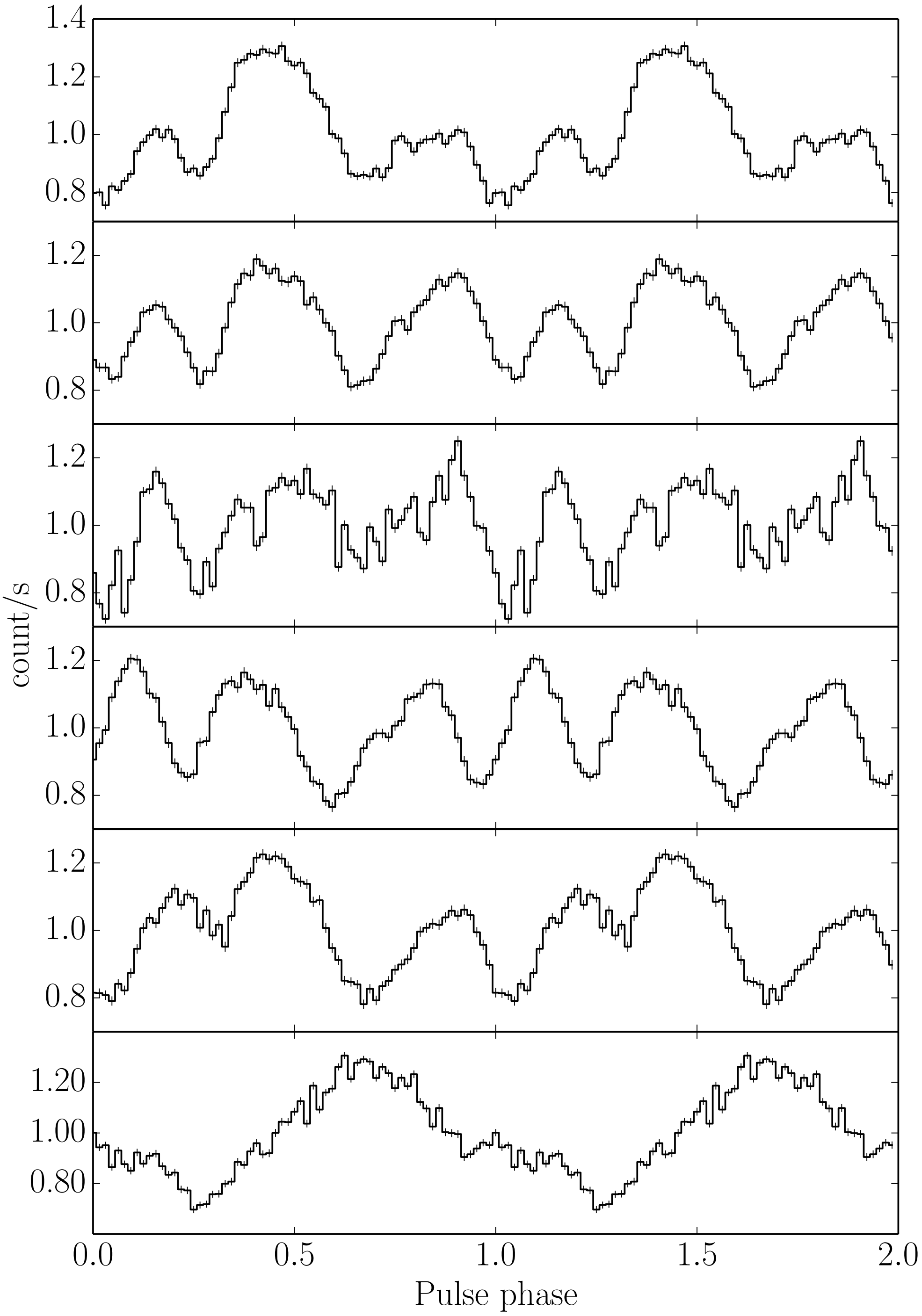

Figure 5.6: JEM-X1 normalized pulse profiles in the $3 - 20\,\mathrm{keV}$ energy range. Panels follow the same Rev. and luminosity stage as in Fig. 5.5. Figure from Malacaria et al. (2015).

and mild peaks result in larger errors compared to sharp and narrow ones. In the ISGRI profiles the features are relatively sharp and narrow. This results in an error of the arrival times of about 0.01 in phase. The uncertainties of P_0 and $\dot{P}$ are calculated from the χ^2 contours at 1σ c.l.

The obtained timing solution is presented in Table 5.1 and illustrated in Fig. 5.4, where a decrease in the observed pulse period over the outburst is clear. The reference pulse period is $P_0 = 274.9817 \pm 0.0001\,\mathrm{s}$ at MJD 55952.4592 and the period derivative is $\dot{P} =$ (-2.04 ± 0.01)×10^{-7} s/s (constant over the time of the observations). This solution turns out to be inconsistent with that found by Sugizaki et al. (2015). However, such a difference is expected due to the different approach of those authors, who also take into account the doppler effects of the binary system and the (positive) time derivative during non-accreting phases.

With the final timing solution, ISGRI light curves have been folded to produce a refined set of pulse profiles as shown in Fig. 5.5. A slight phase shift (up to $\Delta\phi \sim 0.1$) among the pulse profiles is still noticeable, as can be determined, for example, by the phase of the sharp minimum after the highest peak in the different observations. This is probably due to second order ($\ddot{P}$) effects which are not taken into account by our solution (see Eq. 5.1).

The same timing solution has been used to fold JEM-X1 light curves between $3 - 20\,\mathrm{keV}$ and to generate the JEM-X pulse profiles for each of the six observations as shown in Fig. 5.6. In this figure, the panel corresponding to the Rev. 1134 shows a more noisy pulse profile, despite this observation refers to the outburst peak. This is due to shorter JEM-X exposure time during that observation (see Table 5.1).

Overall, pulse profiles show a strong energy- and flux-dependence and, at the same time, a small ($\sim 20\%$) and almost constant pulsed fraction.

5.5 Spectral analysis

5.5.1 Phase-averaged spectroscopy

5.5.1.1 Spectral model

The spectral analysis of the observations has been performed using the version 12.7.1 of the XSPEC fitting software (Arnaud, 1996). To compare the results of the following spectral analysis with those of Klochkov et al. (2012), the same spectral model has been adopted, that is, a high energy exponential rolloff model (the `cutoffpl` component in XSPEC):

$$F(E) \propto E^{-\Gamma} e^{(-E/E_{fold})} \tag{5.3}$$

(where E is the photon energy, Γ is the photon index, and E_{fold} is the folding energy of exponential rolloff in keV). To this, a multiplicative absorption line with a Gaussian optical depth (the `gabs` component in XSPEC) has been included to model the CRSF:

$$G(E) = \exp\left\{-\frac{\eta}{\sqrt{2\pi}\sigma}\exp\left(-\frac{(E-E_{cyc})^2}{2\sigma^2}\right)\right\} \tag{5.4}$$

where E_{cyc} is the cyclotron line centroid energy, η and σ are the line depth (while the optical depth at line center is $\eta/\sqrt{2\pi}/\sigma$), and the width of the line, respectively. Also a 6.4 keV Fe

Table 5.2: Results of the *INTEGRAL* spectral and timing analysis of GX 304-1. The global timing solution has been obtained from the phase connection of IBIS/ISGRI ($18-80$ keV) pulse profiles, while the spectral parameters throughout the outburst have been obtained with OSA 10 plus additional gain correction (see text). Fluxes and luminosities are calculated in the range $3-80$ keV (a distance of 2.4 kpc has been assumed for the latter).

Rev. ID	Global solution[1]	1131	1132	1134	1136	1137	1138
P [s]	274.9817	275.1313	275.0772	274.9763	274.8714	274.8134	274.7597
$Referencetime$ [MJD]	55952.4592	55943.98022	55947.04829	55952.76433	55958.70659	55961.99595	55965.03900
$Flux/(10^{-8}\,\mathrm{erg\,s^{-1}\,cm^{-2}})$	–	$0.659^{+0.002}_{-0.002}$	$1.379^{+0.004}_{-0.004}$	$2.413^{+0.006}_{-0.007}$	$1.231^{+0.004}_{-0.004}$	$0.609^{+0.002}_{-0.002}$	$0.288^{+0.002}_{-0.002}$
$L_\mathrm{X}/(10^{37}\,\mathrm{erg\,s^{-1}})$	–	0.45	0.95	1.66	0.85	0.42	0.19
Γ	–	$1.18^{+0.07}_{-0.05}$	$0.89^{+0.03}_{-0.03}$	$0.93^{+0.09}_{-0.09}$	$1.07^{+0.07}_{-0.07}$	$1.27^{+0.08}_{-0.07}$	$1.56^{+0.06}_{-0.03}$
E_fold[keV]	–	$21.2^{+1.2}_{-0.9}$	$16.8^{+0.6}_{-0.5}$	$16.1^{+0.7}_{-0.7}$	$17.7^{+0.8}_{-0.7}$	$21.3^{+1.2}_{-1.1}$	30^{+2}_{-2}
E_cyc[keV]	–	$55.0^{+0.7}_{-0.7}$	$56.6^{+0.8}_{-0.8}$	$59.3^{+0.9}_{-0.9}$	$54.2^{+0.6}_{-0.5}$	$54.4^{+0.8}_{-0.7}$	$50.6^{+1.1}_{-1.1}$
σ_cyc[keV]	–	$6.6^{+1.1}_{-0.5}$	$8.5^{+0.4}_{-0.4}$	$10.8^{+0.8}_{-0.8}$	$6.5^{+0.5}_{-0.4}$	$6.5^{+0.6}_{-0.5}$	$5.3^{+0.8}_{-0.7}$
η_cyc	–	$11.9^{+1.5}_{-1.4}$	$15.7^{+1.9}_{-1.8}$	17^{+3}_{-3}	$10.5^{+1.2}_{-1.1}$	$10.4^{+1.2}_{-1.3}$	$8.1^{+1.3}_{-1.5}$
χ^2_red	–	0.9	0.8	1.3	0.9	1.0	1.0

[1] Reference values represent the pulse period P at the time T (MJD). The uncertainties of the given pulse periods is ~ 0.10 ms.

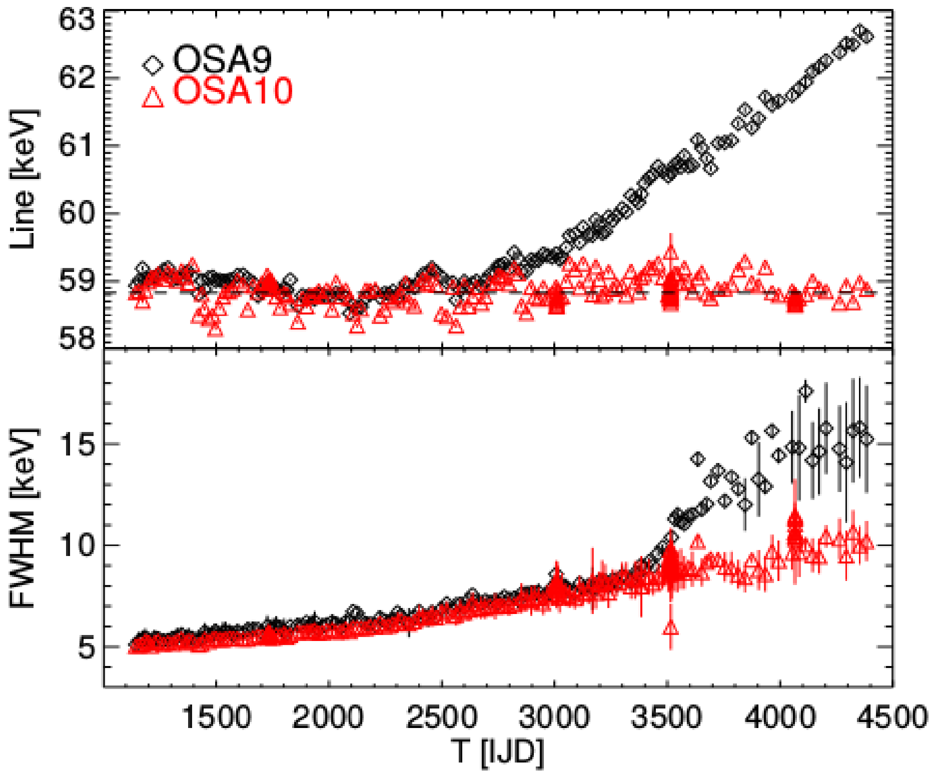

Figure 5.7: Time evolution of the W fluorescence line position (top) and FWHM (bottom) obtained with OSA 9 (black) and OSA 10 (red). The dashed horizontal line in the upper panel shows the nominal position of the W line. Figure from Caballero et al. (2013).

Kα emission line has been included, modeled with an additive Gaussian:

$$G(E) = K\frac{1}{\sigma\sqrt{2\pi}}\exp\left\{-\frac{(E-E_{line})^2}{2\sigma^2}\right\} \tag{5.5}$$

where K is the normalization factor (in units of total photons $\mathrm{cm}^{-2}\,\mathrm{s}^{-1}$), while E_{line} is the line energy. Finally, a photo-electric absorption component has been added (the `wabs` component in XSPEC):

$$M(E) = exp[-N_H\sigma(E)] \tag{5.6}$$

where N_{H} is the equivalent neutral hydrogen column (in units of $10^{22}\,\mathrm{cm}^{-2}$), while $\sigma(E)$ is the photo-electric cross-section (Morrison and McCammon, 1983) not including the Thomson cross-section.

5.5.1.2 The OSA 10 data reduction

INTEGRAL spectral analysis was performed with the OSA 10 software, which at the time of preparation was the latest version of the INTEGRAL analysis software. OSA 10 is supplied

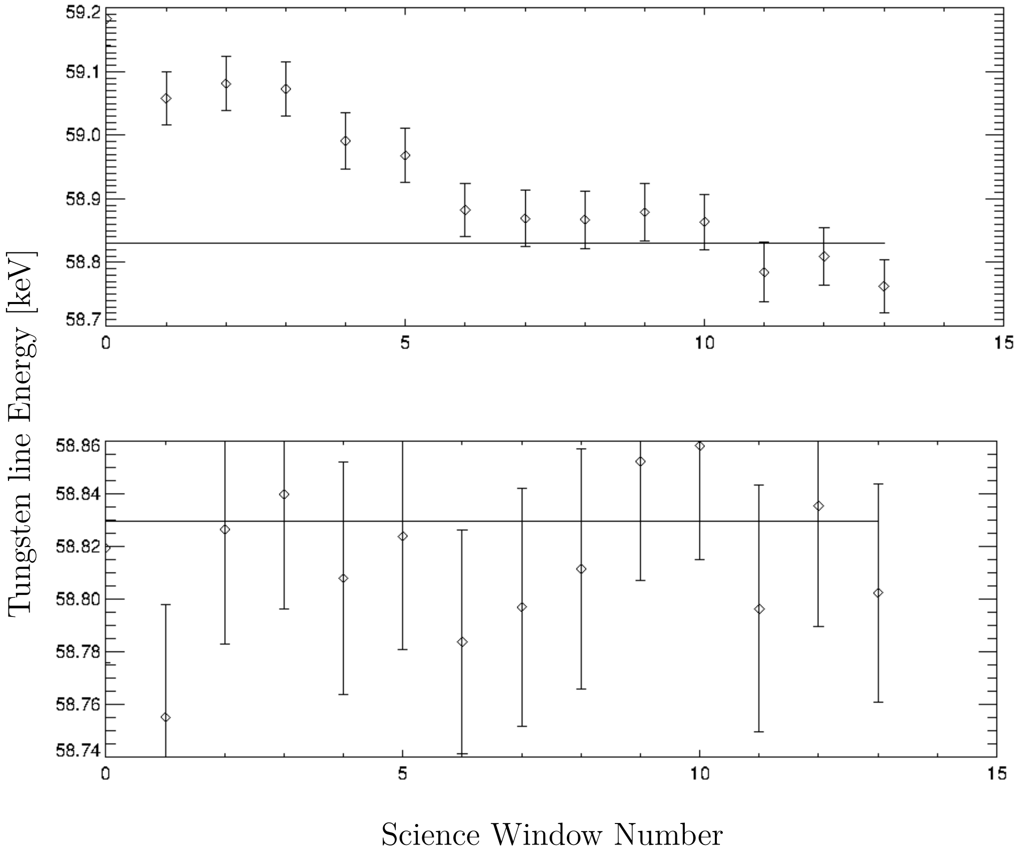

Figure 5.8: Gain corrected energy of the W reference line complex for the Rev. 1132. The vertical axis represents the measured energy [keV] of the W reference line, while the horizontal axis represents the ScW number (starting from the beginning of the *INTEGRAL* revolution). The horizontal black line marks the nominal centroid energy of the W complex, 58.8297 keV. *Top:* OSA 10 data reduction only; *Bottom:* OSA 10 data reduction plus additional gain correction.

with an updated energy calibration of the ISGRI detector with respect to the previous version (OSA 9). The photon energy reconstruction with OSA 9 was not reliable anymore since the revolution 583 (see Fig. 5.7). The conversion factor from electronic pulse-height to incoming photon energy (i.e., the gain G) has been observed to change with time. The main reason was the wrong assumption that the temperature gradient between the different ISGRI modules all along the mission was assumed constant. On the contrary, the dependency of gains and offsets on the temperature was taken into account in the updated calibration. With OSA 10, the energy reconstruction has been improved by using the measured module temperatures of the thermal probes instead of assuming a constant temperature gradient between the different modules. Also, a new set of ancillary response files (ARFs) for different epochs has been produced, using Crab observations in order to account for the detector response evolution. This guarantees that the best available knowledge of the detector response is used in each spectral fitting. As a result, a more reliable photon energy reconstruction is ensured. The details about the new energy reconstruction are reported in Caballero et al. (2013).

To investigate the difference in energy calibration between OSA 9 and OSA 10, the same

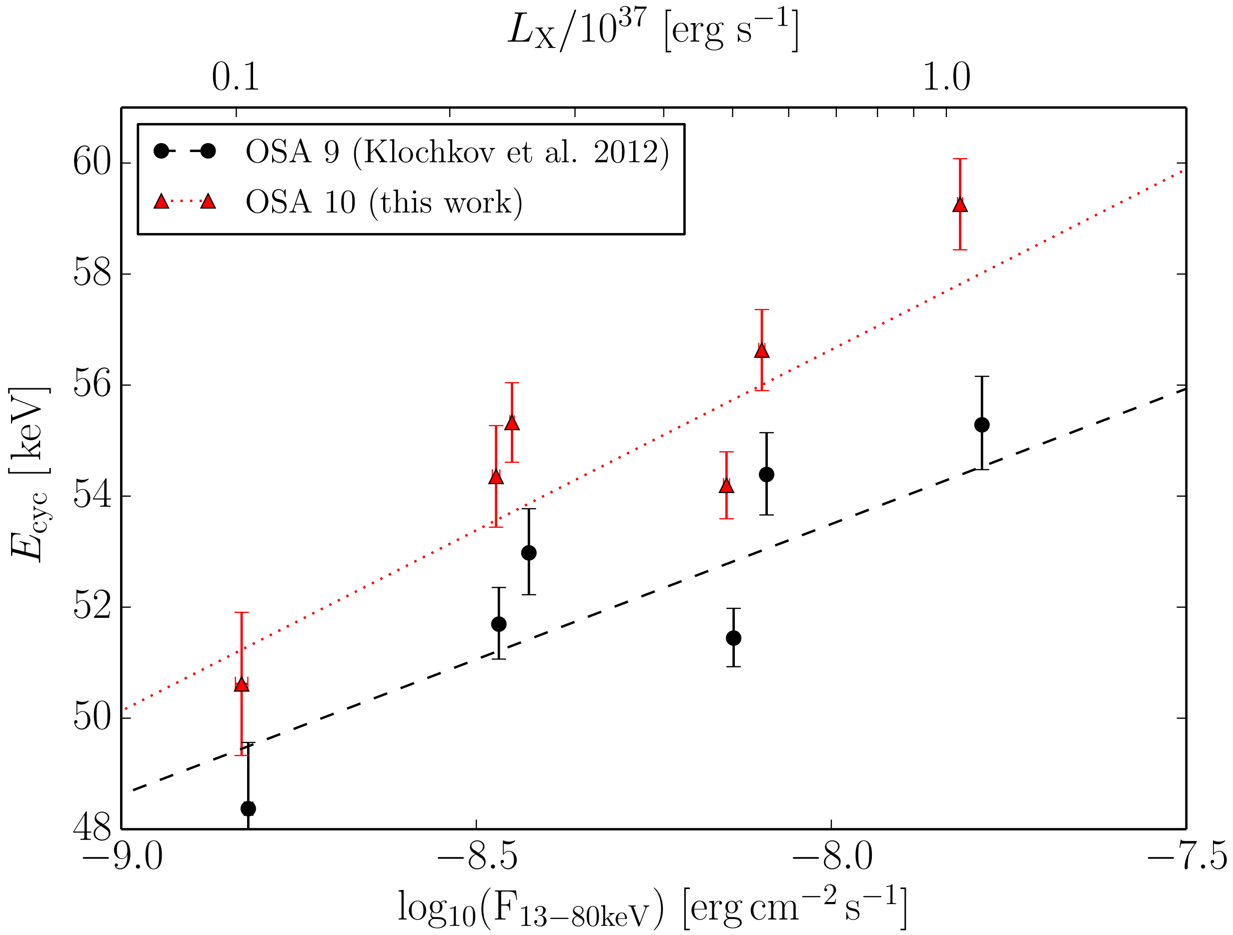

Figure 5.9: Cyclotron line centroid energy $E_{\rm cyc}$ as a function of the logarithm of flux in the $13 - 80$ keV range. The black filled circles are the results of Klochkov et al. (2012), obtained with OSA 9 and corrected for the ISGRI energy gain drift. The red triangles are the results of this work, obtained with OSA 10 and then gain-corrected. The dashed and dotted lines are the results of linear fits to the $E_{\rm cyc} - log_{10}(Flux)$ data for the two sets. The error bars indicate 1σ-uncertainties (the statistical flux uncertainties are smaller than the symbol size). The top x-axis shows the corresponding isotropic source luminosity assuming a distance of 2.4 kpc. Figure from Malacaria et al. (2015).

data set used in this work has been extracted with both the software versions. Following Klochkov et al. (2012), after the OSA 9 data reduction, an additional gain correction has been performed based on the background spectral line complex of Tungsten (W, with a nominal centroid energy at 58.8297 keV). After the OSA 10 data reduction, which includes a more accurate gain correction with respect to OSA 9, a small deviation between the inferred energy and the nominal Tungsten line energy was still noticeable (see top panel of Fig. 5.8). The deviation amounted up to +0.5 keV in the Science Windows (ScWs, i.e., *INTEGRAL* pointings) at the beginning of each *INTEGRAL* revolution. According to the ISGRI instrument team (priv. comm.), the deviation can be attributed to possible orbital drifts in the detector response, which are responsible for systematic scatter when revolutions start. In fact, at the beginning of each orbital revolution, the onboard instruments are switched off to guarantee

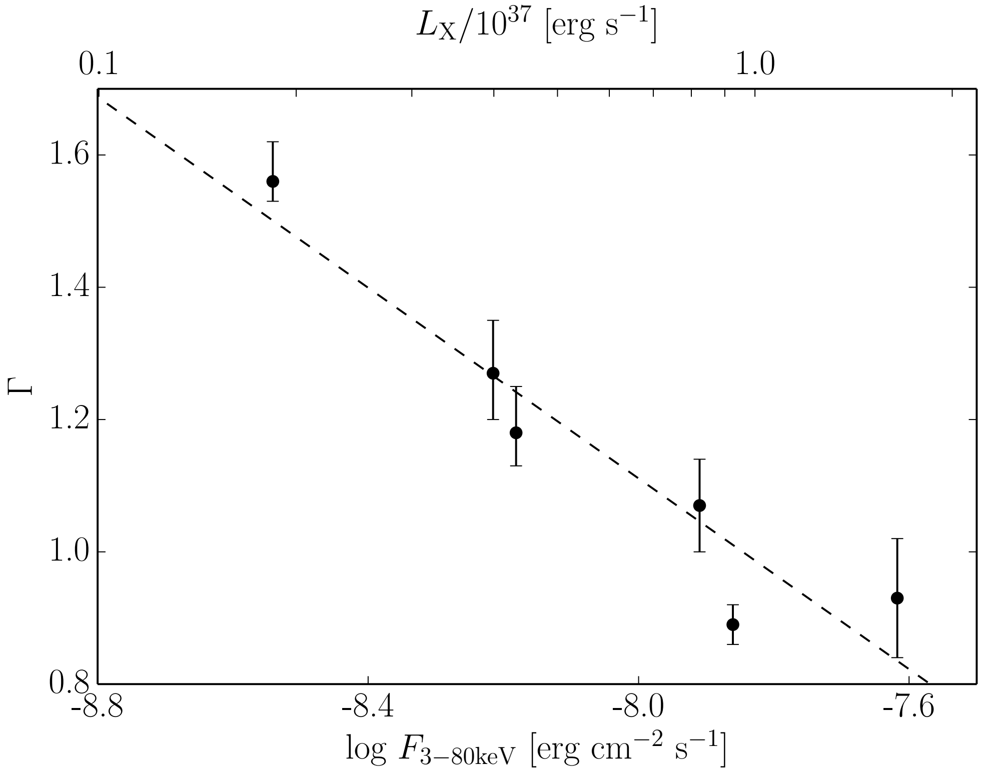

Figure 5.10: The photon index Γ as a function of the observed flux. The dashed line represents the linear fit to the $\Gamma - log_{10}(Flux)$ data points. The luminosity scale on the top x-axis is as in Fig. 5.9. Figure from Malacaria et al. (2015).

their safety at each perigee passage (which is within the magnetospheric radiation belt). Only later the instruments are switched on again, a process that takes some time before the system gets into its nominal state. However, even if orbital variations are not corrected, they are mitigated when averaged over a number of revolutions. Nonetheless, to eliminate this deviation, an additional gain correction has been performed to ensure the stability of the measured Tungsten reference blend. After the correction, the inferred Tungsten line energy in all ScWs is found to be consistent with its nominal value within 2σ (see bottom panel of Fig. 5.8).

To illustrate the effects of the different energy calibrations, the E_{cyc}-flux relation for the spectra obtained with the two software versions is compared in Fig. 5.9 (the used spectral model is explained in detail in the next section). It is important to note that the energy range indicated in Klochkov et al. (2012) for calculating the flux is erroneously reported as $4 - 80$ keV, while the correct range is $13 - 80$ keV (where the lower limit is restricted by the response matrix energy range of the ISGRI instrument). The two different sets of results clearly show a systematic shift of the cyclotron line centroid energy, with a deviation (proportional to the measured energy) up to ~2 keV. This is the result of the new energy calibration implemented in OSA 10.

A new version of OSA is planned to be released in the next future. The new software will account for the residuals in the energy gain corretion that are still present at the beginning of *INTEGRAL* revolutions.

5.5.1.3 Spectral results

Data from both JEM-X modules, ISGRI, and SPI have been employed to produce pulse phase-averaged spectra for each observation (i.e. 6 in total) with the cutoff power-law model described above (see Sec. 5.5.1.1). This allowed to investigate the behavior of best-fit spectral parameters along the entire outrburst. Particularly interesting, is the evolution of the cyclotron line energy ($E_{\rm cyc}$) and of the continuum parameters (i.e., the photon index Γ and the folding energy $E_{\rm fold}$) at different outburst stages (i.e., at different luminosity levels). Spectral results are reported in Table 5.2.

The (variable) cyclotron line energy is found at about 55 keV, consistent with previous works. Also, the cyclotron line energy is positively correlated with flux, as already indicated by Yamamoto et al. (2011) and shown with high significance by Klochkov et al. (2012). The variation of $E_{\rm cyc}$ with flux found with the present analysis is shown in Fig. 5.9. These new results show a systematic offset from those of the latter authors (see Sect. 5.5.1.2). This in turn is reflected in a higher (although consistent) slope of the fitted line, i.e., $6.51 \pm 1.21\,{\rm keV}/\log_{10}({\rm erg/cm^2/s})$.

In addition to the $E_{\rm cyc}$–flux correlation, other correlations have been investigated. One of these is the dependence of the power-law index Γ (which describes the spectral hardness below the folding energy) on flux. In GX 304-1 an anticorrelation between Γ and the flux is clear, as shown in Fig. 5.10. For the two above-mentioed correlations, the Pearson's correlation coefficient ρ, which is a measure of the linear dependence of the two correlated parameters, results to be $\rho_{\rm cyc} = 0.92$ and $\rho_\Gamma = -0.95$, respectively. The corresponding one-sided probability p of obtaining the correlations by chance in a sample of uncorrelated data are $p_{cyc} \sim 0.01$ and $p_\Gamma \sim 0.004$, respectively. The $E_{\rm cyc}$–flux correlation also shows a slope that is significantly (5σ) different from zero. Therefore, the obtained correlations are robust, and actually GX 304-1 is the accreting pulsar in which those correlations are the strongest.

Also, the folding energy $E_{\rm fold}$ is found to be dependent on flux. Similar to the negative $\Gamma - \log_{10}({\rm flux})$ correlation, $E_{\rm fold}$ also shows a negative correlation with flux. Therefore, $E_{\rm fold}$ and Γ are positively correlated with each other. To verify if such a correlation reflects the intrinsic behavior of the source and not a model-driven effect, χ^2-contour plots of the two parameters have been produced, and are shown in Fig. 5.12. Although the contours indicate some intrinsic coupling between $E_{\rm fold}$ and Γ, the confidence regions corresponding to different observations are well separated, indicating that the observed correlation must reflect a real source behavior. The same plot also indicates the respective luminosity L_X (in units of $10^{37}\,{\rm erg\,s^{-1}}$), which shows an anticorrelation between $E_{\rm fold}$ and L_X.

5.5.2 Phase-resolved spectral analysis

As the neutron star rotates, at different times (or pulse phases) we observe the emitting regions of the neutron star at different viewing angles. This may lead to a significant variability of the observed spectrum with pulse phase. To explore the corresponding spectral variability with pulse phase, X-ray spectra of GX 304-1 in five equally spaced pulse phase intervals have

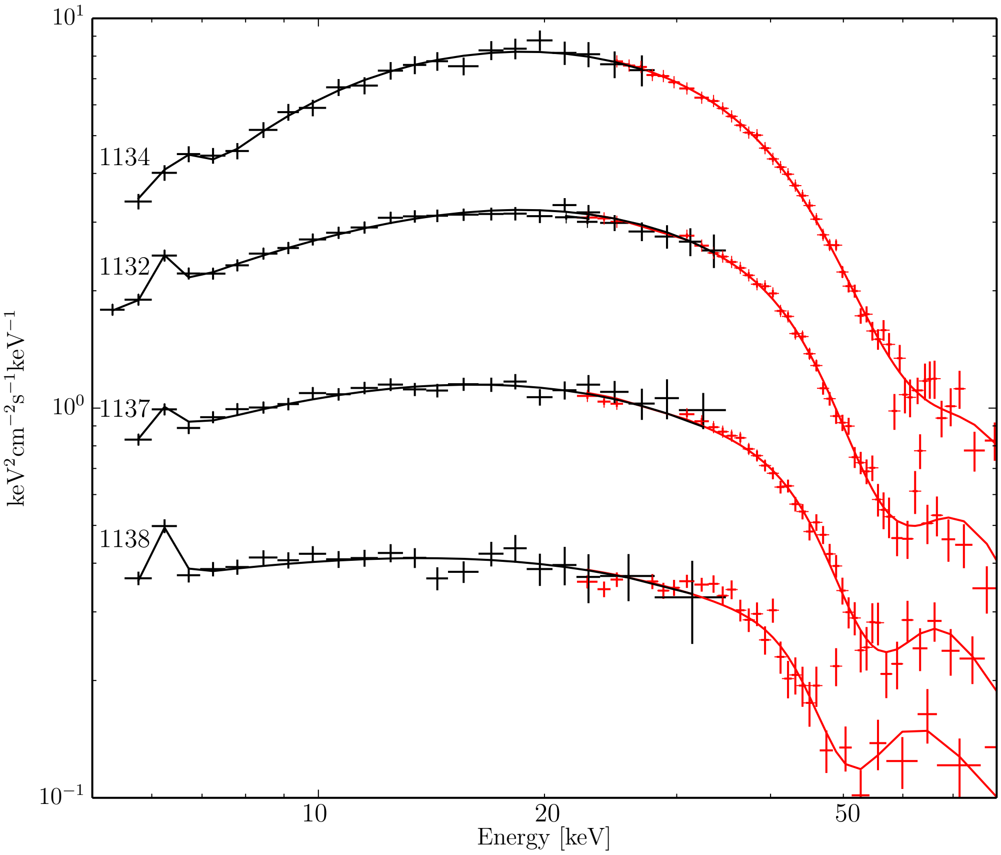

Figure 5.11: Pulse phase-averaged spectra of four observations (labelled above each spectrum), from top to bottom, with decreasing luminosity. The JEM-X1 (black) and ISGRI (red) data and the folded model are shown. The spectra have been scaled for better visualization. Both the $E_{\rm cyc}$–flux and the Γ–flux correlations are clearly visible. Figure from Malacaria et al. (2015).

been extracted. The small number of phase bins is chosen because a finer binning would lead to larger uncertainties. To extract phase-resolved spectra, the timing solution obtained in Sec. 5.3.2 has been used to calculate good time intervals (GTIs) corresponding to the selected phase bins. GTIs have then been used to filter *INTEGRAL* data from both JEM-X modules, ISGRI and SPI.

5.5.2.1 Pulse phase-resolved spectroscopy of individual observations

To fit the phase-resolved spectra, the spectral model described in Sect. 5.5.1.1 has been used. This model provides an acceptable fit (the reduced chi-squared values $\chi^2_{\rm red}$ are between 0.8 and 1.2) to the spectra from all but one phase bin (see Table 5.3). The spectra of the $0.0-0.2$ phase bin of all revolutions, except the one from Rev. 1138, show large positive residuals around 35 keV, which yield $\chi^2_{\rm red} \gtrsim 1.5$. This feature will be thereafter called *bump*, because the residuals that it produces can be modeled with an additional Gaussian emission line. An example of such a spectrum is shown in Fig. 5.13. Alternatively, a Gaussian absorption line

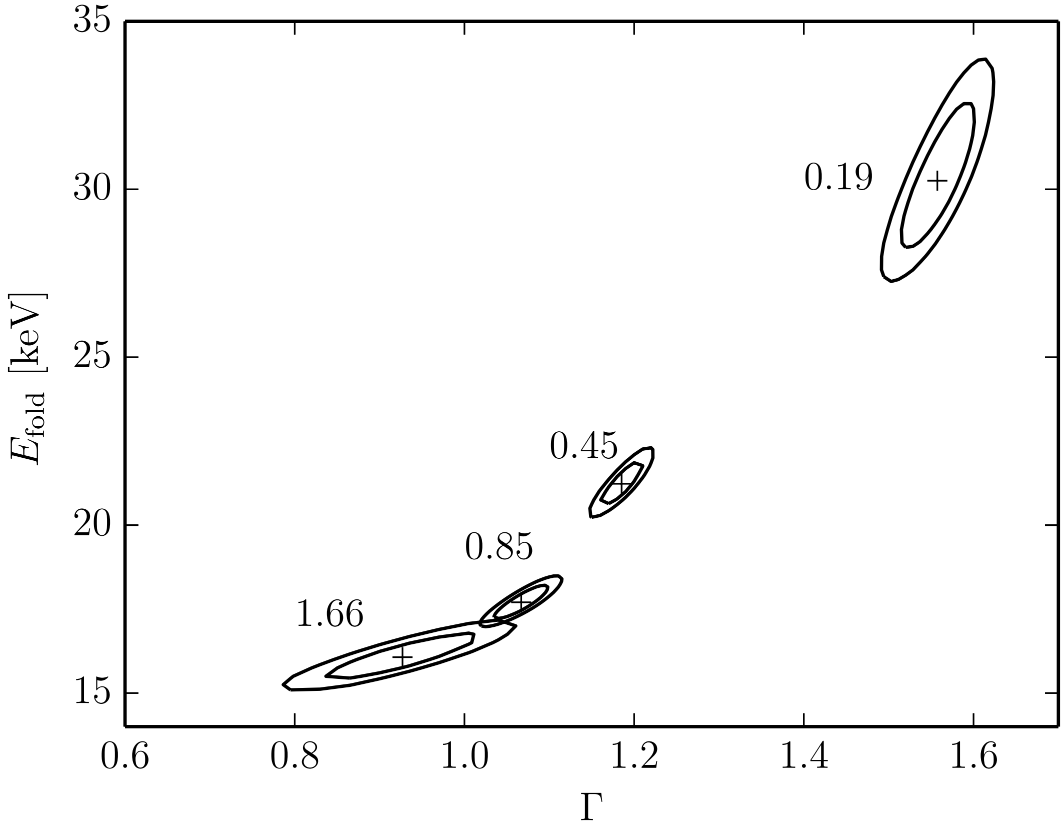

Figure 5.12: χ^2-contour plots of the folding energy E_{fold} and the photon index Γ for four selected INTEGRAL observations. The contours correspond to $\chi^2 + 1.0$ (the projections of this contour to the parameter axes correspond to the 68% c.l. uncertainty for one parameter of interest), and $\chi^2 + 2.3$ (68% uncertainty for two parameters of interest). The respective luminosity ($3 - 80\,\mathrm{keV}$) in units of $10^{37}\,\mathrm{erg\,s^{-1}}$ is indicated for each observation close to the respective contours. Figure from Malacaria et al. (2015).

at lower energies can be used to flatten the residuals, resulting in an equally good fit. In this case, the line centroid energy is about 20 keV.

However, to enable a meaningful comparison of the spectral parameters, the same model in all phase bins has been used. Therefore, the results of the phase-resolved analysis are reported in Table 5.3 using the same model as in Sect. 5.5.1.1 (that is, without any additional components to model the bump) for all phase bins. A comparison of the model parameters with and without the inclusion of the additional Gaussian emission line (for those phase bins that need it) is shown in Table 5.4, where it can be clearly seen that the additional component heavily modifies the spectral parameters. The best-fit results obtained with the model in which the feature is modeled by a Gaussian absorption line are shown in Table 5.5.

Table 5.3: The best-fit parameters of the pulse-phase resolved spectra. Fluxes are calculated in the range 3 – 80 keV. The errors correspond to the 1σ c.l.

Rev#	**1131**					**1132**				
Phase-bin	0.0 – 0.2∗	0.2 – 0.4	0.4 – 0.6	0.6 – 0.8	0.8 – 1.0	0.0 – 0.2∗	0.2 – 0.4	0.4 – 0.6	0.6 – 0.8	0.8 – 1.0
Γ	$1.70^{+0.04}_{-0.04}$	$0.96^{+0.05}_{-0.05}$	$1.14^{+0.12}_{-0.05}$	$1.24^{+0.16}_{-0.17}$	$1.63^{+0.13}_{-0.15}$	$1.29^{+0.08}_{-0.04}$	$0.87^{+0.04}_{-0.07}$	$1.45^{+0.81}_{-0.21}$	$0.63^{+0.17}_{-0.15}$	$0.83^{+0.13}_{-0.13}$
E_{fold} [keV]	49^{+53}_{-45}	19^{+1}_{-1}	19^{+2}_{-2}	21^{+3}_{-2}	28^{+3}_{-3}	27^{+1}_{-1}	18^{+9}_{-1}	23^{+2}_{-3}	13^{+1}_{-1}	15^{+1}_{-1}
E_{cyc} [keV]	55^{+1}_{-3}	56^{+1}_{-1}	53^{+2}_{-1}	56^{+2}_{-2}	56^{+1}_{-1}	$56.4^{+0.9}_{-0.8}$	60^{+2}_{-2}	62^{+1}_{-3}	52^{+2}_{-2}	57^{+1}_{-1}
σ_{cyc} [keV]	$4.3^{+0.7}_{-0.6}$	$7.1^{+1.1}_{-0.9}$	$8.4^{+1.4}_{-1.2}$	$9.9^{+1.6}_{-1.4}$	$5.8^{+0.9}_{-0.9}$	$5.7^{+0.6}_{-0.5}$	11^{+1}_{-2}	13^{+1}_{-3}	$8.3^{+2.1}_{-1.6}$	$7.9^{+1.0}_{-0.9}$
η_{cyc}	$10.5^{+1.8}_{-1.6}$	15^{+4}_{-3}	13^{+4}_{-3}	19^{+5}_{-5}	14^{+3}_{-3}	16^{+2}_{-1}	22^{+6}_{-6}	26^{+6}_{-10}	10^{+5}_{-3}	18^{+4}_{-3}
Flux [10^{-8} erg s^{-1} cm^{-2}]	$0.616^{+0.015}_{-0.014}$	$0.704^{+0.014}_{-0.013}$	$0.776^{+0.015}_{-0.015}$	$0.601^{+0.013}_{-0.013}$	$0.621^{+0.012}_{-0.013}$	$0.137^{+0.023}_{-0.022}$	$1.419^{+0.021}_{-0.020}$	$1.394^{+0.022}_{-0.022}$	$1.262^{+0.020}_{-0.019}$	$1.492^{+0.019}_{-0.019}$
χ^2_{red}	1.8	1.0	0.8	0.9	0.8	2.4	1.0	0.9	0.8	0.8
Rev#	**1134**					**1136**				
Phase-bin	0.0 – 0.2∗	0.2 – 0.4	0.4 – 0.6	0.6 – 0.8	0.8 – 1.0	0.0 – 0.2∗	0.2 – 0.4	0.4 – 0.6	0.6 – 0.8	0.8 – 1.0
Γ	$0.59^{+0.06}_{-0.06}$	$0.39^{+0.12}_{-0.15}$	$0.88^{+0.13}_{-0.20}$	$0.21^{+0.21}_{-0.18}$	$0.59^{+0.15}_{-0.18}$	$1.56^{+0.06}_{-0.03}$	$0.80^{+0.05}_{-0.05}$	$1.07^{+0.18}_{-0.18}$	$0.83^{+0.15}_{-0.16}$	$1.06^{+0.12}_{-0.12}$
E_{fold} [keV]	$17.2^{+0.6}_{-0.6}$	$13.5^{+0.8}_{-1.1}$	17^{+1}_{-1}	13^{+1}_{-1}	13^{+1}_{-1}	33^{+2}_{-1}	$15.3^{+0.9}_{-0.8}$	18^{+3}_{-2}	14^{+1}_{-1}	18^{+1}_{-1}
E_{cyc} [keV]	58^{+1}_{-1}	57^{+1}_{-1}	62^{+1}_{-1}	61^{+2}_{-3}	58^{+1}_{-1}	$55.1^{+0.8}_{-1.1}$	52^{+1}_{-1}	58^{+3}_{-3}	51^{+1}_{-1}	$55.7^{+0.9}_{-0.8}$
σ_{cyc} [keV]	$6.8^{+0.7}_{-0.7}$	$10.5^{+2.3}_{-1.5}$	14^{+2}_{-1}	17^{+2}_{-2}	$10.0^{+1.6}_{-1.2}$	$4.8^{+0.7}_{-0.7}$	$7.7^{+1.3}_{-1.1}$	$10.0^{+3.4}_{-2.2}$	$7.2^{+0.9}_{-0.9}$	$6.0^{+0.7}_{-0.6}$
η_{cyc}	11^{+2}_{-1}	14^{+7}_{-4}	29^{+11}_{-6}	$48.^{+18}_{-14}$	21^{+6}_{-4}	$8.2^{+1.5}_{-1.3}$	11^{+3}_{-3}	18^{+10}_{-7}	13^{+3}_{-2}	16^{+2}_{-2}
Flux [10^{-8} erg s^{-1} cm^{-2}]	$1.903^{+0.033}_{-0.032}$	$2.181^{+0.042}_{-0.162}$	$2.345^{+0.040}_{-0.038}$	$2.240^{+0.032}_{-0.038}$	$2.620^{+0.049}_{-0.049}$	$1.209^{+0.022}_{-0.022}$	$1.279^{+0.019}_{-0.021}$	$1.162^{+0.022}_{-0.024}$	$1.158^{+0.020}_{-0.019}$	$1.261^{+0.019}_{-0.018}$
χ^2_{red}	1.5	1.1	1.0	1.1	1.2	1.9	0.9	0.7	0.9	0.8
Rev#	**1137**					**1138**				
Phase-bin	0.0 – 0.2∗	0.2 – 0.4	0.4 – 0.6	0.6 – 0.8	0.8 – 1.0	0.0 – 0.2	0.2 – 0.4	0.4 – 0.6	0.6 – 0.8	0.8 – 1.0
Γ	$1.56^{+0.10}_{-0.04}$	$1.13^{+0.05}_{-0.05}$	$1.18^{+0.19}_{-0.09}$	$1.51^{+0.14}_{-0.14}$	$1.54^{+0.14}_{-0.15}$	$2.07^{+0.23}_{-0.29}$	$1.82^{+0.09}_{-0.08}$	$1.67^{+0.07}_{-0.07}$	$1.47^{+0.24}_{-0.12}$	$1.47^{+0.22}_{-0.08}$
E_{fold} [keV]	38^{+5}_{-2}	20^{+1}_{-1}	18^{+4}_{-1}	24^{+3}_{-3}	22^{+3}_{-2}	39^{+21}_{-12}	77^{+42}_{-18}	37^{+5}_{-4}	22^{+5}_{-3}	29^{+7}_{-4}
E_{cyc} [keV]	$54.1^{+0.9}_{-0.7}$	53^{+1}_{-1}	56^{+4}_{-2}	56^{+2}_{-2}	56^{+2}_{-2}	52^{+7}_{-3}	53^{+2}_{-2}	50^{+1}_{-1}	45^{+1}_{-1}	53^{+3}_{-3}
σ_{cyc} [keV]	$4.5^{+0.6}_{-0.7}$	$5.7^{+1.0}_{-0.9}$	$10.1^{+3.9}_{-1.8}$	$8.2^{+1.4}_{-1.2}$	$5.7^{+1.8}_{-1.9}$	$5.9^{+7.0}_{-4.9}$	$4.7^{+1.7}_{-1.7}$	$3.4^{+0.9}_{-0.8}$	$2.8^{+1.3}_{-1.6}$	$8.4^{+1.8}_{-1.8}$
η_{cyc}	$9.6^{+1.5}_{-1.4}$	$10.5^{+2.4}_{-1.9}$	$12.7^{+10.9}_{-4.3}$	17^{+5}_{-4}	$8.4^{+3.4}_{-2.8}$	$7.7^{+12.9}_{-5.2}$	$7.5^{+3.5}_{-2.9}$	$6.7^{+2.2}_{-1.9}$	$4.2^{+1.7}_{-1.5}$	$17.2^{+7.2}_{-6.2}$
Flux [10^{-8} erg s^{-1} cm^{-2}]	$0.563^{+0.006}_{-0.012}$	$0.685^{+0.013}_{-0.013}$	$0.645^{+0.028}_{-0.019}$	$0.531^{+0.011}_{-0.011}$	$0.587^{+0.012}_{-0.011}$	$0.265^{+0.018}_{-0.025}$	$0.209^{+0.011}_{-0.010}$	$0.266^{+0.028}_{-0.016}$	$0.354^{+0.014}_{-0.013}$	$0.294^{+0.006}_{-0.012}$
χ^2_{red}	1.9	1.0	1.1	0.9	0.9	0.9	0.9	1.0	0.9	0.9

Notes: The starred phase-bins mark those spectra that need an additional gaussian emission line around 35 keV to get an accettable fit.

Table 5.4: Comparison of the best-fit parameters of the spectra from the phase bin 0.0 – 0.2 using a model with and without additional Gaussian emission line.

	Rev# 1131		**Rev# 1132**		**Rev# 1134**		**Rev# 1136**		**Rev# 1137**	
Parameter	*No bump*	*Bump*	*No bump*	*Bump*	*No bump*	*Bump*	*No bump*	*Bump*	*No bump*	*Bump*
Γ	$1.70^{+0.04}_{-0.04}$	$2.15^{+0.21}_{-0.20}$	$1.29^{+0.08}_{-0.04}$	$2.07^{+0.37}_{-0.54}$	$0.59^{+0.06}_{-0.06}$	$0.80^{+0.50}_{-0.36}$	$1.56^{+0.06}_{-0.03}$	$2.22^{+0.10}_{-0.09}$	$1.56^{+0.10}_{-0.04}$	$2.26^{+0.16}_{-0.15}$
$E_{\rm fold}$ [keV]	49^{+53}_{-45}	72^{+67}_{-16}	27^{+1}_{-1}	47^{+39}_{-23}	$17.2^{+0.7}_{-0.6}$	16^{+6}_{-2}	33^{+2}_{-1}	50^{+2}_{-3}	38^{+5}_{-2}	69^{+31}_{-16}
$E_{\rm cyc}$ [keV]	55^{+1}_{-4}	$51.6^{+0.8}_{-0.9}$	$56.4^{+0.9}_{-0.8}$	$52.1^{+0.6}_{-0.5}$	58^{+1}_{-1}	46^{+8}_{-2}	$54.9^{+0.8}_{-1.0}$	$50.7^{+0.3}_{-0.6}$	$54.1^{+0.9}_{-0.7}$	$49.9^{+0.9}_{-1.3}$
$\sigma_{\rm cyc}$ [keV]	$4.3^{+0.7}_{-0.6}$	$3.9^{+0.8}_{-1.0}$	$5.7^{+0.6}_{-0.5}$	$4.6^{+0.6}_{-0.5}$	$6.8^{+0.7}_{-0.7}$	16^{+9}_{-9}	$4.8^{+0.7}_{-0.7}$	$0.18^{+0.69}_{-0.09}$	$4.5^{+0.6}_{-0.7}$	$3.8^{+0.8}_{-1.1}$
$\eta_{\rm cyc}$	$10.5^{+1.8}_{-1.6}$	68^{+181}_{-36}	21^{+6}_{-6}	20^{+16}_{-6}	11^{+2}_{-1}	24^{+15}_{-9}	$11.0^{+3.4}_{-2.6}$	*unconstrained*	$9.6^{+1.5}_{-1.4}$	90^{+263}_{-48}
$E_{\rm bump}$ [keV]	–	36^{+2}_{-3}	–	25^{+3}_{-2}	–	35^{+1}_{-5}	–	$34.3^{+0.7}_{-0.7}$	–	38^{+1}_{-2}
$\sigma_{\rm bump}$ [keV]	–	12^{+2}_{-2}	–	14^{+2}_{-5}	–	$7.5^{+3.8}_{-1.2}$	–	$6.9^{+0.5}_{-0.5}$	–	10^{+1}_{-1}
$\mathrm{norm}^{a}_{\rm bump}$	–	$0.006^{+0.002}_{-0.002}$	–	$0.014^{+0.010}_{-0.004}$	–	$0.05^{+0.06}_{-0.04}$	–	$0.0015^{+0.0002}_{-0.0002}$	–	$0.003^{+0.001}_{-0.001}$
$\chi^2_{\rm red}/d.o.f.$	1.8/136	1.0/133	2.4/136	0.7/133	1.5/136	1.0/133	1.9/136	0.8/133	1.9/136	0.9/133

[a] XSPEC normalization of the bump component, in units of photons $\mathrm{cm}^{-2}\,\mathrm{s}^{-1}$.

Table 5.5: Best-fit parameters of the phase-resolved spectra (phase bin 0.0 – 0.2) using a model with a Gaussian absorption line instead of the emission line to model the bump.

Rev. #	1131	1132	1134	1136	1137
$\mathrm{Flux}/10^{-8}\,\mathrm{erg\,s^{-1}\,cm^{-2}}$	$0.509^{+0.016}_{-0.010}$	$1.17^{+0.03}_{-0.03}$	$2.04^{+0.05}_{-0.06}$	$1.18^{+0.03}_{-0.03}$	$0.513^{+0.017}_{-0.018}$
Γ	$1.51^{+0.33}_{-0.59}$	$1.46^{+0.73}_{-0.48}$	$0.37^{+0.24}_{-0.28}$	$1.45^{+0.21}_{-0.25}$	$0.91^{+0.18}_{-0.27}$
$E_{\mathrm{fold}}\,[keV]$	19^{+5}_{-5}	18^{+4}_{-2}	13^{+1}_{-1}	20^{+3}_{-4}	18^{+3}_{-3}
$E_{\mathrm{gabs}}\,[keV]$	14^{+4}_{-3}	11^{+2}_{-6}	24^{+1}_{-1}	19^{+1}_{-1}	$22.3^{+0.8}_{-0.8}$
$\sigma_{\mathrm{gabs}}\,[keV]$	16^{+16}_{-5}	13^{+3}_{-3}	8^{+3}_{-2}	11^{+3}_{-2}	9^{+3}_{-2}
η_{gabs}	62^{+51}_{-39}	35^{+21}_{-19}	7^{+11}_{-3}	21^{+27}_{-9}	15^{+19}_{-6}
$E_{\mathrm{cyc}}\,[keV]$	$53.86^{+1.00}_{-0.92}$	$54.11^{+0.73}_{-0.66}$	$55.7^{+1.3}_{-1.1}$	$53.35^{+1.02}_{-0.95}$	$52.62^{+0.95}_{-0.84}$
$\sigma_{\mathrm{cyc}}\,[keV]$	$6.5^{+1.1}_{-1.1}$	$5.8^{+0.9}_{-0.8}$	$8.3^{+1.8}_{-1.5}$	$6.4^{+1.4}_{-1.3}$	$6.8^{+1.1}_{-1.1}$
η_{cyc}	$17.6^{+6.1}_{-4.8}$	$12.8^{+3.0}_{-2.1}$	$11.8^{+6.5}_{-3.7}$	$10.7^{+5.8}_{-3.1}$	$14.8^{+6.4}_{-3.7}$
$\chi^2_{\mathrm{red}}/\mathrm{d.o.f.}$	1.0/133	0.7/133	1.0/133	0.8/133	0.9/133

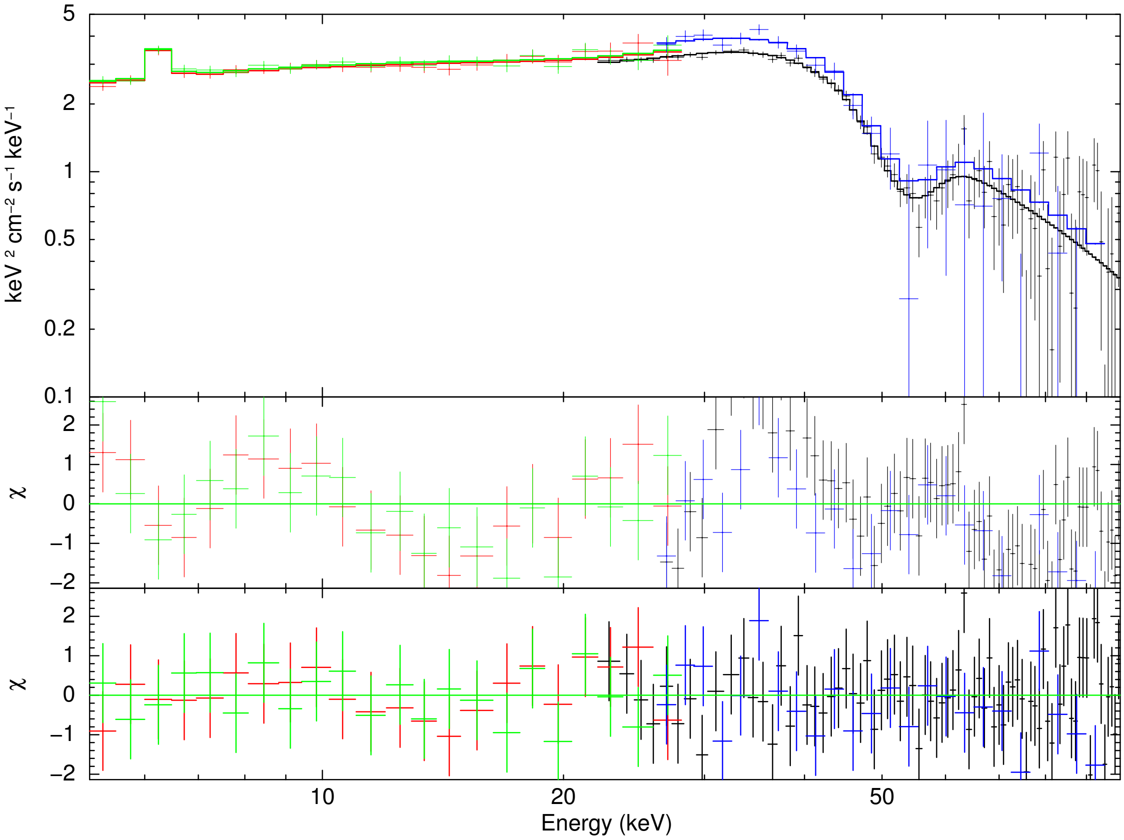

Figure 5.13: *Top:* The unfolded spectrum of the phase bin $0.0-0.2$ from revolution 1132 modeled with a power-law/rolloff model including the cyclotron line and an additional Gaussian component to account for a bump around 35 keV (see text). JEM-X (red and green), ISGRI (black), and SPI (blue) data are used. *Middle:* The residuals of a fit with the model without the additional Gaussian component. Large residuals appear around the cut-off energy. *Bottom:* The residuals after including the Gaussian emission component to model the bump.

As can be seen in Table 5.3, the shape of the continuum changes with pulse phase. At the same time, the cyclotron line energy $E_{\rm cyc}$ shows only slight variation with pulse phase. A selection of the spectral parameters obtained from the Rev. 1136 as a function of the pulse phase is shown in Fig. 5.14. However, the results shown in this plot and, more generally, in Table 5.3 are characterized by large uncertainties and the variation of many parameters with the pulse phase can not be firmly established. Nominal values of the $E_{\rm cyc}$ show a variation with pulse phase up to $\sim 16\%$ (Rev. 1136 and 1132). However, upper limits on the spectral parameters variation can also be estimated. Concerning the cyclotron line energy, the phase resolved spectroscopy excludes a variation larger than 21% at 1σ c.l. (Rev. 1132). Other spectral parameters, e.g., the photon index and the folding energy show a variation less than a factor of ~ 2 at 1σ c.l.

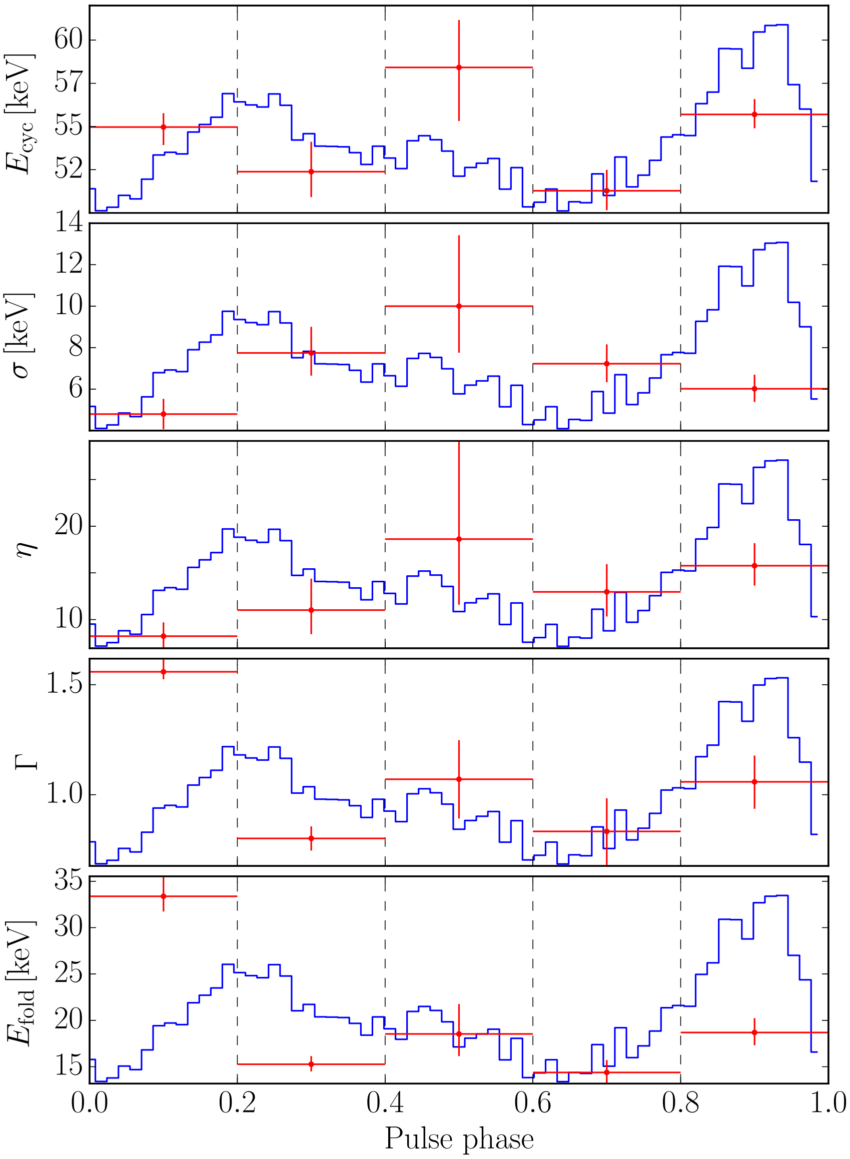

Figure 5.14: A selection of the best-fit parameters from the Rev. 1136 phase-resolved spectra, as a function of the pulse phase. The vertical dashed lines indicate the phase-bins. The solid blue curve is the corresponding ISGRI pulse profile. The vertical error bars are at 1σ c.l., while the horizontal bars indicate the phase bin width. Figure from Malacaria et al. (2015).

5.5.2.2 Stacked phase-resolved spectroscopy

For a deeper investigation of the spectrum variability with pulse phase, the statistics of the phase-resolved spectra has been improved by stacking observations at different fluxes. This is justified by the successfully achieved phase-connection, which resulted in a global timing solution that spans the entire outburst, thus allowing to identify pulse phases at different outburst stages (see Sect. 5.4.1). In this approach, the information on the luminosity dependence of the spectra is lost, and it possibly introduces some systematic effects due

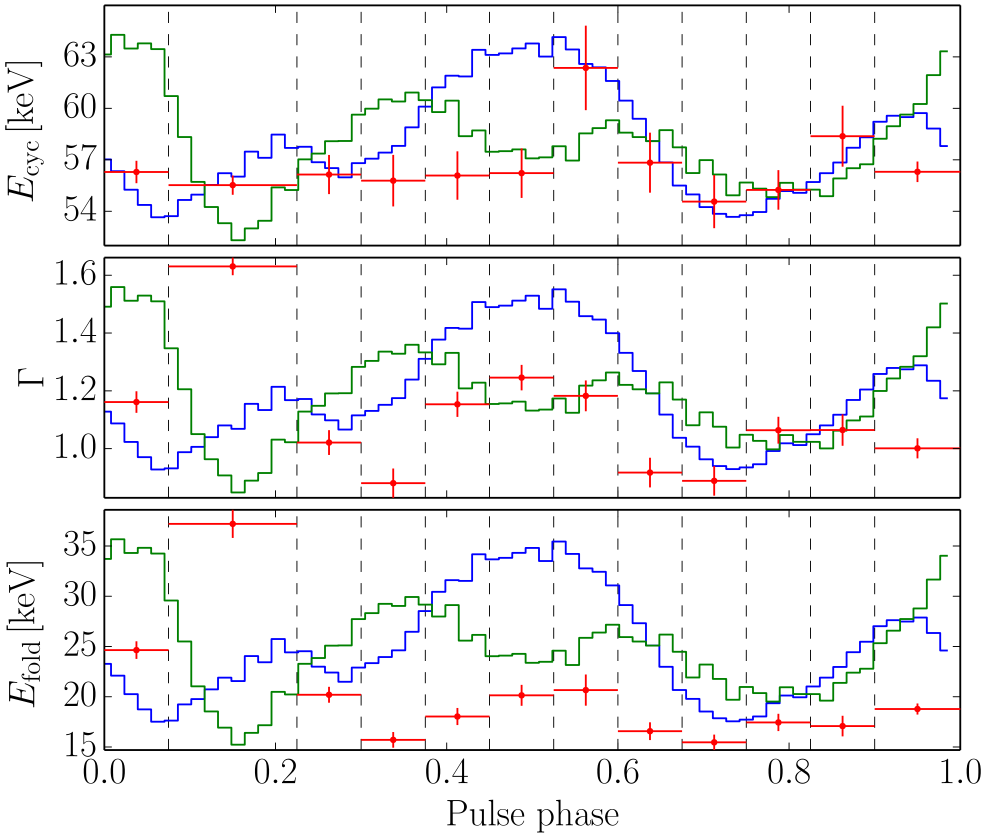

Figure 5.15: Best fit parameters of the phase-resolved spectra using the five stacked INTEGRAL observations. The vertical dashed lines indicate the phase-bins. The solid blue curve is the JEM-X average pulse profile, while the green curve is the ISGRI average pulse profile. The vertical error bars are 1σ uncertainties, while the horizontal bars indicate the phase bin width. Figure from Malacaria et al. (2015).

to the stacking of the spectra with different shapes. This allows, however, to study the flux-averaged dependence of the spectrum on pulse phase with a finer phase binning. X-ray spectra in 12 pulse phase intervals have been extracted after the stacking procedure. The number of phase bins was chosen to ensure adequate statistics in each interval. The width of the bin was kept equal to 0.075, except for two cases where larger bin sizes were used to obtain a meaningful fit.

In the presented analysis, the data of Rev. 1138 have been excluded, since they have much lower photon statistics, and the correspondent pulse profile indicates a clearly different emission pattern (see Fig. 5.5 and Fig. 5.6). The model used for spectral fitting is the same as described in Section 5.5.1.1. It provides a good fit ($\chi^2_{\rm red}$ between 0.9 and 1.2) for all phase bins except three: $0-0.075$, $0.075-0.225$ and $0.675-0.75$. Similar to the $0.0-0.2$ phase-bin spectra of the individual observations, those phase bins require an additional component to get an acceptable χ^2, which can be modeled either by a Gaussian emission line around 35 keV, or by an absorption line around 17 keV (as discussed in Sect. 5.5.2.1). Owing to the presence of this feature in the phase-resolved spectra of individual observations, it is unlikely that the feature is a result of systematic effects. As in the case of individual observations, to ensure a meaningful comparison of the results, the same model has been used for all phase bins, i.e., the model in which the positive residuals around 35 keV are left unmodeled. Furthermore, to compare the stacked phase-resolved results with the pulse profile, average ISGRI and JEM-X pulse profiles have been produced ($18-80$ and $3-20$ keV, respectively), excluding the data from Rev. 1138. The results are shown in Fig. 5.15, where a selection of best-fit parameters from the stacked phase-resolved analysis is shown together with the ISGRI and JEM-X average pulse profiles. As expected, the parameter values shown in this plot present smaller error bars compared to the individual observations. Yet, the E_{cyc} does not show significant variation with pulse phase (except for the phase bin $0.525-0.6$ whose value, however, is consistent with the values at other phase bins within 2σ). On the other hand, the photon index Γ and the folding energy E_{fold} confirm the variation seen in the individual observations, i.e., less than a factor of ~ 2.

5.6 Summary

The main observational results of the *INTEGRAL* analysis of GX 304-1 can be summarized as follows:

- The timing analysis has allowed to extract pulse profiles at different luminosity levels and for different energy bands. A clear pulse period derivative is observed throughout the outburst, while the pulse profiles show a strong energy- and luminosity-dependence. Pulsed fraction is low and independent from luminosity and energy;
- Pulse phase-averaged spectroscopy has confirmed the positive correlation between the cyclotron line energy and the luminosity. The spectral photon index and the folding energy show a negative correlation with the observed luminosity;
- The obtained global timing solution has been used to extract pulse phase-resolved spectra. Phase resolved spectroscopical results seems to indicate that the cyclotron line energy changes only of a small amount as the pulsar rotates;
- Some phase resolved spectra need an additional component with respect to the phase averaged spectral model.

In the chapter 8 these results will be discussed within the context of possible physical scenarios.

6

MAXI OBSERVATIONS OF VELA X-1

6.1 Introduction

Vela X-1 is a very well studied system and is considered as the prototype of the class of wind-fed accreting X-ray binaries. The source has been discovered in 1967 (Chodil et al., 1967), and is located at a distance of ∼2 kpc (Nagase, 1989). It is an eclipsing supergiant HMXB, consisting of a pulsating NS ($P_{\rm spin} \sim 283\,{\rm s}$) with a mass $\rm M_{NS} \sim 1.8\,M_\odot$ (Rawls et al., 2011), and a B0.5Ib supergiant optical companion, HD 77581, with a mass $\rm M_B \sim 23\,M_\odot$ and a radius $\rm R_B \sim 30\,R_\odot$ (van Kerkwijk et al., 1995).

A sketch of the binary system is shown in Fig. 6.1. The NS orbits at a close distance from the companion surface, $0.7\,\rm R_B$ at the apastron, in an almost circular orbit (eccentricity $\rm e \sim 0.089$), with a period of ∼8.9 d (Kreykenbohm et al., 2008). This binary configuration implies that the NS is continuously embedded in the strong stellar wind from the companion, characterized by a substantial mass loss rate of $\dot{M}_{\rm wind} = (1.5-2)\times10^{-6}\,{\rm M_\odot\,yr^{-1}}$ (Watanabe et al., 2006), and a terminal velocity (i.e., the stellar wind velocity at a large distance from the progenitor star) $v_\infty \sim 1100\,{\rm km\,s^{-1}}$ (Prinja, Barlow, and Howarth, 1990). Passing within the NS accretion radius (also called the gravitational capture radius), $r_{\rm acc} = 2GM_{\rm NS}/v_{rel}^2$, this wind is accreted by the compact object, powering the X-ray emission with a luminosity

$$L_{\rm X} = \frac{(GM_{\rm NS})^3\,\dot{M}_{\rm wind}}{R_{\rm NS}\,v_{\rm rel}^4\,D^2} \tag{6.1}$$

where G is the gravitational constant, $R_{\rm NS} \sim 10\,{\rm km}$ is the canonical NS radius, $v_{\rm rel}$ is the relative velocity of the wind and the NS, and D is the distance of the compact object from the center of the companion.

The estimated average X-ray luminosity of $\sim4\times10^{36}$ erg/s is consistent with the wind-fed accreting pulsar scenario described by Eq. (6.1). However, it is typical of Vela X-1 to show "off-states" in which it becomes fainter for several 10^2-10^3 s, as well as "giant flares", when the source flux suddenly increases up to a factor of 20 (Kreykenbohm et al., 2008). The reason for this strong variability is not yet unambiguously established. However, the observation of density inhomogeneities in the matter during accretion episodes (see Martínez-Núñez et al. 2014, and references therein), and the expectations of a highly structured stellar ambient (Runacres and Owocki, 2005), indicate that density variations in the surroundings of the NS are a likely explanation for the observed phenomenon. A different approach (see Shakura, Postnov, and Hjalmarsdotter 2013, and references therein) considers the off-states as the result of an inefficient radiative cooling of the plasma accreted through the NS magnetosphere via Rayleigh-Taylor instability.

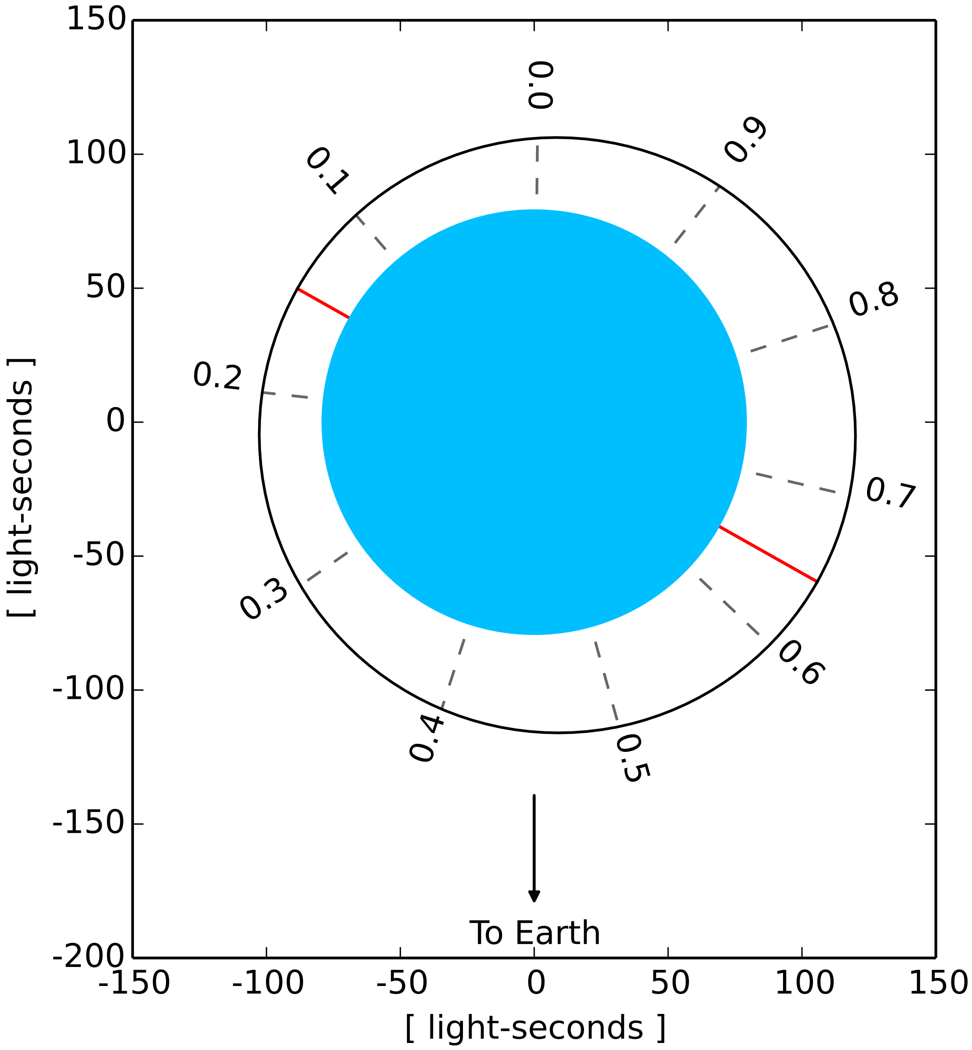

Figure 6.1: Orbital sketch of the binary system Vela X-1 as observed from the Earth. The blue disk centered at $(0, 0)$ is the optical companion HD 77581. The black solid line is the NS elliptical orbit. The grey dashed rays and the respective numbers indicate the orbital phases. The phase-zero is taken at the mid-eclipse time. The red straight solid line crossing the ellipse represents the major axis, intersecting with the NS orbit at the periastron and the apastron. Figure from Malacaria et al. (2016).

Orbital phase-resolved studies of Vela X-1, both observational and theoretical (see Blondin, Stevens, and Kallman 1991, and references therein), provide evidence of a strong systematic modulation of the absorbing column density with orbital phase. This is also observed in other HMXBs (see the seminal case of Cen X–3, Jackson 1975 and, more recently, the study of IGR J17252–3616 by Manousakis, Walter, and Blondin 2012). Such modulation is generally attributed to the NS influence on the stellar wind by various mechanisms (see Sect. 3.3.1.2), which leads to the formation of: (1) a tidal stream, that departs from the almost filled Roche lobe of the companion and trails the NS along its orbit; (2) a Strömgren sphere and a photoionization wake (both following the X-ray pulsar), due to the X-ray photoionization of the companion wind; and (3) an accretion wake that also trails the compact object, resulting

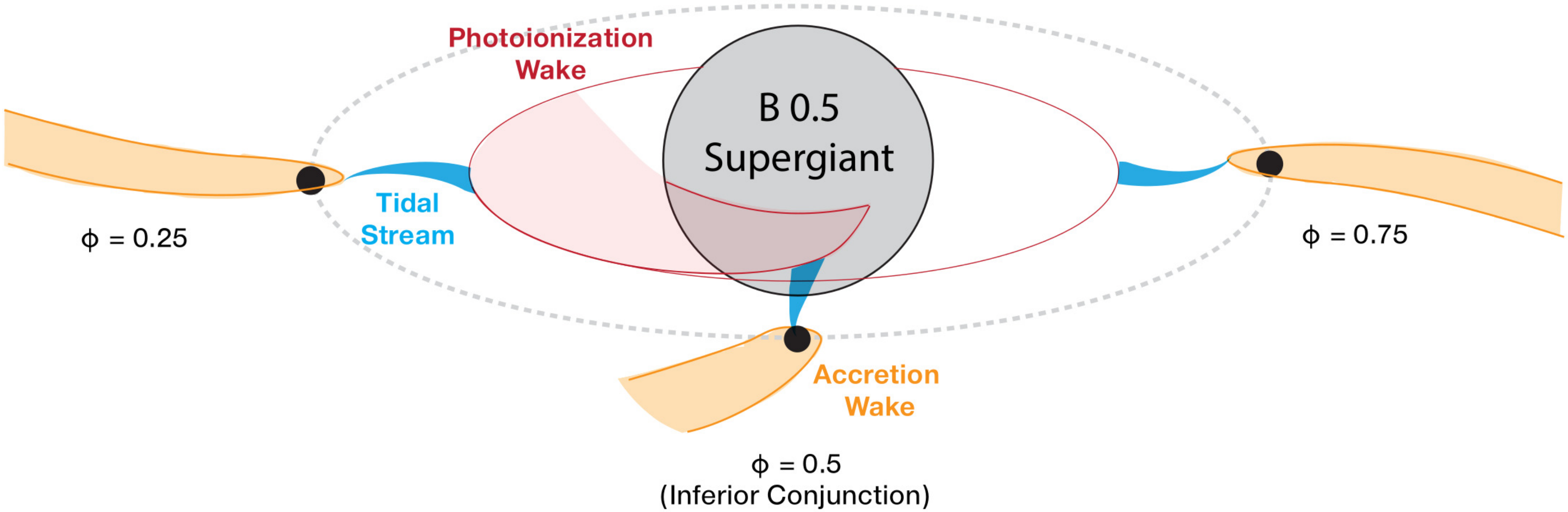
Photoionization
Wake
B 0.5
Supergiant
Tidal
Stream
ϕ = 0.25
ϕ = 0.75
Accretion
Wake
ϕ = 0.5
(Inferior Conjunction)

Figure 6.2: Sketch of the binary system Vela X-1 where both radiative and gravitational effects are illustrated at three different orbital phases. For the sake of clarity, a perfectly circular orbit has been adopted. The photoionization wake is represented as a disk-like structure to show both the cumulative effect along one entire orbit (the red ring), and the more localized effect (the softer-red tail) trailing the NS at the inferior conjunction. A clumpy stellar wind, not shown in the picture, may also be taken into account for a more complete scenario. Figure from Malacaria et al. (2016).

from the focusing of the stellar wind medium by the NS gravitational field. A sketch of the binary system where all these structures are illustrated is shown in Fig. 6.2. Here, all the three structures are illustrated at different orbital phases. Collisions between the undisturbed radiation-driven wind and the stagnant, highly ionized plasma inside the Strömgren sphere will result in strong shocks and create dense sheets of gas. Since this effect derives from the ionizing power of the X-ray radiation, this structure naturally trails the NS. According to this scenario, the observed X-ray spectrum from the compact source undergoes modifications along the binary orbit due to the asymmetric distribution of the formed structures. In particular, the photoionization wake is responsible of high absorption at later ($\phi > 0.5$) orbital phases, when it is found between the X-ray source and the observer.

Previous authors have reported about the X-ray light curve and spectral modulation of Vela X-1 around the inferior conjunction (e.g., Eadie et al. 1975, Watson and Griffiths 1977, Nagase 1989). At the same time, the emission from the optical companion also shows modulation with the orbital phase. An absorption feature is reported by Smith (2001), who observed a dip in the UV light curve of Vela X-1 around the transit phase ($0.46 < \phi < 0.70$ in their work, where $\phi = 0$ is the mid-eclipse). Moreover, Goldstein, Huenemoerder, and Blank (2004), analyzing spectroscopic *Chandra* data taken at three different phases (i.e., eclipse $\phi = 0$, $\phi = 0.25$ and $\phi = 0.5$), found an absorbed "eclipse-like" spectrum at $\phi = 0.5$ in the $1 - 10$ keV X-ray energy range. Similarly, Watanabe et al. (2006) found an extended structure of dense material which partially covers the NS, and that is between the X-ray emitter and the observer at the inferior conjunction. More recently, Naik et al. (2009) analyzed orbital phase-resolved spectra of Vela X-1 observed with *RXTE*, finding large variation of the absorbing column density along the orbital phase (up to 10^{24} atoms per cm^2 around the eclipse phases), but their observations do not cover the whole orbit, i.e., their data do not include observations between the inferior conjunction and the apastron. Doroshenko et al. (2013) have shown that the observed increasing absorption at late orbital phase does not agree with expectations for a smooth spherically symmetric wind. Finally, Sidoli et al. (2015) found that the Vela X-1 off-states are more likely to happen at the pre-egress orbital phases, suggesting that they are due to the scattering of the X-rays induced by the photoionization wake.

6.2 Motivation

This chapter is dedicated to the spectroscopical and timing analysis of Vela X-1 observed with *MAXI*. The orbital profiles have been analysed in different energy ranges, with the aim of exploring systematic orbital variations. Particular effort has been put to investigate the effects of the accretion wake at the inferior conjunction, where its influence on the observed X-rays from the compact object is more prominent. Orbital phase-resolved spectroscopy has also been performed in order to investigate the ambient wind in which the NS is embedded. In fact, the surroundings of the X-ray pulsar strongly affect the observational features of the emitted X-ray spectra at different orbital phases.

Table 6.1: Observation time and ephemeris used for light curves folding.

Parameter	Value
ΔT_{Obs} [MJD][a]	55133 – 56674
P [d]	8.964357 ± 0.000029
$T_{Mid-Eclipse}$ [MJD][b]	55134.63704

[a] Time span of the *MAXI* observations used in this work;
[b] Taken as the phase-zero.

6.3 MAXI/GSC archival data

The Vela X-1 data analyzed in this work consist of archival data collected with *MAXI*/GSC for more than 4 years, from 55133 to 56674 MJD (see Table 6.1).

In general, every sky source is observed by *MAXI* at each ISS revolution (∼ 90 min), for an average exposure time of ∼ 50 s (see Sect. 4.2). Therefore, *MAXI* represents an excellent opportunity to study Vela X-1 at different orbital phases and with a fair statistics achieved by the stacking of multiple scans.

Our data have been corrected to account for the time-dependent effective area of the GSC cameras. All extracted spectra have been rebinned in order to contain at least 200 photons per energy bin. Following the *MAXI* team recommendation, we added a systematic error at a level of 1% to the final count rates of the extracted spectra.

6.4 Analysis of the orbital profiles

Inspecting the Vela X-1 light curve at different energy bands reveals a rich variety of timing phenomena. For illustration, the (almost) mission-long *MAXI*/GSC light curve of Vela X-1 is shown in Appendix A (the light curve of each *MAXI*/GSC detected source is provided by the *MAXI* team[1] and can be easily explored by the reader). However, the main focus of this work is to study the orbital behavior of the source. To this aim, *MAXI*/GSC light curves of Vela X-1 have been extracted with a time resolution of 6 h in 2 energy bands, 4 – 10 and 10 – 20 keV. Then, the light curves have been folded with the orbital period to produce average orbital profiles in the two chosen energy bands, using the orbital ephemeris from Kreykenbohm et al. (2008), reported in Table 6.1. The phase zero is taken at the mid-eclipse time (see Fig. 6.1). The resulting average orbital light curves are shown in Fig. 6.3, where the strongest changes are observed in the softer band. This is explained by the strong absorption column modulation along the binary orbit (see Sec. 6.1).

Subsequently, the difference between the light curves of individual orbital cycles (referred to as the *members* of the sample) and the average orbital profile (defined as the *template*) has

---

[1] `http://maxi.riken.jp/top/index.php?cid=000000000001&disp_mode=source`

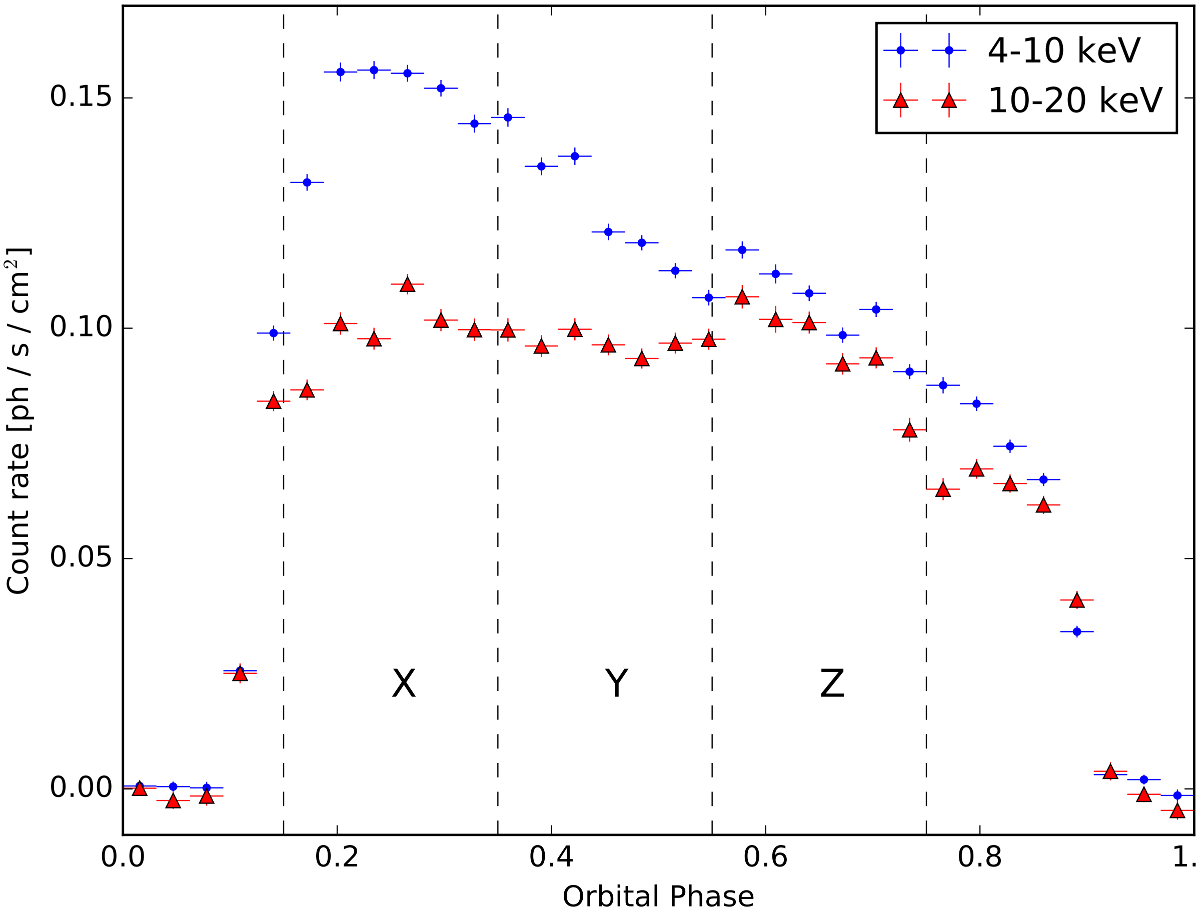

Figure 6.3: The folded orbital light curves of Vela X-1 in the $4-10$ (blue dots), and $10-20$ keV (red triangles) energy ranges. The horizontal bars indicate the phase-bin. The mid-eclipse time is taken as the phase zero. The three orbital phase bins (X, Y, and Z) used for the phase-resolved spectroscopy of the double-peaked sample are indicated (see text). Figure from Malacaria et al. (2016).

been considered, and calculated according to the following procedure. First, a smooth and continuous template in both energy bands has been obtained by interpolating with a cubic spline function between all the pairs of consecutive data points (the *knots*) of the average orbital profiles. In this way, a continuous function is derived, which allows to determine its value at any orbital phase (without limitations imposed by the chosen binning).

Second, a number of orbital phase bins have been defined in order to characterize the various effects at play in Vela X-1. From the observer's point of view, the accretion wake effects are more prominent for about 0.2 in orbital phase (i.e., about 1.5 days) around the inferior conjunction (i.e., $\phi \sim 0.45$, see Fig. 6.1). To properly sample these effects, three orbital phase bins have been defined, namely X, Y, Z, corresponding to phase intervals $0.15 - 0.35$, $0.35 - 0.55$, and $0.55 - 0.75$, respectively (see Fig. 6.3).

For the comparison between the template and each member, a minimum number of four data points in each of the X, Y and Z phase bins has been imposed, in order to ensure enough statistics for a meaningful analysis. This selection leaves a total of 84 suitable cycles, which thereafter will represent the analysed sample. Therefore, for these 84 cycles it is possible to

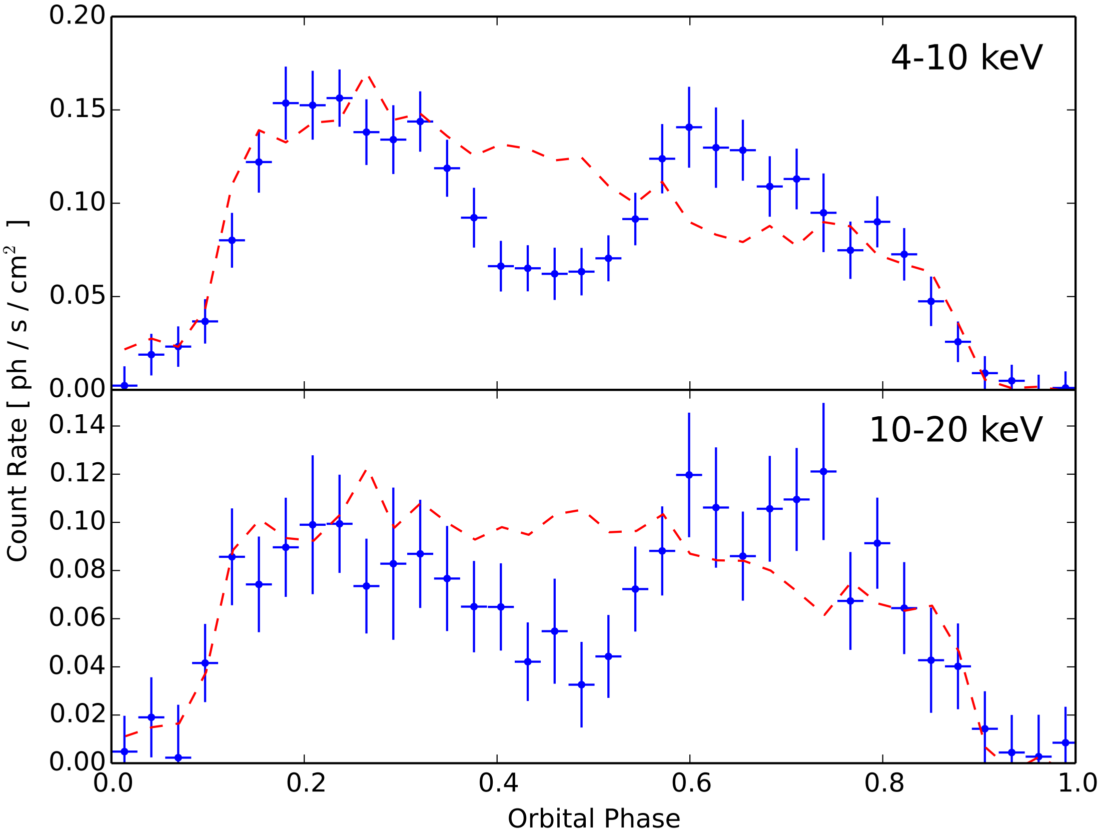

Figure 6.4: Average orbital profiles of the double-peaked (blue dots) and of the standard samples (red dashed lines) in $4-10\,\mathrm{keV}$ (top) and $10-20\,\mathrm{keV}$ (bottom). The vertical error bars correspond to the standard deviation of the average of the count rates in each phase bin, while the horizontal bars indicate the phase-bin width. The red dashed lines represent the functions interpolated between the data points of the standard sample, in each energy band. Figure from Malacaria et al. (2016).

perform a systematic analysis of those members which differ from the template in each of the three defined phase bins.

For the systematic comparison of the members' profile against the template, only the relative shape has been considered, avoiding any bias from flux variation. For this reason, each member has been divided with a normalization factor equal to the ratio of the average count rate between phase $0.10-0.85$ and the template average count rate in the same phase interval.

Finally, the difference between the count rates of the template and the normalized count rates of each member has been calculated (the latter subtracted to the former) in the X, Y, and Z phase bins. To evaluate the members count rate in each phase bin, the median of the data points has been used, because it is less affected by the instrinsic count rate fluctuations than the mean. For the template, the value of the continuous function at the correspondent phase has been used. The obtained count rate difference is referred to as the *residuals* with respect to the template.

Such a definition of the residuals allows to investigate the variation of members with respect to the template at each of the three defined orbital phase bins. In particular, residuals can be used to investigate the effects of the accretion wake at the inferior conjunction (see Sect. 6.1). To this aim, a new analysis has been performed, in order to stack only those members with high negative residuals in the Y phase bins and, at the same time, low residuals in the X and Z phase bins. High negative residuals have been defined as residuals with (negative) values lower than 30% of the template's median, while low residuals have absolute values less than 30%.

The stacking procedure allowed to obtain a new average orbital profile, in the $4-10\,\mathrm{keV}$ energy band, made of 12 out of 84 total orbital cycles (i.e., about 15% of the analyzed sample). These members represent what will hereafter be referred to as the *double-peaked sample*, and their profiles are characterized by a double-peaked morphology, with a flux drop around the inferior conjunction (i.e., around $\phi \sim 0.45$). Another independent sample has been extracted out of the 84 cycles, stacking all the orbital profiles except the double-peaked members in the same energy band. This sample will be referred to as the *standard sample*. Both samples are shown in Fig. 6.4 (top).

Since the adopted normalization procedure could remove flux-dependent features, one question that arises is whether there is a given luminosity dependence behind the observation of double-peaked profiles. However, this has been carefully checked, resulting that, before normalization, the double-peaked profiles are not associated with any specific luminosity level. Also, for all of these 12 selected profiles, the null hypothesis that these profiles represent a statistical fluctuation of the template has been tested with normality tests (χ^2, Kolmogorov-Smirnov, Shapiro-Wilk), and rejected at a significance level higher than 3σ. Furthermore, they all show a median value in the Y phase-bin that deviates at least 3σ from the template value at the same orbital phase. The latter result is a direct consequence of the criteria used to select the double-peaked profiles, and does not represent itself the significance of the their statistical independency. However, it is worthy to note that the median represents the count rate behavior in a wide phase bin (about 30% of the out-of-eclipse orbit). Thus, the 3σ deviation indicates that the dip in the Y phase bin of the double-peaked profiles is likely not the result of a pure fluctuation. To demonstrate that the double-peaked sample is not the result of statistical fluctuations, an in-depth analysis has been carried out in Sect. 6.4.1.

The same selection procedure as for the double-peaked sample in the $4-10\,\mathrm{keV}$ has been performed in the $10-20\,\mathrm{keV}$ energy band as well. In this case, the selected profiles are 11 out of 84. The overall profile shape is very similar to the profile obtained in the $4-10\,\mathrm{keV}$ energy band, with a double-peaked morphology and a dip around the inferior conjunction. Both the double-peaked and the standard sample in the $10-20\,\mathrm{keV}$ energy band are shown in Fig. 6.4 (bottom).

6.4.1 Statistical and physical significance of the double-peaked sample

To assess the significance of the double-peaked sample, both on a statistical and on a physical level, many tests have been performed. In the following, the different tests on the double peaked-sample will be discussed separately for the statistical and physical significance.

6.4.1.1 Statistical significance of the double-peaked sample

To assess whether the double-peaked sample is just the result of statistical fluctuations or, on the contrary, if it represents an intrinsically different sample with respect to the template, the following statistical tests have been performed:

- Simulations of synthetic profiles;
- Analysis of statistics distributions;
- Extraction of complementary orbital profiles.

  Simulations of synthetic profiles. To assess the statistical relevance of the double-peaked sample, synthetic profiles have been generated in order to investigate the probability to obtain a double-peaked sample as a result of pure fluctuations (i.e. *by chance*). In the following, the selection of a synthetic double-peaked profile has to meet the same criteria exposed in Sect. 6.4 (i.e. high negative residuals in the Y phase bin and, at the same time, low - absolute - residuals in the X and Z phase bins). First, synthetic profiles have been produced by allowing purely Poissonian fluctuations around the data points of the template profile. Over 10^7 synthetic profiles, not even one met the double-peaked criteria. This led to a probability of obtaining a single double-peaked profile of less than 10^{-7}. However, Vela X-1 variability is clearly not purely Poissonian (see light curve in Appendix A), since it reflects accretion dynamics variability. Modeling accretion dynamics variability is not an easy task, and the mechanisms behind have not completely understood up to now. Therefore, the law that regulates the variability around the template at each data point has to be inferred by other means. One possible way, is to calculate the standard deviation of count rates at each orbital phase, and using this value as the width of a Gaussian distribution that describes the fluctuations around the template. This, of course, results in an overestimation of the "amplitude" of possible fluctuations, since the standard deviation calculated in such a way is mixing together a number of effects, like flares, off-states and outliers in general. Nonetheless, this can furnish an upper limit of the probability to get a double-peaked sample considering the effects of accretion dynamics variability. The standard deviation σ has been calculated as

$$\sigma = \sqrt{\frac{1}{N-1}\sum_{i=1}^{N}(y_i - \overline{y})^2} \tag{6.2}$$

  where y_i are the data points, $\overline{y}$ is the average value at a given time (or phase bin), and N is the sample size. The distribution of standard deviations as a function of the orbital phase is shown in Fig. 6.5. It clearly follows the overall shape of the template (see Fig. 6.3). By using these values as widths of Gaussian distributions at each orbital phase of the template, 10^7 simulated orbital profiles have been obtained. Of these, only about 5% meet the double-peaked criteria. As already mentioned, this is an overestimation of the double-peaked profiles obtainable by chance, and in any case it represents only one third of the double-peaked sample obtained by actual data. This can be interpreted as a further proof that the double-peaked sample extracted from actual data can not simply be the result of statistical fluctuations.

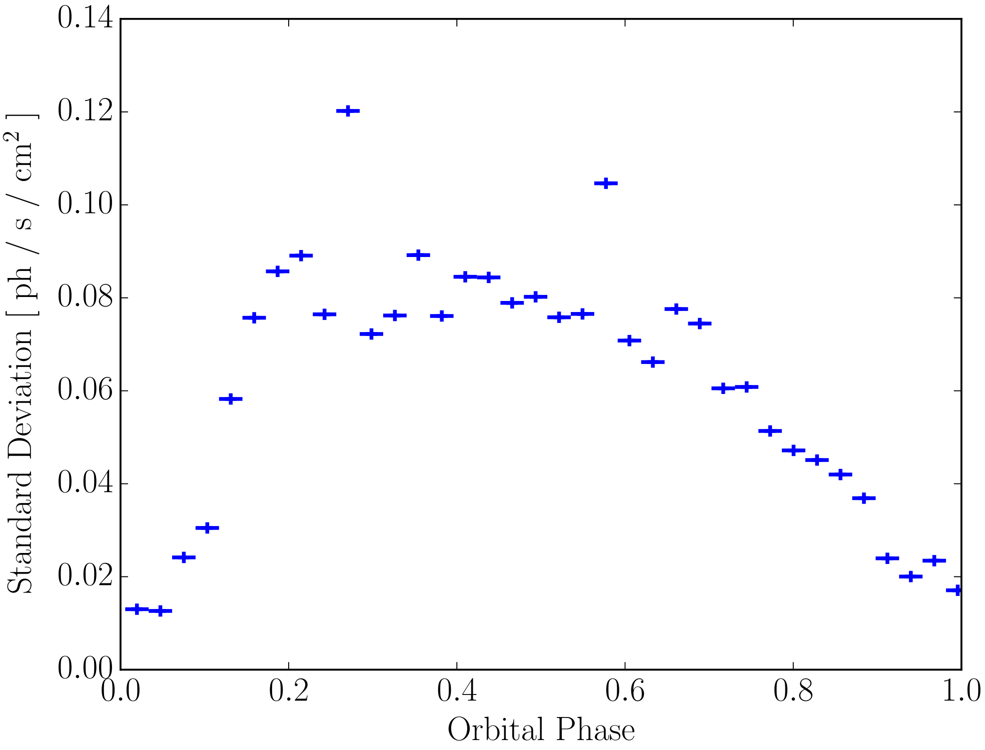

Figure 6.5: Distribution of the standard deviations at each orbital phase. Horizontal bars mark the phase-bin size.

Analysis of statistics distributions. Another test performed to assess the statistical relevance of the double-peaked sample, is the analysis of frequency distributions of the statistics used to calculate the sample: the median. Histograms of median distributions in the X, Y and Z phase bins have been produced, and these distributions have been analysed by means of statistical tools. Within this context, the most significant result is represented by the skewness of those distributions. The skewness is a measure of the asymmetry of the distribution around its mean value. The traditional Fisher-Pearson coefficient of skewness is defined as (Joanes and Gill, 1998):

$$S = \frac{\sum_{i=1}^{N}(y_i - \overline{y})^3/N}{\sigma^3} \tag{6.3}$$

The distributions of medians in the X, Y and Z phase bins and their relative skewness is shown in Fig. 6.6. Here, all distributions show a positive value of the skewness. A positive skewness means that the distribution is right-tailed, with respect to a symmetric, bell-shaped, normal distribution. Fig. 6.6 also shows that $S_Y > S_Z > S_X$, where S_Y, S_Z and S_X are the skewness coefficients calculated for the distributions in the Y, Z, and X phase bins, respectively. A right-tailed distribution is characterized by a peak of the distribution (the *mode*) that veers towards left, that is towards lower values of the count rates. In other words, for positive skewness values, there is more weight in the left tail of the distribution. Fig. 6.6 shows that the medians distribution in the Y phase bin is the one whose weight tends to lower count rates than in other phase bins, while the right tail is composed by median values that are far from the distribution peak.

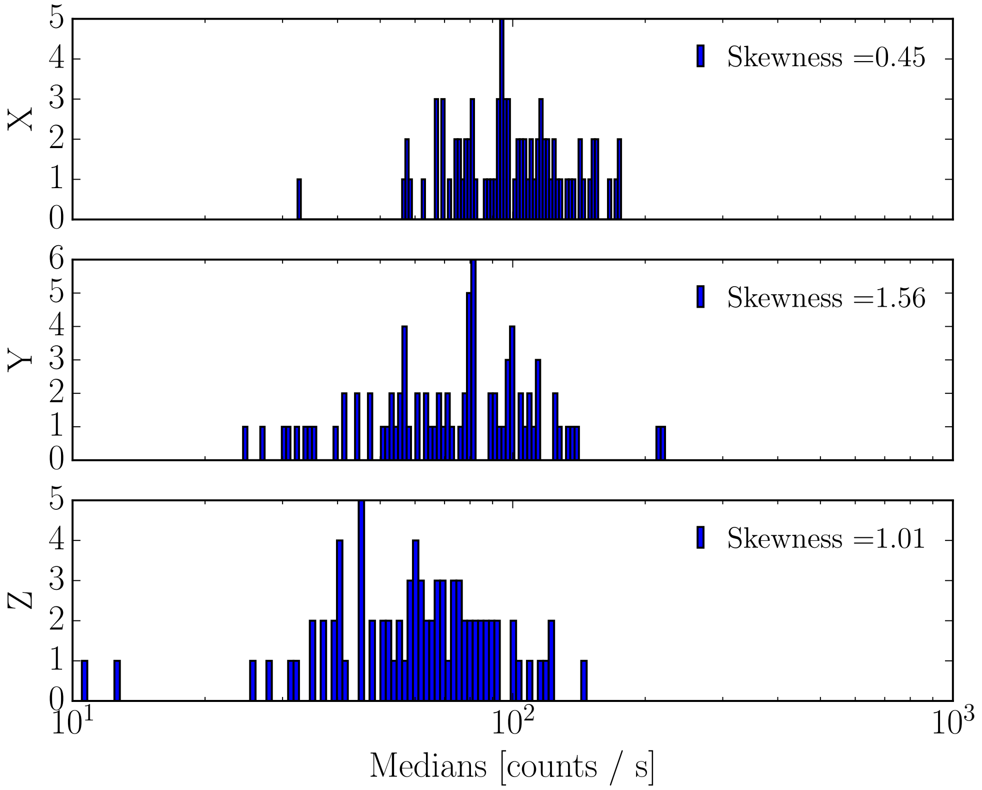

Figure 6.6: Distributions of the medians and relative skewness in the X, Y and Z phase bins. The skewness in the Y phase bin is larger than in the other phase bins, thus indicating that the bulk of median values in Y tends toward lower count rates.

This can be interpreted as if the bulk of the medians in the Y phase bin is more shifted towards lower count rates than in the X and Z phase bins. As a consequence, the Y phase bin is more keen than X and Z to represent lower count rates, and therefore double-peaked profiles are more frequent than profiles with a flux in dip in the X or Z phase bins.

Extraction of complementary orbital profiles. A third test performed to check the statistical significance of the double-peaked sample, is the extraction of orbital profiles samples according to criteria complementary to those applied to obtain the double-peaked sample. While double-peaked profiles have been extracted by applying the criteria of high negative residuals in the Y phase bin and low (absolute) residuals in the X and Z phase bins, different profiles have been extracted (and then stacked together) for any possible configuration of high (low) residuals in one given phase bin, and low (high) residuals (respectively) in the other two. For example, a sample of profiles "complementary" to the double-peaked ones has been extracted by selecting profiles with high positive residuals in the Y phase bin and low (absolute) residuals in the X and Z phase bins (a "mexican hat" shape). Another example of extracted sample, is that composed of orbital profiles with high negative residuals in the X phase bin and low (absolute) residuals in the Y and Z phase bins. In the same fashion, all possible configurations of selection criteria using the residuals have been applied. This allows to check whether such selected samples show features or an occurrence rate

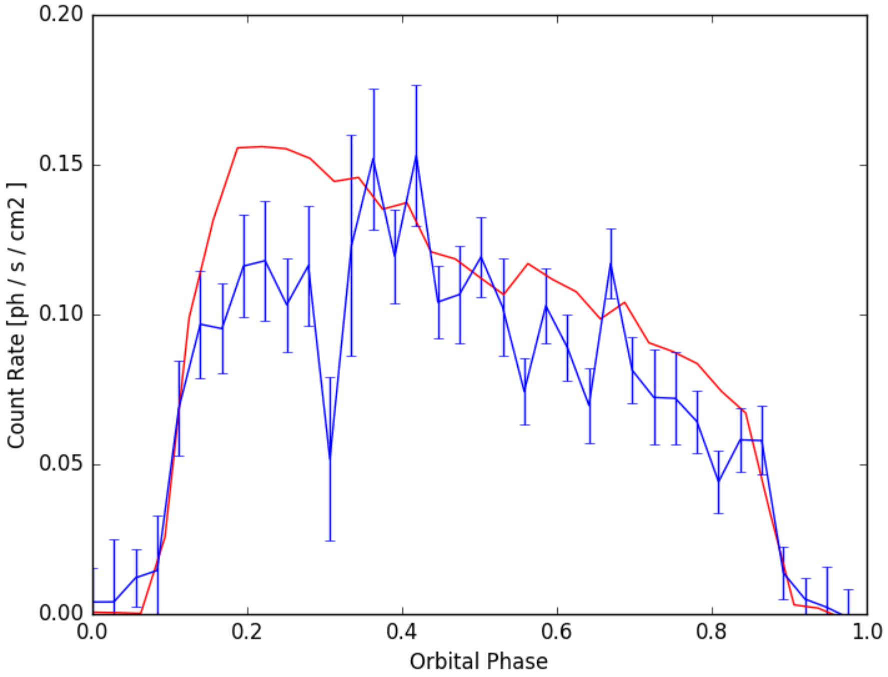

Figure 6.7: Orbital profile obtained by stacking members with high negative residuals in the X phase bins, and low (absolute) residuals in the Y and Z phase bins (blue data). The vertical error bars correspond to the standard deviation of the average of the count rates in each phase bin. The red continuous line represents the template. This sample represents the 5% of the entire analyzed sample and its feature in the X phase bin shows a scattering behaviour.

similar to that of the double-peaked sample (i.e. a smooth and long flux modulation and an occurrence of about 15%, respectively). The results of such a process show that the samples obtained by applying selection criteria based on the residuals in all possible configurations represent only a minor fraction of the total population ($3-5\%$). Furthermore, such samples are unable to reproduce smooth and clear features, rather showing a more scattered behaviour in the phase bin where the selection criteria to meet is that of high residuals. For example, Fig. 6.7 shows the orbital profile resulting by the stacking procedure of those members that show high negative residuals in the X phase bin, and low (absolute) residuals in the Y and Z phase bins. This plot shows that the feature in the X phase bin is not as clear as the dip in the double-peaked sample, and that this profile represents only the 5% of the entire analysed sample. Therefore, the criteria used to select double-peaked profiles is able to efficiently extract a significant sample with a well defined feature and, at the same time, to reject a significant amount of spurious detections.

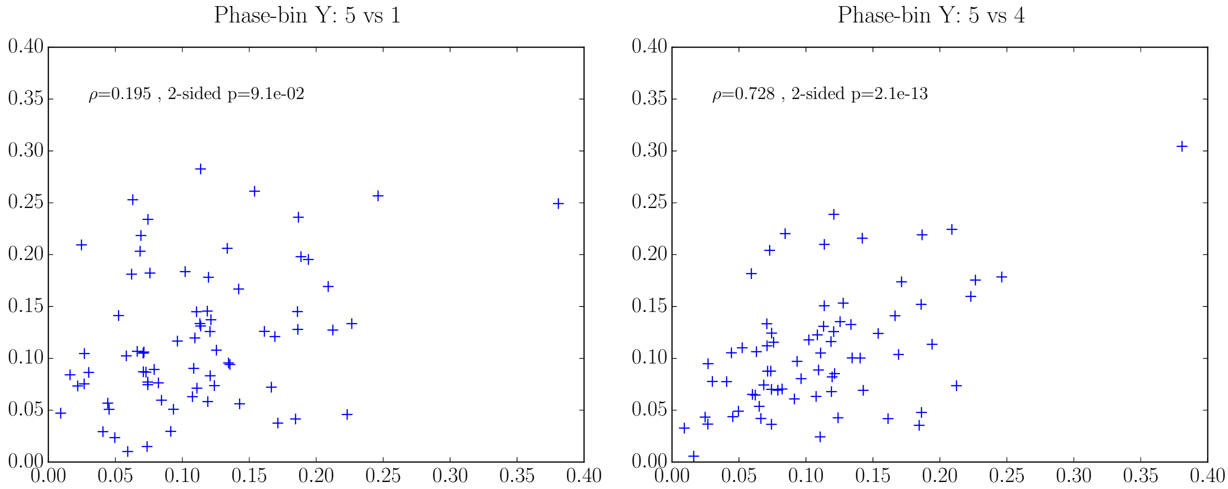

Figure 6.8: Scatter plots for data points in the Y phase bin. The title on top of each plot describes to which data points the plot refers to. Also reported in each plot are the Pearson's correlation coefficient ρ and the 2-sided probability that the correlation is obtained by chance. *Left*: Scatter plot for data points separated by 4 bins ($\Delta\phi \sim 24$ hours). The fifth data point of the Y phase bin is reported on the x-axis, while the first - on the y-axis. *Right*: Scatter plot for adjacent data points ($\Delta\phi \sim 6$ hours). The fifth data point of the Y phase bin is reported on the x-axis, while the fourth - on the y-axis. The Pearson's correlation coefficient ρ between data points in each plot increases as the time separation between considered data points becomes shorter.

6.4.1.2 Physical significance of the double-peaked sample

Analogously to the last section, a number of tests have been performed to assess the significance of the double-peaked sample on the basis of its physical relevance. To this aim, a characterization of the accretion dynamics variability has been carried out, based on the observational properties of Vela X-1.

The first goal of this process was to characterize the typical timescale of X-ray variability. For this, scatter plots have been produced to compare the coherence in the count rates of orbital profiles at different timescales. Such scatter plots are constructed by reporting, on one axis, the count rates of a certain data point in one of the three X, Y or Z phase bins, while on the other axis the count rates of previous (yet fixed for each plot) data points. This process has been done for all the 84 statystically significant members, each of which represents one point in the scatter plots. Two examples of scatter plots are reported in Fig. 6.8. These plots clearly show how the scattering among the data points changes when different time separations are considered. More specifically, the Pearson's correlation coefficient ρ between the data points in each plot increases as the time separation between considered data points becomes shorter. In fact, the correlation tends to become significant ($\rho \gtrsim 0.6$) for adjacent data points. This furnishes an estimation of the *coherence time*, that is the timescale at which the source flux tends to stay coherent, as opposite to randomly scatter due to accretion dynamics variability. Thus, the coherence time results to be of the order of the time separation between two

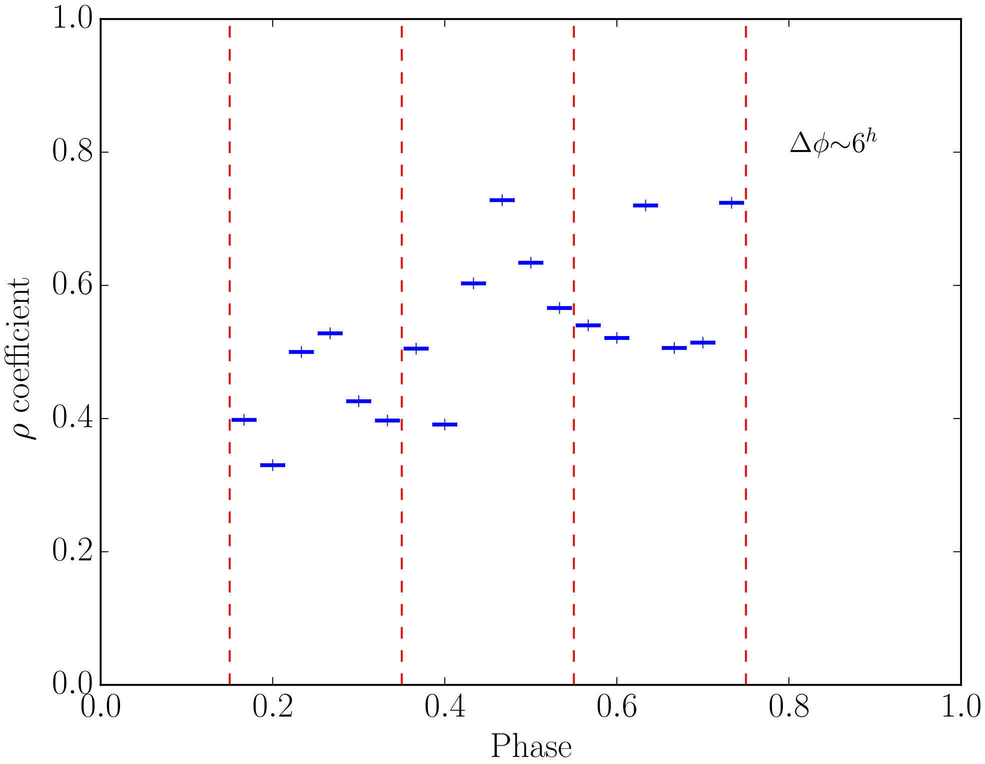

Figure 6.9: Correlation coefficient ρ calculated for a time separation of $\sim$ 6 hours between data points as a function of the orbital phase.

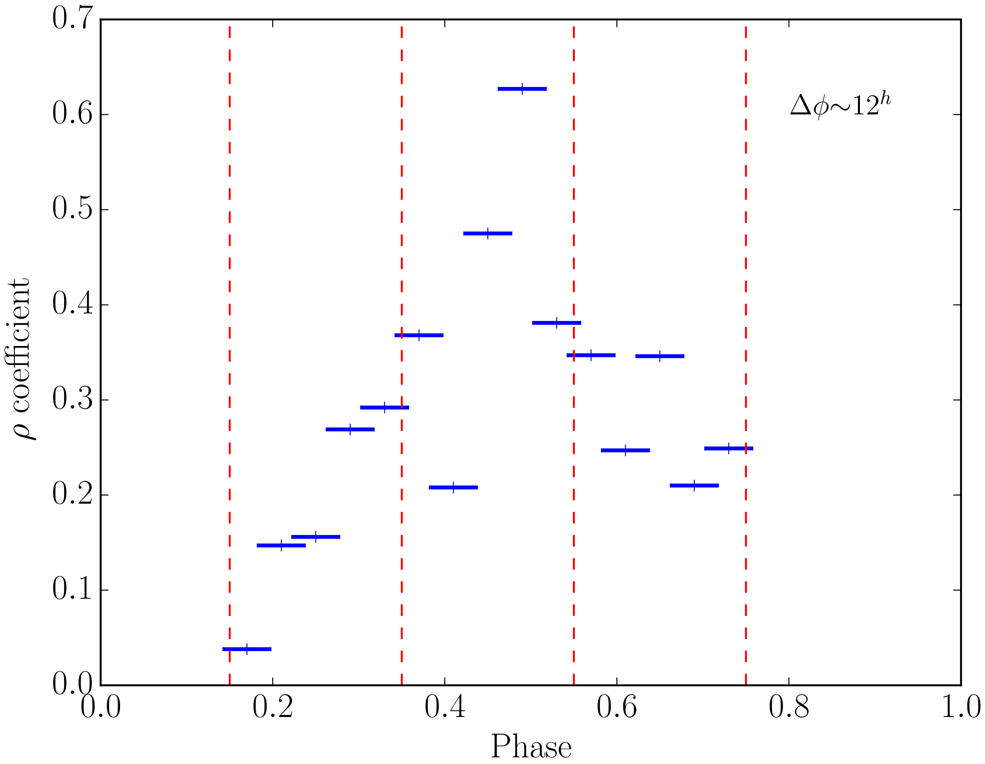

Figure 6.10: Correlation coefficient ρ calculated for a time separation of $\sim$ 12 hours between data points as a function of the orbital phase.

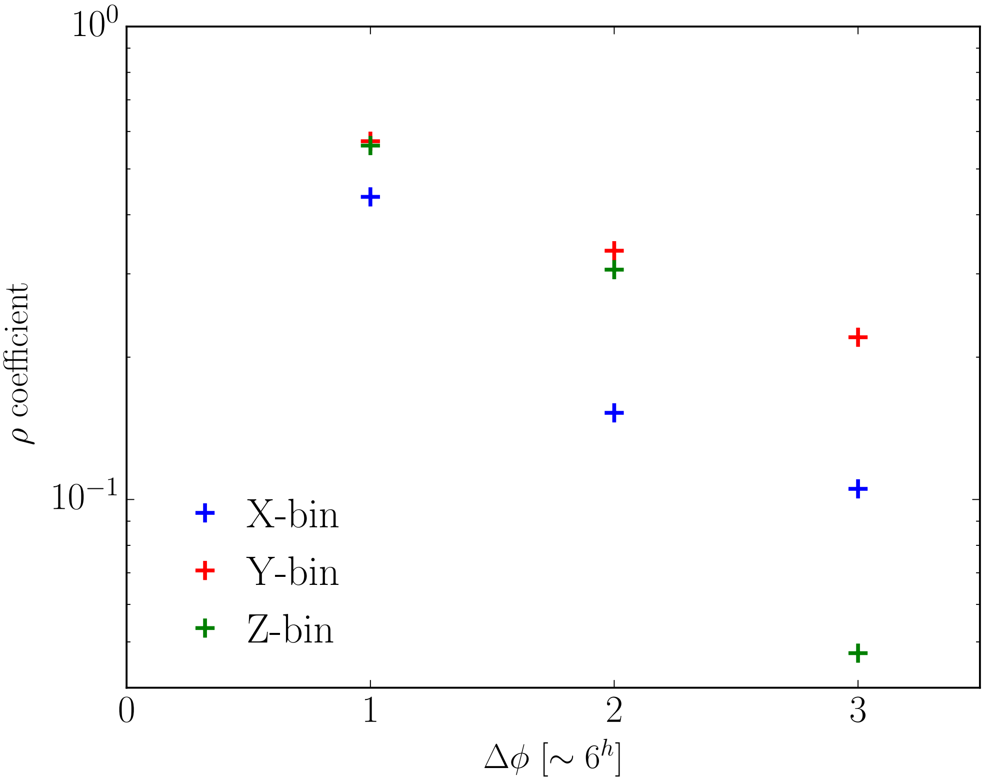

Figure 6.11: Average correlation coefficient ρ as a function of the time separation between the data points for which the average ρ has been calculated. The three phase bins X, Y and Z are illustrated separately for clarity. The x-axis reports the time separation between the data points for which the coefficient ρ has been calculated, in units of 6 hours. The correlation in the Y phase bin is always higher than in the other two.

adjacent data points, or shorter, i.e. $\sim$ 6 hours.

For comparison, the ρ coefficient calculated for scatter plots made by adjacent data points is shown in Fig. 6.9 as a function of the orbital phase. These results indicate that accretion dynamics variability can only account for short-time variability, of the order of $\sim$ 6 hours, and can not justify a flux dip like that observed in the double-peaked sample, that lasts for about 1.5 days.

Furthermore, a plot similiar to that in Fig. 6.9 has been produced by considering data points separated by two bins instead of one, i.e. a time separation of $\sim$ 12 hours instead of $\sim$ 6 hours. This plot is shown in Fig. 6.10. Here it is clear how the correlation coefficient ρ as a function of the orbital phase tends to have a local peak around the inferior conjunction, while the correlation disappears at earlier and later phases. This supports the physical significance of the double-peaked sample, since a longer coherence time appears only at the inferior conjunction, where the characteristic dip of the double-peaked sample is found. Such extention of the coherence time is therefore most likely due to a local physical contribution from the accretion wake.

Finally, a third plot has been produced where the average correlation coefficient ρ is reported as a function of the time separation between the data points for which the average ρ has been calculated. This plot is shown in Fig. 6.11, where the ρ coefficients

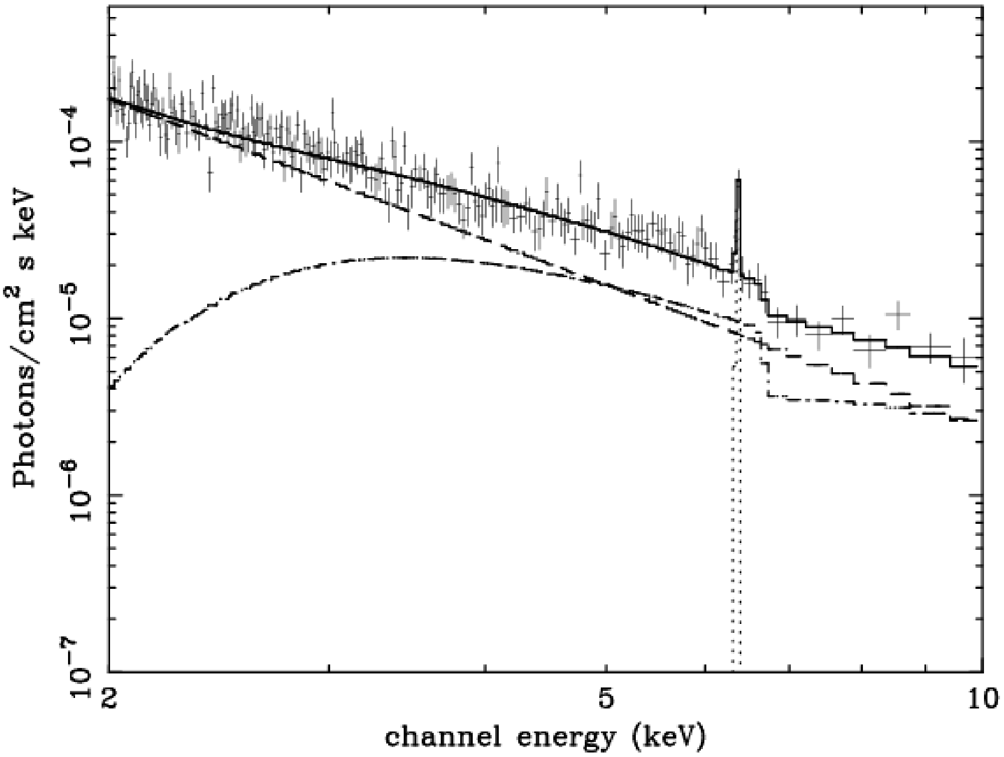

Figure 6.12: Illustration of partial covering absorption model. The resulting spectrum (solid line) is the combination of both an absorbed power-law (with less flux at low energies) and an unabsorbed power-law. Figure from Longinotti et al. (2003).

for the three phase bins X, Y and Z are illustrated separately for clarity. Here it is clear that the correlation coefficient in the Y phase bin is always higher than in the other two. This supports the interpretation given of Fig. 6.10, that is an additional physical effect that increases the coherence time only at the inferior conjunction and that can physically justify the long duration of the dip in the double-peaked sample.

6.5 Orbital-phase averaged spectral analysis

The orbital phase-averaged spectral analysis of Vela X-1 has been performed separately for the two samples defined in Sect. 6.4. Due to the complexity of the physical problem, a fully physically justified model of the X-ray production mechanism in accreting X-ray pulsars has not been numerically implemented so far. Therefore, a phenomenological model has to be used. Following the common phenomenological model used in literature for accreting pulsars in general, and Vela X-1 in particular (see, e.g., Schanne et al. 2007), a cutoff power-law model has been adopted (*cutoffpl* in XSPEC, see Eq. (5.3)), to which a blackbody component has been added to account for the soft excess (see Hickox, Narayan, and Kallman 2004 and references therein). The resulting model is indicated as *bbody*cutoffpl* in the XSPEC terminology. On the other hand, to account for the expected inhomogeneous structure of the ambient wind in Vela X-1, also a partial covering absorption model has been tested (*pcfabs*powerlaw* in XSPEC).

The partial covering multiplicative component is defined as

$$M(E) = f \times \exp[-N_{\mathrm{H}}^{pc}\sigma(E)] + (1-f) \tag{6.4}$$

where $0 < f < 1$ is the covering fraction, $\sigma(E)$ is the photo-electric cross-section (not including Thomson scattering), and $\mathrm{N}_{\mathrm{H}}^{pc}$ is the *local* neutral hydrogen column density (in units of $10^{22}\,\mathrm{cm}^{-2}$). By definition, the local absorbing component $\mathrm{N}_{\mathrm{H}}^{pc}$ affects only a fraction f of the original spectrum, leaving the other part unabsorbed. An illustrative example of partial covering model is shown in Fig. 6.12. This model resulted succesfull to fit *NuStar* data of Vela X-1 (Fürst et al., 2014). In this context, i.e., when the X-ray source is a point source, the partial covering model represents the temporal variation of the absorption column density. A partially covered source is therefore a source whose spectrum is absorbed by different column densities at different times.

To both models, photoelectric absorption by neutral matter N_{H} (Morrison and McCammon, 1983) has been included (the *wabs* component in XSPEC, see Eq. (5.6)), to account for the absorption column densitiy along the entire line of sight. Solar abundances by Anders and Grevesse (1989) have been assumed to derive N_{H}. Using the metal abundances reported in Kaper, Hammerschlag-Hensberge, and van Loon (1993) for HD 77581 (i.e., sub-solar C, and super-solar N, Al) does not affect the obtained results, which are well consistent within 1σ. The results from the second procedure, only show a tendency for the N_{H} toward slightly higher values. Therefore, solar abundances throughout the rest of the analysis have been kept. Also, two iron Gaussian line components (Odaka et al., 2013), Kα and Kβ at 6.4 and 7.08 keV respectively, have been added. The same components have been included in the models used for the orbital phase-resolved spectroscopy (see Sec. 6.6). The results of the fits are given in Table 6.2. Both models return acceptable fits for both the standard and the double-peaked sample. However, for the standard sample, the partial covering model describes the data not as well as the cutoff power-law model.

6.6 Phase-resolved spectral analysis

6.6.1 Orbital phase-resolved spectroscopy of the double-peaked sample

To investigate the nature of the dip in the double-peaked sample, X-ray spectra of Vela X-1 in the X, Y and Z orbital phase bins have been extracted. For this, *MAXI*/GSC data have been filtered with GTIs corresponding to the three phase bins in the double-peaked profiles (see Section 6.4). Based on the results from Section 6.5, the same spectral models applied in the phase-averaged case have been used to fit the orbital phase-resolved spectra, namely: (a) a cutoff power-law model plus a blackbody component

Table 6.2: Best-fit spectral parameters of the orbital phase-averaged spectra from both the double-peaked and the standard samples. The errors correspond to the 1σ c.l.

Model	**Cutoff PL + BB**		**Part. Cov.**	
Sample	Double-peaked	Standard	Double-peaked	Standard
$N_H/10^{22}\,\mathrm{cm}^{-2}$	$3.91^{+0.43}_{-0.36}$	$4.29^{+0.31}_{-0.30}$	$2.55^{+2.18}_{-2.55}$	$2.02^{+0.68}_{-0.79}$
$N_H^{pc}/10^{22}\,\mathrm{cm}^{-2}$	–	–	$14.9^{+16.0}_{-5.4}$	$12.7^{+2.5}_{-1.7}$
Cov. Fract.^{pc}	–	–	$0.63^{+0.21}_{-0.18}$	$0.64^{+0.07}_{-0.06}$
Γ	$0.27^{+0.04}_{-0.03}$	$0.48^{+0.06}_{-0.06}$	$1.09^{+0.10}_{-0.07}$	$1.13^{+0.03}_{-0.03}$
E_{cut} [keV]	$15.3^{+0.4}_{-3.4}$	$20.1^{+2.5}_{-2.0}$	–	–
kT_{BB} [keV]	$0.16^{+0.04}_{-0.04}$	$0.14^{+0.06}_{-0.08}$	–	–
$\chi^2/\text{D.o.F.} = \chi^2_{\text{red}}$	$285/311 = 0.92$	$393/351 = 1.12$	$318/311 = 1.02$	$480/352 = 1.36$

^{pc} Partial Covering Model.

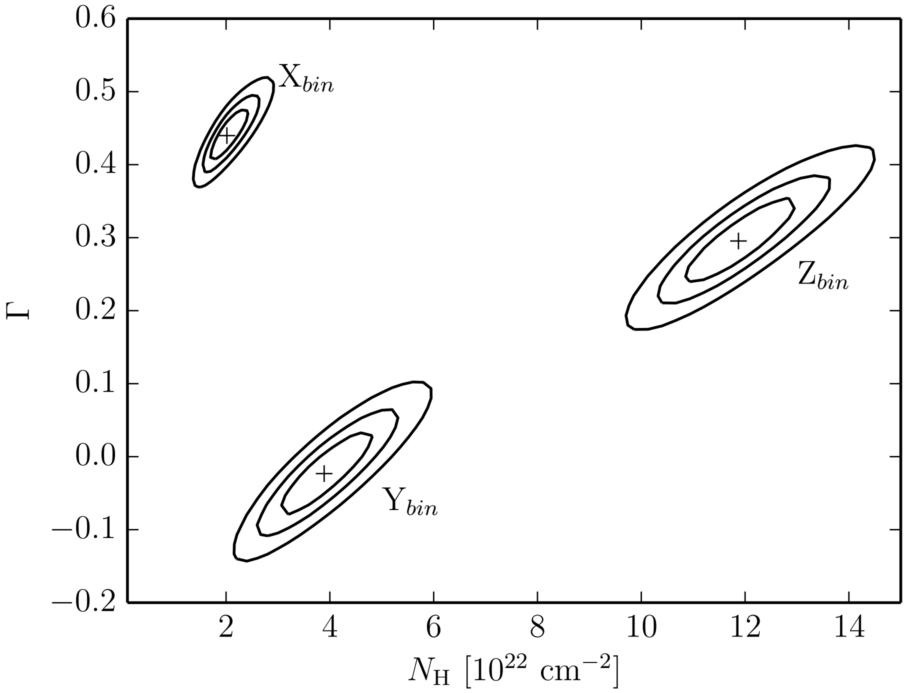

Figure 6.13: χ^2-contour plots for the Vela X-1 double-peaked sample fitted with an absorbed cutoff power-law model including a blackbody component (model *a*, see Table 6.3). The ellipses are χ^2-contours for two parameters (N_H and Γ). The contours correspond to $\chi^2_\mathrm{min} + 1.0$ (the projections of this contour to the parameter axes correspond to the 68%-uncertainty for one parameter of interest), $\chi^2_\mathrm{min} + 2.3$ (68%-uncertainty for two parameters of interest), and $\chi^2_\mathrm{min} + 4.61$ (90%-uncertainty for two parameters of interest). The respective orbital phase bins are indicated. Figure from Malacaria et al. (2016).

(i.e., *bbody*cutoffpl* in XSPEC), and (b) a partial covering model (i.e., *pcfabs*powerlaw* in XSPEC). Both models are provided with the iron line and absorption components introduced in Sect. 6.5. To avoid unphysical best-fit solutions when model (a) is used, the cutoff energy and the blackbody temperature were fixed to their respective phase-averaged values.

For model (a), a further test has been performed: the results in the case of fixed photon index (to the phase-averaged value of $\Gamma = 0.27$, see Table 6.2) were compared to those in the case of free photon index. The model with free photon index turns out to be statistically preferable at a confidence level $> 99\%$ (evaluated by means of the F-test). Furthermore, fitting the Y phase bin spectrum, the model with a fixed photon index leads to unphysically large values of the blackbody normalization (to compensate for the soft excess). Thus, the cutoff power-law model with a fixed photon index has not been considered as a viable model in the following analysis (similar considerations also hold for the phase-resolved spectroscopy of the standard sample, see Sec. 6.6.2).

Concerning model (b), it is worth to mention that, it is often possible to find a statistically equivalent solution where the partial covering component is not necessary

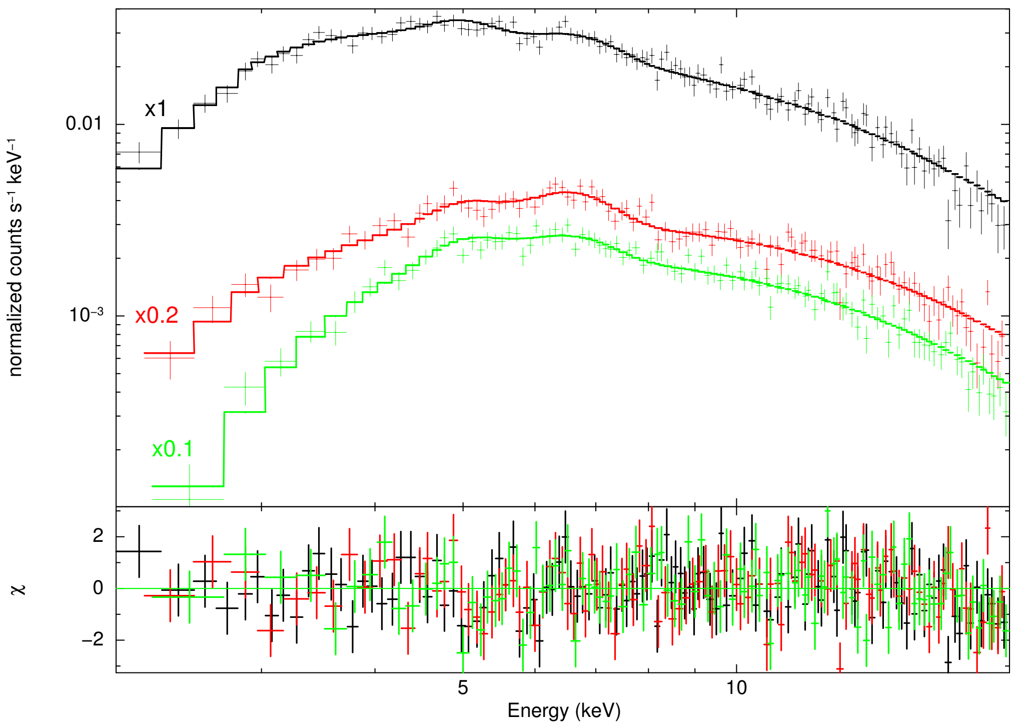

Figure 6.14: Orbital phase-resolved spectra of the double-peaked sample fitted with a partial covering model, when significant (see text). Top panel shows, from top to bottom, data and folded model of the three spectra in phase bins X, Y, Z, respectively. The spectra have been multiplied by the indicated factor, for better visualization. Bottom panel shows the residuals for the best-fit model (model b). See Table 6.3 for all spectral parameters. Figure from Malacaria et al. (2016).

(i.e., resulting in a covering fraction $f = 0$ or $\mathrm{N}_{\mathrm{H}}^{pc} = 0$). As a consequence, the significance of the partial covering component has been tested with the F-test, and included only when significant at a 99% c.l. Otherwise, the solutions without the partial covering component were used. The same criterion has been adopted for the standard sample case (see Sec. 6.6.2).

Both models (a) and (b) return a good fit. The best-fit results are given in Table 6.3. The results show that model (a) exhibits orbital modulation of the spectral photon index Γ. To better explore the orbital modulation of the spectra, χ^2-contour plots for Γ and N_{H} in the three phase bins have been produced (Fig. 6.13). On the contrary, model (b) does not show photon index modulation along the orbital phase, although it shows variation of the column density. A plot of the double-peaked phase-resolved spectra fitted with the partial covering model is shown in Fig. 6.14.

Table 6.3: Best-fit spectral parameters of the phase-resolved spectra from the double-peaked sample. The errors correspond to the 1σ-uncertainties.

Phase-bins	**X**		**Y**		**Z**	
Model	Cutoff PL + BB	Part. Cov.	Cutoff PL + BB	Part. Cov.	Cutoff PL + BB	Part. Cov.
$N_H/10^{22}\,\mathrm{cm}^{-2}$	$2.02^{+0.41}_{-0.31}$	$3.68^{+0.29}_{-2.16}$	$3.89^{+0.93}_{-0.87}$	$2.49^{+2.07}_{-2.49}$	$11.9^{+1.1}_{-1.0}$	16^{+1}_{-3}
$N_H^{pc}/10^{22}\,\mathrm{cm}^{-2}$	–	–	–	$16.1^{+11.3}_{-5.3}$	–	–
Cov. Fract.^{pc}	–	–	–	$0.64^{+0.17}_{-0.09}$	–	–
E_{cut} [keV]	15.3 (fixed)	–	15.3 (fixed)	–	15.3 (fixed)	–
Γ	$0.44^{+0.04}_{-0.03}$	$1.12^{+0.02}_{-0.04}$	$-0.02^{+0.06}_{-0.06}$	$0.91^{+0.29}_{-0.11}$	$0.29^{+0.06}_{-0.06}$	$1.10^{+0.05}_{-0.05}$
Norm$_{PL}$	–	$0.235^{+0.014}_{-0.017}$	–	$0.129^{+0.151}_{-0.038}$	–	$0.256^{+0.042}_{-0.031}$
kT$_{BB}$ [keV]^b	0.16 (fixed)	–	0.16 (fixed)	–	0.16 (fixed)	–
$\chi^2/_{\mathrm{D.o.F.}}= \chi^2_{\mathrm{red}}$	$113/121 = 0.93$	$121/120 = 1.00$	$113/108 = 1.05$	$117/107 = 1.09$	$101/102 = 0.99$	$113/101 = 1.11$

^{pc} Partial Covering Model.

^{b} Blackbody component.

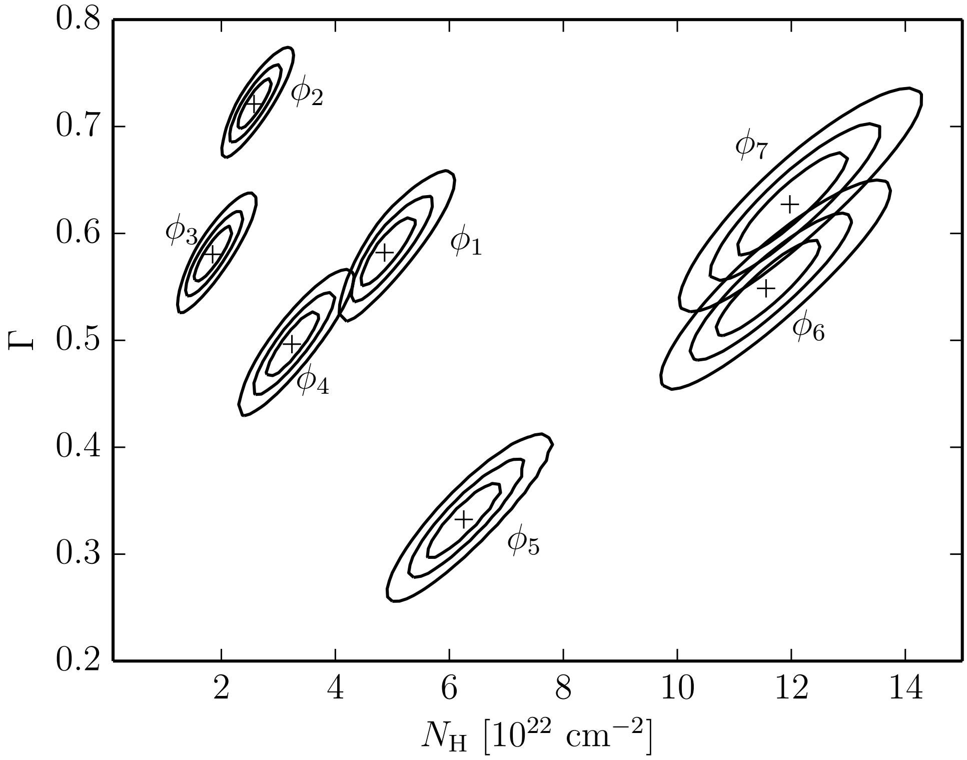

Figure 6.15: χ^2-contour plots for the Vela X-1 standard sample fitted with an absorbed cutoff power-law model including a blackbody component (see Table 6.4). The ellipses are χ^2-contours for two parameters (N_H and Γ). Contours confidence levels are the same as in Fig. 6.13. The respective orbital phase bins labels (as defined in Sect. 6.6.2) are indicated. Figure from Malacaria et al. (2016).

6.6.2 Orbital phase-resolved spectroscopy of the standard sample

Similarly to the double-peaked sample, orbital phase-resolved spectroscopy of the standard sample has also been performed. However, for this sample, the statistics is much higher than in the previous case, so that a finer binning is possible. Thus, the standard sample profile has been divided in 7 phase bins, each one wide 0.1 in phase, from 0.1 to 0.8. Phase bins around the eclipse are not suitable for the purpouses of the present analysis, and suffer of lower statistics. Thus, phase bins around the eclipse have not been considered in this work. The analyzed phase bins are labelled by ϕ_i, with $i = 1, ..., 7$. Then, the data have been filtered with GTIs corresponding to the 7 orbital phase bins, to extract orbital phase-resolved spectra of the standard sample. Based on the results from Section 6.5, the same two models have been employed to fit the phase-resolved spectra: (a) a cutoff power-law with a blackbody component, and (b) a partial covering model. To avoid unphysical best-fit solutions, the cutoff energy and the blackbody temperature of model (a) were fixed to their respective phase-averaged values. As already mentioned in Section 6.6.1, model (b) returns two solutions: one where

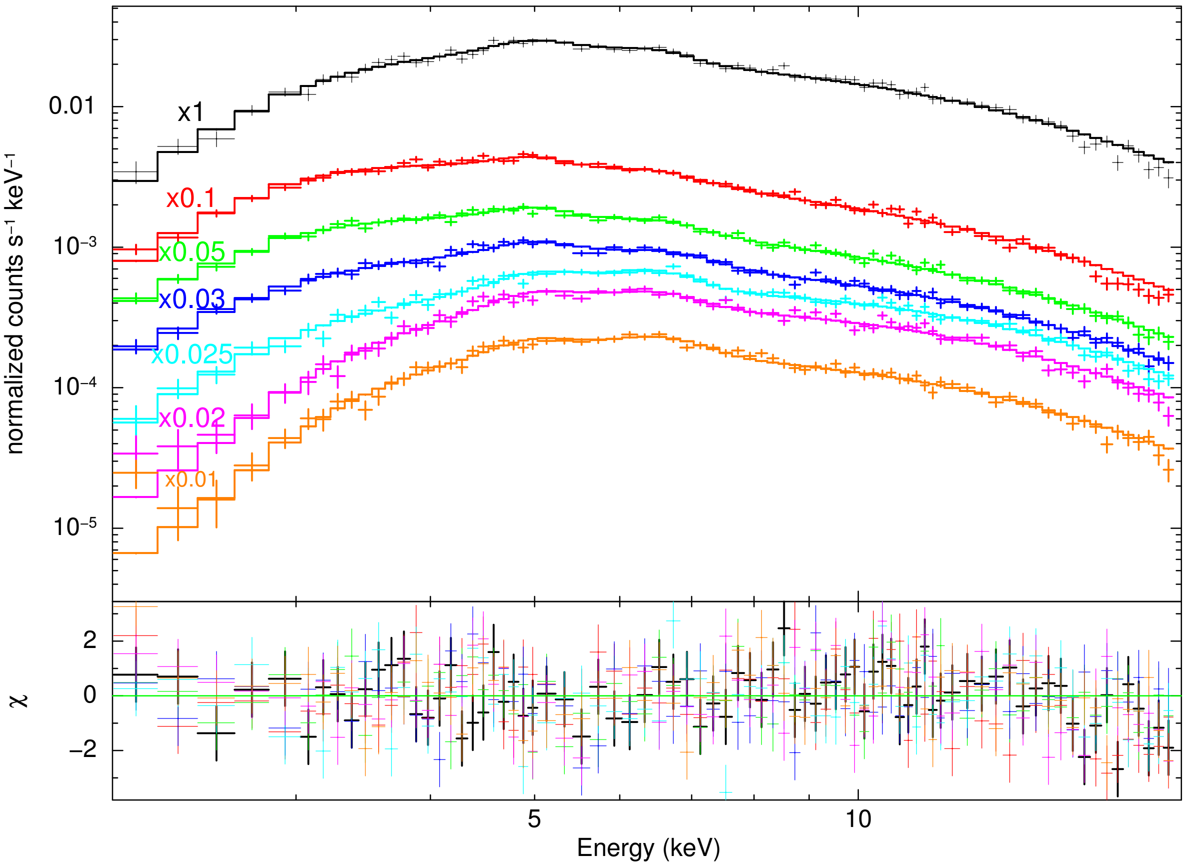

Figure 6.16: Orbital phase-resolved spectra of the standard sample fitted with a partial covering model, when significant (see text). Top panel shows, from top to bottom, data and folded model of the spectra in phase bins from ϕ_1 to ϕ_7. Bottom panel shows the residuals for the best fit model. Symbols are like in Fig. 6.14. See Table 6.4 for all spectral parameters. Figure from Malacaria et al. (2016).

the partial covering component is included, and the other where the same component is not necessary. In such cases, the adopted solution is the one in which the partial covering component is not required, unless it is significant at a 99% c.l. The results are given in Table 6.4. All phase-resolved spectra return a good fit for each of the two tested models. However, the cutoff power-law model with blackbody shows a marked modulation of the spectral photon index Γ along the orbital phase. The trend of this modulation is similar to that observed for the double-peaked sample (see Section 6.6.1). For a deeper investigation of these results, χ^2-contour plots of Γ and N_H have been produced (see Fig. 6.15). On the other hand, the partial covering model shows only marginal variation of the photon index Γ, while the column density clearly changes along the orbital phase. Among the phase bins where the partial covering component is needed, the covering fraction is consistent with a constant value of $50-60\%$. A plot of the standard sample phase-resolved spectra fitted with the partial covering model is shown in Fig. 6.16.

Table 6.4: Best-fit spectral parameters of the orbital phase-resolved spectra from the standard sample. The errors correspond to the 1σ-uncertainties.

Sample	**Cutoff PL + BB** ($E_{cut} = 20.1\,\mathrm{keV}$ fixed, $kT^{b}_{BB} = 0.14\,\mathrm{keV}$ fixed)						
Phase-bin	ϕ_1	ϕ_2	ϕ_3	ϕ_4	ϕ_5	ϕ_6	ϕ_7
$N_H/10^{22}\,\mathrm{cm}^{-2}$	$4.86^{+0.55}_{-0.42}$	$2.57^{+0.31}_{-0.29}$	$1.85^{+0.35}_{-0.33}$	$3.24^{+0.48}_{-0.46}$	$6.25^{+0.68}_{-0.64}$	$11.5^{+0.9}_{-0.8}$	$11.9^{+1.0}_{-0.9}$
Γ	$0.58^{+0.03}_{-0.03}$	$0.72^{+0.02}_{-0.02}$	$0.58^{+0.03}_{-0.03}$	$0.49^{+0.03}_{-0.03}$	$0.33^{+0.04}_{-0.03}$	$0.55^{+0.04}_{-0.04}$	$0.63^{+0.05}_{-0.05}$
Norm_{PL}	$0.111^{+0.009}_{-0.008}$	$0.194^{+0.010}_{-0.009}$	$0.126^{+0.007}_{-0.007}$	$0.095^{+0.007}_{-0.006}$	$0.066^{+0.005}_{-0.005}$	$0.11^{+0.01}_{-0.01}$	$0.12^{+0.01}_{-0.01}$
$\chi^2/\mathrm{D.o.F.} = \chi^2_{\mathrm{red}}$	$173/212 = 0.82$	$233/247 = 0.94$	$244/237 = 1.03$	$216/228 = 0.95$	$246/228 = 1.08$	$216/205 = 1.05$	$204/199 = 1.03$
Model	**Partial Covering**						
Phase-bin	ϕ_1	ϕ_2	ϕ_3	ϕ_4	ϕ_5	ϕ_6	ϕ_7
$N_H/10^{22}\,\mathrm{cm}^{-2}$	$6.3^{+0.3}_{-1.0}$	$1.7^{+1.2}_{-1.7}$	$0.^{+1.4}$	$2.2^{+0.93}_{-1.5}$	$5.6^{+0.9}_{-0.6}$	$13.3^{+0.7}_{-1.7}$	$13.7^{+0.7}_{-1.7}$
$N^{pc}_H/10^{22}\,\mathrm{cm}^{-2}$	–	$7.1^{+7.9}_{-2.0}$	$6.4^{+4.4}_{-1.0}$	13^{+8}_{-4}	32^{+10}_{-8}	–	–
Cov. Fract.^{pc}	–	$0.49^{+0.29}_{-0.24}$	$0.68^{+0.02}_{-0.25}$	$0.51^{+0.19}_{-0.10}$	$0.61^{+0.05}_{-0.03}$	–	–
Γ	$1.09^{+0.03}_{-0.02}$	$1.26^{+0.05}_{-0.03}$	$1.13^{+0.05}_{-0.04}$	$1.12^{+0.08}_{-0.06}$	$1.23^{+0.18}_{-0.19}$	$1.08^{+0.04}_{-0.04}$	$1.15^{+0.04}_{-0.04}$
Norm_{PL}	$0.21^{+0.01}_{-0.01}$	$0.40^{+0.06}_{-0.04}$	$0.26^{+0.03}_{-0.02}$	$0.26^{+0.07}_{-0.04}$	$0.39^{+0.27}_{-0.17}$	$0.22^{+0.02}_{-0.02}$	$0.23^{+0.02}_{-0.02}$
$\chi^2/\mathrm{D.o.F.} = \chi^2_{\mathrm{red}}$	$192/211 = 0.91$	$250/247 = 1.01$	$248/236 = 1.05$	$212/227 = 0.94$	$251/227 = 1.11$	$237/204 = 1.16$	$219/198 = 1.11$

^{b} Blackbody component; ^{pc} Partial Covering Model.

6.7 Summary

The main observational results of the *MAXI* analysis of Vela X-1 can be summarized as follows:

- About 15% of the orbital light curves in Vela X-1 shows a double-peaked orbital profile, with a dip around the inferior conjunction, both in the $4-10\,\mathrm{keV}$ and $10-20\,\mathrm{keV}$ energy bands;
- Orbital phase-resolved spectra of both the double-peaked and the standard sample are well fit by a cutoff power-law model and by a partial covering model;
- The cutoff power-law model leads to orbital modulation of both the spectral photon index and the column density;
- A partial covering model fits the data equally well. No orbital modulation of the spectral photon index is observed in this case. In contrast, orbital modulation of the column density is observed.

In the following chapter these results will be discussed within the context of the most recent wind accretion scenarios that have been proposed for Vela X-1.

7

DISCUSSION

7.1 GX 304-1

7.1.1 A timing solution for the entire outburst

The behavior of the pulse period in GX 304-1 during its January–February 2012 outburst has been studied using a pulse phase-connection technique. The obtained timing solution is used to construct pulse profiles in two energy bands, $3-20\,\mathrm{keV}$ (JEM-X) and $18-80\,\mathrm{keV}$ (ISGRI), as shown in Figs. 5.5 and 5.6, and to identify pulse phases at different stages of the outburst. A decrease in the pulse period over the outburst is clearly seen. The measured period derivative is $\dot{P} = (-2.04 \pm 0.01) \times 10^{-7}$ (Fig. 5.4 and Table 5.5.1.1). This trend is most probably due to a combination of the Doppler effect caused by the orbital motion of the neutron star and an intrinsic spin-up caused by the transfer of angular momentum from the accretion disk to the neutron star.

7.1.1.1 Energy- and luminosity-dependence of the pulse profiles

In the JEM-X ($3-20\,\mathrm{keV}$) and ISGRI ($18-80\,\mathrm{keV}$) energy bands, pulse profiles of GX 304-1 strongly depend on energy. The only exception is given by Rev. 1138, that presents a profile with a less complex structure with respect to the higher luminosity states, while showing a similar pattern between the different analized energy bands.

The ISGRI pulse profiles presented in Fig. 5.5 show two sharp peaks and a hint of a third peak in between (around phase 0.5) which is not present in all observations. In the JEM-X pulse profiles (Fig. 5.6), however, all three peaks are clearly visible in all observations, with the exception of Rev. 1138. When comparing the pulse profiles in the two energy bands, it appears that the most prominent of the peak in the JEM-X pulse profiles (centered around phase 0.5 in the top panel of Fig. 5.6) tends to disappear at higher energies.

Although the overall morphology of the profile remains the same in all observations (which permits phase connection of the observations, see Sec. 7.1.3), the relative intensities of the peaks vary slightly with luminosity. Furthermore, in the last stage of the outburst (Rev. 1138), that is at the lowest flux level, the pulse profile resembles a single broad peak. A similar flux and energy dependence of the pulse profiles is also observed by Devasia et al. (2011) during a GX 304-1 outburst in August 2010, when the source reached a peak flux of $\sim 700\,\mathrm{mCrab}$ (that is, ~30% less than the outburst analyzed in this work). Very likely, the different pulse profiles of Rev. 1138 indicate a possible change in the beaming pattern from a predominantly pencil beam at lower luminosities, to a mixed pencil-fan beam as the luminosity increases. The pulse profiles luminosity dependence most likely reflects a change in the physical condition of the accretion column (Basko and Sunyaev, 1975). In subcritical sources, the accretion column has not fully formed yet, thus there is not significant contribution to the fan-beam component. This leads the pencil beam pattern of radiation, directed along the magnetic field axis, to dominate (Basko and Sunyaev, 1975). As the luminosity increases, the increasing column height results in a widening of the geometric area of the column side walls, and the X-ray photons escaping through these walls make the fan-beam component important. This scenario is consistent with the observed luminosity dependence of the pulse profiles in GX 304-1, where a single-peaked profile is observed at the lowest luminosity, while a more complex profile emerges as the luminosity increases.

For subcritical sources (such as GX 304-1), the height of the accretion mound is anti-correlated with the accretion rate, and this could be at least partially responsible for the luminosity dependence of the pulse profiles (see Becker et al. 2012, and references therein). As already discussed in Sect. 3.4.3, other factors may influence the observed pulse profile luminosity dependence (e.g. light deflection, magnetic configuration, and others).

While there is no commonly accepted interpretation of the pulse profile dependence on energy and luminosity, a similar behavior is observed in 4U 0115+63 and V 0332+63 (Tsygankov et al., 2007), and an energy-dependent pulse profile is also observed in Her X-1 (Klochkov et al., 2008). A qualitative interpretation of the pulse profile energy-dependence in V 0332+63 (based on the results of Mowlavi et al. 2006) has been proposed by Tsygankov et al. (2007) to explain it in a purely geometric fashion: if the axis of the magnetic dipole is at an angle to the rotation axis (a necessary condition to observe pulsation), the neutron star itself can eclipse some of the lower parts of the accretion columns, which are thought to primarily emit the harder photons. Thus, compared to the pulse profile at softer energies, the harder one lacks (at least) one peak. In contrast, the softer photons are primarily from regions higher up in the accretion column, hence visible during most of the spin period. Although the energy-dependence of GX 304-1 pulse profiles is comparable to that of V 0332+63, it is difficult to adopt a similar interpretation due to the subcritical nature of GX 304-1. On the other hand, in the case of Her X-1 (i.e. another subcritical source), the energy-dependent pulse profiles have been reproduced by a model whose only assumption is a sligthly distorted magnetic dipole field (Blum and Kraus, 2000). Most likely, a combination of the two above-mentioned phenomena is at work in GX 304-1, while additional complexity to this problem can come from asymmetric accretion onto the two (or more) magnetic poles.

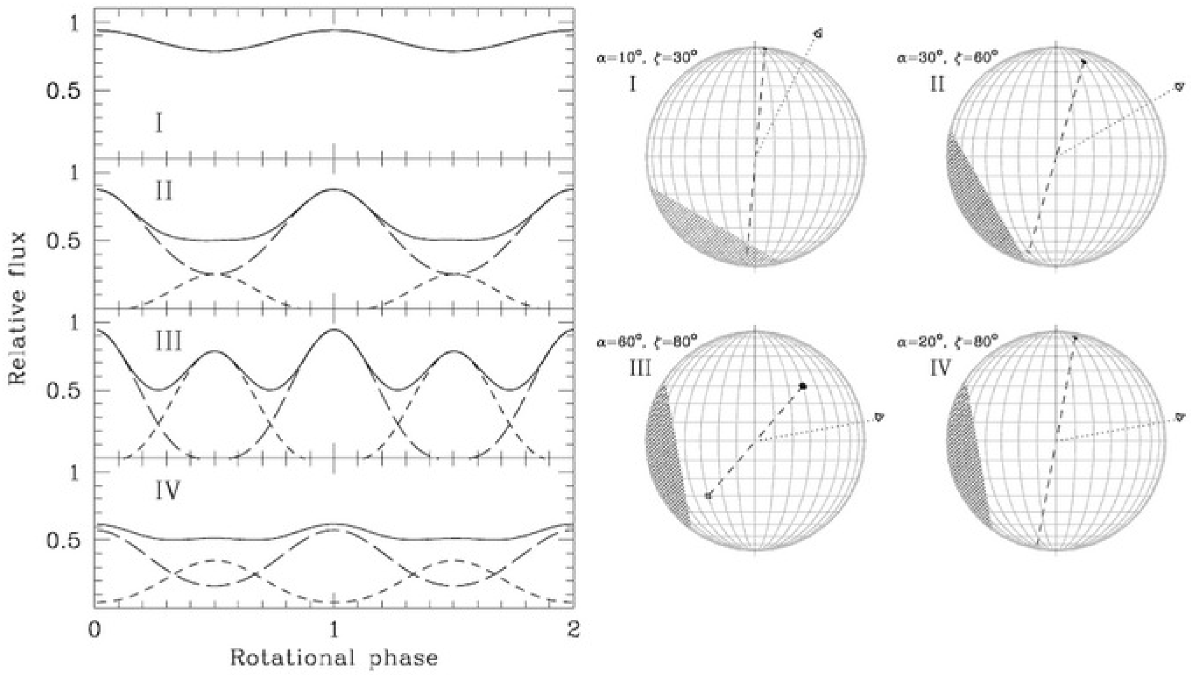

Figure 7.1: Representative pulse profiles for different geometrical configurations in the case of thermally emitting hot polar caps on the surface of a pulsar. The dashed lines show individual flux contribution from the two hot spots while the solid line shows the total observed flux Figure from Becker (2009).

It is also important to mention that, other accreting X-ray pulsars show the opposite behavior, where the low-energy pulse profiles are absorbed, and the extra peak only appears at higher energies (see, e.g., Kreykenbohm et al. 2004, for the case of GX 301-2).

For an accurate description of the pulse profiles dependences, more complicated models need to account for the magnetic field configuration, the scattering cross section along the accretion column, the shape of the emission beam and its dependence on luminosity and energy, and other parameters. Gravitational light deflection also plays a crucial role in shaping the observed pulse profile. Indeed, depending on to the geometry of the emitting region and the observer's line of sight, this effect could make the accretion structures visible from all directions (Kraus, 2001; Kraus et al., 2003), thus affecting the pulse profile in a significant way.

7.1.1.2 Pulsed fraction

Pulsed fraction of ISGRI and JEM-X pulse profiles has been calculated as described in Sec. 3.4.3. The pulsed fraction is only ~20% in both energy bands, and it shows only slight variation along the outburst, uncorrelated with the flux (see Fig. 5.5 and 5.6). This is contrary to many other X-ray pulsars, where a pulsed fraction > 50% is observed, correlated with energy and flux (Lutovinov and Tsygankov, 2008). However, a pulsed fraction behaviour similar to that observed for GX 304-1 in this work has also been observed by Devasia et al. (2011) and Jaisawal, Naik, and Epili (2016) for the same source. This again may be understood in a qualitative manner following a geometrical interpretation: it is possible that, as the star rotates, we are exploring only a small area of the beam pattern, which in turn leads to an observed low and steady pulsed fraction. Assuming that the two magnetic poles are located diametrically opposite on the magnetic axis (i.e. a dipole configuration), a possible geometrical configuration leading to the observed results would be one in which the angle between the observer's line of sight and the magnetic axis is small, or one in which the angle between the magnetic axis and the rotational axis is small (a comparison of such geometries for thermally emitting pulsars is illustrated in Fig. 7.1). This scenario is supported by the results of the pulse phase-resolved analysis showing that the cyclotron line energy is mostly insensitive to the rotational phase (see discussion in Sect. 7.1.2).

7.1.2 Phase-averaged spectral results

Phase-averaged spectral analysis has been performed for the six INTEGRAL observations of GX 304-1 during the outburst event in January–February 2012. The analysis has been carried out with an updated INTEGRAL calibration (Caballero et al., 2013) and analysis software (OSA 10), which leads to a more precise measurement of the cyclotron line energy. The cyclotron line has been found to vary around the energy of $E_{\text{cyc}} \sim 55\,\text{keV}$. The E_{cyc} found in the present work results higher than that found by Klochkov et al. (2012) and especially from that reported in Yamamoto et al. (2011). While the difference between the present results and those of the former authors is explained by the new energy calibration of the ISGRI detector (see Sec. 5.5.1.1), the discrepance with the results from Yamamoto et al. (2011) is of a different nature. Those authors take advantage of a different set of facilities (i.e., *Suzaku* and *RXTE*), and it is therefore possible that the discrepancy is due to a different instrumental calibration. An incorrect spectral model may also be the reason that yelds to different spectral results. Indeed, Yamamoto et al. (2011) use *Suzaku* and *RXTE* data fitted with an NPEX model (Negative and Positive power laws with exponential cutoff, Mihara, Makishima, and Nagase (1998). However, they did not include the extra Gaussians at the energies of the prominent background lines to properly model the *RXTE* data, which drastically affects the cyclotron line energy estimation. Nevertheless, they have been able to discover the cyclotron line in this source, with a centroid energy of $49 - 54\,\text{keV}$ (although with large uncertainties at low luminosities).

7.1.2.1 Positive correlation of the cyclotron line energy and luminosity

A dependence of the cyclotron line energy E_{cyc} with the observed luminosity has already been reported for several accreting X-ray pulsars. The E_{cyc}–flux correlation is positive in Her X-1 (Staubert et al., 2007), Vela X-1 (Fürst et al., 2014), A 0535+26 (Sartore, Jourdain, and Roques, 2015), and, as some indications suggest, also in GX 301-2 (La

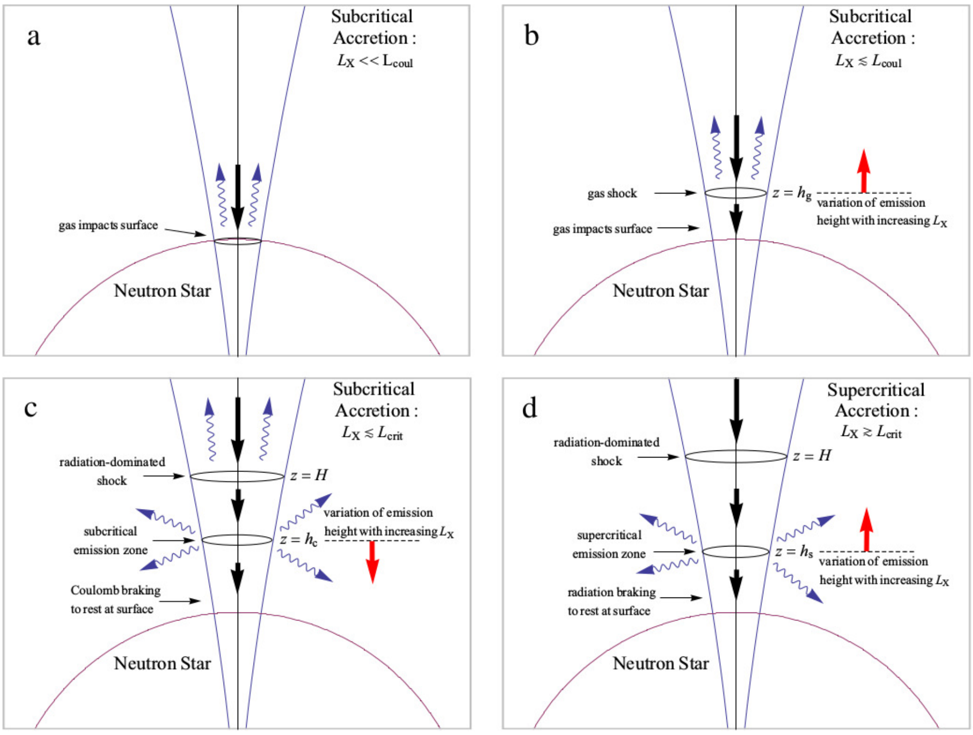
a
Subcritical Accretion : $L_X << L_{coul}$
gas impacts surface
Neutron Star
b
Subcritical Accretion : $L_X \lesssim L_{coul}$
gas shock
gas impacts surface
$z = h_g$
variation of emission height with increasing L_X
Neutron Star
c
Subcritical Accretion : $L_X \lesssim L_{crit}$
radiation-dominated shock
$z = H$
subcritical emission zone
$z = h_c$
variation of emission height with increasing L_X
Coulomb braking to rest at surface
Neutron Star
d
Supercritical Accretion : $L_X \gtrsim L_{crit}$
radiation-dominated shock
$z = H$
supercritical emission zone
$z = h_s$
variation of emission height with increasing L_X
radiation braking to rest at surface
Neutron Star

Figure 7.2: Geometry of the accretion column as a function of the luminosity in a magnetized accreting X-ray pulsar. As the accretion rate changes, so do the characteristic emission height and the emission beam pattern. Four accretion regimes are shown. Figure from Becker et al. (2012).

Barbera et al., 2005). The only pulsar with a confirmed negative $E_{\rm cyc}$–flux correlation is V 0332+63 (Tsygankov et al., 2006b), while for 4U 0115+63 the negative dependence is still ambiguous (Nakajima et al., 2006; Müller et al., 2013; Iyer et al., 2015). The analysis by Klochkov et al. (2011) focused on the pulse-to-pulse variability (i.e. on short timescales), confirmed the positive luminosity-dependence of the cyclotron line energy in Her X-1 and A 0535+26, and the negative luminosity-dependence in V 0332+53 as well as in 4U 0115+63.

The luminosity dependence of the cyclotron line energy $E_{\rm cyc}$ reported in Klochkov et al. (2012) for GX 304-1 has been confirmed in this work with a more reliable photon energy reconstruction and therefore a more accurate measurement of the spectral parameters. Thus, GX 304-1 further enlarges the group of sources showing the positive $E_{\rm cyc}$-flux correlation.

In the present work, the observed $E_{\rm cyc}$ shows a systematic shift of ~5% with respect to the energies reported in the previous work. As a consequence, the resulting correlation has a slightly higher (but still consistent) slope than that found by Klochkov et al. (2012).

The dependence of $E_{\rm cyc}$ on luminosity is usually interpreted in terms of the variation of the emission region height with accretion rate, and hence with luminosity (see, e.g., Staubert et al. 2007; Becker et al. 2012 and Fig. 7.2). In these models, the critical luminosity L_c distinguishes between two accretion regimes: one in which the height of

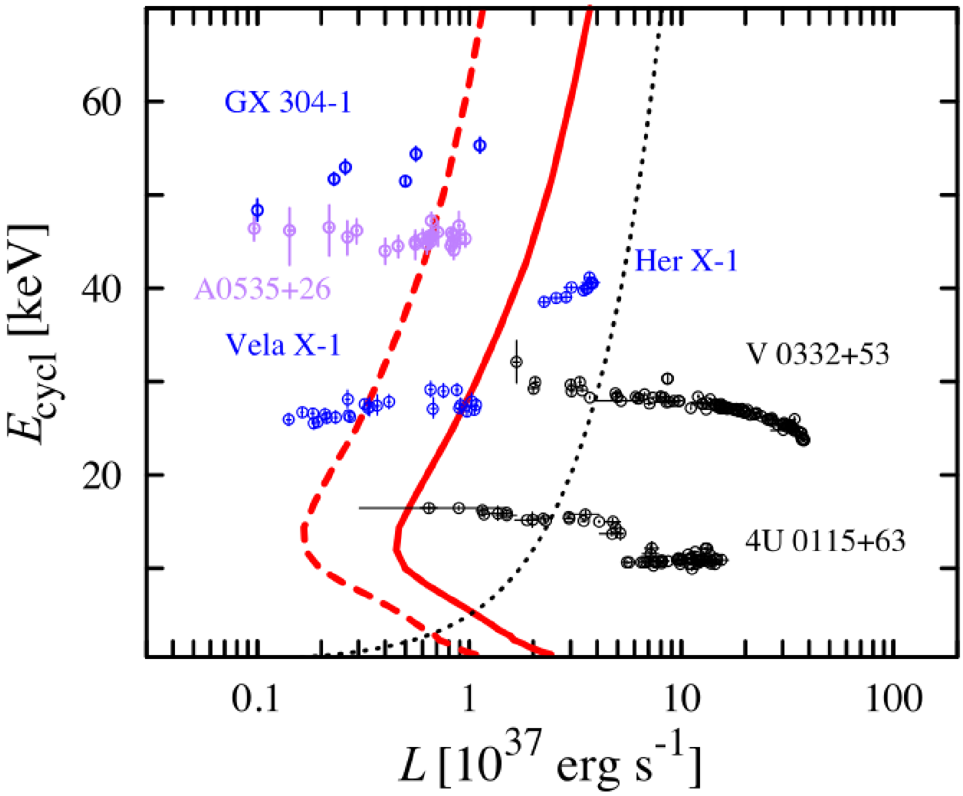

Figure 7.3: Comparison of the theoretical critical luminosity-E$_{cyc}$ dependence to the data. Red solid and dashed curves correspond to the disc-accretion case with different parameters (mixed X- plus O-modes polarization for the red dashed line and pure X-mode polarization for the red solid line). The predictions by Becker et al. (2012) are shown with the black dotted line. Figure from Mushtukov et al. (2015b).

the emitting structure is governed by the ram pressure of the infalling material (for $L < L_c$, i.e. "subcritical sources"), and the other where a radiation-pressure-dominated emitting column is formed (for $L > L_c$, i.e. "supercritical sources"). As the luminosity L varies, the X-ray emitting region also moves within the accretion column, sampling different values of the local magnetic field, thus leading to a variable cyclotron line energy with luminosity. The critical luminosity below which a positive $E_{\rm cyc}$–luminosity correlation is expected, has been calculated by Becker et al. (2012) as a function of the magnetic field and other physical parameters of the NS. For typical neutron star parameters, it results in

$$L_c \sim 1.5 \times 10^{37}\ B_{12}^{16/15}\, erg\ s^{-1} \tag{7.1}$$

For GX 304-1, this leads to $L_c \sim 8 \times 10^{37}$ erg s^{-1}. During the analyzed outburst, the source luminosity clearly remains below this value (see Figs. 5.9 and 5.10). Thus, the observed positive $E_{\rm cyc}$–flux correlation is consistent with the expected behavior for a subcritical source according to the physical picture outlined in Becker et al. (2012). More recently, a new calculation of the L_c function has been proposed by Mushtukov et al. (2015b), using the exact Compton scattering cross-section in a strong magnetic field. The observed positive $E_{\rm cyc}$–flux relation in GX 304-1 is consistent with their

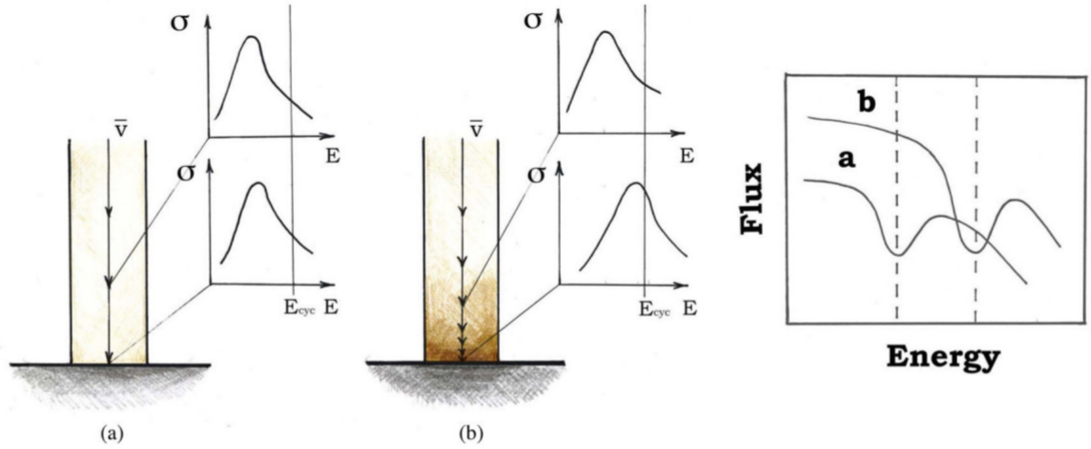

Figure 7.4: Schematic presentation of the dependence of the cyclotron line energy on the velocity profile in the line-forming region. The radiation pressure within the accretion column affects the velocity profile of the infalling plasma: the higher the luminosity, the lower the velocity in the vicinity of NS surface. The lower the electron velocity, the lower the redshift and the higher the resonant energy at a given height. As a result, a positive correlation between the line centroid energy and the luminosity is expected. Panel (a) corresponds to the low-luminosity case when the gas is in a free-fall. The observed cyclotron line is redshifted relative to the rest-frame value. Panel (b) is for the higher luminosity when the gas is decelerated close to the surface and the line shifts closer to the rest-frame position. Figure from Mushtukov et al. (2015a).

model as well. A comparison of the two models for the L_c-E$_{cyc}$ dependence to the data is shown in Fig. 7.3.

A more recent model to explain the correlation at low luminosities (where a column structure is not yet expected) has been proposed by Mushtukov et al. (2015a). These authors interpret the positive $E_{\rm cyc}$–luminosity correlation as a consequence in the variations of the velocity profile in the line forming region, i.e., as a Doppler effect. In fact, plasma in the accretion funnel moves with a velocity of several fractions of c towards the NS surface, and the scattering feature must be redshifted due to the Doppler effect. Therefore, an observer will see the line at a lower energy than the cyclotron one associated with the magnetic field at the pole. The amplitude of the shift depends on the electron velocity and the angle between the photon momentum and the accretion flow velocity. As a consequence, the observed position and the shape of the cyclotron scattering feature depend on the velocity profile in the accretion channel (see Fig. 7.4). The velocity profile is, in turn, affected by the radiation pressure: the higher the luminosity, the lower the velocity in the vicinity of NS surface. This results in a positive correlation between the line centroid energy and the observed luminosity.

7.1.2.2 Correlation of the continuum parameters

In this work, the correlation between the spectral photon index Γ and luminosity has also been investigated, finding that GX 304-1 exhibits a negative correlation of the two parameters. In many accreting X-ray pulsars, Γ is luminosity dependent. It had been found that in accreting pulsars showing a positive E_{cyc}–flux correlation, the correlation between Γ and the flux is negative (i.e. the spectrum gets harder as the luminosity increases) and vice versa (Klochkov et al., 2011). The variations of spectral hardness and its correlation with the mass accretion rate for X-ray Binary Pulsars were discussed recently by Postnov et al. (2015). According to these authors, the observed hardening of the spectrum with flux (Fig. 5.10) for sub-critical sources, including GX 304-1, can be understood when assuming that the pressure and electron density inside the emitting structure (the accretion mound) increase with increasing mass accretion rate and luminosity. Indeed, such an increase should lead to a higher optical depth τ, thus to a larger Comptonization parameter $y = \tau k T_e/(m_e c^2)$. The spectrum formed by Comptonization of the seed photons from the base of the column would then become harder. On the other hand, at higher accretion rates (i.e., $L > L_c$), the height of the column increases, such that the contribution of the reflected component (i.e., the amount of flux that is reflected from the NS surface) to the total emission starts decreasing. Since the reflected radiation is harder than the incident one (due to the atmospheric absorption of soft X-rays), the spectrum of the total emission (direct plus reflected) stops hardening (and even becomes slightly softer).

Finally, the dependence of the folding energy E_{fold} on the photon index Γ and, at the same time, on luminosity has been also investigated for GX 304-1. These correlations are shown in the contour plot in Fig. 5.12. The plot shows that E_{fold} is positively correlated with Γ, and negatively correlated with flux (E_{fold} increases at lower luminosities). Similar behavior is reported for two other sub-critical accreting pulsars: A 0535+26 (Müller et al., 2013) and RX J0440.9+4431 (Ferrigno et al., 2013). These correlations can be qualitatively understood as follows. It is generally accepted that the cutoff power-law spectrum of accreting pulsars is a result of Comptonization, i.e., scattering of soft photons off hot electrons supplied by the infalling plasma. As the luminosity increases toward L_{c}, the radiation field begins to affect the accretion flow and Compton cooling becomes more efficient (as a consequence of the increased scattering rate). This might lead to the observed shift of E_{fold}, which reflects the electron temperature T_e shift toward lower energies, while at the same time, the Comptonization process makes the spectrum harder, as indicated by the Γ-flux dependence.

The dependence of the spectral hardness on flux has recently been investigated for a number of accreting pulsars in BeXRBs also by Reig and Nespoli (2013). These authors found that the X-ray emission of the sources follows certain patterns in the hardness/intensity diagram. This method has the great advantage to be model-independent, while spectral fitting results can heavily depend on the assumed model. Reig and Nespoli (2013) found that, at lower fluxes, the emission first becomes harder with increasing flux. At a certain flux a “turn-over” occurs, so that at higher fluxes the emission again becomes softer (Fig. 6 in Reig and Nespoli 2013). The luminosities

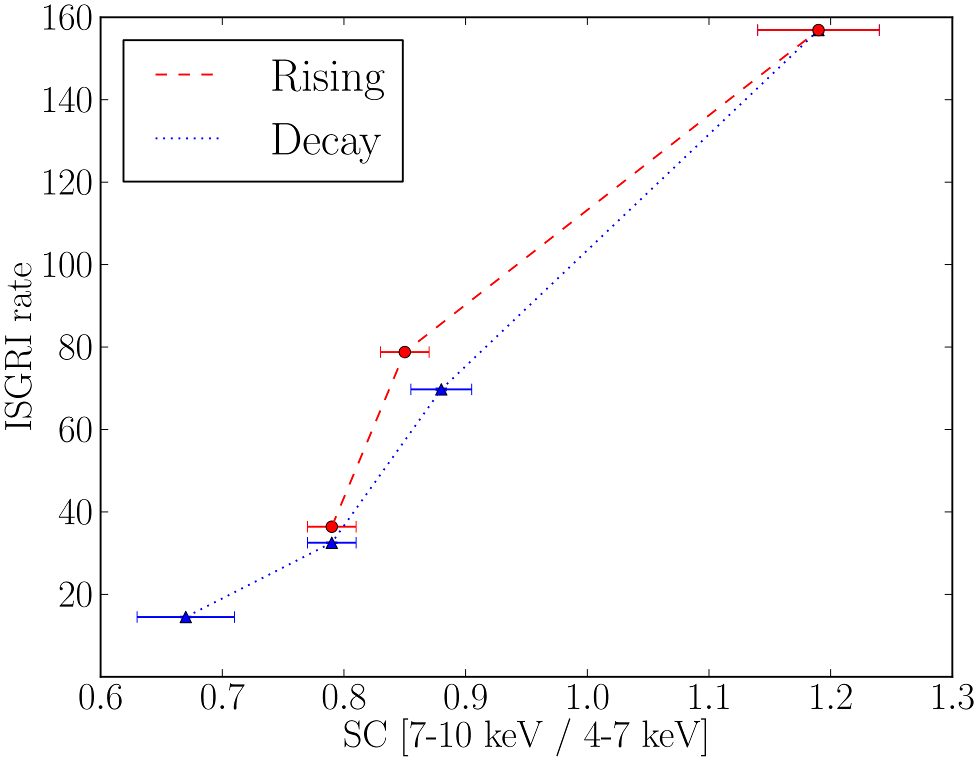

Figure 7.5: Hardness/intensity diagram for GX 304-1 during the analyzed outburst. The soft color definition is given in the text. The errors are 1σ uncertainties. Errors on the ISGRI rates are smaller than the symbol size. The dashed red curve corresponds to the rising part of the outburst, the dotted blue one – to the decay. Figure from Malacaria et al. (2015).

corresponding to the fluxes of the turn-over are in all cases close to the critical luminosity L_c discussed above. Thus, the turnovers in the hardness/flux dependences may reflect a transition between the aforementioned sub- and super-critical regimes characterized by the opposite E_{cyc}–flux and Γ–flux correlations. To compare our results with those presented in Reig and Nespoli (2013), a hardness/intensity diagram for GX 304-1 has been constructed (Fig. 7.5), using the same definitions of the soft-color (SC), i.e., the ratio between the fluxes in the $7-10\,$keV and $4-7\,$keV ranges. As expected in a subcritical source, the luminosity corresponding to the turnover is not reached in GX 304-1 and the diagram shows only the part where the hardness increases with luminosity, i.e., the “horizontal branch” according to the terminology used in Reig and Nespoli (2013).

7.1.3 Phase-resolved spectral analysis

Thanks to the successful phase connection (see Sec. 5.4.1), phase bins of the rotating neutron star have been identified at different stages of the outburst, thus allowing to perform phase-resolved spectroscopy in order to explore the spectral variability with pulse phase. Results from the phase-resolved spectroscopy have been compared by adopting a rolloff power-law model and a multiplicative Gaussian absorption line to account for the CRSF, i.e., using the same model as in the phase-averaged analiysis (see Sec. 5.5.1.1). Phase-bins that need additional spectral components are also discussed.

7.1.3.1 Phase-resolved spectral results of individual observations

Each *INTEGRAL* observation has been analysed to derive phase-resolved spectral parameters. The maximum (nominal) value of the cyclotron line energy, $E_{\rm cyc} \sim 62\,\rm keV$, is reached during Rev. 1132, in the pulse phase bin $0.4-0.6$ and during the peak of the outburst, Rev. 1134, in the same phase bin (see Table 5.3). Using a value of $z_g = 0.3$ for the gravitational redshift (assuming canonical neutron star parameters of radius $R = 10\,\rm km$ and mass $M = 1.4\,M_\odot$), this corresponds (Eq. 3.38) to a magnetic field strength of 6.9×10^{12} Gauss. This is among the strongest observed magnetic fields in an accreting X-ray pulsar. (while the highest belongs to GRO J1008-57 with a cyclotron line energy of ∼80 keV, Bellm et al. 2014). The centroid energy of the cyclotron line shows only slight variations with pulse phase, which do not exceed ∼16% (using 0.2 wide phase bins) for the nominal values (or ∼20% at 1σ c.l.). This is contrary to some other X-ray pulsars (see, e.g., the cases of Cen X-3, Burderi et al. 2000; GX 301-2, Kreykenbohm et al. 2004; and Her X-1, Klochkov et al. 2008; Vasco, Klochkov, and Staubert 2011), where the energy of the cyclotron line shows up to 30% variation with pulse phase. GX 304-1, however, is not the only accreting X-ray pulsar where the cyclotron line energy varies only by $\lesssim 20\%$ with pulse phase: see, e.g., the case of 4U 1538-52 (Coburn et al., 2002). Physical implications of this result may imply a certain geometrical configuration of the accreting system, and are discussed below (see Sect. 7.1.3.3), compared to the results from the timing analysis that also support the same proposed scenario.

The standard rolloff power-law model resulted inappropriate for the $0.0-0.2$ phase bins of all observations (except the Rev. 1138). These spectra need an additional component to obtain an acceptable fit. This component can be modelled with a Gaussian emission line around 35 keV. The extra component is reminiscent of the "10 keV feature" observed in the spectra of many accreting X-ray pulsars (Coburn et al., 2002; Klochkov et al., 2008; Müller et al., 2013), for which no accepted explanation of its physical origin exists. However, the centroid energy of the feature in GX 304-1 is at a much higher energy compared to the "10 keV feature" in other pulsars, i.e., $\sim 35\,\rm keV$. Interpreted within this context, the feature is likely due to the inadequacy of the underlying phenomenological model. Alternatively, the same feature can be fit by a Gaussian absorption line at lower energies, instead of an emission line. In this case, the absorption line centroid energy is measured (see Table 5.5) between 12 keV (with $\sigma = 14\,\rm keV$, $\eta = 37$), and 25 keV (with $\sigma = 9\,\rm keV$, $\eta = 8$). This feature results not correlated with the observed luminosity. To explore the possibility of the feature being the fundamental cyclotron line, the harmonic ratio has been calculated between the confirmed cylotron line at ∼55 keV, assumed to be the first harmonic, and the centroid energy of the absorption feature. It is found that the ratio significantly deviates from the canonical ratio of 2. For the feature at 12 keV, the ratio results in an unacceptably high value of ∼4.6, while for the feature at 25 keV the ratio is reduced to ∼2.3, about half of the one at 12 keV. Relatively high deviations from an expected integer value of the harmonic ratios are also observed in other sources, for example, Vela X-1 (Fürst et al. 2014, and references therein), where the ratio between the confirmed harmonic and fundamental line energies spans the range $2.1 - 2.7$. Those authors invoke photon spawning caused by the harmonic lines as responsible for influencing the shape of the fundamental line, thereby shifting its measured centroid energy from its real value. However, values of the harmonic ratio as high as 4.6 have never been observed for the first harmonic line, and they seem to exclude the possibility that the absorption feature is the fundamental cyclotron line.

7.1.3.2 Phase-resolved spectral results of stacked observations

Phase-resolved spectroscopy has also been carried out by stacking together all observations (with the exception of Rev. 1138), in order to improve the statistics and to investigate the pulse phase variability of spectral parameters with better phase resolution (12 phase bins). The results are shown in Fig. 5.15 for three selected parameters: the cyclotron line centroid energy, the photon index and the folding energy of the high-energy rolloff. Averaged JEM-X and ISGRI pulse profiles have also been produced, and are shown in Fig. 5.15. The value of E_{cyc} is constant at ~ 56 keV (with one phase bin showing a ∼10% higher value, although the difference is not statistically significant). The photon index Γ and the folding energy E_{fold} show more prominent variations with pulse phase. A similar variation in the continuum parameters is also observed in other accreting pulsars (see, e.g., Her X-1, Vasco et al. 2013; GX 301-2, Suchy et al. 2012; Vela X-1, Maitra and Paul 2013), but a consistent theoretical scenario that supports such variations is still missing. It is possible that, the variation of the photon index with pulse phase is a consequence of the variable column density at certain pulse phases. Recent results from Jaisawal, Naik, and Epili (2016) also find that phase-resolved *Suzaku* spectra of GX 304-1 have a variable photon index. This variation seems to be negatively correlated with the absorption column density (that is, the spectrum becomes harder as the column density increases, see Figs. 7 and 8 of Jaisawal, Naik, and Epili 2016). The same correlation can not be explored in the context of our analysis due to the limited statistics and to the limited energy range covered by the JEM-X detectors ($3 - 30$ keV), which does not allow to put significant constraints on the absorption column density values.

Similar to the phase-resolved analysis of the separated observations, a few phase bins of the stacked phase-resolved spectra need an additional component to give an acceptable χ^2. This component has been modeled by a Gaussian emission line around 35 keV. An equally good fit is obtained with an absorption Gaussian line at lower energies, i.e., between 16 keV (with $\sigma = 9$ keV, $\eta = 17$), and 21 keV (with $\sigma = 13$ keV, $\eta = 24$).

Recently, Jaisawal, Naik, and Epili (2016) reported of significant pulse phase variation of the cyclotron line energy for GX 304-1 observed with *Suzaku* during two outbursts, the first in August 2010, the second in January 2012 (the same outburst analyzed here). Their findings result in an energy variation up to 17% and 24% for the first and second analyzed outbursts, respectively. A variation of $17 - 24\%$ is consistent (within 2σ) to what found in the present phase-resolved analysis of individual observations, while a variation of 24% is about twice that found in the stacked analysis. However, it is worth to note that, the available statistics from the *Suzaku* observation allows to get 0.1 wide phase-bins with a 90% c.l. error of a few keV (see Fig. 8 in Jaisawal, Naik, and Epili (2016)), and that a different spectral model is used to fit the *Suzaku* spectra, i.e., the partially absorbed NPEX model. The NPEX continuum model is a combination of two power-laws with positive and negative indices and a high-energy cut-off (Makishima et al., 1999). To exclude the possibility that the small variability of the E_{cyc} with pulse phase observed in this work was model-dependent, the partially absorbed NPEX model has also been tested for the phase-resolved spectra. However, this does not yeld to larger variations of the E_{cyc} than the cutoff power-law model (up to 16% using nominal values of the cyclotron line energies). Therefore, the different results obtained by Jaisawal, Naik, and Epili (2016) are likely a consequence of their higher available statistics.

7.1.3.3 A common scenario

Since the timing analysis performed in Sect. 5.3.2 shows a low pulsed fraction ($\sim$ 20%) that is flux- and energy-independent, and both the individual and the stacked phase-resolved analysis (Sect. 7.1.3) show only a small variation of the cyclotron line energy E_{cyc} with pulse phase (up to $\sim$ 16% for nominal values), these results can be interpreted within the context of the same qualitative scenario (as already anticipated in Sect. 7.1.1.2). Indeed, while the observed low and flux-/energy-independent pulsed fraction can be explained in terms of a geometrical configuration that allows the observer to explore only a small portion of the beam pattern, the steadiness of the cyclotron line energy along the pulse phase can be understood in a similar fashion. Model calculations predict a significant ($\sim$ 20%) variation of the cyclotron line energy with the viewing angle, thus, on the pulse phase (see Mukherjee and Bhattacharya 2012, and references therein). However, if the geometrical configuration is such that we are exploring only a small portion of the beam pattern, then the parameters are mostly insensitive to the pulsar rotation. Therefore, the viewing angle at which we observe the accretion column does not vary strongly with the NS rotation, and as a consequence, the E_{cyc} turns out to be almost independent of the rotational phase.

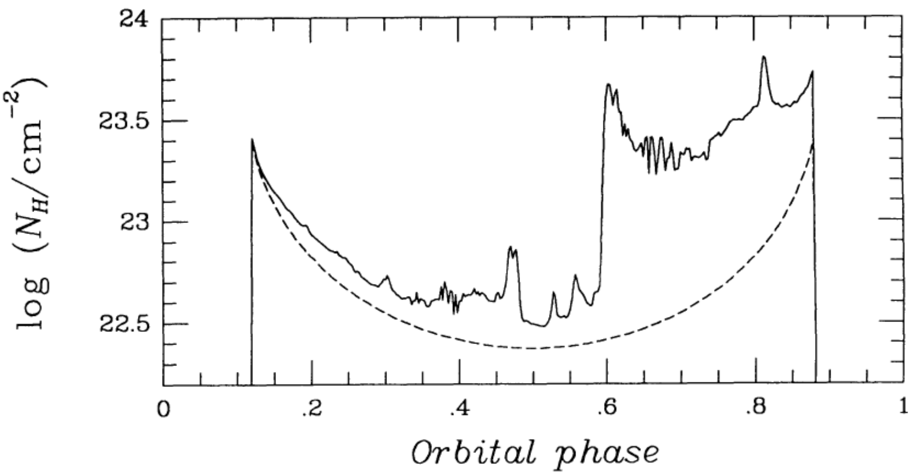

Figure 7.6: Column density as a function of the orbital phase in Vela X-1. Figure from Blondin, Stevens, and Kallman (1991).

7.2 Vela X-1

7.2.1 Double-peaked orbital light curve

The light curve behaviour of the accreting X-ray pulsar Vela X-1 has been explored on a timescale within the orbital period with a very long *MAXI* data set (more than 4 years of continuous observations). Particular attention has been put on the analysis of the orbital profile at the inferior conjunction, with the aim to explore the presence of possible features at the corresponding orbital phase.

7.2.1.1 Previous works

Indications of a double-peaked orbital light curve in Vela X-1 have already been pointed out by earliest observations of the source with *Ariel V* (Eadie et al., 1975; Watson and Griffiths, 1977). Those authors were the first to introduce the concept of an accretion wake, in order to explain the observed feature.

Based on *Tenma* data, Nagase (1989) claimed an increase of the column density along the NS orbit, in particular after the transit phase of the neutron star ($\phi \gtrsim 0.5$). However, at that time it was not clear if the accretion wake was able to reproduce the later phase absorption, or if an additional structure needs to be considered. Blondin, Stevens, and Kallman (1991), taking into account both gravitational and radiative effects (that also consider a more extendend photoionization wake), reproduced the observed orbital phase dependence of the column density and find that the presence of an accretion wake, extended towards the observer's line of sight at the inferior conjuction, produces a local peak in the column density absorption at that orbital phase ($\phi \sim 0.45$, see Fig. 7.6).

Additional constrains on the accretion wake properties in Vela X-1 have been provided by the following authors. Smith (2001), by analyzing He λ1640 absorption line strenghts, inferred the presence of a hot absorber around the transit phase of the NS. Similar results were obtained by Watanabe et al. (2006) who, analyzing *Chandra* data, have inferred the presence of a dense cloud obscuring the compact source at the inferior conjunction. All these results are tightly related to the observational features reported in this work.

7.2.1.2 What do we see at the inferior conjunction?

The presented sample of double-peaked orbital profiles, obtained in this work thanks to the very long *MAXI/GSC* monitoring of Vela X-1, shows a remarkable dip at phase Y ($0.35 < \phi < 0.55$), both in the $4-10$ and the $10-20$ keV band. This makes it difficult to explain solely by absorption caused by neutral matter. In fact, the X-ray flux observed at the dip phase is about half of that in the standard sample (i.e., the sample of orbital light curves which do not show the dip) at the same orbital phase (see Fig. 6.3). To halve a luminosity of $\sim 4 \times 10^{36}$ erg/s in the $10-20$ keV band, a column density value of $\mathrm{N_H} \sim 2 \times 10^{24}\,\mathrm{cm^{-2}}$ is needed, $\sim$10 times larger than that obtained by X-ray spectroscopy in this work (see Table 6.3) or in others.

On the other hand, hydrodynamical simulations of stellar winds in HMXBs (Blondin, Stevens, and Kallman 1991, Manousakis, Walter, and Blondin 2012), predict a local peak of the column density $\mathrm{N_H}$ around the inferior conjunction, of the order of $10^{23}\,\mathrm{cm^{-2}}$ (see Fig. 7.6). X-ray spectral analysis reported in the present work confirms this expectation (see Table 6.3 and Table 6.4). However, the *INTEGRAL* analysis of Fürst et al. (2010) highlights a possible dip-like feature around the transit, in the orbital phase-resolved flux histograms of Vela X-1 at $20-60$ keV, i.e., at an energy band almost unaffected by absorption. Therefore, some additional mechanism must be at work that contributes to the flux reduction at the inferior conjunction, and that is triggered only in a limited sample of orbital cycles.

7.2.1.3 Solving the puzzle: putting evidences together

A contribution to the flux reduction in the dip at the inferior conjunction could come from the Compton scattering at the low energy limit, where the cross-section is characterized by only a weak dependence on the photon energy, and can be approximated by the Thomson scattering cross-section ($\sigma_T = 6.65 \times 10^{-25}\,\mathrm{cm^2}$). In order to efficiently scatter X-rays from the NS, the ambient surrounding the compact object needs to be ionized (to provide free electrons) and dense enough to allow the process. Recent

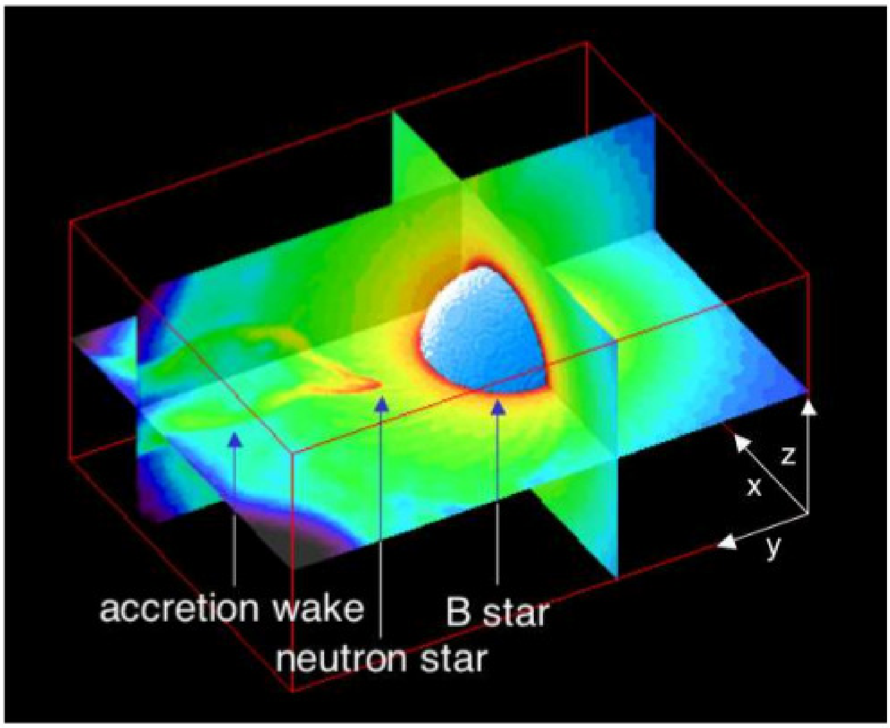

Figure 7.7: Color-coded map of electron density n_e in Vela X-1. Colors indicate variation of $log\, n_e\, [\mathrm{cm}^{-3}] = [7.4, 12.1]$. Note that the lowest values of the n_e refer to the empty zones with darkest colors, not affected by the stellar wind. Figure from Mauche et al. (2008).

hydrodinamical 2D and 3D simulations of stellar winds in Vela X-1 by Mauche et al. (2008) (and by Manousakis, Walter, and Blondin 2012 for HMXB IGR J17252-3616) show that the interaction of the stellar wind with the NS gravitational field leads to strong variations of the wind parameters. These authors find that the accretion wake reaches high temperatures ($\sim 10^8$ K) and is characterized by a high ionization parameter $\xi = L_\mathrm{X}/(n_e\, R_\mathrm{ion}^2) \sim 10^4\,\mathrm{erg\,cm\,s^{-1}}$, where n_e is the electron number density at a given point, R_ion is the distance from that point to the X-ray source, L_X is the source X-ray luminosity. The accretion wake extends up to scales of the order of the optical companion size ($R \sim 10^{12}$ cm). Its electron number density is $\sim 10^{9-12}\,\mathrm{cm}^{-3}$ (see Fig. 7.7) which, taking an average value of $n_e \sim 10^{10}\,\mathrm{cm}^{-3}$, leads to a column density of $\sim 10^{23}\,\mathrm{cm}^{-2}$. This value is comparable to the values obtained from the spectral analysis of the double-peaked sample in the Y phase bin (see Section 7.2.2.2 and Table 6.3).

If a considerable part of material in the accretion wake is ionized, it does not contribute to the photoelectric absorption column density (which reflects only neutral gas), but it nonetheless scatters a given amount of the original flux F_0 out of the line of sight. The resulting flux F, is given by:

$$F = F_0\, e^{-(n_e\, \sigma_T\, l)} \tag{7.2}$$

where l is the length over which the given electron density n_e is extendend (i.e., the accretion wake size). The argument of the exponential (its absolute value) is the *optical* *depth* τ:

$$d\tau = n_e\,\sigma_T\,dl \tag{7.3}$$

where the integral of the electron density n_e extended over a length l gives the column density N_H, in case of neutral matter:

$$N_H = \int n_e\,dl \tag{7.4}$$

To halve the original flux F, an optical depth of $\tau \simeq 0.69$ is necessary which, for an accretion wake size of $l = 2 \times 10^{12}$ cm, needs an electron density of $n_e = 5 \times 10^{11}\,\mathrm{cm}^{-3}$, i.e., an amount of matter that is well in agreement with the expectations from Mauche et al. (2008). This is 50 times the above-used electron density, thus implying that the electron density observable by means of the X-ray absorption is only a small fraction of the total amount present in the accretion wake.

Moreover, the bremsstrahlung cooling time is of the order of $10^{11}\sqrt{T[\mathrm{K}]}/n_\mathrm{e}[\mathrm{cm}^{-2}]$ s (Rybicki and Lightman, 1979). Using the above-mentioned values ($T = 10^8$[K], $n_\mathrm{e} = 10^{10}\,\mathrm{cm}^{-3}$), the resulting bremsstrahlung cooling time is $\sim 10^5$ s, i.e., about one day, which is in agreement with the observed time duration of the dip.

In other words, the gas is ionized and dense enough to allow efficient Thomson scattering for a time long enough to allow the dip of the observed duration. Thus, when the ionized stream of the accretion wake passes through the observer's direction, i.e., during the transit, a substantial part of the X-ray radiation can be efficiently scattered out of our line of sight. This scenario is further supported by the normalization of the power-law component, which appears to be modulated along the orbit (see Table 6.3), indicating for an intrinsically dimmer flux at the inferior conjunction (although large parameters uncertainties need to be considered).

Stellar wind variability is most likely responsible for the accretion wake modifications, which in turn modify the orbital light curve shape, alternating double-peaked and standard morphologies.

7.2.2 Spectral results

7.2.2.1 Orbital phase-averaged spectroscopy

Orbital phase-averaged spectra in the $2-20$ keV energy range have been extracted for both the double-peaked and the standard sample. The two samples have then been fitted with a cutoff power-law model, to which a blackbody component has been added to account for the soft excess, and with an absorption partial covering model (see Sect. 5.5.1.1 and 6.5 for the analytical expressions of such models, shortned as *bbody*cutoffpl* and *pcfabs*powerlaw*, respectively). Results are given in Table 6.2. For the double-peaked sample, both models return a good fit of the phase-averaged spectrum.

On the other hand, for the phase-averaged spectrum of the standard sample the cutoff power-law model describes the data better than the partial covering model. For a given sample, the best-fit parameters are often inconsistent (within 3σ) between the two tested models. However, there is only marginal difference between the best-fit parameters of the two samples fitted by the same model.

Due to the inhomogeneous environment in which the NS travels along its orbit, our phase-averaged results are not straightforward to interprete. These results have only been used to avoid unphysical best-fit solutions of the orbital phase-resolved spectra, fixing some of the model parameters to their phase-averaged values (see Sections 7.2.2.2 and 7.2.2.3).

In the next sections, the orbital-phase resolved spectroscopy of double-peaked and standard samples will be discussed separately.

7.2.2.2 Phase-resolved spectroscopy of the double-peaked sample

Orbital-phase resolved spectra of the double-peaked sample were fitted with the same models used for the analysis of the phase-averaged spectra: a cutoff power-law plus blackbody component and an absorption partial covering model. Both models fit the spectra well. Adopting the former model results in an orbital modulation of the photon index which, to the best of our knowledge, has never been observed in Vela X-1 (see Table 6.3). The observed spectral modulation is characterized by a hardening of the emitted X-ray spectrum around the inferior conjunction (Y phase bin), with respect to earlier and later phases (X and Z phase bins, respectively). Contour plots for two parameters of interest (N_{H} and Γ) are shown in Fig. 6.13, and appear clearly distinct from one phase bin to another, indicating that the modulation is not due to the intrinsic coupling between the two parameters.

Similar results are reported by Prat et al. (2008). These authors use both a phenomenological model (an absorbed cutoff power-law model) and a more physical Comptonization model (Titarchuk, 1994) to fit orbital phase-resolved spectra of the HMXB IGR J19140+0951. Their results indicate photon index modulation along the binary orbit of the source. These authors ascribe the observed orbital modulation to a region of stagnant wind trailing the compact object, producing a spectral soft excess when it is hit by the stellar wind. The observed soft excess is visible only at certain configurations of the binary, that is, only at certain orbital phases, and it is modeled by an additional blackbody component. Since we do not observe any modulation of the blackbody component, our study does not support the same interpretation for Vela X-1orbital modulation of the photon index.

Since the photon index Γ is determined by the emission mechanisms at the polar caps of a NS (see Sect. 3.5), its variation with orbital phase is not expected and difficult to explain.

As a consequence, the analysis has been focused on the partial covering model, which does not show orbital modulation of the photon index. Instead, it shows increasing of

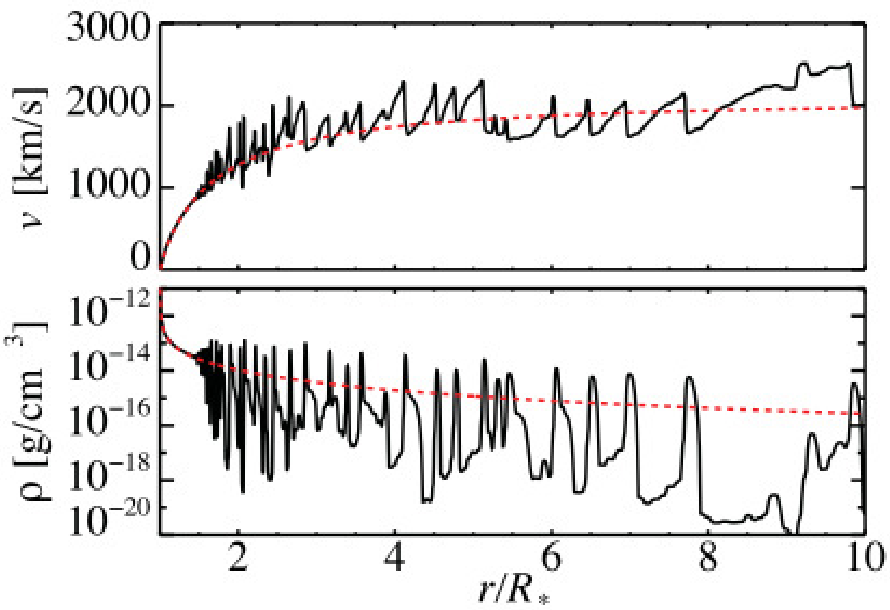

Figure 7.8: Density and velocity variations in OB-stars winds as a function of the distance from the stellar surface. Sensible variations start to form at larger distances than the NS orbital radius in Vela X-1, i.e., after 1.1 $R_\star$ (see text). Figure from Sundqvist and Owocki (2013).

the absorption column density for orbital phases $\phi \gtrsim 0.5$ (see Sec. 7.2.2.3 for a more comprehensive discussion about this result), with a partial covering component with high covering fraction needed at the Y phase bin but not required at earlier or later phases (see Table 6.3). A possible interpretation of this behaviour is given by the oscillation of the accretion wake (Blondin et al., 1990). Due to orbit-to-orbit variations of the ambient wind, the tail of the accretion wake is expected to oscillate with respect to our line of sight. This effect is enhanced when observed at the inferior conjunction, when the accretion wake is extended towards the observer. Averaging this behaviour over several orbital periods would result in a covering fraction $0 < f < 1$, where the wobbling accretion wake represents an inhomogeneous absorbing environment.

An alternative interpretation might be that an intrinsically inhomogeneous structure is present around the inferior conjunction and partially (i.e., temporarily) covers the X-ray source. Inhomogeneous stellar winds from supergiant stars (i.e., *clumps*) are expected (Runacres and Owocki, 2005) and observed (Goldstein, Huenemoerder, and Blank 2004, and references therein), and have been suggested as the reason for the flaring activity in Vela X-1 (see Kreykenbohm et al. 2008 and Martínez-Núñez et al. 2014). The timescale for clumps hitting the NS is of the order of the wind's dynamic timescale

$$\frac{0.5R_\mathrm{B}}{v_\infty} \sim \frac{10^{11}\,\mathrm{cm}}{1100\,\mathrm{km/s}} \sim 1000\,\mathrm{s} \tag{7.5}$$

where $0.5\,\mathrm{R_B}$ is the average separation between clumps (Sundqvist, Puls, and Feldmeier, 2010). Thus, if we look at the X-ray source on longer timescales, the resulting effect is a partially absorbed spectrum. However, if the partial covering was due to the inhomogeneous structure of the ambient wind, there would not be any modulation of this component with the orbital phase. On the contrary, our results require the partial covering only for the Y phase bin spectra, where the obscuration effect of the accretion wake is maximized. Hydrodinamical simulations (Blondin et al., 1990; Blondin, Stevens, and Kallman, 1991) revealed that the accretion wake is composed by compressed filaments of gas as well as by rarefied bubbles. Morever, recent models also show that density perturbations (that is, clumps) in stellar winds of OB stars only develop at distances larger than the NS orbital radius in Vela X-1 ($r \sim 1.1\,R_\star$, see Fig. 2 in Sundqvist and Owocki 2013, reproduced in Fig. 7.8). Therefore, intrisic stellar wind clumps around the X-ray pulsar in Vela X-1 may not be structured enough to trigger the observed high X-ray flux variability.

On the other hand, the inhomogeneous structure characterizing the accretion wake proves that the compact object is able to perturbate the ambient wind such that clumps are formed as the NS travels in the medium. The gravitational sphere of influence of the NS is dictated by its accretion radius, $r_{\rm acc}{\sim}10^{11}\,{\rm cm}$ (Feldmeier et al., 1996), while its ionizing sphere of influence is dictated by the Strömgren sphere defined by the photoionization parameter $\xi = L_x/(n_e\,R_{\rm ion}^2)$, which leads (see Sec. 7.2.1 for parameters definitions and values) to a photoionization radius $R_{\rm ion} \sim 0.2R_B \sim 6 \times 10^{11}\,{\rm cm} \sim r_{\rm acc}$. Since the orbital velocity of the NS is $v_{\rm orbit} \approx 280\,{\rm km/s}$, the perturbation timescale is of the order of

$$t_{\rm pert} = \frac{R_{\rm ion}}{v_{\rm orbit}} \approx 2 \times 10^4\,{\rm s} \sim 5.5\,{\rm h} \tag{7.6}$$

which can be considered as an upper limit for the X-ray variability induced by accretion of *locally formed clumps*. This is consistent with observations of flares in Vela X-1 lasting from 10^2 s up to 10^4 s (see Ducci et al. 2009; Martínez-Núñez et al. 2014, and references therein). Moreover, the perturbation timescale $\rm t_{pert}$ is also very similar to the coherence time of $\sim$ 6 hours found in Sect. 6.4.1.2

Even though the inhomogeneous structure characteristic of the accretion wake might be a possible reason for the observed partial covering around the inferior conjunction, it can not be directly probed within the context of our *MAXI* analysis, which only allows to infer the long-timescale properties of the source averaged over several orbital phase bins.

High-resolution spectroscopic observations carried out at critical orbital phases are necessary in future to discriminate among different models and constrain stellar wind scenarios and accretion modalities in Vela X-1.

7.2.2.3 Phase-resolved spectroscopy of the standard sample

Phase-resolved spectra of the standard sample have been modelled with a cutoff power-law model and with an absorption partial covering model. The cutoff power-law including a soft blackbody component fits the seven phase-resolved spectra well (see Table 6.4). However, this model shows the same spectral modulation trend as observed in the double-peaked sample case (see Section 6.6.1), with harder spectra around the inferior conjunction with respect to earlier and later phases (see ϕ_5 in Fig. 6.15). The modulation shows a hardening of the spectra of about $\Delta\Gamma{\sim}0.35$ in terms of the photon index, which is approximately the same value as observed in the double-peaked sample. However, compared with the latter, the standard sample phase-resolved spectra show generally softer values of the spectral photon index. As already pointed out in Sec. 7.2.2.2, a physical mechanism for such an orbital dependence of the photon index is not known. Thus, the partial covering model represents a more phyisical scenario.

Fitting the phase-resolved spectra with a partial covering model shows that neutral matter column density $\mathrm{N_H}$ increases along the orbital phase. More specifically, the $\mathrm{N_H}$ shows a general increase towards later phases, varying from $\sim 10^{22}\mathrm{cm}^{-2}$ after the eclipse egress (ϕ_1), to $\sim 10^{23}\,\mathrm{cm}^{-2}$ before the eclipse ingress (ϕ_7). This is in agreement with earlier studies of Vela X-1 (see, e.g., Nagase 1989), and a similar phenomenon has been observed in other HMXBs as well, e.g., in 4U 1700-37 (Haberl, White, and Kallman, 1989). Based on the analysis of both optical (Carlberg, 1978; Kaper, Hammerschlag-Hensberge, and Zuiderwijk, 1994) and X-ray data (Feldmeier et al., 1996), it has been shown that the accretion wake is not adequate to explain the later phase ($\phi > 0.5$) absorption, and that a more extendend photoionization wake is necessary.

Using the partial covering model, the spectral photon index modulation along the orbital phase is only marginal. Similarly to the double-peaked sample, the partial covering component is included only at certain phase bins. Based on the best-fit results of this model, it is possible to apply here a similar interpretation as for the double-peaked sample results, i.e. an inhomogeneous ambient which produces strong absorption of the X-ray emission, and whose absorption efficiency depends on the orbital phase (see Sec. 7.2.2.2). The column density shows a local peak of $N_{\mathrm{H}}^{pc}{\sim}3 \times 10^{23}\,\mathrm{cm}^{-2}$ around the inferior conjunction, similar to what is observed for the double-peaked sample, strengthening the connection with the accretion wake. Moreover, for this sample, the partial covering component is needed also for the phase bin ϕ_2, which is around the NS greatest eastern elongation (see Fig. 6.1). Whether the partial covering is due to a wobbling or an inhomogeneous accretion wake, these results hint to a wake that comes into play at earlier phases than the inferior conjunction.

In conclusion, the absorbing (and likely inhomogeneous) material which partially covers the NS, could be due to a varying influence of the accretion wake at different orbital phases.

8

SUMMARY AND CONCLUSIONS

In this work, observational data of two accreting pulsars have been analysed: GX 304-1 and Vela X-1. The data are taken by the *INTEGRAL* observatory for GX 304-1, and by *MAXI* for Vela X-1. The obtained results contribute to characterize the two accreting binary X-ray pulsars. Study of the Be/X-Ray Binary GX 304-1 allowed a better understanding of the physics of the accretion column, while the analysis of the wind-fed Vela X-1 allowed to study the ambient wind structures and the X-ray orbital variability that they lead to.

The main results are summarized in the following for each source separately.

8.1 *INTEGRAL* observations of GX 304-1

- ISGRI ($18 - 80\,\mathrm{keV}$) and JEM-X ($3 - 20\,\mathrm{keV}$) pulse profiles have been obtained for GX 304-1, and a period derivative has been measured throughout the outburst event, which is a likely indication of spin-up due to angular momentum transferred by the accreted material from an accretion disk.
- Pulse profiles show a strong energy- and luminosity-dependence. The energy dependence can be interpreted in terms of a geometrical effect arising from the rotation of the neutron star or from a sligthly distorted magnetic dipole field, while the luminosity dependence probably reflects changes in the beaming pattern at different accretion regimes. The only exception to this energy-dependence is represented by the pulse profiles at the end of the outburst (Rev. 1138), where a single broad peak is observed, likely reflecting a switch to pencil-beam pattern at low luminosities.
- The positive luminosity dependence of the cyclotron line energy has been confirmed with a more precise instrumental calibration. GX 304-1 is confirmed to be the X-ray accreting pulsar with the most significant correlation between the cyclotron line energy and the flux.
- Photon index and cutoff energy correlations with luminosity have been investigated. These correlations fit well in the context of an emergent spectrum shaped by Comptonization of blackbody seed photons radiating from the accretion mound and scattered off hot accreting electrons. In this context, the observed spectral changes are a consequence of the increasing Compton cooling efficiency at higher luminosity.

- The phase-resolved spectral analysis shows that the cyclotron line is detectable at all rotational phases. The maximum reached centroid energy (~62 keV) allowed to infer one of the strongest magnetic fields on an accreting X-ray pulsar.
- Observations seem to favor a remarkably stable cyclotron line energy with pulse phase. However, a variation up to 20 % is still consistent with the present results (due to the large uncertainties).
- Both the timing and spectral results are consistent with a qualitative geometrical scenario in which, as the pulsar rotates, only a small portion of its beaming pattern is explored by the observer.
- A few phase-resolved spectra need an additional component to fit large residuals at ∼ 35 keV. Phase-resolved spectra show that the feature is phase-locked while varying in energy at different luminosities. This feature most likely indicates that the underlying phenomenological model is inadequate, rather than physical changes in the conditions creating the feature.

8.2 *MAXI* analysis of Vela X-1

- About 15% of the orbital light curves in Vela X-1 shows a double-peaked orbital profile, with a ~1.5 days dip around the inferior conjunction, both in 4 – 10 keV and 10 – 20 keV energy bands.
- Explaining the dip around the inferior conjunction by solely absorption requires column density values of $\sim 2 \times 10^{24}\,\mathrm{cm}^{-2}$, which are not observed in our analysis or in others.
- The dip in the double-peaked sample could be produced considering contribution from Thomson scattering by an ionized accretion wake that is elongated toward the observer during the transit. Intrinsic variability of the stellar wind leads to strong variations of the accretion wake, included its density and ionization degree, thus alternating double-peaked and standard profiles.
- The ususal phenomenological cutoff power-law model results inadequate to fit orbital-phase resolved spectra of Vela X-1. Instead, we modeled the spectra using a partial covering component around the inferior conjunction. This component indicates a highly inhomogeneous environment and local column density peak values of $\sim 3 \times 10^{23}\,\mathrm{cm}^{-2}$ around the inferior conjunction (orbital phases around the eclipse have not been analyzed).
- Our results suggest either a wobbling or an inhomogeneous accretion wake as the reason for partial covering around the inferior conjunction. Moreover, the absorption properties of the accretion wake seem to take place at earlier phases than the inferior conjunction.

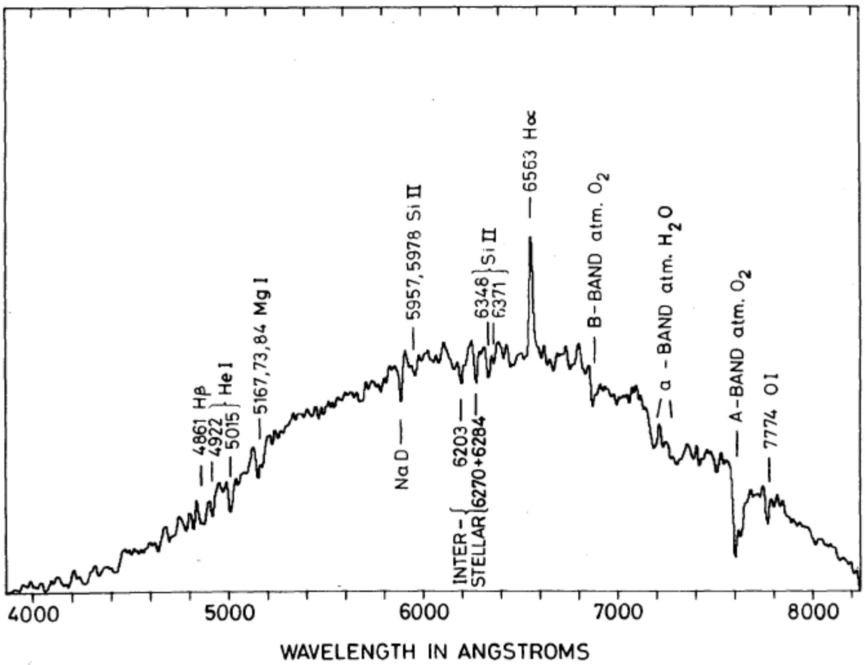

Figure 8.1: Optical spectrum of V850 Cen obtained with the RGO spectrograph at the Anglo-Australian Telescope. The main spectral features are labelled, while the overall shape of the spectrum reflects primarily the instrumental response. Figure from Mason et al. (1978).

- Gravitational and radiative effects from the X-ray pulsar may be responsible of locally induced clumps in the ambient wind that successively feed the observed high X-ray variability.
- Some of the analyzed orbital phase-resolved spectra do not need a partial covering component. Therefore, spectral analysis of Vela X-1 needs to consider the orbital phase at which the observation has been carried out.

8.3 Future prospects

8.3.1 Optical observations of GX 304-1

Future analysis of GX 304-1 is already planned with the aim of further investigating the system's properties and the interaction between the NS and the Be disk. The author of this thesis has been leading an intensive optical campaign to observe the binary system at different orbital phases. Optical observations of BeXRBs are crucial for (at least) two main reasons. First, the optical spectrum of the Be companion contains a wealth

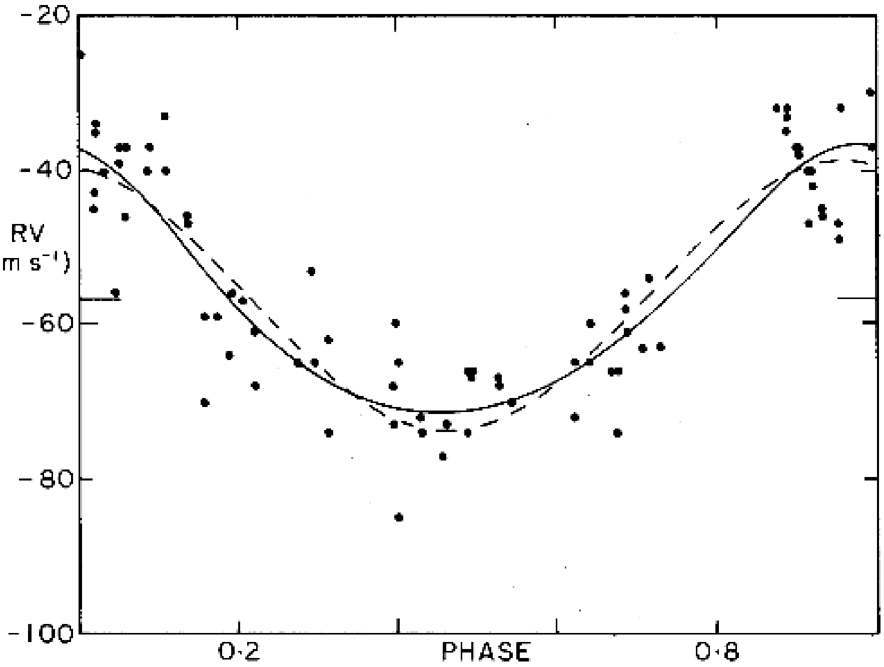

Figure 8.2: Radial velocities of absorption lines as a function of the orbital phase for the BeXRB 2S 0114+650. The solid and the dotted lines represent two orbital solutions fitted to the data points. Figure from Crampton, Hutchings, and Cowley (1985).

of information on the decretion disk status. In fact, emission lines (Hα in particular) detection, profile, intensity and variability can constrain the size and the geometry of the decretion disk (see, e.g., Reig et al. 2007), and therefore furnish useful insights on the feeding mechanism of the accreting pulsar. Second, optical observations of the Be star can constrain the ephemeris of the binary system. This may be accomplished if the optical companion presents suitable absorption lines that can be used to measure the Doppler shift they undergo as a consequence of the gravitational pull from the NS. Fortunately, an optical spectrum of V850 Cen had already been obtained by Mason et al. (1978). This spectrum is shown in Fig. 8.1 (a higher resolution spectrum is available in Parkes, Murdin, and Mason 1980). It shows a number of absorption lines that are intrinsic to V850 Cen, and are therefore suitable for the radial velocity measurements (e.g., HeI 4471, FeII 6516, SiII 6371). An example of the application of this method is shown in Fig. 8.2. Although orbital ephemeris for GX 304-1 have been recently derived by Sugizaki et al. (2015), an independent derivation of the orbital parameters can be of great scientific relevance.

Such a scientific rationale turns out to be even more intriguing if one considers the outburst activity of GX 304-1 in 2012, due to the peculiar X-ray activity shown by the source. A plot that illustrates such episodes is shown in Fig. 5.3, and argued in Sec. 5.1.1.

Driven by these motivations, the optical campaign has been successfully accomplished. A series of 7 optical broad-band medium-resolution spectra has been collected. The first observation has been carried out on the 16th of April, 2014 at the Anglo-Australian

Telescope (AAT) as a partial fullfillment of a 6 hours retrived observing time. Part of the obtained AAT spectrum is shown in Fig. 8.3. In this plot, a number of features can be noticed: a double-peaked Hα emission line, a structured HeI 7065 emission line, and a HeI 6678 emission line with a P Cyg profile.

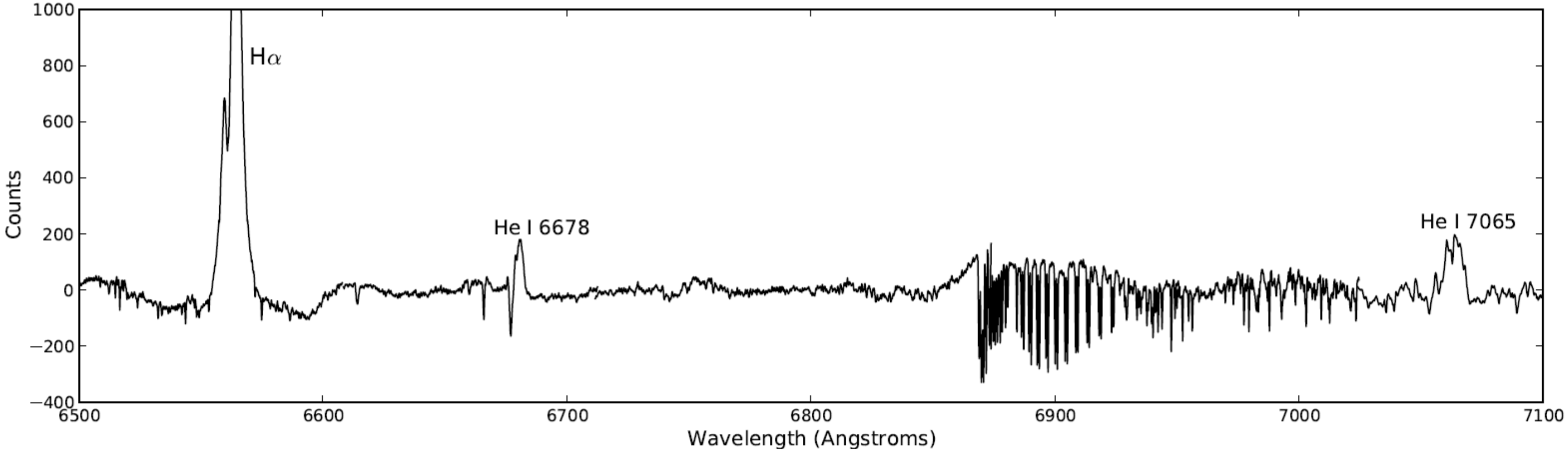

Figure 8.3: Optical spectrum of V850 Cen in the 6500 – 7100 Åband. This spectrum has been optained on April 2014, as a part of the optical campaign carried out specifically to study the binary and Be disk properties of this system (see text). Prominent emission lines are labelled.

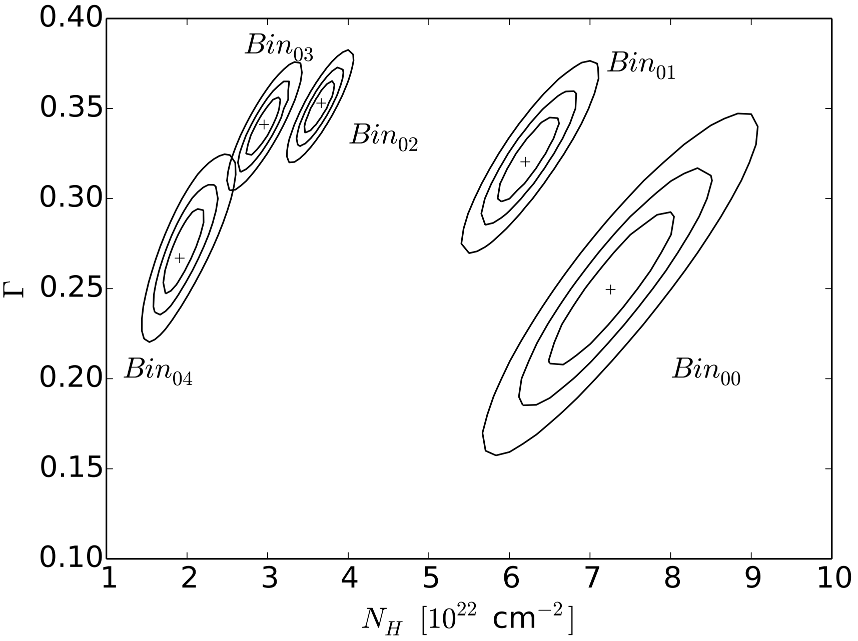

Figure 8.4: χ^2-contour plots for Vela X-1 flux-resolved spectra fitted with a cutoff power-law model. The ellipses represent χ^2-contours for two parameters of interest (N_H and Γ). The contours correspond to $\chi^2_{\mathrm{min}} + 1.0$ (the projections of this contour to the parameter axes correspond to the 68%-uncertainty for one parameter of interest), $\chi^2_{\mathrm{min}} + 2.3$ (68%-uncertainty for two parameters of interest), and $\chi^2_{\mathrm{min}} + 4.61$ (90%-uncertainty for two parameters of interest). Flux bins are indicated as increasing from Bin_{00} to Bin_{04}.

The next set of 6 observations has been carried out at the South African Large Telescope (SALT) during an entire orbital period of the binary system between February and April 2015. The entire optical campaign has therefore furnished a considerable amount of features and spectra. This data represent an important source of information, and are currently under analysis.

8.3.2 Flux-resolved analysis of Vela X-1

Also planned for the future, is a complementary analysis of Vela X-1 to corroborate the present study. The next investigation will possibly take into account a flux-resolved spectroscopy of the X-ray source. This technique is important to explore the behaviour of the pulsar at different flux levels, thus investigating possible spectral changes with flux, with special regard to the flaring activity which is characteristic of Vela X-1.

An example of such an analysis is shown in Fig. 8.4, for a data set correspondent to the standard sample light curves of Sec. 6.4. Here, χ^2-contour plots are shown for two parameters of the fitting model. The fitting model is a cutoff power-law, while the two plotted parameters are the photon index Γ and the column density N_H. A number of flux bins equal to 5 has been chosen to preliminary explore the available statistics. The analyzed flux bins are labelled by Bin_{0i}, with $i = 0, ..., 4$, where the flux increases from $i = 0$ to $i = 4$. From the plot it can be noticed that the photon index Γ seems to favor a stable spectral hardness disregarding the flux level. However, large uncertainties prevent to firmly explore the actual behaviour of the spectral parameter, especially at lower fluxes. The plot also shows a significant increase of the column density at lower fluxes. This is expected, since the lower flux levels are likely representing the ingress and egress phases, where the photoionization wake effects are more prominent, thus leading to a sensible absorption of the observed X-ray flux.

In the future, flux-resolved spectroscopy of Vela X-1 can be carried out with more *MAXI*/GSC data, in order to increase the available statistics, and also with other facilities, to take advantage of more sensible instruments. For example, *INTEGRAL* data are available for Vela X-1 for a total observational time of the order of 10^6 s, and would allow broadband spectroscopy along with investigation of the pulse profiles variability at different flux levels. High spectral resolution and broader energy band would be ideal also to test different spectral models for different flux-resolved spectra, thus investigating possible changes in the X-ray emission processes.

Finally, the same technique used in this work to analyze Vela X-1 light curves and spectra can be applied to other sources as well. Particularly interesting is the case of other wind-fed HMXBs, especially for binary systems with a small separation and a strong stellar wind, where the gravitational and radiative effects are comparable to those of Vela X-1. Suitable candidates for such a study are Cen X-3 (Naik, Paul, and Ali, 2011) and 4U 1538-52 (Rodes-Roca et al., 2015).

Bibliography

Agrawal, P. C. (Jan. 2006). “A broad spectral band Indian Astronomy satellite *Astrosat*”. In: *Advances in Space Research* 38, pp. 2989–2994. DOI: `10.1016/j.asr.2006.03.038`.

Anders, E. and N. Grevesse (Jan. 1989). “Abundances of the elements - Meteoritic and solar”. In: Geochimica Cosmochimica Acta 53, pp. 197–214. DOI: `10.1016/0016-7037(89)90286-X`.

Araya, R. A. and A. K. Harding (Nov. 1996). “Cylotron line models for the X-ray pulsar A 0535+26.” In: A&AS 120, p. C183. eprint: `arXiv:astro-ph/9606074`.

Arimoto, M. et al. (Feb. 2015). “Wide-Field MAXI: soft X-ray transient monitor”. In: *ArXiv e-prints*. arXiv: `1502.03675 [astro-ph.IM]`.

Arnaud, K. A. (1996). “XSPEC: The First Ten Years”. In: *Astronomical Data Analysis Software and Systems V*. Ed. by G. H. Jacoby and J. Barnes. Vol. 101. Astronomical Society of the Pacific Conference Series, p. 17.

Baade, W. and F. Zwicky (May 1934). “Cosmic Rays from Super-novae”. In: *Proceedings of the National Academy of Science* 20, pp. 259–263. DOI: `10.1073/pnas.20.5.259`.

Basko, M. M. and R. A. Sunyaev (Sept. 1975). “Radiative transfer in a strong magnetic field and accreting X-ray pulsars”. In: A&A 42, pp. 311–321.

– (May 1976). “The limiting luminosity of accreting neutron stars with magnetic fields”. In: MNRAS 175, pp. 395–417.

Becker, P. A. and M. T. Wolff (Mar. 2005). “Spectral Formation in X-Ray Pulsar Accretion Columns”. In: ApJ 621, pp. L45–L48. DOI: `10.1086/428927`. eprint: `arXiv:astro-ph/0501434`.

– (Jan. 2007). “Thermal and Bulk Comptonization in Accretion-powered X-Ray Pulsars”. In: ApJ 654, pp. 435–457. DOI: `10.1086/509108`. eprint: `arXiv:astro-ph/0609035`.

Becker, P. A. et al. (Aug. 2012). “Spectral formation in accreting X-ray pulsars: bimodal variation of the cyclotron energy with luminosity”. In: A&A 544, A123, A123. DOI: `10.1051/0004-6361/201219065`. arXiv: `1205.5316 [astro-ph.HE]`.

Becker, W. (2009). *Neutron Stars and Pulsars*. Astrophysics and Space Science Library. Springer Berlin Heidelberg. ISBN: 9783540769651. URL: `https://books.google.de/books?id=APD5UiG-VJQC`.

Bellm, E. C. et al. (Sept. 2014). “Confirmation of a High Magnetic Field in GRO J1008-57”. In: ApJ 792, 108, p. 108. DOI: `10.1088/0004-637X/792/2/108`. arXiv: `1403.5249 [astro-ph.HE]`.

Bildsten, L. et al. (Dec. 1997). “Observations of Accreting Pulsars”. In: ApJS 113, pp. 367–408. DOI: `10.1086/313060`. eprint: `astro-ph/9707125`.

Blondin, J. M., I. R. Stevens, and T. R. Kallman (Apr. 1991). “Enhanced winds and tidal streams in massive X-ray binaries”. In: ApJ 371, pp. 684–695. DOI: `10.1086/169934`.

Blondin, J. M. et al. (June 1990). “Hydrodynamic simulations of stellar wind disruption by a compact X-ray source”. In: ApJ 356, pp. 591–608. DOI: `10.1086/168865`.

Blum, S. and U. Kraus (Feb. 2000). “Analyzing X-Ray Pulsar Profiles: Geometry and Beam Pattern of Hercules X-1”. In: ApJ 529, pp. 968–977. DOI: `10.1086/308308`. eprint: `astro-ph/9909449`.

Boella, G. et al. (Apr. 1997). “BeppoSAX, the wide band mission for X-ray astronomy”. In: A&AS 122, pp. 299–307. DOI: `10.1051/aas:1997136`.

Bondi, H. and F. Hoyle (1944). “On the mechanism of accretion by stars”. In: MNRAS 104, p. 273.

Bouchet, L. et al. (Feb. 2013). “Simultaneous analysis of large INTEGRAL/SPI[1] datasets: Optimizing the computation of the solution and its variance using sparse matrix algorithms”. In: *Astronomy and Computing* 1, pp. 59–69. DOI: `10.1016/j.ascom.2013.03.002`. arXiv: `1305.5683 [astro-ph.IM]`.

Burderi, L. et al. (Feb. 2000). “The 0.1-100 KEV Spectrum of Centaurus X-3: Pulse Phase Spectroscopy of the Cyclotron Line and Magnetic Field Structure”. In: ApJ 530, pp. 429–440. DOI: `10.1086/308336`.

Caballero, I. et al. (Apr. 2013). “INTEGRAL IBIS/ISGRI energy calibration in OSA 10”. In: *[arXiv:1304.1349]*. arXiv: `1304.1349 [astro-ph.IM]`.

Canizares, C. R. (1990). “The advanced X-ray Astrophysics Facility (AXAF)”. In: *Advances in Space Research* 10, pp. 261–272. DOI: `10.1016/0273-1177(90)90151-O`.

Carlberg, R. G. (1978). *PhD Thesis*. The University of British Columbia (Canada).

Caroli, E. et al. (Sept. 1987). “Coded aperture imaging in X- and gamma-ray astronomy”. In: Space Sci. Rev. 45, pp. 349–403. DOI: `10.1007/BF00171998`.

Casares, J. et al. (Jan. 2014). “A Be-type star with a black-hole companion”. In: Nature 505, pp. 378–381. DOI: `10.1038/nature12916`. arXiv: `1401.3711 [astro-ph.SR]`.

Castor, J. I., D. C. Abbott, and R. I. Klein (Jan. 1975). “Radiation-driven winds in Of stars”. In: ApJ 195, pp. 157–174. DOI: `10.1086/153315`.

Chadwick, J. (1932). “POSSIBLE EXISTENCE OF A NEUTRON”. In: *Nature* 129, p. 312. DOI: `10.1038/129312a0`.

Chandrasekhar, S. (July 1931). “The Maximum Mass of Ideal White Dwarfs”. In: ApJ 74, p. 81. DOI: `10.1086/143324`.

Chodil, G. et al. (Oct. 1967). “X-Ray Intensities and Spectra from Several Cosmic Sources”. In: ApJ 150, p. 57. DOI: `10.1086/149312`.

Clark, Stephen.

Coburn, W. et al. (Nov. 2002). “Magnetic Fields of Accreting X-Ray Pulsars with the Rossi X-Ray Timing Explorer”. In: *ApJ* 580, pp. 394–412.

Crampton, D., J. B. Hutchings, and A. P. Cowley (Dec. 1985). “The supergiant X-ray binary system 2S 0114 + 650”. In: ApJ 299, pp. 839–844. DOI: `10.1086/163750`.

Das, U. and B. Mukhopadhyay (June 2014). “Maximum mass of stable magnetized highly super-Chandrasekhar white dwarfs: stable solutions with varying magnetic fields”. In: J. Cosmology Astropart. Phys. 6, 050, p. 050. DOI: `10.1088/1475-7516/2014/06/050`. arXiv: `1404.7627 [astro-ph.SR]`.

Davidson, K. (Nov. 1973). “Accretion at a Magnetic Pole of a Neutron Star”. In: *Nature Physical Science* 246, pp. 1–4. DOI: `10.1038/physci246001a0`.

Davidson, K. and J. P. Ostriker (Jan. 1973). “Neutron-Star Accretion in a Stellar Wind: Model for a Pulsed X-Ray Source”. In: ApJ 179, pp. 585–598. DOI: `10.1086/151897`.

Deeter, J. E., P. E. Boynton, and S. H. Pravdo (Aug. 1981). “Pulse-timing observations of Hercules X-1”. In: ApJ 247, pp. 1003–1012. DOI: `10.1086/159110`.

Devasia, J. et al. (Oct. 2011). “Timing and spectral studies of the transient X-ray pulsar GX 304-1 during an outburst”. In: MNRAS 417, pp. 348–358. DOI: `10.1111/j.1365-2966.2011.19269.x`. arXiv: `1106.3251 [astro-ph.HE]`.

Doroshenko, V. et al. (June 2013). “Footprints in the wind of Vela X-1 traced with MAXI”. In: A&A 554, A37, A37. DOI: `10.1051/0004-6361/201321305`. arXiv: `1304.5965 [astro-ph.HE]`.

Dubath, P. et al. (2005). “The INTEGRAL spectrometer SPI: performance of point-source data analysis”. In: *Monthly Notices of the Royal Astronomical Society* 357.2, pp. 420–428. ISSN: 1365-2966. DOI: `10.1111/j.1365-2966.2005.08675.x`. URL: `http://dx.doi.org/10.1111/j.1365-2966.2005.08675.x`.

Ducci, L. et al. (Oct. 2009). “The structure of blue supergiant winds and the accretion in supergiant high-mass X-ray binaries”. In: MNRAS 398, pp. 2152–2165. DOI: `10.1111/j.1365-2966.2009.15265.x`. arXiv: `0906.3185 [astro-ph.HE]`.

Eadie, G. et al. (Sept. 1975). “Ariel V Sky Survey - Observations of the accretion wake in Vel X-1”. In: MNRAS 172, 35P–39P.

Edgar, R. (Sept. 2004). “A review of Bondi-Hoyle-Lyttleton accretion”. In: New Astron. Rev. 48, pp. 843–859. DOI: `10.1016/j.newar.2004.06.001`. eprint: `astro-ph/0406166`.

Eggleton, P. P. (May 1983). “Approximations to the radii of Roche lobes”. In: ApJ 268, p. 368. DOI: `10.1086/160960`.

Feldmeier, A. et al. (July 1996). “VELA X-1: how to produce asymmetric eclipses.” In: A&A 311, pp. 793–802.

Ferrigno, C. et al. (May 2013). “RX J0440.9 + 4431: a persistent Be/X-ray binary in outburst”. In: A&A 553, A103, A103. DOI: `10.1051/0004-6361/201321053`. arXiv: `1303.7087 [astro-ph.HE]`.

Forman, W. et al. (Dec. 1978). “The fourth Uhuru catalog of X-ray sources.” In: ApJS 38, pp. 357–412. DOI: `10.1086/190561`.

Frank, J., A. King, and D. Raine (1992). *Accretion power in astrophysics.*

Fransson, C. and A. C. Fabian (July 1980). “X-ray induced shocks in stellar winds”. In: A&A 87, pp. 102–108.

Friedman, H., S. W. Lichtman, and E. T. Byram (Sept. 1951). “Photon Counter Measurements of Solar X-Rays and Extreme Ultraviolet Light”. In: *Physical Review* 83, pp. 1025–1030. DOI: `10.1103/PhysRev.83.1025`.

Fürst, F. et al. (Sept. 2010). “X-ray variation statistics and wind clumping in Vela X-1”. In: A&A 519, A37, A37. DOI: `10.1051/0004-6361/200913981`. arXiv: `1005.5243 [astro-ph.HE]`.

Fürst, F. et al. (Jan. 2014). “NuSTAR Discovery of a Luminosity Dependent Cyclotron Line Energy in Vela X-1”. In: ApJ 780, 133, p. 133. DOI: `10.1088/0004-637X/780/2/133`. arXiv: `1311.5514 [astro-ph.HE]`.

Gehrels, N. et al. (Aug. 2004). “The Swift Gamma-Ray Burst Mission”. In: ApJ 611, pp. 1005–1020. DOI: `10.1086/422091`.

Gendreau, K. C., Z. Arzoumanian, and T. Okajima (Sept. 2012). “The Neutron star Interior Composition ExploreR (NICER): an Explorer mission of opportunity for soft x-ray timing spectroscopy”. In: *Society of Photo-Optical Instrumentation Engineers (SPIE) Conference Series.* Vol. 8443. Society of Photo-Optical Instrumentation Engineers (SPIE) Conference Series, p. 13. DOI: `10.1117/12.926396`.

Ghosh, P. and F. K. Lamb (Nov. 1979). “Accretion by rotating magnetic neutron stars. III - Accretion torques and period changes in pulsating X-ray sources”. In: ApJ 234, pp. 296–316. DOI: `10.1086/157498`.

Giacconi, R. et al. (Dec. 1962). “Evidence for x Rays From Sources Outside the Solar System”. In: *Physical Review Letters* 9, pp. 439–443. DOI: `10.1103/PhysRevLett.9.439`.

Giacconi, R. et al. (Apr. 1971). “An X-Ray Scan of the Galactic Plane from UHURU”. In: ApJ 165, p. L27. DOI: `10.1086/180711`.

Giacconi, R. et al. (June 1979). “The Einstein /HEAO 2/ X-ray Observatory”. In: ApJ 230, pp. 540–550. DOI: `10.1086/157110`.

Goldstein, G., D. P. Huenemoerder, and D. Blank (Apr. 2004). “Variation in Emission and Absorption Lines and Continuum Flux by Orbital Phase in Vela X-1”. In: AJ 127, pp. 2310–2321. DOI: `10.1086/382514`. eprint: `astro-ph/0403495`.

Goldwurm, A. et al. (Nov. 2003). “The INTEGRAL/IBIS scientific data analysis”. In: A&A 411, pp. L223–L229. DOI: `10.1051/0004-6361:20031395`. eprint: `arXiv:astro-ph/0311172`.

Haberl, F., N. E. White, and T. R. Kallman (Aug. 1989). “An EXOSAT X-ray observation of one orbital cycle of 4U 1700-37/HD 153919”. In: ApJ 343, pp. 409–425. DOI: `10.1086/167714`.

Harding, A. K. and A. G. Muslimov (June 1998). “Pulsar X-Ray and Gamma-Ray Pulse Profiles: Constraint on Obliquity and Observer Angles”. In: ApJ 500, pp. 862–872. DOI: `10.1086/305763`. eprint: `astro-ph/9802038`.

Harrison, F. A. et al. (June 2013). “The Nuclear Spectroscopic Telescope Array (NuSTAR) High-energy X-Ray Mission”. In: ApJ 770, 103, p. 103. DOI: `10.1088/0004-637X/770/2/103`. arXiv: `1301.7307 [astro-ph.IM]`.

Heger, A. et al. (July 2003). “How Massive Single Stars End Their Life”. In: ApJ 591, pp. 288–300. DOI: `10.1086/375341`. eprint: `astro-ph/0212469`.

Hertzsprung, E. (1911). “Ueber die Verwendung photographischer effektiver Wellenlaengen zur Bestimmung von Farbenaequivalenten”. In: *Publikationen des Astrophysikalischen Observatoriums zu Potsdam* 63.

Hewish, A. et al. (Feb. 1968). “Observation of a Rapidly Pulsating Radio Source”. In: Nature 217, pp. 709–713. DOI: `10.1038/217709a0`.

Hickox, R. C., R. Narayan, and T. R. Kallman (Oct. 2004). “Origin of the Soft Excess in X-Ray Pulsars”. In: ApJ 614, pp. 881–896. DOI: `10.1086/423928`. eprint: `astro-ph/0407115`.

Hoyle, F. and R. A. Lyttleton (1939). “The effect of interstellar matter on climatic variation”. In: *Proceedings of the Cambridge Philosophical Society* 35, p. 405. DOI: `10.1017/S0305004100021150`.

Hynes, R. I. (Oct. 2010). “Multiwavelength Observations of Accretion in Low-Mass X-ray Binary Systems”. In: *ArXiv e-prints*. arXiv: `1010.5770 [astro-ph.HE]`.

Iben Jr., I. (May 1991). “Single and binary star evolution”. In: ApJS 76, pp. 55–114. DOI: `10.1086/191565`.

Iben Jr., I. and A. V. Tutukov (Feb. 1984). “Supernovae of type I as end products of the evolution of binaries with components of moderate initial mass (M not greater than about 9 solar masses)”. In: ApJS 54, pp. 335–372. DOI: `10.1086/190932`.

Illarionov, A. F. and R. A. Sunyaev (Feb. 1975). “Why the Number of Galactic X-ray Stars Is so Small?” In: A&A 39, p. 185.

in't Zand, J. J. M., J. Heise, and R. Jager (Aug. 1994). "The optimum open fraction of coded apertures. With an application to the wide field X-ray cameras of SAX". In: A&A 288, pp. 665–674.

Iyer, N. et al. (June 2015). "Variations in the Cyclotron Resonant Scattering Features during 2011 outburst of 4U 0115+63". In: *[arXiv:1506.03376]*. arXiv: `1506.03376 [astro-ph.HE]`.

Jackson, J. C. (Sept. 1975). "Parameters of CEN X-3 deduced from observations of its accretion wake". In: MNRAS 172, pp. 483–492.

Jaisawal, G. K., S. Naik, and P. Epili (Jan. 2016). "Suzaku view of Be/X-ray binary pulsar GX 304-1 during Type I X-ray outbursts". In: *ArXiv e-prints*. arXiv: `1601.02348 [astro-ph.SR]`.

Jenke, P. et al. (Nov. 2012). "Giant outburst of the Be X-ray binary GX 304-1". In: *The Astronomer's Telegram* 4547.

Joanes, D. N. and C. A. Gill (1998). "Comparing measures of sample skewness and kurtosis". In: *Journal of the Royal Statistical Society: Series D (The Statistician)* 47.1, pp. 183–189. ISSN: 1467-9884. DOI: `10.1111/1467-9884.00122`. URL: `http://dx.doi.org/10.1111/1467-9884.00122`.

Kahabka, P. et al. (Oct. 2006). "The super-soft source XMMU J052016.0-692505 in the LMC. A likely white dwarf Be/X-ray binary". In: A&A 458, pp. 285–292. DOI: `10.1051/0004-6361:20065490`.

Kaper, L., G. Hammerschlag-Hensberge, and J. T. van Loon (Nov. 1993). "Observations of stellar winds in high-mass X-ray binaries: Evidence for a non-monotonic velocity structure". In: A&A 279, pp. 485–498.

Kaper, L., G. Hammerschlag-Hensberge, and E. J. Zuiderwijk (Sept. 1994). "Spectroscopic evidence for photo-ionization wakes in VELA X-1 and 4U 1700–37". In: A&A 289, pp. 846–854.

Klochkov, D. et al. (May 2008). "INTEGRAL observations of Hercules X-1". In: A&A 482, pp. 907–915. DOI: `10.1051/0004-6361:20078953`. arXiv: `0802.1168`.

Klochkov, D. et al. (Aug. 2011). "Pulse-amplitude-resolved spectroscopy of bright accreting pulsars: indication of two accretion regimes". In: A&A 532, A126, A126. DOI: `10.1051/0004-6361/201116800`. arXiv: `1107.2202 [astro-ph.HE]`.

Klochkov, D. et al. (June 2012). "Outburst of GX 304-1 monitored with INTEGRAL: positive correlation between the cyclotron line energy and flux". In: A&A 542, L28, p. L28. DOI: `10.1051/0004-6361/201219385`. arXiv: `1205.5475 [astro-ph.HE]`.

Kraus, U. (Dec. 2001). "Hollow Accretion Columns on Neutron Stars and the Effects of Gravitational Light Bending". In: ApJ 563, pp. 289–300. DOI: `10.1086/323791`.

Kraus, U. et al. (Sept. 1995). "Analyzing X-Ray Pulsar Profiles: Asymmetry as a Key to Geometry and Beam Pattern". In: ApJ 450, p. 763. DOI: `10.1086/176182`.

Kraus, U. et al. (Aug. 1996). "Analyzing X-Ray Pulsar Profiles: Geometry and Beam Pattern of Centaurus X-3". In: ApJ 467, p. 794. DOI: `10.1086/177653`.

Kraus, U. et al. (June 2003). "X-Ray Pulses from Accretion Columns: Contributions to the Energy Dependence of the Pulse Shape". In: ApJ 590, pp. 424–431. DOI: `10.1086/375011`.

Kreykenbohm, I. (2004). *PhD Thesis*. Eberhard-Karls-Universität Tübingen (Germany).

Kreykenbohm, I. et al. (Dec. 2004). “The variable cyclotron line in GX 301-2”. In: A&A 427, pp. 975–986. DOI: `10.1051/0004-6361:20035836`. eprint: `arXiv:astro-ph/0409015`.

Kreykenbohm, I. et al. (Dec. 2008). “High variability in Vela X-1: giant flares and off states”. In: A&A 492, pp. 511–525. DOI: `10.1051/0004-6361:200809956`. arXiv: `0810.2981`.

Kuster, M. (2003). “Combined Spectral and Temporal Analysis of a Her X-1 Turn-On”. In: *Ph.D. thesis, University of Tübingen*.

La Barbera, A. et al. (Aug. 2005). “A study of an orbital cycle of GX 301-2 observed by BeppoSAX”. In: A&A 438, pp. 617–632. DOI: `10.1051/0004-6361:20041509`.

Lai, D. (Jan. 2014). “Theory of Disk Accretion onto Magnetic Stars”. In: *European Physical Journal Web of Conferences*. Vol. 64. European Physical Journal Web of Conferences, p. 1001. DOI: `10.1051/epjconf/20136401001`. arXiv: `1402.1903 [astro-ph.SR]`.

Landau, L. D. (Dec. 1932). “To the Stars theory”. In: *Phys. Zs. Sowjet., vol.1, p.285, 1932 (English and German)* 1, p. 285.

Large, M. I., A. E. Vaughan, and B. Y. Mills (Oct. 1968). “A Pulsar Supernova Association?” In: Nature 220, pp. 340–341. DOI: `10.1038/220340a0`.

Latal, H. G. (Oct. 1986). “Cyclotron radiation in strong magnetic fields”. In: ApJ 309, pp. 372–382. DOI: `10.1086/164609`.

Lattimer, J. M. and M. Prakash (Apr. 2004). “The Physics of Neutron Stars”. In: *Science* 304, pp. 536–542. DOI: `10.1126/science.1090720`. eprint: `astro-ph/0405262`.

– (Apr. 2007). “Neutron star observations: Prognosis for equation of state constraints”. In: Phys. Rep. 442, pp. 109–165. DOI: `10.1016/j.physrep.2007.02.003`. eprint: `astro-ph/0612440`.

Leahy, D. A. (June 1987). “Searches for pulsed emission - Improved determination of period and amplitude from epoch folding for sinusoidal signals”. In: A&A 180, pp. 275–277.

Lebrun, F. et al. (Nov. 2003). “ISGRI: The INTEGRAL Soft Gamma-Ray Imager”. In: A&A 411, pp. L141–L148. DOI: `10.1051/0004-6361:20031367`. eprint: `astro-ph/0310362`.

Lewin, W. H. G., G. W. Clark, and W. B. Smith (Apr. 1968). “Observation of CEN XR-2 and Other High-Energy X-Ray Sources in the Southern Sky”. In: ApJ 152, p. L49. DOI: `10.1086/180176`.

Lewin, W. H. G., J. van Paradijs, and E. P. J. van den Heuvel (Jan. 1997). *X-ray Binaries*.

Li, K. L. et al. (Dec. 2012). “A Luminous Be+White Dwarf Supersoft Source in the Wing of the SMC: MAXI J0158-744”. In: ApJ 761, 99, p. 99. DOI: `10.1088/0004-637X/761/2/99`. arXiv: `1207.5023 [astro-ph.HE]`.

Lipunov, V. M. (1987). *The astrophysics of neutron stars*.

Longair, M. S. (1981). *High energy astrophysics*.

Longinotti, A. L. et al. (Nov. 2003). “The complex FeK line of the Narrow-Line Seyfert 1 galaxy IRAS 13349+2438”. In: A&A 410, pp. 471–479. DOI: `10.1051/0004-6361:20031124`. eprint: `astro-ph/0307461`.

Lorimer, D. R. and M. Kramer (Oct. 2012). *Handbook of Pulsar Astronomy*.

Lovelace, R. V. E., M. M. Romanova, and G. S. Bisnovatyi-Kogan (July 1995). “Spin-up/spin-down of magnetized stars with accretion discs and outflows”. In: MNRAS 275, pp. 244–254. eprint: `astro-ph/9412030`.

Lund, N. et al. (Nov. 2003). “JEM-X: The X-ray monitor aboard INTEGRAL”. In: A&A 411, pp. L231–L238. DOI: `10.1051/0004-6361:20031358`.

Lutovinov, A. and S. Tsygankov (Sept. 2008). “X-ray pulsars through the eyes of INTEGRAL”. In: *American Institute of Physics Conference Series*. Ed. by M. Axelsson. Vol. 1054. American Institute of Physics Conference Series, pp. 191–202. DOI: `10.1063/1.3002502`. arXiv: `0808.2034`.

Maitra, C. and B. Paul (Feb. 2013). “Pulse-phase-resolved Spectroscopy of Vela X-1 with Suzaku”. In: ApJ 763, 79, p. 79. DOI: `10.1088/0004-637X/763/2/79`. arXiv: `1212.1538 [astro-ph.HE]`.

Makishima, K. et al. (Nov. 1999). “Cyclotron Resonance Effects in Two Binary X-Ray Pulsars and the Evolution of Neutron Star Magnetic Fields”. In: ApJ 525, pp. 978–994. DOI: `10.1086/307912`.

Malacaria, C. et al. (Sept. 2015). “Luminosity-dependent spectral and timing properties of the accreting pulsar GX 304-1 measured with INTEGRAL”. In: A&A 581, A121, A121. DOI: `10.1051/0004-6361/201526417`. arXiv: `1507.00595 [astro-ph.HE]`.

Malacaria, C. et al. (Jan. 2016). “Probing the stellar wind environment of Vela X-1 with MAXI”. In: *ArXiv e-prints*. arXiv: `1601.07735 [astro-ph.HE]`.

Manousakis, A., R. Walter, and J. M. Blondin (Nov. 2012). “Neutron star masses from hydrodynamical effects in obscured supergiant high mass X-ray binaries”. In: A&A 547, A20, A20. DOI: `10.1051/0004-6361/201219717`. arXiv: `1210.2952 [astro-ph.HE]`.

Manousakis, A. et al. (July 2008). “INTEGRAL hard X-ray detection of HMXB GX 304-1 and H 1417-624”. In: *The Astronomer’s Telegram* 1613, p. 1.

Maraschi, L., A. Treves, and E. P. J. van den Heuvel (Jan. 1976). “B-emission stars and X-ray sources”. In: Nature 259, p. 292. DOI: `10.1038/259292a0`.

Martínez-Núñez, S. et al. (Mar. 2014). “The accretion environment in Vela X-1 during a flaring period using XMM-Newton”. In: A&A 563, A70, A70. DOI: `10.1051/0004-6361/201322404`. arXiv: `1401.2848 [astro-ph.HE]`.

Mason, K. O. et al. (Aug. 1978). “The optical counterpart of GX 304-1”. In: MNRAS 184, 45P–48P.

Mason, K. O. et al. (July 1995). “The XMM observatory”. In: *Advances in Space Research* 16, pp. 41–50. DOI: `10.1016/0273-1177(95)00207-U`.

Matsuoka, M. et al. (Oct. 2009). “The MAXI Mission on the ISS: Science and Instruments for Monitoring All-Sky X-Ray Images”. In: PASJ 61, pp. 999–. DOI: `10.1093/pasj/61.5.999`. arXiv: `0906.0631 [astro-ph.IM]`.

Mauche, C. W. et al. (Sept. 2008). “The Physics of Wind-Fed Accretion”. In: *American Institute of Physics Conference Series*. Ed. by M. Axelsson. Vol. 1054. American Institute of Physics Conference Series, pp. 3–11. DOI: `10.1063/1.3002508`. arXiv: `0806.1073`.

Mayer, W. F. (Dec. 1975). “The SAS-3 X-ray observatory”. In: *Johns Hopkins APL Technical Digest* 14, pp. 14–22.

McClintock, J. E. et al. (Aug. 1977). “Discovery of a 272 second periodic variation in the X-ray source GX 304-1”. In: ApJ 216, pp. L15–L18. DOI: `10.1086/182499`.

Mereghetti, S. (2011). “X-ray emission from isolated neutron stars”. In: *High-Energy Emission from Pulsars and their Systems*. Ed. by D. F. Torres and N. Rea, p. 345. DOI: `10.1007/978-3-642-17251-9_29`. arXiv: `1008.2891 [astro-ph.HE]`.

Merloni, A. et al. (Sept. 2012). “eROSITA Science Book: Mapping the Structure of the Energetic Universe”. In: *ArXiv e-prints*. arXiv: `1209.3114 [astro-ph.HE]`.

Mihara, T., K. Makishima, and F. Nagase (Oct. 1998). “Cyclotron line variability”. In: *Advances in Space Research* 22, pp. 987–996. DOI: `10.1016/S0273-1177(98)00128-8`.

Mihara, T. et al. (July 1990). “New observations of the cyclotron absorption feature in Hercules X-1”. In: Nature 346, pp. 250–252. DOI: `10.1038/346250a0`.

Mihara, T. et al. (Aug. 2010). “MAXI/GSC detects an outburst from a Be/X-ray binary GX 304-1”. In: *The Astronomer’s Telegram* 2779, p. 1.

Mihara, T. et al. (Nov. 2011). “Gas Slit Camera (GSC) onboard MAXI on ISS”. In: PASJ 63, p. 623. DOI: `10.1093/pasj/63.sp3.S623`. arXiv: `1103.4224 [astro-ph.IM]`.

Mihara, T. et al. (July 2014). “MAXI: all-sky observation from the International Space Station”. In: *Space Telescopes and Instrumentation 2014: Ultraviolet to Gamma Ray*. Vol. 9144. Proc. SPIE, 91441O. DOI: `10.1117/12.2055792`. arXiv: `1410.6245 [astro-ph.HE]`.

Mitsuda, K. et al. (Oct. 2004). “Astro-E2 mission”. In: *Society of Photo-Optical Instrumentation Engineers (SPIE) Conference Series*. Ed. by G. Hasinger and M. J. L. Turner. Vol. 5488. Society of Photo-Optical Instrumentation Engineers (SPIE) Conference Series, pp. 177–186. DOI: `10.1117/12.562697`.

Moritani, Y. et al. (Aug. 2013). “Precessing Warped Be Disk Triggering the Giant Outbursts in 2009 and 2011 in A0535+262/V725Tau”. In: PASJ 65, p. 83. DOI: `10.1093/pasj/65.4.83`. arXiv: `1304.4649 [astro-ph.SR]`.

Morrison, R. and D. McCammon (July 1983). “Interstellar photoelectric absorption cross sections, 0.03-10 keV”. In: ApJ 270, pp. 119–122. DOI: `10.1086/161102`.

Morton, D. C. (Aug. 1964). “Neutron Stars as X-Ray Sources.” In: ApJ 140, p. 460. DOI: `10.1086/147940`.

Mowlavi, N. et al. (May 2006). “INTEGRAL observation of the high-mass X-ray transient V 0332+53 during the 2005 outburst decline”. In: A&A 451, pp. 187–194. DOI: `10.1051/0004-6361:20054235`. eprint: `astro-ph/0512414`.

Mukherjee, D. and D. Bhattacharya (Feb. 2012). “A phase-dependent view of cyclotron lines from model accretion mounds on neutron stars”. In: MNRAS 420, pp. 720–731. DOI: `10.1111/j.1365-2966.2011.20085.x`. arXiv: `1110.2850 [astro-ph.HE]`.

Müller et al. (Apr. 2013). “A 0535+26 in the April 2010 outburst: probing the accretion regime at work”. In: A&A 552, A81, A81. DOI: `10.1051/0004-6361/201220347`. arXiv: `1303.6068 [astro-ph.HE]`.

Müller et al. (Mar. 2013). “No anticorrelation between cyclotron line energy and X-ray flux in 4U 0115+634”. In: A&A 551, A6, A6. DOI: `10.1051/0004-6361/201220359`. arXiv: `1211.6298 [astro-ph.HE]`.

Munar-Adrover, P. et al. (May 2014). “Discovery of X-Ray Emission from the First Be/Black Hole System”. In: ApJ 786, L11, p. L11. DOI: `10.1088/2041-8205/786/2/L11`. arXiv: `1404.0901 [astro-ph.HE]`.

Mushtukov, A. A. et al. (Dec. 2015a). “Positive correlation between the cyclotron line energy and luminosity in sub-critical X-ray pulsars: Doppler effect in the accretion channel”. In: MNRAS 454, pp. 2714–2721. DOI: `10.1093/mnras/stv2182`. arXiv: `1509.05628 [astro-ph.HE]`.

Mushtukov, A. A. et al. (Feb. 2015b). “The critical accretion luminosity for magnetized neutron stars”. In: MNRAS 447, pp. 1847–1856. DOI: `10.1093/mnras/stu2484`. arXiv: `1409.6457 [astro-ph.HE]`.

Nagase, F. (1989). “Accretion-powered X-ray pulsars”. In: PASJ 41, pp. 1–79.

Naik, S. and B. Paul (Dec. 2012). “Investigation of variability of iron emission lines in Centaurus X-3”. In: *Bulletin of the Astronomical Society of India* 40, p. 503. arXiv: `1212.0949 [astro-ph.SR]`.

Naik, S., B. Paul, and Z. Ali (Aug. 2011). “X-Ray Spectroscopy of the High-mass X-Ray Binary Pulsar Centaurus X-3 over Its Binary Orbit”. In: ApJ 737, 79, p. 79. DOI: `10.1088/0004-637X/737/2/79`. arXiv: `1106.0370 [astro-ph.SR]`.

Naik, S. et al. (Mar. 2009). “Orbital phase spectroscopy of four high mass X-ray binary pulsars to study the stellar wind of the companion”. In: *Advances in Space Research* 43, pp. 900–904. DOI: `10.1016/j.asr.2008.12.011`. arXiv: `0812.4519`.

Nakajima, M. et al. (Aug. 2006). “A Further Study of the Luminosity-dependent Cyclotron Resonance Energies of the Binary X-Ray Pulsar 4U 0115+63 with the Rossi X-Ray Timing Explorer”. In: *ApJ* 646, pp. 1125–1138.

Nakajima, M. et al. (Feb. 2014). “Precursors and outbursts of A 0535+26 in 2009-2011 observed by the MAXI/GSC and the Swift/BAT”. In: PASJ 66, 9, p. 9. DOI: `10.1093/pasj/pst002`. arXiv: `1308.5498 [astro-ph.HE]`.

Nandra, K. et al. (June 2013). “The Hot and Energetic Universe: A White Paper presenting the science theme motivating the Athena+ mission”. In: *ArXiv e-prints*. arXiv: `1306.2307 [astro-ph.HE]`.

Nelson, R. W., E. E. Salpeter, and I. Wasserman (Dec. 1993). “Nonthermal Cyclotron Emission from Low-Luminosity Accretion onto Magnetic Neutron Stars”. In: ApJ 418, p. 874. DOI: `10.1086/173445`.

Odaka, H. et al. (Apr. 2013). “Short-term Variability of X-Rays from Accreting Neutron Star Vela X-1. I. Suzaku Observations”. In: ApJ 767, 70, p. 70. DOI: `10.1088/0004-637X/767/1/70`. arXiv: `1304.5838 [astro-ph.HE]`.

Okazaki, A. T., K. Hayasaki, and Y. Moritani (Apr. 2013). “Origin of Two Types of X-Ray Outbursts in Be/X-Ray Binaries. I. Accretion Scenarios”. In: PASJ 65, p. 41. DOI: `10.1093/pasj/65.2.41`. arXiv: `1211.5225 [astro-ph.HE]`.

Oppenheimer, J. R. and G. M. Volkoff (Feb. 1939). “On Massive Neutron Cores”. In: *Physical Review* 55, pp. 374–381. DOI: `10.1103/PhysRev.55.374`.

Owocki, S. P. (1994). “The Basic Physics of Hot-Star Winds”. In: *Pulsation; Rotation; and Mass Loss in Early-Type Stars.* Ed. by L. A. Balona, H. F. Henrichs, and J. M. Le Contel. Vol. 162. IAU Symposium, p. 475.

Pacini, F. (Nov. 1967). “Energy Emission from a Neutron Star”. In: Nature 216, pp. 567–568. DOI: `10.1038/216567a0`.

Paczynski, B. (1976). “Common Envelope Binaries”. In: *Structure and Evolution of Close Binary Systems.* Ed. by P. Eggleton, S. Mitton, and J. Whelan. Vol. 73. IAU Symposium, p. 75.

Parkes, G. E., P. G. Murdin, and K. O. Mason (Feb. 1980). “The shell spectrum of the optical counterpart of GX 304-1 /4U 1258-61/”. In: MNRAS 190, pp. 537–542.

Peterson, L. E. (1975). “Instrumental technique in X-ray astronomy”. In: ARA&A 13, pp. 423–509. DOI: `10.1146/annurev.aa.13.090175.002231`.

Pfahl, E. et al. (July 2002). “A New Class of High-Mass X-Ray Binaries: Implications for Core Collapse and Neutron Star Recoil”. In: ApJ 574, pp. 364–376. DOI: `10.1086/340794`. eprint: `astro-ph/0109521`.

Phillips, A. C. (July 1999). *The Physics of Stars, 2nd Edition*, p. 262.

Pietsch, W. et al. (July 1986). “EXOSAT observations of GX 304-1 in an X-ray off state”. In: A&A 163, pp. 93–96.

Postnov, K. A. et al. (Sept. 2015). “On the dependence of the X-ray continuum variations with luminosity in accreting X-ray pulsars”. In: MNRAS 452, pp. 1601–1611. DOI: `10.1093/mnras/stv1393`. arXiv: `1506.07082 [astro-ph.HE]`.

Poutanen, J. et al. (Nov. 2013). “A Reflection Model for the Cyclotron Lines in the Spectra of X-Ray Pulsars”. In: ApJ 777, 115, p. 115. DOI: `10.1088/0004-637X/777/2/115`. arXiv: `1304.2633 [astro-ph.HE]`.

Prada Moroni, P. G. and O. Straniero (Dec. 2009). “Very low-mass white dwarfs with a C-O core”. In: A&A 507, pp. 1575–1583. DOI: `10.1051/0004-6361/200912847`. arXiv: `0909.2742 [astro-ph.SR]`.

Prat, L. et al. (Sept. 2008). “Peering through the stellar wind of IGR J19140+0951 with simultaneous INTEGRAL/RXTE observations”. In: MNRAS 389, pp. 301–310. DOI: `10.1111/j.1365-2966.2008.13558.x`. arXiv: `0806.1973`.

Priedhorsky, W. C. and J. Terrell (Oct. 1983). “Long-term X-ray observations of CEN X-3, GX 301-2 (4U 1223-62), GX 304-1 (4U 1258-61) and 4U 1145-61”. In: ApJ 273, pp. 709–715. DOI: `10.1086/161406`.

Pringle, J. E. and M. J. Rees (Oct. 1972). “Accretion Disc Models for Compact X-Ray Sources”. In: A&A 21, p. 1.

Prinja, R. K., M. J. Barlow, and I. D. Howarth (Oct. 1990). “Terminal velocities for a large sample of O stars, B supergiants, and Wolf-Rayet stars”. In: ApJ 361, pp. 607–620. DOI: `10.1086/169224`.

Rawls, M. L. et al. (Mar. 2011). “Refined Neutron Star Mass Determinations for Six Eclipsing X-Ray Pulsar Binaries”. In: ApJ 730, 25, p. 25. DOI: `10.1088/0004-637X/730/1/25`. arXiv: `1101.2465 [astro-ph.SR]`.

Reig, P. and E. Nespoli (Mar. 2013). “Patterns of variability in Be/X-ray pulsars during giant outbursts”. In: A&A 551, A1, A1. DOI: `10.1051/0004-6361/201219806`. arXiv: `1212.5944 [astro-ph.HE]`.

Reig, P. et al. (Feb. 2007). “The Be/X-ray transient 4U 0115+63/V635 Cassiopeiae. III. Quasi-cyclic variability”. In: A&A 462, pp. 1081–1089. DOI: `10.1051/0004-6361:20066217`. eprint: `astro-ph/0611516`.

Riffert, H. and P. Meszaros (Feb. 1988). “Gravitational light bending near neutron stars. I - Emission from columns and hot spots”. In: ApJ 325, pp. 207–217. DOI: `10.1086/165996`.

Ritz, S. M. et al. (Dec. 2007). “The Gamma-ray Large Area Space Telescope (GLAST) Mission”. In: *American Astronomical Society Meeting Abstracts*. Vol. 39. Bulletin of the American Astronomical Society, p. 909.

Rodes-Roca, J. J. et al. (Aug. 2015). “Orbital phase-resolved spectroscopy of 4U 1538-52 with MAXI”. In: A&A 580, A140, A140. DOI: `10.1051/0004-6361/201425323`. arXiv: `1507.04274 [astro-ph.HE]`.

Roger, C.M., I. Pérez-Fournon, and F. Sanchez (1999). *Globular Clusters*. Cambridge Contemporary Astrophysics. Cambridge University Press. ISBN: 9780521770583. URL: `https://books.google.de/books?id=fJKOBr2aMAQC`.

Rosenberg, H. (Oct. 1910). "Über den Zusammenhang von Helligkeit und Spektraltypus in den Plejaden". In: *Astronomische Nachrichten* 186, p. 71. DOI: `10.1002/asna.19101860503`.

Runacres, M. C. and S. P. Owocki (Jan. 2005). "A pseudo-planar, periodic-box formalism for modelling the outer evolution of structure in spherically expanding stellar winds". In: A&A 429, pp. 323–333. DOI: `10.1051/0004-6361:20041281`. eprint: `astro-ph/0405315`.

Russell, H. N. (May 1914). "Relations Between the Spectra and Other Characteristics of the Stars". In: *Popular Astronomy* 22, pp. 275–294.

Rybicki, G. B. and A. P. Lightman (1979). *Radiative processes in astrophysics*. New York, Wiley-Interscience, 1979.

Salpeter, E. E. (Aug. 1964). "Accretion of Interstellar Matter by Massive Objects." In: ApJ 140, pp. 796–800. DOI: `10.1086/147973`.

Santangelo, A. and R. Madonia (Jan. 2014). "Fifty years of X-ray astronomy: A look back and into the (near) future". In: *Astroparticle Physics* 53, pp. 130–151. DOI: `10.1016/j.astropartphys.2013.11.005`.

Santangelo, A. et al. (Sept. 1999). "A BEPPOSAX Study of the Pulsating Transient X0115+63: The First X-Ray Spectrum with Four Cyclotron Harmonic Features". In: ApJ 523, pp. L85–L88. DOI: `10.1086/312249`.

Sartore, N., E. Jourdain, and J.-P. Roques (Apr. 2015). "The INTEGRAL/SPI view of A0535+26 during the giant outburst of February 2011". In: *[ArXiv: 1504.03726]*. arXiv: `1504.03726 [astro-ph.HE]`.

Schanne, S. et al. (2007). "INTEGRAL Observations of the Vela Region Focusing on Vela X-l". In: *ESA Special Publication*. Vol. 622. ESA Special Publication, p. 479. eprint: `astro-ph/0701641`.

Schönherr, G. et al. (Sept. 2007). "A model for cyclotron resonance scattering features". In: A&A 472, pp. 353–365. DOI: `10.1051/0004-6361:20077218`. arXiv: `0707.2105`.

Shakura, N., K. Postnov, and L. Hjalmarsdotter (Jan. 2013). "On the nature of 'off' states in slowly rotating low-luminosity X-ray pulsars". In: MNRAS 428, pp. 670–677. DOI: `10.1093/mnras/sts062`. arXiv: `1209.4962 [astro-ph.HE]`.

Shakura, N. I. and R. A. Sunyaev (1973). "Black holes in binary systems. Observational appearance." In: A&A 24, pp. 337–355.

Shen, Z.-J. and J.-F. Zhou (June 2008). "Improving the Angular Resolution of Coded-Mask Telescopes by Direct Demodulation". In: Chinese J. Astron. Astrophys. 8, pp. 343–348. DOI: `10.1088/1009-9271/8/3/11`.

Shklovsky, I. S. (Apr. 1967). "On the Nature of the Source of X-Ray Emission of SCO XR-1." In: ApJ 148, p. L1. DOI: `10.1086/180001`.

Sidoli, L. et al. (Feb. 2015). "Probing large-scale wind structures in Vela X-1 using off-states with INTEGRAL". In: MNRAS 447, pp. 1299–1303. DOI: `10.1093/mnras/stu2533`. arXiv: `1411.7869 [astro-ph.HE]`.

Skinner, G. K. and T. J. Ponman (Apr. 1994). "On the Properties of Images from Coded Mask Telescopes". In: MNRAS 267, p. 518. DOI: `10.1093/mnras/267.3.518`.

Smith, J. F. and G. M. Courtier (Oct. 1976). “The Ariel 5 Programme”. In: *Royal Society of London Proceedings Series A* 350, pp. 421–439. DOI: `10.1098/rspa.1976.0115`.

Smith, M. A. (Dec. 2001). “Ultraviolet Spectrophotometry of Variable Early-Type Be and B Stars Derived from High-Resolution IUE Data”. In: ApJ 562, pp. 998–1011. DOI: `10.1086/323846`. eprint: `astro-ph/0107186`.

Soffitta, P. et al. (Dec. 2013). “XIPE: the X-ray imaging polarimetry explorer”. In: *Experimental Astronomy* 36, pp. 523–567. DOI: `10.1007/s10686-013-9344-3`. arXiv: `1309.6995 [astro-ph.HE]`.

Staelin, D. H. and E. C. Reifenstein III (Dec. 1968). “Pulsating Radio Sources near the Crab Nebula”. In: *Science* 162, pp. 1481–1483. DOI: `10.1126/science.162.3861.1481`.

Staubert, R. et al. (Apr. 2007). “Discovery of a flux-related change of the cyclotron line energy in Hercules X-1”. In: A&A 465, pp. L25–L28. DOI: `10.1051/0004-6361:20077098`. eprint: `astro-ph/0702490`.

Staubert, R. et al. (Dec. 2014). “Long-term change in the cyclotron line energy in Hercules X-1”. In: A&A 572, A119, A119. DOI: `10.1051/0004-6361/201424203`. arXiv: `1410.3647 [astro-ph.HE]`.

Strömgren, B. (May 1939). “The Physical State of Interstellar Hydrogen.” In: ApJ 89, p. 526. DOI: `10.1086/144074`.

Sturm, R. et al. (Jan. 2012). “A new super-soft X-ray source in the Small Magellanic Cloud: Discovery of the first Be/white dwarf system in the SMC?” In: A&A 537, A76, A76. DOI: `10.1051/0004-6361/201117789`. arXiv: `1112.0176 [astro-ph.HE]`.

Sturner, S. J. and C. D. Dermer (July 1996). “On the Nature of the Bursting X-Ray Pulsar GRO J1744-28”. In: ApJ 465, p. L31. DOI: `10.1086/310126`. eprint: `astro-ph/9602102`.

Suchy, S. et al. (Feb. 2012). “Broadband Spectroscopy Using Two Suzaku Observations of the HMXB GX 301-2”. In: ApJ 745, 124, p. 124. DOI: `10.1088/0004-637X/745/2/124`. arXiv: `1111.2088 [astro-ph.HE]`.

Sugizaki, M. et al. (Nov. 2011). “In-Orbit Performance of MAXI Gas Slit Camera (GSC) on ISS”. In: PASJ 63, p. 635. DOI: `10.1093/pasj/63.sp3.S635`. arXiv: `1102.0891 [astro-ph.IM]`.

Sugizaki, M. et al. (Apr. 2015). “Luminosity and spin-period evolution of GX 304$-$1 during outbursts from 2009 to 2013 observed with the MAXI/GSC, RXTE/PCA, and Fermi/GBM”. In: *accepted for PASJ [arXiv e-prints: 1504.04895]*. arXiv: `1504.04895 [astro-ph.HE]`.

Sundqvist, J. O. and S. P. Owocki (Jan. 2013). “Clumping in the inner winds of hot, massive stars from hydrodynamical line-driven instability simulations”. In: MNRAS 428, pp. 1837–1844. DOI: `10.1093/mnras/sts165`. arXiv: `1210.1861 [astro-ph.SR]`.

Sundqvist, J. O., J. Puls, and A. Feldmeier (Jan. 2010). “Mass loss from inhomogeneous hot star winds. I. Resonance line formation in 2D models”. In: A&A 510, A11, A11. DOI: `10.1051/0004-6361/200912842`. arXiv: `0911.3361 [astro-ph.SR]`.

Tananbaum, H. et al. (June 1972). “Discovery of a Periodic Pulsating Binary X-Ray Source in Hercules from UHURU”. In: ApJ 174, p. L143. DOI: `10.1086/180968`.

Tavani, M. et al. (Apr. 2008). “The AGILE space mission”. In: *Nuclear Instruments and Methods in Physics Research A* 588, pp. 52–62. DOI: `10.1016/j.nima.2008.01.023`.

Titarchuk, L. (Oct. 1994). “Generalized Comptonization models and application to the recent high-energy observations”. In: ApJ 434, pp. 570–586. DOI: `10.1086/174760`.

Tomida, H. et al. (Apr. 2011). “Solid-State Slit Camera (SSC) Aboard MAXI”. In: PASJ 63, pp. 397–405. DOI: `10.1093/pasj/63.2.397`. arXiv: `1101.3651 [astro-ph.IM]`.

Tousey, R., K. Watanabe, and J. D. Purcell (Aug. 1951). “Measurements of Solar Extreme Ultraviolet and X-Rays from Rockets by Means of a $CoSO_4$:Mn Phosphor”. In: *Physical Review* 83, pp. 792–797. DOI: `10.1103/PhysRev.83.792`.

Trümper, J. et al. (1977). “Evidence for strong cyclotron emission in the hard X-ray spectrum of HER X-1”. In: *Mitteilungen der Astronomischen Gesellschaft Hamburg* 42, pp. 120–126.

Tsygankov, S. S. et al. (Sept. 2006a). “V0332+53 in the outburst of 2004-2005: luminosity dependence of the cyclotron line and pulse profile”. In: MNRAS 371, pp. 19–28. DOI: `10.1111/j.1365-2966.2006.10610.x`. eprint: `astro-ph/0511237`.

– (Sept. 2006b). “V0332+53 in the outburst of 2004-2005: luminosity dependence of the cyclotron line and pulse profile”. In: *MNRAS* 371, pp. 19–28.

– (June 2007). “4U 0115+63 from RXTE and INTEGRAL data: Pulse profile and cyclotron line energy”. In: *Astronomy Letters* 33, pp. 368–384.

Ubertini, P. et al. (Nov. 2003). “IBIS: The Imager on-board INTEGRAL”. In: A&A 411, pp. L131–L139. DOI: `10.1051/0004-6361:20031224`.

Van Horn, H. M. (2015). *Unlocking the Secrets of White Dwarf Stars.* DOI: `10.1007/978-3-319-09369-7`.

van Kerkwijk, M. H. et al. (Nov. 1995). “Spectroscopy of HD77581 and the mass of VELA X-1.” In: A&A 303, p. 483. eprint: `astro-ph/9505070`.

Vasco, D., D. Klochkov, and R. Staubert (Aug. 2011). “Hercules X-1: the positive cyclotron line energy/luminosity correlation”. In: A&A 532, A99, A99. DOI: `10.1051/0004-6361/201116863`. arXiv: `1107.1118 [astro-ph.HE]`.

Vasco, D. et al. (Feb. 2013). “Pulse phase and precession phase resolved spectroscopy of Hercules X-1: studying a representative Main-On with RXTE”. In: A&A 550, A111, A111. DOI: `10.1051/0004-6361/201220181`. arXiv: `1301.3378 [astro-ph.HE]`.

Vedrenne, G. et al. (Nov. 2003). “SPI: The spectrometer aboard INTEGRAL”. In: A&A 411, pp. L63–L70. DOI: `10.1051/0004-6361:20031482`.

Verbunt, F. and E. P. J. van den Heuvel (1995). “Formation and evolution of neutron stars and black holes in binaries.” In: *X-ray Binaries*, pp. 457–494.

Vink, J. (Dec. 2012). “Supernova remnants: the X-ray perspective”. In: A&A Rev. 20, 49, p. 49. DOI: `10.1007/s00159-011-0049-1`. arXiv: `1112.0576 [astro-ph.HE]`.

Voges, W. et al. (Dec. 1982). “Cyclotron lines in the hard X-ray spectrum of Hercules X-1”. In: ApJ 263, pp. 803–813. DOI: `10.1086/160550`.

Walder, R., D. Folini, and G. Meynet (May 2012). “Magnetic Fields in Massive Stars, Their Winds, and Their Nebulae”. In: Space Sci. Rev. 166, pp. 145–185. DOI: `10.1007/s11214-011-9771-2`. arXiv: `1103.3777 [astro-ph.SR]`.

Watanabe, S. et al. (Nov. 2006). “X-Ray Spectral Study of the Photoionized Stellar Wind in Vela X-1”. In: ApJ 651, pp. 421–437. DOI: `10.1086/507458`. eprint: `astro-ph/0607025`.

Watson, M. G. and R. E. Griffiths (Mar. 1977). “Ariel V Sky Survey Instrument - Extended observations of 3U 0900-40”. In: MNRAS 178, pp. 513–524.

Weekes, T. C. (2003). *Very high energy gamma-ray astronomy.*

Weidenspointner, G. et al. (Nov. 2003). “First identification and modelling of SPI background lines”. In: A&A 411, pp. L113–L116. DOI: `10.1051/0004-6361:20031209`.

Weisskopf, M. C. et al. (July 2000). “Chandra X-ray Observatory (CXO): overview”. In: *Society of Photo-Optical Instrumentation Engineers (SPIE) Conference Series*. Ed. by J. E. Truemper and B. Aschenbach. Vol. 4012. Society of Photo-Optical Instrumentation Engineers (SPIE) Conference Series, pp. 2–16. eprint: `arXiv:astro-ph/0004127`.

Winkler, C. et al. (Nov. 2003). “The INTEGRAL mission”. In: A&A 411, pp. L1–L6. DOI: `10.1051/0004-6361:20031288`.

Wolschin, G. (2003). “Thermonuclear Processes in Stars and Stellar Neutrinos”. In: *Time, Quantum and Information*. Ed. by L. Castell and O. Ischebeck, p. 115.

Woltjer, L. (Oct. 1964). “X-Rays and Type i Supernova Remnants.” In: ApJ 140, pp. 1309–1313. DOI: `10.1086/148028`.

Woosley, S. E., A. Heger, and T. A. Weaver (Nov. 2002). “The evolution and explosion of massive stars”. In: *Reviews of Modern Physics* 74, pp. 1015–1071. DOI: `10.1103/RevModPhys.74.1015`.

Yakovlev, Dmitrii G et al. (2013). “Lev Landau and the concept of neutron stars”. In: *Physics-Uspekhi* 56.3, p. 289. URL: `http://stacks.iop.org/1063-7869/56/i=3/a=289`.

Yamamoto, T. et al. (Nov. 2011). “Discovery of a Cyclotron Resonance Feature in the X-Ray Spectrum of GX 304-1 with RXTE and Suzaku during Outbursts Detected by MAXI in 2010”. In: PASJ 63, p. 751. arXiv: `1102.4232 [astro-ph.HE]`.

Yamamoto, T. et al. (Jan. 2012). “MAXI/GSC detects the onset of a recurrent outburst of GX 304-1”. In: *The Astronomer’s Telegram* 3856, p. 1.

Zel’dovich, Y. B. and N. I. Shakura (Oct. 1969). “X-Ray Emission Accompanying the Accretion of Gas by a Neutron Star”. In: Soviet Ast. 13, p. 175.

A

Appendix A

Here it is reported the entire (MJD $= 55134.125 \div 56673.375$) *MAXI*/GSC light curve of Vela X-1 in the $4 - 10\,\mathrm{keV}$ energy band. The time resolution is of 6 h.

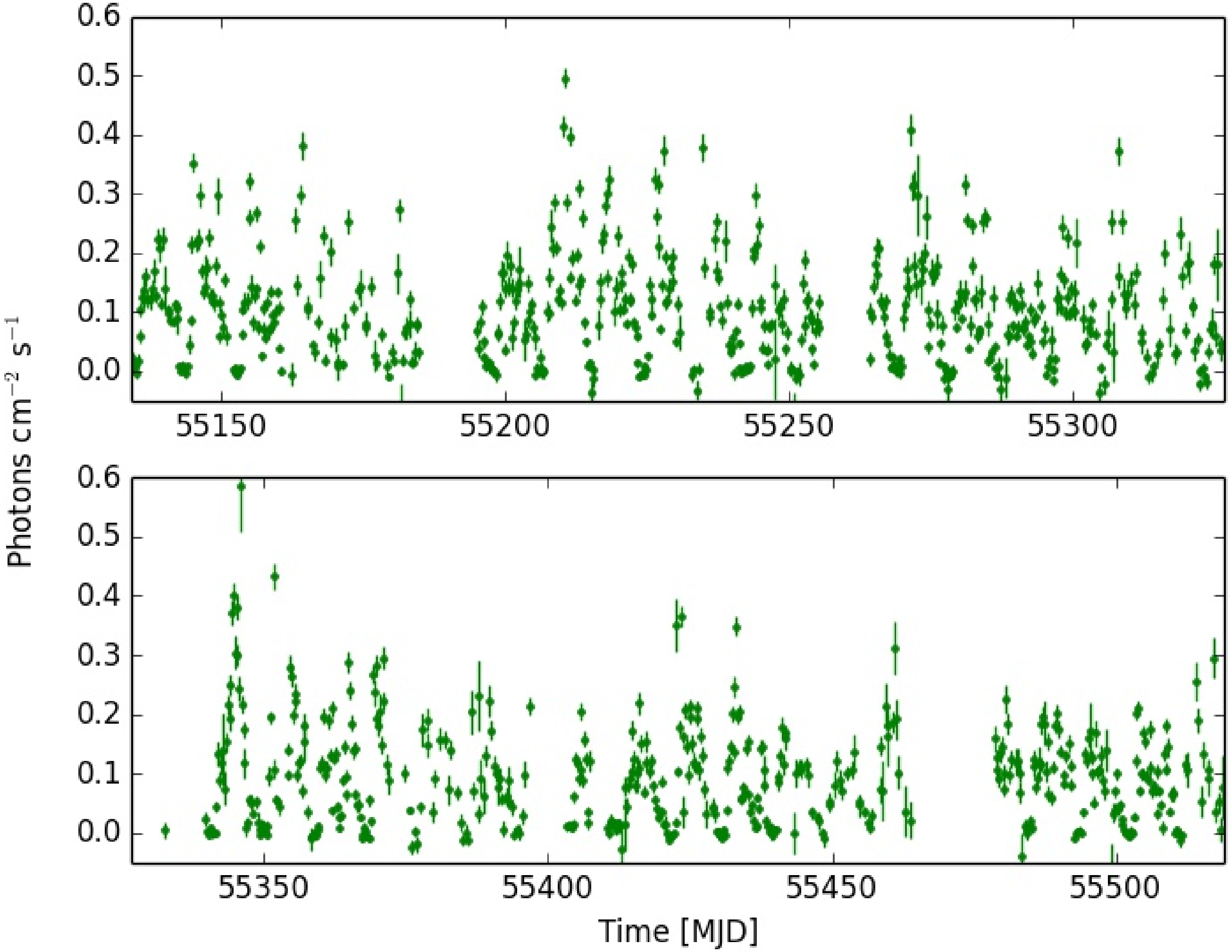

Photons cm^{-2} s^{-1}
0.6
0.5
0.4
0.3
0.2
0.1
0.0
55150
55200
55250
55300
0.6
0.5
0.4
0.3
0.2
0.1
0.0
55350
55400
55450
55500
Time [MJD]

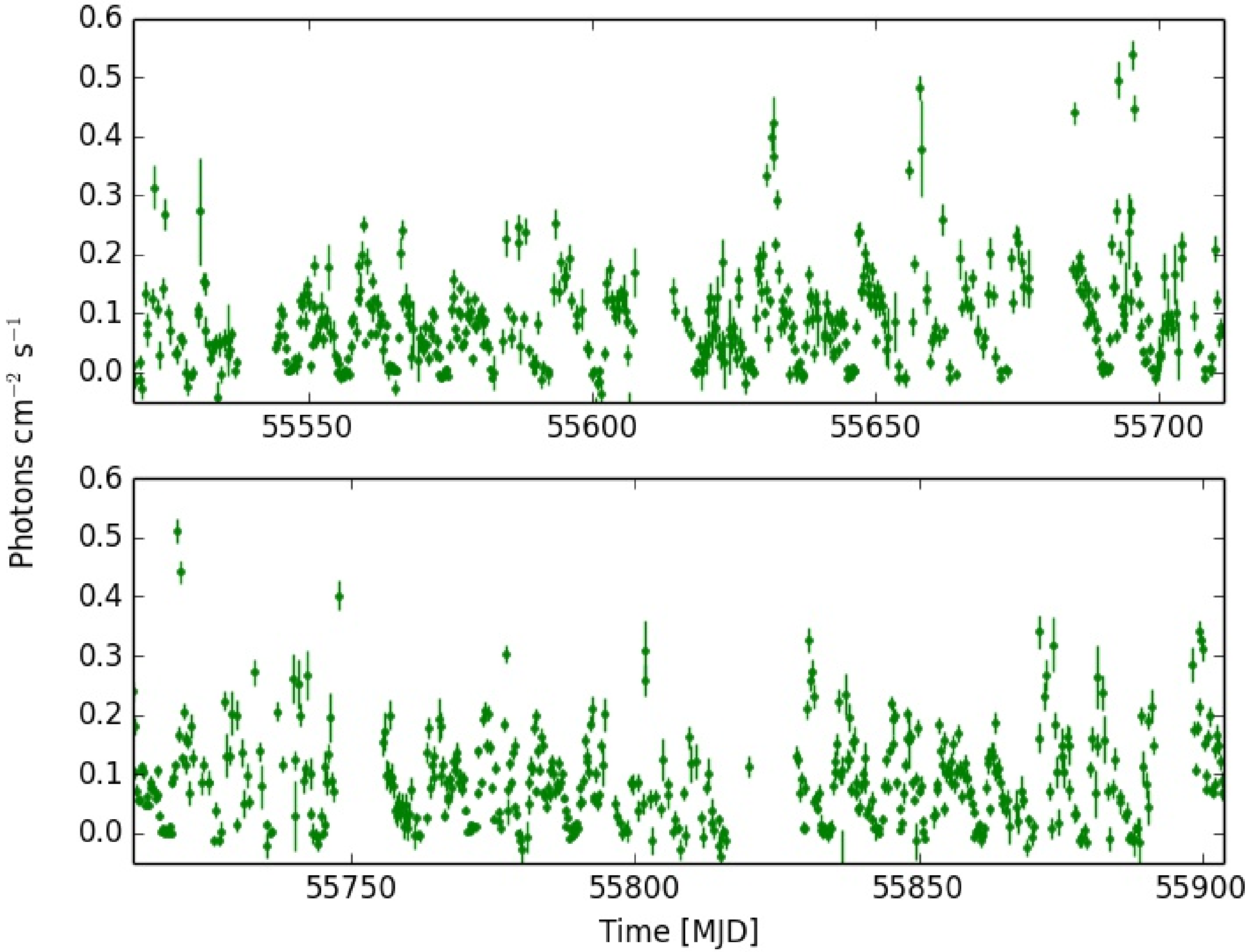
0.6
0.5
0.4
0.3
0.2
0.1
0.0
55550
55600
55650
55700
55750
55800
55850
55900
Photons cm^{-2} s^{-1}
Time [MJD]

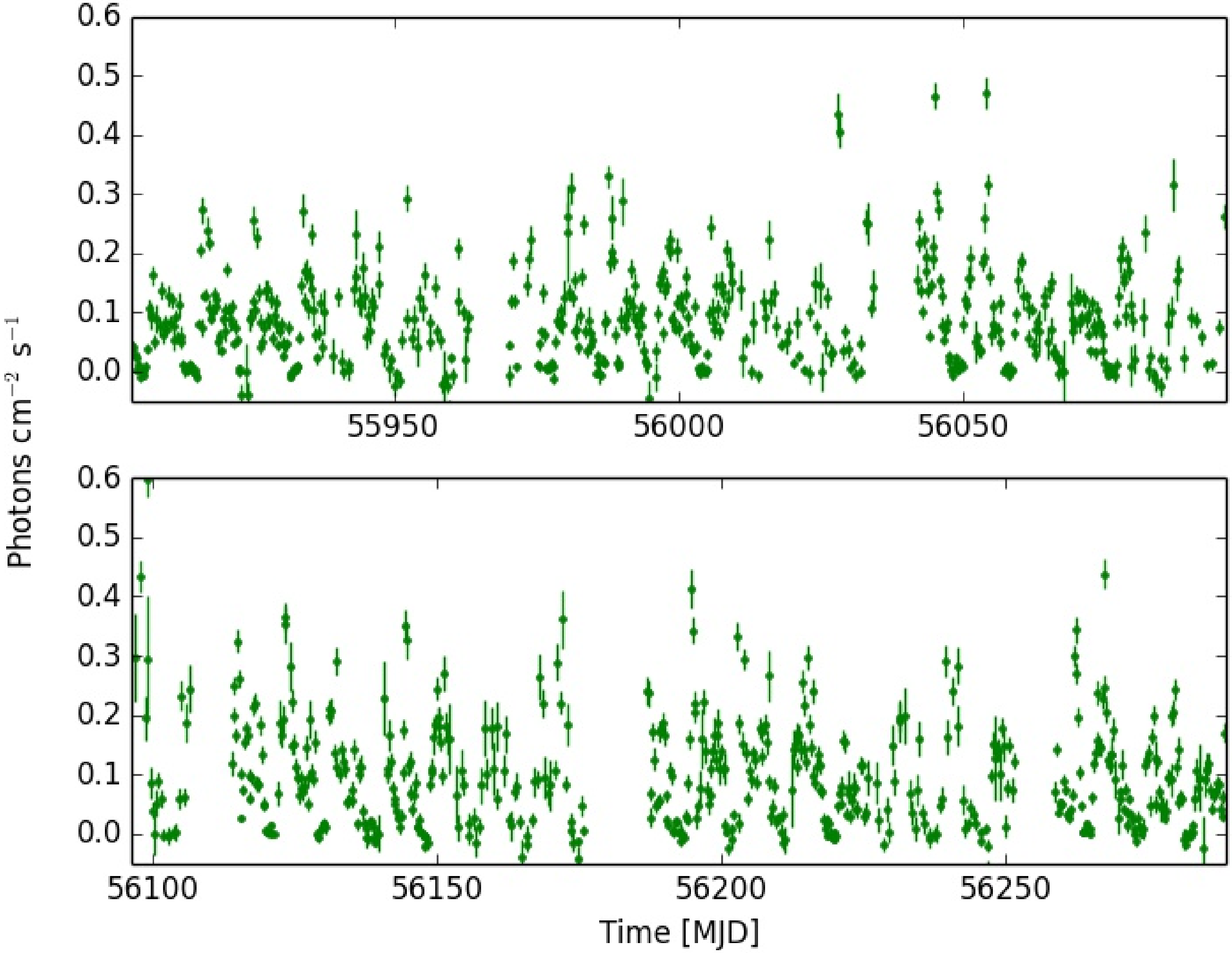
Photons cm^{-2} s^{-1}
0.6
0.5
0.4
0.3
0.2
0.1
0.0
55950
56000
56050
56100
56150
56200
56250
Time [MJD]

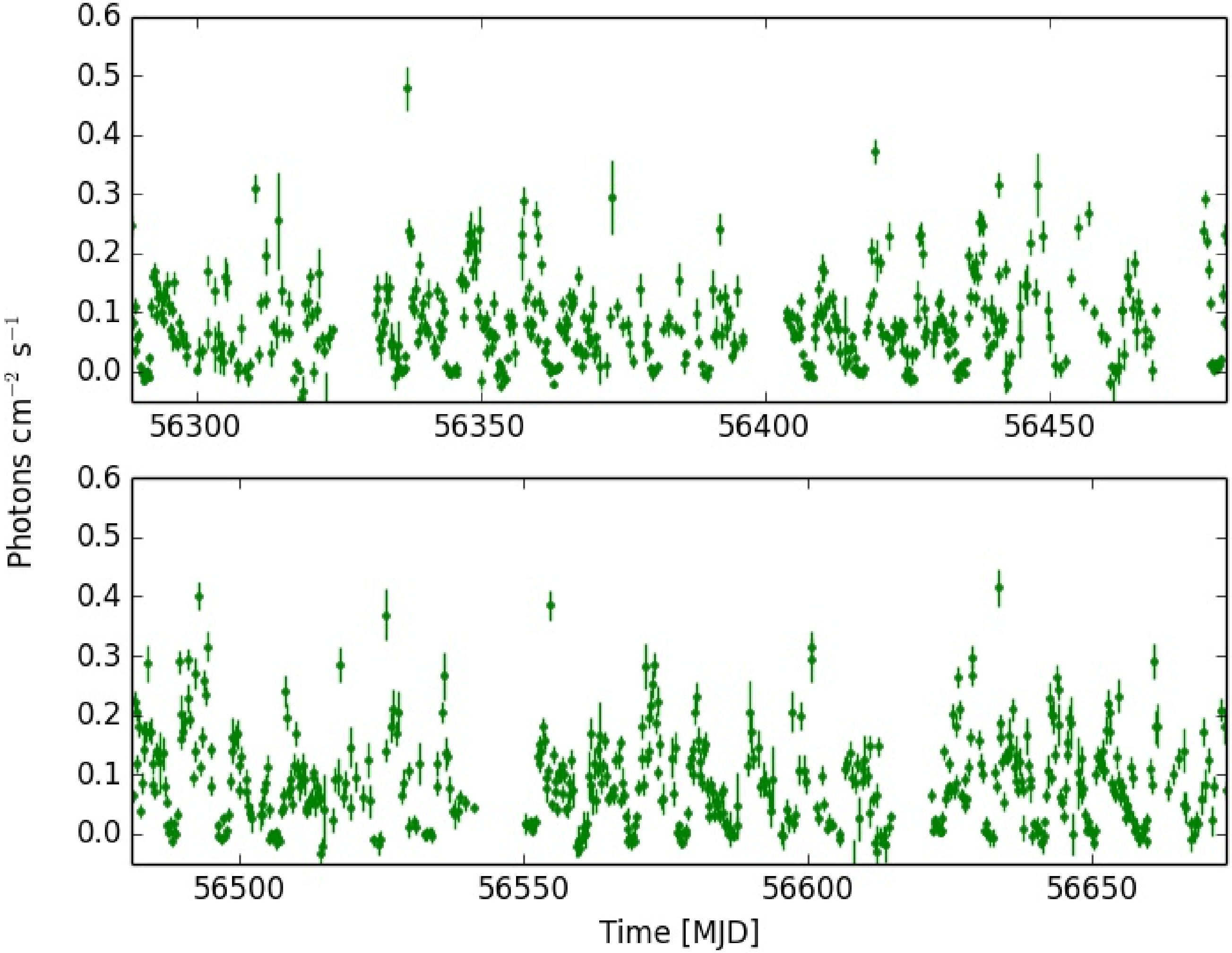
0.6
0.5
0.4
0.3
0.2
0.1
0.0
56300
56350
56400
56450
0.6
0.5
0.4
0.3
0.2
0.1
0.0
56500
56550
56600
56650
Photons cm^{-2} s^{-1}
Time [MJD]

ACKNOWLEDGEMENTS

Many people have contributed to make this work possible: to them I want to express my sincerest gratitude. First of all, I want to thank my supervisor Prof. Dr. Andrea Santangelo, who gave me the possibility of carrying out my own research in the first place. He always found time to share his professional experience and knowledge with me, either in a technical or a practical or a phylosophycal way. His guidance has been essential for this work, and for a deep understanding of "the physics beyond the numbers". I would additionally like to deeply thank Dmitry Klochkov, who helped me in countless ways to grow as a professional astronomer, and carefully checked every step of this work, with passion and patience.

I am indebted to the entire MAXI team in RIKEN, and in particular to Makishima-sensei and Mihara-san, for giving me the opportunity to carry out part of my Ph.D. project in collaboration with them, for their hospitality and their help with the realization of an important piece of work. My experience with the MAXI team has been very exciting and gave me the invaluable advantage to work with one of the most active and productive science teams in Japan: their professionality and their approach to science will always be part of my scientific background.

I feel very honoured to have worked with Prof. Dr. Rüdiger Staubert at IAAT, whose still and clear way of thinking and expressing himself I greatly admire. I am also grateful to Lorenzo Ducci and Victor Doroshenko, with whom I have had important discussions about this work and physics in a wider sense. I want to thank Chris Tenzer because my life in Tübingen would have been much harder without his help. I am also greatful to Sebastian Diebold who volunteered to translate in German the abstract of this thesis. Also, I am grateful to all my colleagues at IAAT: everybody has been important, in one way or another. Finally, I want to thank my office mates at IAAT, with whom I shared the every-day life in our common journey: Victor and Davide, Sara and Gabi, Jonathan, and Yudong!

Besides my working life, I want to thank my friends, who are always there for me in the good as well as in the less good moments, and especially I thank Agostino, Claudia and Iljia, plus all my Tübingen friends, especially Marius, Timo and Rita, who made me happy to live here.

My hearthful thanks are for Daniele: without him I do not know where I would be now.

Finally, my deepest thanks go to my family, to my Brothers Matteo and Danilo, with whom I share so many things despite of the distance, and to my parents Antonio and Rosalba, who always put their trust in me and encouraged me to choose the Astronomy life in the first place, opening doors wide for me, that I might do one of the most fascinating jobs in the Universe!
To you this work is dedicated.

Grazie Ma e Pa per tutto quello che avete fatto e che mi avete dato l'opportunità di fare. Non ci sono parole per descrivere quanto vi sono riconoscente, per tutta la fiducia, il sostegno, e l'affetto che mi avete dimostrato.

Dedico questo lavoro a voi.

Curriculum Vitae

4.3.1983	Born in Catanzaro, Italy
1989 - 1994	Elementary School (Catanzaro, Italy)
1994 - 1997	Middle School (Catanzaro, Italy)
1997 - 2002	High School (Catanzaro, Italy)
2007	Bc. in Physics and Astrophysics University "La Sapienza" of Rome
2011	Mc. in Astronomy and Astrophysics University "La Sapienza" of Rome
2012 – 2014	Scientific employee at Eberhard-Karls-Universität Tübingen Institut für Astronomie und Astrophysik (IAAT) Tübingen, Germany
Jan 2014 – Dec. 2014	International Program Associate MAXI Team - RIKEN (Japan)
2015 –	Scientific employee at Eberhard-Karls-Universität Tübingen Institut für Astronomie und Astrophysik (IAAT) Tübingen, Germany

List of Figures

1.1 First detection of Sco X-1 . . . 2

2.1 Proton-proton chain reaction . . . 6
2.2 Onion-like model of shell nuclear fusion . . . 8
2.3 Measured and estimated masses of Neutron Stars . . . 9
2.4 Interior model of a Neutron Star . . . 10

3.1 Roche equipotential surfaces for a binary system . . . 16
3.2 Illustration of mass transfer mechanism in a LMXB . . . 18
3.3 Sketch of the Bondi–Hoyle–Lyttleton accretion geometry . . . 20
3.4 Streamlines of stellar wind accretion onto a Neutron Star . . . 21
3.5 Sketch of the different structures in the Vela X-1 binary system . . . 22
3.6 Schematic model of a Be/X-ray binary system . . . 23
3.7 Sketch of a strongly magnetized NS accreting from a disk . . . 25
3.9 Accretion geometries and radiation patterns of accreting columns . . . 27
3.10 Energy-resolved X-ray pulse profiles of Her X-1 . . . 28
3.11 X-ray spectrum of Her X-1 cyclotron line . . . 31

4.1 INTEGRAL spacecraft . . . 37
4.2 IBIS imaging system . . . 38
4.3 The working principle of a coded mask. . . . 39
4.4 The JEM-X detector . . . 41
4.5 The SPI detector . . . 42
4.6 The SPI background . . . 43
4.7 INTEGRAL dithering patterns . . . 45
4.8 The GSC cameras . . . 46
4.9 A GSC camera unit . . . 47
4.10 The GSC cameras viewing properties . . . 48
4.11 GSC exposure maps . . . 49

5.1 *Swift*/BAT light curve of GX 304-1 . . . 52
5.2 *Swift*/BAT light curve of GX 304-1 during the 2012 January - February outburst . . . 54
5.3 A comparison of GX 304-1 2012 outbursts . . . 55
5.4 The pulse period derivative of GX 304-1 . . . 58
5.5 ISGRI pulse profiles of GX 304-1 . . . 59
5.6 JEM-X pulse profiles of GX 304-1 . . . 60
5.7 Time evolution of the W fluorescence line position with OSA 9 and OSA 10 63
5.8 Gain corrected energy of the W reference line complex . . . 64
5.9 Cyclotron line centroid energy versus luminosity for GX 304-1 with OSA 9 and OSA 10 . . . 65
5.10 Photon index as a function of the flux . . . 66
5.11 Phase-averaged INTEGRAL spectra of GX 304-1at different luminosity levels . . . 68
5.12 χ^2-contour plots of the folding energy and the photon index . . . 69

5.13 *Top:* The unfolded spectrum of the phase bin $0.0-0.2$ from revolution 1132 modeled with a power-law/rolloff model including the cyclotron line and an additional Gaussian component to account for a bump around 35 keV (see text). JEM-X (red and green), ISGRI (black), and SPI (blue) data are used. *Middle:* The residuals of a fit with the model without the additional Gaussian component. Large residuals appear around the cut-off energy. *Bottom:* The residuals after including the Gaussian emission component to model the bump. 73
5.14 Best fit parameters of the GX 304-1 phase-resolved spectra for the Rev. 1136 74
5.15 Best fit parameters of the GX 304-1 stacked phase-resolved spectra . . 75

6.1 Orbital sketch of the binary system Vela X-1 as observed from the Earth 78
6.2 Sketch of the different structures in the stellar wind of Vela X-1 79
6.3 The folded orbital light curves of Vela X-1 in the $4-10$ and $10-20$ keV 82
6.4 Average orbital profiles of the double-peaked and the standard samples in $4-10$ keV and $10-20$ keV 83
6.5 Distribution of the standard deviations at each orbital phase 86
6.6 Distributions of the medians and relative skewness in the X, Y and Z phase bins 87
6.7 Orbital profile obtained by stacking members with high negative residuals in the X phase bin, and low (absolute) residuals in the Y and Z phase bins 88
6.8 Scatter plots for data points in the Y phase bin 89
6.9 Correlation coefficient ρ as a function of the orbital phase calculated for $\Delta/t \sim 6$ hours 90
6.10 Correlation coefficient ρ as a function of the orbital phase calculated for $\Delta/t \sim 12$ hours 90
6.11 Average correlation coefficient ρ as a function of the time separation . . 91
6.12 Illustration of partial covering model 92
6.13 χ^2-contour plots for the Vela X-1 double-peaked sample 95
6.14 Orbital phase-resolved spectra of the double-peaked sample 96
6.15 χ^2-contour plots for the Vela X-1 standard sample 98
6.16 Orbital phase-resolved spectra of the standard sample 99

7.1 Representative pulse profiles for different geometrical configurations. . . 105
7.2 Geometry of the accretion column as a function of the luminosity . . . 107
7.3 Comparison of the theoretical critical luminosity-E_{cyc} dependence to the data. 108
7.4 Cyclotron line energy as a function of the velocity profile 109
7.5 Hardness/intensity diagram for GX 304-1 during the analyzed outburst 111
7.6 Column density as a function of the orbital phase 115
7.7 Color-coded map of electron density in Vela X-1 117
7.8 Density and velocity variations in OB-stars winds 120

8.1 Optical spectrum of V850 Cen 125
8.2 Radial velocities of absorption lines in 2S 0114+650 as a function of the orbital phase 126
8.3 AAT optical spectrum of V850 Cen 128

8.4 χ^2-contour plots for Vela X-1 flux-resolved spectra 129